TECHNISCHE UNIVERSITÄT MÜNCHEN
Fakultät für Chemie
Lehrstuhl I für Technische Chemie

Investigation of the deactivation behavior of Ni-Al catalysts for CO_2 methanation

Stefan Hans Ewald

Vollständiger Abdruck der von der Fakultät für Chemie der Technischen Universität München zur Erlangung des akademischen Grades eines

Doktor-Ingenieurs (Dr.-Ing.)

genehmigten Dissertation.

Vorsitzender: Prof. Dr. Klaus Köhler

Prüfer der Dissertation: 1. Prof. Dr.-Ing. Kai-Olaf Hinrichsen
2. Prof. Dr.-Ing. Harald Klein

Die Dissertation wurde am 18.02.2019 bei der Technischen Universität München eingereicht und durch die Fakultät für Chemie am 09.07.2019 angenommen.

Danksagung

Mein besonderer Dank gilt Herrn Prof. Dr.-Ing. Kai-Olaf Hinrichsen für die Aufnahme in seinen Arbeitskreis und die Möglichkeit an dieser interessanten Themenstellung zu arbeiten. Außerdem möchte ich Herrn Prof. Hinrichsen für die wissenschaftliche Betreuung und das mir entgegengebrachte Vertrauen danken.

Besonderer Dank gilt auch Herrn Prof. Dr. Klaus Köhler für die Übernahme des Prüfungsvorsitzes und Herrn Prof. Dr.-Ing. Harald Klein für die Übernahme des Korreferats.

Ein großer Dank gilt meinen Arbeitskollegen und Freunden am Lehrstuhl für eine großartige Arbeitsatmosphäre. Vielen Dank an Julia, Chris, Johanna, Daniel, Jennie, Heidi, Thomas, Franz, Franz, Flo, Tassilo, David, Yefei, Matthias und Conny! Besonders bedanken möchte ich mich bei Sebastian und Philipp für Ihre Unterstützung bei Modellierungsproblemen sowie bei Thomas und Moritz für ihr kompetentes Fachwissen bei Fragen rund um die CO_2-Methanisierung.

Ein weiterer Dank gilt den Mitarbeitern der Elementaranalyse, der Feinmechanik- und der Elektronikwerkstatt für ihre teilweise sehr unkomplizierte Unterstützung. Weiterhin möchte ich mich bei Prof. Dr. Johannes Lercher, Prof. Dr. Andreas Jentys, Christoph, Edith sowie Prof. Dr. Klaus Köhler und Christoph für die kompetente Hilfe und Unterstützung bei der Durchführung und Auswertung der IR-Messungen bedanken. Auch möchte ich mich bei Prof. Dr. Thomas Fässler, Dr. Wilhelm Klein, Maria Müller und Henrik für die Einweisung in die Durchführung von Kapillarmessungen am XRD bedanken.

Zudem möchte ich allen Studenten für Ihre Unterstützung bei meiner Arbeit danken, insbesondere Sebastian und Michael für ihr großes Engagement.

Mein ganz besonderer Dank gilt meiner Familie und meiner Freundin Jasmine für die goße Unterstützung, ihren grenzenlosen Rückhalt und ihr großes Verständnis vor allem in schwierigen Zeiten während der Promotion.

Abstract

CO_2 methanation plays a central role in the power-to-gas (PTG) concept, which is an efficient technology for renewable energy storage. High standards have been defined for synthetic natural gas (SNG) to be fed into the natural gas grid. In order to meet these standard, namely a high conversion and product gas purity, highly selective and active catalysts have to be applied. In this context, supported Ni is of great interest due to its price, availability and high CH_4 selectivity. However, these catalysts are prone to deactivation under severe conditions typically present at high conversions, leading to a decrease in SNG quality. Therefore, thermostable catalyst systems have to be developed, which necessitates the knowledge of governing deactivation phenomena. With regard to CO_2 methanation, however, detailed deactivation studies are lacking. In this work, the deactivation of Ni-Al catalysts in CO_2 methanation is systematically investigated. Both a detailed characterization study as well as a kinetic description of deactivation are presented. In this context, also the interaction of the reactants CO_2 and H_2 with the catalyst is studied. Moreover, the chemisorption of N_2O for metallic Ni surface area determination is evaluated. The results are summarized in four chapters.

In the first chapter, the structure of the catalyst samples is studied by XRD and N_2 physisorption. The reduction behavior is investigated by means of TPR measurements in a TG-MS setup. Ni-Al catalysts of varying Ni loadings are synthesized via co-precipitation of the corresponding metal nitrate solutions at a constant pH 9 and 303 K followed by calcination in synthetic air. For reference purposes, NiO and $NiAl_2O_4$ are synthesized in the same way. Also incipient wetness impregnation of γ-Al_2O_3 with a Ni nitrate solution is applied for catalyst synthesis. XRD analysis reveals that the precursors after precipitation consist of mixed basic carbonates. The carbonate structure depends on the Ni content in the precursor. A takovite-like structure is observed in the sample with a Ni/Al molar ratio of 3/1. Calcination of the precipitated precursors at 723 K leads to the formation of Ni-Al mixed oxides with varying structure depending in the Ni content. Bunsenite and γ-Al_2O_3 are the only observable crystalline phases in impregnated samples after calcination independent from the Ni loading. N_2 physisorption measurements indicate mesoporosity of all samples with the porosity of NiO and $NiAl_2O_4$ being significantly lower as compared to the other samples. Multiple Ni species in all samples are observed by TPR. Precipitated catalysts exhibit at least two Ni species of varying crystallinity. The reducibility of these species decreases with rising Al content and calcination temperature. TPR reveals multiple, partly amorphous Ni species and strong-metal

support interactions in impregnated samples, hampering the reducibility in comparison to pure NiO.

The second chapter presents a characterization study of the active Ni phase and its surface area by means of H_2-TPD, pulsed and static H_2 chemisorption as well as N_2O chemisorption. H_2-TPD from 84 - 753 K is capable of completely characterizing the H_2 interaction with Ni-Al catalysts. Varying adsorption and pre-treatment conditions significantly affect the desorption pattern and imply reversible morphologic changes as well as a restructuring of the adsorbed hydrogen layer. Additionally, spillover effects and multiple overlapping desorption signals impede the calculation of the exposed Ni surface area. In contrast to this, pulsed H_2 adsorption leads to results which are in good agreement with static H_2 chemisorption and therefore can be applied for Ni surface area determination. N_2O chemisorption follows a three step process, comprising fast decomposition and oxygen uptake, oxide layer growth and subsequent layer thickening due to subsurface and bulk oxidation. Suppression of subsurface/bulk oxidation is achievable at temperatures between 190 and 195 K for Ni-Al systems and at temperatures within the range from 265 - 285 K for NiO. The ratio of oxygen atoms on the surface and the number of Ni surface atoms (O/Ni_S) is 0.38 ± 0.07 in the first and 0.96 ± 0.05 in the latter case. Those conditions can be applied for Ni surface area determination. The extent of Ni subsurface/bulk oxidation does not change upon switching from N_2O adsorption in a continuous flow to titration.

In the third chapter, selected samples were aged for 165 h at 8 bar and 523, 573 as well as 623 K under hydrothermal conditions. Periodic activity measurements under kinetically controlled conditions allowed for following the deactivation process with time on stream (TOS). Fresh and deactivated samples are characterized by means of XRD, XPS, H_2-TPD, CO_2-TPD, pulsed H_2 and CO_2 chemisorption, N_2 physisorption and FT-IR measurements. All samples investigated exhibit a severe activity loss within the first 25 h on stream. Thereby, the stability of Ni-Al mixed oxide catalysts increases with decreasing Ni loading at the expense of the activity. The stability of an impregnated system is lower as compared to a Ni-Al mixed oxide catalyst with a similar initial Ni surface area. Characterization results indicate that a loss of active Ni surface area and the BET surface area are predominant deactivation mechanisms in impregnated catalysts. A loss of medium basic sites, a reduction of CO_2 adsorption capacity and structural changes are additional deactivation phenomena for precipitated Ni-Al mixed oxide systems. Carbon formation has a negligible influence on deactivation under the experimental conditions applied. Structure-activity correlations indicate a complex interplay of governing deactivation mechanisms but also support structure sensitivity. The kind of active sites seems to remain unchanged upon aging but the site density decreases.

The fourth chapter presents a detailed investigation of the CO_2 interaction with the Ni-Al catalysts synthesized. For this, FT-IR and CO_2-TPD are applied next to pulsed and static CO_2 chemisorption. Results show that carbonates are formed upon CO_2 adsorption under flow close to room temperature. Under static adsorption conditions, additional Ni-CO species are formed. The binding strength of the carbonates to the catalyst surface increases in the order bicarbonate < bidentate carbonate < monodentate carbonate < bridged/"organic"-like species. Weak

basic sites in precipitated samples forming bicarbonate decline with rising Ni content, whereas medium and strong basic sites forming bidentate, monodentate and bridged/"organic"-like species increase. The Ni loading only has a minor influence on the catalyst basicity of impregnated systems. A high density of weak basic sites is observed in these systems. A more complete characterization of the CO_2 interaction with Ni-Al catalysts is obtained when conducting TPD measurements within the range from 218 - 753 K. The CO_2 uptake determined from pulsed adsorption and subsequent TPD, respectively, is significantly lower than results obtained from static CO_2 chemisorption.

Kurzzusammenfassung

Die CO_2-Methanisierung spielt eine zentrale Rolle im Power-to-gas (PTG) Prozess, einem effizienten Speicherkonzept für erneuerbare Energien. Dabei gelten hohe Ansprüche an die Qualität des erzeugten CH_4, um es in das Erdgasnetz einspeisen zu können. Um die geforderten hohen Umsätze und Produktgasreinheiten zu gewährleisten, müssen sehr selektive und aktive Katalysatorsysteme eingesetzt werden. Aufgrund ihrer Wirtschaftlichkeit und hohen CH_4-Selektivität kommt dabei geträgerten Nickelkatalysatoren große Bedeutung zu. Allerdings kommt es bei solchen Systemen unter harschen Reaktonsbedingungen, wie sie typischerweise bei hohen Umsätzen auftreten, zu schneller Desaktivierung, wodurch die Anforderungen an die Produktgasreinheit nicht mehr erfüllt werden können. Deshalb ist die Entwicklung von stabilen und robusten Katalysatoren unabdingbar und setzt ein breites Verständnis über vorherrschende Desaktivierungsmechanismen voraus. Allerdings gibt es bisher nur wenige detaillierte Studien zur Katalysatordesaktivierung bei der CO_2-Methanisierung. In dieser Arbeit wird daher die Desaktivierung von Ni-Al-Katalysatoren in der CO_2-Methanisierung systematisch untersucht. Dabei wird neben einer detaillierten Charakterisierungsstudie auch ein Modell zur kinetischen Beschreibung des Desaktivierungsverhaltens abgeleitet. In diesem Zusammenhang wird auch die Wechselwirkung der beiden Reaktanden, CO_2 und H_2, mit den Katalysatoren untersucht. Darüber hinaus wird die Eignung der N_2O-Chemisorption zur Bestimmung der Nickeloberfläche bewertet. Die Ergebnisse sind in vier Kapiteln zusammengefasst.

Im ersten Kapitel wird die Struktur der eingesetzten Katalysatorsysteme mittels XRD und N_2-Physisorption untersucht. TPR-Messungen geben Aufschluss über das Reduktionsverhalten der Katalysatoren. Die Synthese von Ni-Al-Katalysatoren erfolgt über Ko-Fällung der entsprechenden Metallnitrate bei einem konstantem pH-Wert von 9 und 303 K sowie nachfolgender Kalzinierung in synthetischer Luft. Auf gleiche Weise wurden NiO und $NiAl_2O_4$ als Referenzmaterialien hergestellt. Geträgerte Nickelsysteme werden auch über Kapillarimprägnierung von γ-Al_2O_3 mit einer Nickelnitrat-Lösung synthetisiert. Die XRD-Analyse zeigt, dass das Fällungsprodukt aus Mischcarbonaten besteht. Die Carbonatstruktur hängt dabei vom Nickelanteil ab. Eine takovitartige Struktur liegt im System mit einem molaren Ni/Al-Verhältnis von 3/1 vor. Kalzinierung bei 723 K führt zur Bildung von Ni-Al-Mischoxiden, wobei auch die Oxidstruktur vom Ni/Al-Verhältnis im Katalysator abhängt. In imprägnierten Systemen sind Bunsenit und γ-Al_2O_3 die einzigen, über XRD detektierbaren, kristallinen Phasen nach dem Kalzinieren, unabhängig von der Nickelbeladung. Sämtliche Proben weisen

Mesoporen auf, wobei die Porosität von NiO und $NiAl_2O_4$ deutlich unter den entsprechenden Werten der restlichen Proben liegt. TPR-Messungen belegen das Vorhandensein von mindestens zwei Spezies unterschiedlicher Kristallinität in gefällten Systemen. Die Reduzierbarkeit dieser Spezies nimmt mit zunehmendem Aluminiumgehalt und steigender Kalziniertemperatur ab. Auch in imprägnierten Systemen deuten TPR-Ergebnisse auf mehrere, teilweise amorphe, Ni-Spezies sowie starken Metall-Träger-Wechselwirkungen, welche die Reduzierbarkeit dieser Katalysatorsysteme deutlich verringern im Vergleich zu reinem NiO.

Im zweiten Kapitel wird die aktive Nickelphase sowie ihre Oberfläche mittels H_2-TPD, gepulster und statischer H_2-Chemisorption sowie N_2O-Chemisorption charakterisiert. H_2-TPD von 84 bis 753 K ermöglicht die vollständige Beschreibung der H_2-Wechselwirkung mit Ni-Al-Katalysatoren. Änderungen der Adsorptionsbedingungen sowie der Katalysatorvorbehandlung haben dabei signifikanten Einfluss auf das resultierende Desorptionsspektrum und deuten auf reversible morphologische Änderungen der Nickeloberfläche und auf eine Restrukturierung der adsorbierten Wasserstoffschicht. Zusätzlich erschweren auch Spillover-Effekte und sich überlagernde Desorptionssignale die quantitative Bestimmung der exponierten Nickeloberfläche. Im Gegensatz dazu führt die gepulste H_2-Chemisorption zu Ergebnissen in guter Übereinstimmung mit denen der statischen H_2-Chemisorption und kann folglich für die Bestimmung der Nickeloberfläche angewendet werden. Die N_2O-Chemisorption folgt einem Drei-Stufen-Prozess, bestehend aus einer schnellen Zersetzung bzw. Sauerstoffaufnahme, Wachstum der Oxidschicht sowie nachfolgender Subsurface- und Bulk-Oxidation. Die Unterdrückung von Subsurface/Bulk-Oxidation von Ni-Al-Systemen ist bei Temperaturen zwischen 190 und 195 K möglich, wohingegen bei NiO dies schon bei Temperaturen zwischen 265 und 285 K der Fall ist. Das Verhältnis der adsorbierten Sauerstoffatome zur Anzahl der Nickeloberflächenatome (O/Ni_S) ist 0.38 ± 0.07 im ersteren und 0.96 ± 0.05 im letzteren Fall. Diese Bedingungen können für die Bestimmung der Nickeloberfläche eingesetzt werden. Der N_2O-Adsorptionsmodus (Adsorption im Gasfluss oder über Titration) hat keinen Einfluss auf das Ausmaß an Subsurface/Bulk-Oxidation.

Im dritten Beitrag werden ausgewählte Proben für 165 h bei 523, 573 und 623 K unter hydrothermalen Bedingungen gealtert. Periodische Aktivitätsmessungen unter kinetisch kontrollierten Bedingungen ermöglichen die Nachverfolgung der Desaktivierung mit der Standzeit der Katalysatoren. Frische und gealterte Proben werden mittels XRD, XPS, H_2-TPD, CO_2-TPD, gepulste H_2- und CO_2-Chemisorption sowie N_2-Physisorptions- und FT-IR-Messungen charakterisiert. Alle Proben zeigen einen deutlichen Aktivitätsverlust innerhalb der ersten 25 h. Die Stabilität von Ni-Al-Mischoxid-Katalysatoren steigt mit abnehmendem Nickelgehalt zu Lasten der Katalysatoraktivität. Die Stabilität eines imprägnierten Systems ist niedriger im Vergleich zu einem Mischoxid mit einer ähnlichen anfänglichen Nickeloberfläche. Charakterisierungsergebnisse zeigen, dass der Verlust an aktiver Nickel- und BET-Oberfläche dominierende Desaktivierungsmechanismen in imprägnierten Ni-Al-Systemen sind. Zusätzlich tragen ein Verlust an mittelstarken basischen Zentren und eine Abnahme an CO_2-Adsorptionskapazität zur Desaktivierung von Ni-Al-Mischoxid-Katalysatoren bei. Dabei treten auch strukturellen Änderungen

auf. Der Beitrag von Kohlenstoffablagerungen zur Desaktivierung ist unter den angewendeten Bedingungen vernachlässigbar. Die Analyse von Struktur-Aktivitäts-Beziehungen deutet auf ein komplexes Zusammenspiel mehrerer Desaktivierungsmechanismen und/oder Strukturensitivität. Die Art der aktiven Zentren bleibt unverändert. Deren Dichte nimmt jedoch ab.
Im vierten Kapitel wird die Wechselwirkung von CO_2 mit Ni-Al-Katalysatoren detailliert untersucht. Hierzu werden neben der gepulsten und statischen CO_2-Chemisorption auch FT-IR- und CO_2-TPD-Messungen eingesetzt. Die Ergebnisse zeigen, dass durch die CO_2-Adsorption nahe Raumtemperatur im Fluss Carbonate auf der Katalysatoroberfläche gebildet werden. Unter statischen Adsorptionsbedingungen werden zusätzlich Ni-CO-Spezies gebildet. Die Bindungsstärke der gebildeten Carbonate zur Oberfläche nehmen in der Reihenfolge Bicarbonat < bidentates Carbonat < monodentates Carbonat < gebrückte Carbonatspezies zu. In Ni-Al-Mischoxid-Katalysatoren nehmen schwach basische Zentren, die zur Ausbildung von Bicarbonat führen, mit zunehmendem Nickelgehalt ab. Mittel und stark basische Zentren, die bidentates und monodentates Carbonat sowie verbrückte Carbonatspezies bilden, nehmen dagegen zu. Nur ein schwacher Einfluss der Nickelbeladung auf die Basizität von imprägnierten Systemen wird beobachtet. In diesen Systemen ist die Dichte an schwach basischen Zentren am höchsten. CO_2-TPD im Temperaturbereich von 218 - 753 K ergibt ein vollständigeres Bild der CO_2-Wechselwirkung mit Ni-Al-Katalysatoren. Berechnete Werte für die CO_2-Aufnahme basierend auf gepulster CO_2-Chemisorption bzw. nachfolgender TPD liegen deutlich unter entsprechenden Ergebnissen der statischen CO_2-Chemisorption.

Contents

List of Figures

List of Tables

Nomenclature

Latin Symbols

a	lattice parameter	m
A_{N_2}	cross-sectional area of a N_2 molecule	m^2
a_{rel}	relative activity	-
$a_{rel,eq}$	relative activity in steady state	-
B	inflection point	-
c	lattice parameter	m
c	speed of light	$m\,s^{-1}$
C	BET constant	-
C_α	atomic carbon	-
C_β	polymeric, amorphous carbon	-
C_c	graphitic, crystalline, carbon	-
C_d	polymeric, amorphous carbon	-
C_v	vermicular carbon filaments, fibers and whiskers	-
D_a	axial dispersion coefficient	$m^2\,s^{-1}$
d_b	catalyst bed diameter	m
D_e	effective diffusion coefficient	$m^2\,s^{-1}$
d_{hkl}	interplanar distance	m
d_i	particle size of species i	m
d_i^0	initial particle size of species i	m
d_{Me}	average metal particle diameter	m
D_{Me}	metal dispersion	-
D_{Ni}	Ni dispersion	-
d_{Ni}	Ni crystallite size	m
d_P	average pore diameter	m
E_A	activation energy	$J\,mol^{-1}$
$E_{A,des}$	activation energy of desorption	$J\,mol^{-1}$
E_b	electron binding energy	eV
E_{kin}	kinetic energy of an electron	eV
E_p	photon energy	eV
f	shape factor	-

F	factor	-
ΔG_R^0	standard Gibbs free energy	$J\,mol^{-1}$
ΔH_R^0	standard reaction enthalpy	$J\,mol^{-1}$
h	Miller index	-
j	order	-
K	Scherrer constant	-
k	Miller index	-
k	rate constant	s^{-1}
$k_{d,0}$	pre-exponential factor	s^{-1}
$k_{0,des}$	pre-exponential factor of desorption	s^{-1}
k_d	rate constant of deactivation	s^{-1}
k_s	sintering constant	s^{-1}
l	number of metal atoms forming an active site	-
l	Miller index	-
L_b	catalyst bed length	m
m	reaction order	-
M	molar mass	$kg\,mol^{-1}$
m_{cat}	catalyst mass	kg
m_{CO_2}	reaction oder of CO_2	-
m_{H_2}	reaction oder of H_2	-
m_i	reaction oder of species i	-
m_{N_2}	mass of adsorbed N_2	kg
m_S	samples mass	kg
M_{Ni}	molar mass of Ni	$kg\,mol^{-1}$
n	diffraction order	-
N_A	Avogadro´s constant	mol^{-1}
$\dot{n}_{CH_4,in}$	CH_4 molar flow into the reactor	$mol\,s^{-1}$
$\dot{n}_{CH_4,out}$	CH_4 molar flow in the product gas	$mol\,s^{-1}$
$\dot{n}_{CO_2,in}$	CO_2 molar flow into the reactor	$mol\,s^{-1}$
$\dot{n}_{CO_2,out}$	CO_2 molar flow in the product gas	$mol\,s^{-1}$
N_H	amount of adsorbed H_2 molecules	mol
N_N	amount of released N_2 molecules	mol
N_{PM}	amount of adsorbed probe molecules	mol
Ni_S	number of Ni surface atoms	-
p	pressure	Pa
p_0	saturation pressure of probe gas	Pa
p_{CO_2}	CO_2 partial pressure	Pa
p_{H_2}	H_2 partial pressure	Pa
Q	volume flow	$m^3\,s^{-1}$
r	reaction rate	$mol\,s^{-1}$

r_0	initial reaction rate	$\mathrm{mol\,s^{-1}}$
r_{CH_4}	integral reaction rate	$\mathrm{mol\,s^{-1}}$
R	universal gas constant	$\mathrm{J\,mol^{-1}\,K^{-1}}$
R_p	particle radius	m
S	specific surface area for gas adsorption	$\mathrm{m^{-1}}$
s	sticking coefficient	-
S_{BET}	BET surface area	$\mathrm{m^2\,kg^{-1}}$
S_{CH_4}	CH_4 selectivity	-
S_{Me}	specific metal surface area	$\mathrm{m^2\,kg^{-1}}$
S_{Ni}	specific Ni surface area	$\mathrm{m^2\,kg^{-1}}$
T	temperature	K
t	reaction time	s
T_0	initial temperature	K
T_{Aging}	aging temperature	K
T_f	final temperature	K
T_H	Hüttig temperature	K
T_{melt}	melting temperature	K
T_T	Tamman temperature	K
U_{CO_2}	CO_2 uptake	$\mathrm{mol\,kg^{-1}}$
V_{ads}	adsorbed volume	$\mathrm{m^3}$
V_{loop}	sample loop volume	$\mathrm{m^3}$
V_M	molar volume	$\mathrm{m^3\,mol^{-1}}$
$V_{M,N_2,l}$	molar volume of liquid N_2	$\mathrm{m^3\,mol^{-1}}$
V_{N_2}	volume of adsorbed N_2	$\mathrm{m^3}$
$V_{N_2,ML}$	volume of N_2 forming monolayer	$\mathrm{m^3}$
V_P	pore volume	$\mathrm{m^3\,kg^{-1}}$
V_{PM}	chemisorbed monolayer volume of probe gas	$\mathrm{m^3}$
w	weight fraction of Ni	-
W	width of diffraction peak	°
w_{Me}	weight fraction of active metal	-
$x_{CH_4,in}$	fraction of CH_4 in the freed	-
$x_{CH_4,out}$	fraction of CH_4 in the product gas	-
X_{CO_2}	CO_2 conversion	-
$x_{CO_2,in}$	fraction of CO_2 in the feed	-
$x_{CO_2,out}$	fraction of CO_2 in the product gas	-
$x_{i,in}$	fraction of species i in the feed	-
$x_{i,out}$	fraction of species i in the product gas	-
$x_{N_2,in}$	fraction of N_2 in the feed	-
$x_{N_2,out}$	fraction of N_2 in the product gas	-
Y_{CH_4}	CH_4 yield	-

z	stoichiometry factor	-

Greek Symbols

α_1	desorption signal	-
α_2	desorption signal	-
β	desorption signal	-
β	heating rate	$\mathrm{K\,min^{-1}}$
γ	desorption signal	-
ε_b	catalyst bed porosity	-
Θ	diffraction angle	$^\circ$
Θ_0	initial coverage	-
Θ_S	sulfur coverage	-
λ	wavelength	m
$\tilde{\nu}$	wavenumber	$\mathrm{m^{-1}}$
ρ_cat	catalyst density	$\mathrm{kg\,m^{-3}}$
ρ_Me	active metal density	$\mathrm{kg\,m^{-3}}$
ρ_{Ni_2}	density of liquid $\mathrm{N_2}$	$\mathrm{kg\,m^{-3}}$
σ_Me	number of metal atoms per unit area	$\mathrm{m^{-2}}$
σ_Ni	number of Ni atoms per unit area	$\mathrm{m^{-2}}$
ϕ_S	spectrometer work function	eV

Abbreviations

AAS	atom absorption spectroscopy
BET	Brunauer Emmett Teller
CSTR	continuously stirred tank reactor
CVD	chemial vapor deposition
EEG	Erneuerbare-Energien-Gesetz
EXAFS	extended x-ray absorption fine structure
FT-IR	Fourier-Transform-Infra-red
FWHM	full width at half maximum
IR	infra-red

MSN	mesoporous silica nanoparticles
PFR	plug flow reactor
PLM	power law model
PtG	Power-to-Gas
QMS	quadrupole mass spectrometer
SNG	synthetic natural gas
TEM	transmission electron microscopy
TG	thermogravimetry
TOS	time on stream
TPD	temperature programmed desorption
TPH	temperature programmed hydrogenation
TPR	temperature programmed reduction
UHV	ultra high vacuum
WTY	weight time yield
XPS	X-ray photoelectron microscopy
XRD	X-ray diffractometry

1 Introduction

1.1 Motivation

Melting polar ice, rising sea level, droughts and extreme weather phenomena - these are the effects of the climate change which cannot be denied. Although there is natural warming, anthropogenic contributions to global warming are significant. In 2017, human-induced global warming reached 1 °C above the pre-industrial level and is assumed to further increases at a rate of 0.2 °C per decade [1]. In December 2015, 195 countries adopted the Paris Agreement and agreed on the attempt to limit further warming to 1.5 °C but to hold global warming by all means below 2 °C [2]. For meeting this ambiguous target, CO_2 emissions have to be reduced to 25 - 30 Gt y^{-1} in 2030 and net CO_2 emissions should reach zero by the end of 2050 [1, 3]. Against the background of a rising world population and energy demand within the next decades, however, this is a challenging task. Strategies to limit global warming include electrification and simultaneous carbon intensity reduction of electricity, the usage of H_2 and biogenic feedstock as well as CO_2 capture storage and utilization [3–5]. In this context, the development and access to an efficient renewable energy supply are essential [5].
In the context of energy transition and energy supply from renewables, Germany wants to set an example and passed a law (EEG) in 2014 with the aim to increase the contribution of renewable energy to 80 % of the gross electricity consumption by 2050 [6]. Energy production from renewable resources in Germany has been rising continuously within the last decade and increased significantly from 162.5 TW h in 2014, when the EEG was introduced, to 216.4 TW h in 2017 (Figure 1.1A) [7]. A major drawback of the energy production from renewables, however, is the fluctuating supply due to the dependence on weather and seasonal conditions. For example, solar energy production is increased during the summer when most sunny hours per year occur (Figure 1.1B). This is a big challenge for power suppliers, who have to compensate for fluctuations in order to keep the power grid stable. This implies that conventional power plants have to be operated dynamically and brought online when power generation from renewables decreases or have to be shut down during windy and sunny days. An dynamic operation mode of conventional power plants, however, is often difficult to achieve or even impossible. Moreover, distribution problems can arise, especially in the case of Germany, where the highest percentage of renewable energy is produced in the North, whereas some of the largest energy consumers

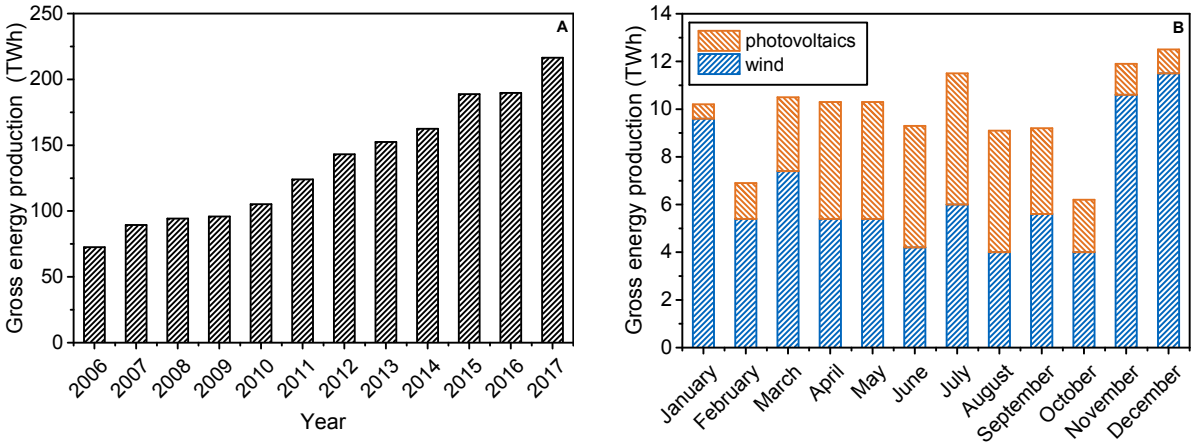

Figure 1.1: (A) Energy production from renewable resources in Germany (data taken from [7]); (B) Fluctuations of the energy production from renewables in 2015 in Germany (data taken from [8]).

are located in the South. Currently, the strategy to overcome the latter issue is the extension of the power grid and building new power lines. This, however, often leads to controversy.
For compensating fluctuations in the power supply, the development and implementation of efficient storage technologies are important. This is even more essential when taking into consideration a power supply solely based on renewables. Efficient technologies imply a high storage capacity and the simultaneous possibility to store energy over a long period of time. It is also important that the energy loss upon storage is reduced to a minimum. Figure 1.2 gives an overview and comparison of existing energy storage technologies.

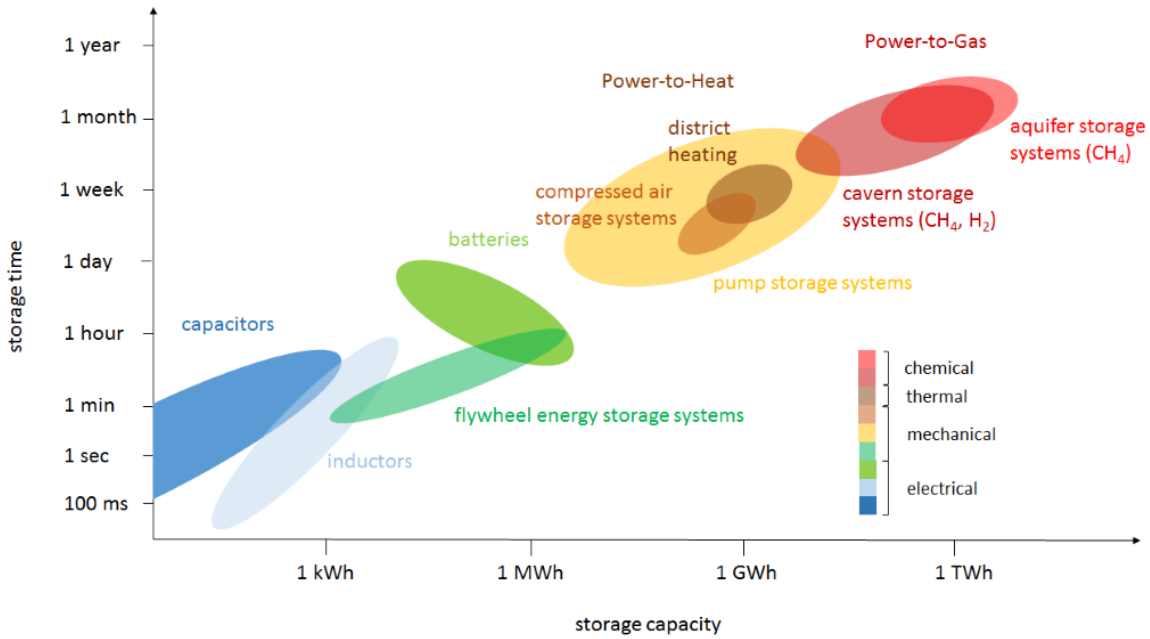

Figure 1.2: Storage technologies for renewable energy in comparison (adapted from [9, 10]).

The comparison shows that electric and mechanic technologies are lacking storage capacity

and time. Chemical storage technologies on the other hand allow for a high capacity in the range of TW h that can be stored up to several month or years. Among them, the Power-to-Gas (PtG) concept (schematically depicted in Figure 1.3) is one of the most promising. Herein, H_2 is produced from renewable resources, via electrolysis of water. H_2 itself is already an energy carrier but is lacking a high energy density and is challenging for storage due to its reactive character and energy intensive compression. To overcome this dilemma, H_2 can be further converted with CO_2 to CH_4, synthetic natural gas (SNG), which is of a higher energy density than H_2. SNG can be stored and transported in the already existing gas grid and reconverted for energy production when needed [10]. CO_2 can be derived from biogenic feedstock [11], flue gases of conventional power plants or off-gases from industry, such as cement production or refineries, which are among the biggest producers of industrial CO_2 emissions [12]. Also CO_2 capture from the atmosphere has been proposed and commercialized. A major challenge originating from the application of bio-derived feed as well as flue and off-gases are NO_x and sulfur compounds present in such feed, whereas CO_2 capture from air results in a very clean CO_2 feed stream [13].

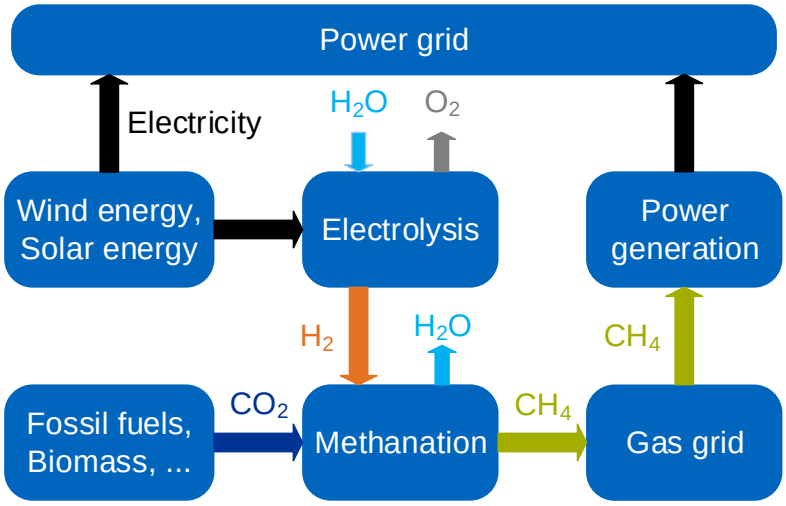

Figure 1.3: Schematic illustration of the Power-to-Gas concept (adapted from [9, 10]).

The efficiency of CO_2 methanation, from a thermodynamic point of view, lies between 80 and 83 % without taking into consideration waste heat recovery [10, 14]. The efficiency of water electrolysis, in contrast, is within 75 - 80 %. The overall efficiency of the PtG process according to Figure 1.3 is between 45 and 60 % assuming a clean CO_2 feed [10]. However, this is significantly lower as compared to an efficiency of roughly 90 % of hydroelectricity generation. On the upside, the storage capacity of the German gas grid currently is about 200 TW h with an energy loss during transport being lower by a factor of 10 as compared to power lines. Therefore, the PtG concept not only allows access to a high storage capacity but also represents an alternative transport system for energy.

Germany is pioneering CO_2 methanation. Several pilot and demonstration plants are in operation with the corresponding plant power input ranging from 25 kW to 6.3 MW [15]. Thereby, high standards of the product gas have been defined in order to be fed into the gas grid [13, 16, 17]. The maximum H_2 content in the dry product gas may not exceed 5 Vol-% [13]. However, there are also applications and situations, like storage tanks in vehicles or the operation of gas turbines, where a maximum H_2 concentration of only 1 Vol-% is required [17]. Moreover, the CO_2 content should be lower than 2.5 mol %. To meet those high standards, highly active and selective catalysts in the methanation step are required. Additionally, the catalysts should be thermostable to ensure a long operation at a high CO_2 conversion and selectivity towards CH_4. Also in the context of feed gas impurities mentioned earlier, which lead to severe catalyst deactivation, the development of highly stable, active and selective catalysts is essential. This necessitates the knowledge of governing deactivation mechanisms. However, with regard to CO_2 methanation, deactivation studies are scarce and a detailed knowledge of causes leading to deactivation is lacking.

1.2 Objective

The scope of this thesis is to develop an understanding of the catalyst deactivation in CO_2 methanation. Ni-Al systems are applied for the studies as they are of industrial interest. The catalytic performance is highly depended on the properties of the active metal phase and the basicity of the catalyst material [18–21]. Therefore, adequate methods to characterize the active Ni phase and its surface area, respectively, have to be developed. A basic knowledge of the H_2 and CO_2 interaction with the catalyst is to be established which can be used, together with structural and morphological investigations, to elucidate deactivation phenomena. Within this work, this achieved in the following chapters:

- **Chapter 2** summarizes thermodynamic and mechanistic aspects of CO_2 methanation. An overview of investigated catalyst systems in literature is given. Concluding, the theoretical background of catalyst deactivation in methanation is derived.

- **Chapter 3** describes the basics of the catalyst synthesis procedures and all characterization and measurement techniques used.

- **Chapter 4** presents catalyst characterization results by means of N_2 physisorption, XRD and TG-MS measurements. Parts of this chapter were published in:

  S. Ewald, M. Kolbeck, T. Kratky, M. Wolf, O. Hinrichsen, *On the deactivation of Ni-Al catalysts in CO_2 methanation*, Applied Catalysis A: General, **2019**, *570*, 376-386.

- **Chapter 5** examines the interaction of H_2 and N_2O with Ni-Al catalysts by means of static and pulsed H_2 chemisorption, H_2-TPD as well as N_2O chemisorption. The potential of those techniques in characterizing Ni-Al catalysts and the active Ni surface area, respectively, is evaluated. This chapter was published in:

  S. Ewald, S. Standl, O. Hinrichsen, *Characterization of nickel catalysts with transient methods*, Applied Catalysis A: General, **2018**, *549*, 93-101.

- **Chapter 6** presents a detailed study of catalyst deactivation in CO_2 methanation. Selected samples are aged up to 165 h under defined conditions and their loss of intrinsic activity is evaluated. A kinetic description of the deactivation behavior is derived. Comprehensive catalyst characterization, comprising both standard and transient techniques, allows to gain insight into governing deactivation mechanisms. Structure-activity relations are analyzed. This chapter was published in:

  S. Ewald, M. Kolbeck, T. Kratky, M. Wolf, O. Hinrichsen, *On the deactivation of Ni-Al catalysts in CO_2 methanation*, Applied Catalysis A: General, **2019**, *570*, 376-386.

- **Chapter 7** applies FT-IR measurements, CO_2-TPD as well as static and pulsed CO_2 adsorption to investigate the interaction of CO_2 with the catalysts applied. CO_2 adsorption modes and their stability are analyzed. Results obtained from transient techniques are compared with those from static measurements on a quantitative basis. This chapter was published in:

  S. Ewald and O. Hinrichsen, *On the interaction of CO_2 with Ni-Al catalysts*, Applied Catalysis A: General, **2019**, *580*, 71-80.

- **Chapter 8** summarizes the results obtained in this work and outlines issues worth further research.

2 Theoretical Background

2.1 Thermodynamic aspects of CO_2 methanation

The hydrogenation for CO_2 to CH_4 according to equation 2.1 was first described by Sabatier and Senderens [22]. Possible side reactions include CO methanation (equation 2.2), the reverse water gas-shift reaction (equation 2.3) and the Boudouard reaction (equation 2.4) [23–25]:

$$CO_2 + 4H_2 \rightleftharpoons CH_4 + 2H_2O \quad \Delta H_R^0 = -165.0\,\mathrm{kJ\,mol^{-1}} \quad \Delta G_R^0 = -113.2\,\mathrm{kJ\,mol^{-1}}, \tag{2.1}$$

$$CO + 3H_2 \rightleftharpoons CH_4 + H_2O \quad \Delta H_R^0 = -206.1\,\mathrm{kJ\,mol^{-1}} \quad \Delta G_R^0 = -141.8\,\mathrm{kJ\,mol^{-1}}, \tag{2.2}$$

$$CO_2 + H_2 \rightleftharpoons CO + H_2O \quad \Delta H_R^0 = 41.2\,\mathrm{kJ\,mol^{-1}} \quad \Delta G_R^0 = 28.6\,\mathrm{kJ\,mol^{-1}}, \tag{2.3}$$

$$2CO \rightleftharpoons C + CO_2 \quad \Delta H_R^0 = -172.4\,\mathrm{kJ\,mol^{-1}} \quad \Delta G_R^0 = -119.7\,\mathrm{kJ\,mol^{-1}}. \tag{2.4}$$

Under standard conditions, CO_2 methanation is an exothermic and exergonic reaction, leading to volume contraction. Consequently, product formation is thermodynamically favoured at elevated pressures and low temperature. Exemplary thermodynamic data, presented in Figure 2.1, was calculated through the Gibbs free energy minimization approach using the NIST-database and the *Shomate*-equation. CO, CH_4 as well as carbon were considered as compounds in the reaction network [24] assuming ideal gas behavior. The results correspond well with those of Gao et al. [23]. At low reaction temperatures around 400 K, CO_2 conversion > 99 % can be achieved with the CH_4 yield also exceeding 99 %. With increasing temperature and decreasing pressure both CO_2 conversion and CH_4 yield decrease according to Le Chatelier´s principle. At temperatures higher than 800 K, reverse water gas-shift reaction is gaining influence. As a consequence, CO_2 conversion and CO yield increase, whereas CH_4 yield continuously decreases.
For the storage of SNG in the natural gas grid in Germany, the CO_2 content in the dry product gas, pressurized to 8 - 12 bar, may not exceed a content of 2.5 mol % as mentioned above, whereas the CH_4 content should be above 95 %. This corresponds to a CO_2 conversion higher than 97 % [14]. For CO_2 methanation at 8 bar using a stoichiometric feed gas composition (Figure 2.1), this is achieved at temperatures below 593 K. At those temperatures, however,

the reaction, which is an eight electron transfer process, underlies kinetic limitation. This necessitates the application of a suitable catalyst. Moreover, theoretical studies revealed low stability and runaway of common tubular reactors and efficient heat removal has to be ensured when operating at stoichiometric feed gas composition [26].

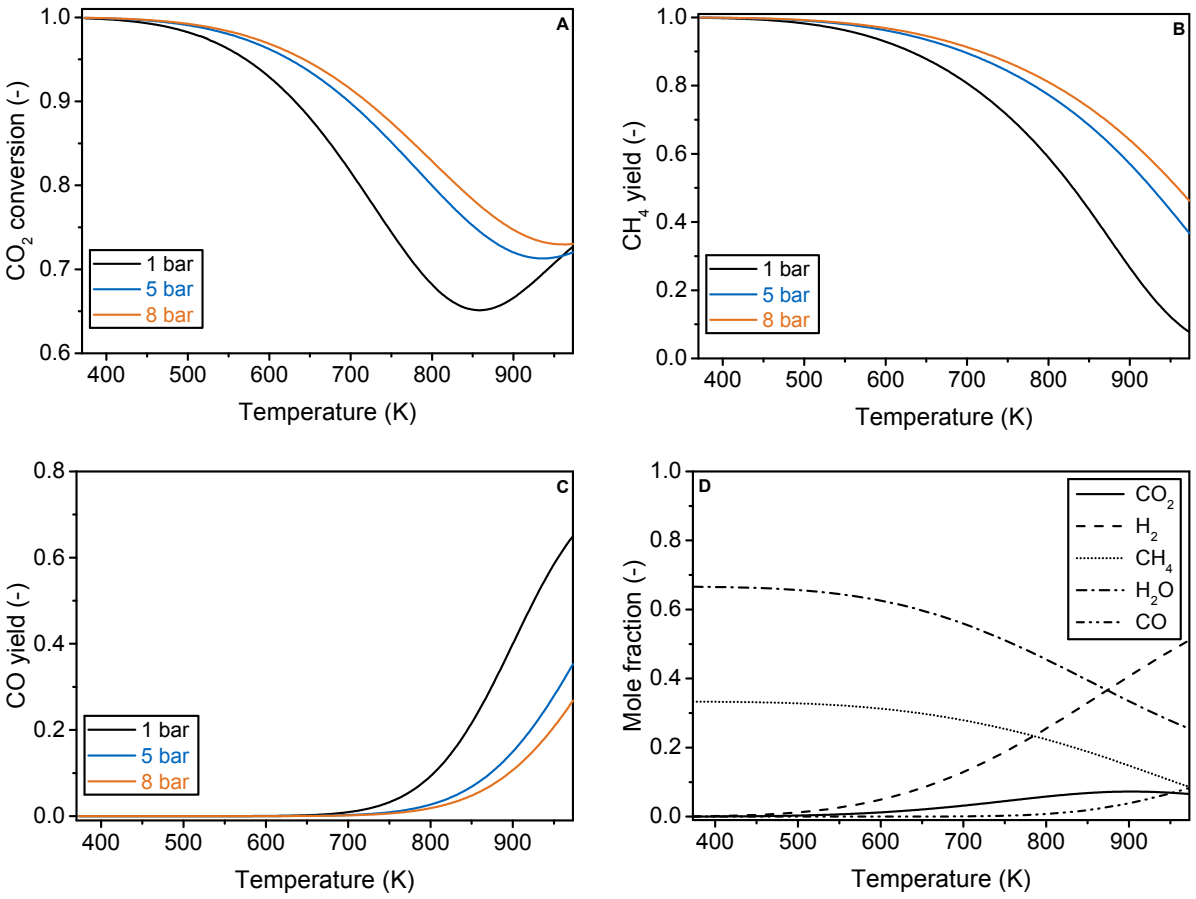

Figure 2.1: (A-C) Influence of total pressure and temperature on CO_2 methanation using a stoichiometric feed gas composition; (D) Equilibrium product gas composition at various temperatures ($p = 8\,\text{bar}, H_2/CO_2 = 4/1$).

The influence of the H_2/CO_2 ratio in the feed gas on CO_2 methanation is depicted in Figure 2.2. Both CO_2 conversion and CH_4 yield significantly decrease with declining H_2/CO_2 ratios. The maximum values for the CH_4 yield are about 74 and 42 % for a H_2/CO_2 ratio of 3 and 2, respectively. The temperature dependence of the CO_2 conversion remains unchanged upon altering the H_2/CO_2 ratio. With increasing temperature, the CO_2 conversion declines, before it rises again at temperatures higher than 800 K due to the reverse water gas-shift reaction. This is in line with an increasing CO yield at these temperatures. Only a minor influence of the H_2/CO_2 ratio on the CO yield is observed. The CH_4 yield initially increases with temperature at H_2/CO_2 ratios below 4, before it decreases again at higher temperatures. In addition, significant amounts of carbon are observed at temperatures below 500 and 900 K at H_2/CO_2 ratios of 3 and 2, respectively. Carbon is not observed when using a stoichiometric feed gas composition. The formation of carbonaceous species are known to drastically reduce the catalyst activity.

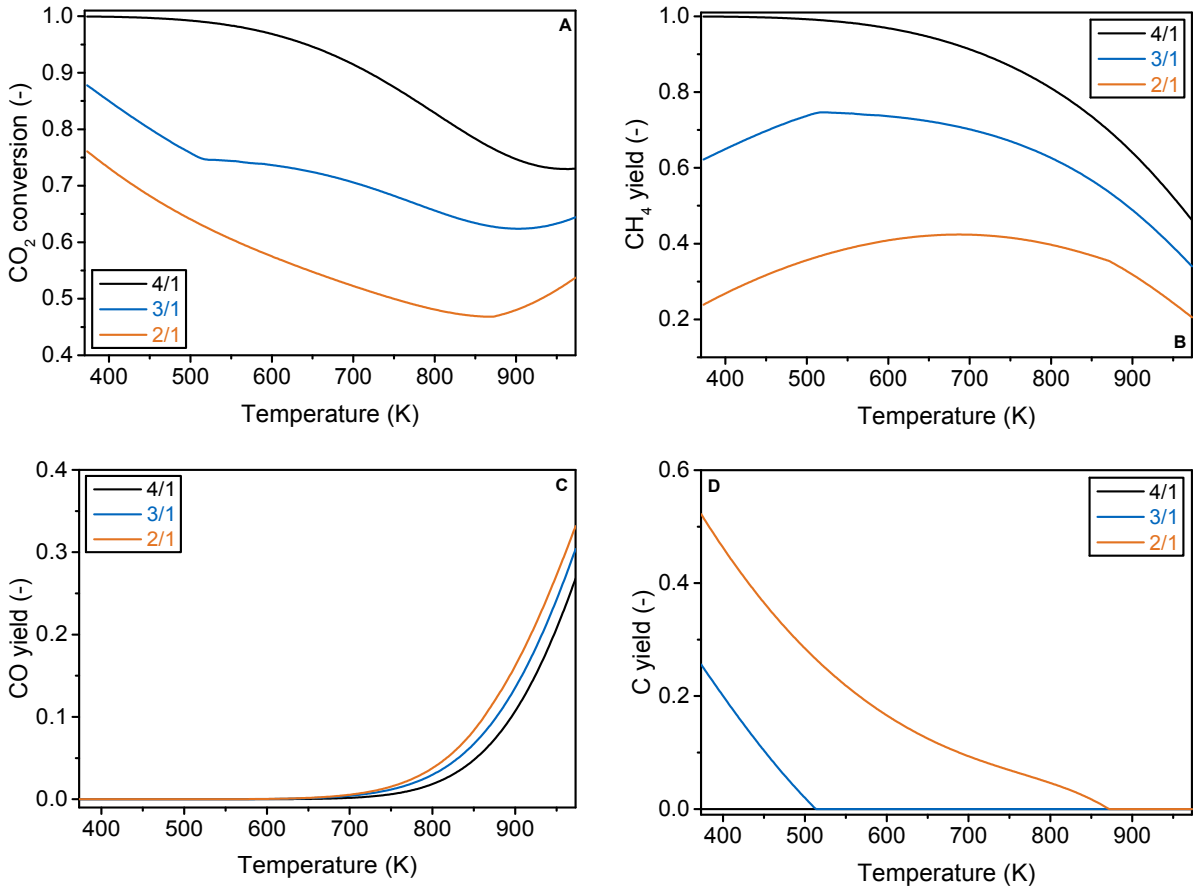

Figure 2.2: Influence of the H_2/CO_2 ratio in the feed gas and the reaction temperature on equilibrium product gas composition in CO_2 methanation ($p = 8$ bar).

2.2 Catalysts for CO_2 methanation

For the catalytic methanation of CO_2 group 8 - 10 transition metals have been proven to be very active [15, 27]. The activity was found to decrease in the order Fe > Ni > Ru > Co for SiO_2 supported systems, whereas the catalyst selectivity towards CH_4 rises in the order Fe < Co < Ni < Ru [28]. Similarly, the activity for alumina-supported catalysts increases successively from Pt over Rh to Ru, whereas Ir and Pd revealed activities in the same range as Pt. The selectivity for these alumina-supported systems exceeds 90 % [29].

Rh has been investigated in numerous studies in literature [30–33]. It was found that the activity of larger Rh particles is higher as compared to smaller ones at temperatures below 458 K, whereas no influence of particle size was observed between 458 and 473 K [32]. A comparison of the specific activity of Rh supported on Al_2O_3, SiO_2, MgO and TiO_2 revealed that Rh/TiO_2 is the most and Rh/SiO_2 is the least active system [31]. Also Pt supported on TiO_2 nanotubes exhibited good performance for CO_2 methanation [34, 35]. Strong metal-support interactions are well known for TiO_2 supported systems and they were proposed to alleviate carbon-oxygen bond cleavage increasing the catalytic activity [34, 36–38]. Small amounts of O_2 in the feed gas increases the specific activity of Rh/Al_2O_3 probably due to the formation of reactive Rh

gem-dicarbonyls [39]. With regard to Pd-containing catalysts, good performance was achieved by supporting Pd on Mg-containing oxides [40, 41]. Moreover, the orientation of the exposed crystallographic planes have been shown to significantly influence the activity and selectivity of Pd nanoparticles embedded in mesoporous silica [42].

Ru catalysts are the most active for CO_2 methanation. For example, Abe et al. reported a CH_4 yield close to 100 % percent at a temperature of about 433 K and a reaction rate of $0.04\,\mu mol\,min^{-1}\,g^{-1}$ close to room temperature for Ru/TiO_2 prepared by a barrel-sputtering method [43]. Kowalczyk et al. [44] investigated the influence of different support materials on the performance of supported Ru catalysts. It was found that for high metal dispersions, the turn over frequency increases in the order $Ru/C < Ru/MgO < Ru/MgAl_2O_4 < Ru/Al_2O_3$. Also CeO_2 [45] and ceria-zirconia [46] as support material were investigated and found to significantly promote CH_4 formation due to the presence of oxygen vacancies, enlargement of the specific surface area and faster reaction of intermediates with H_2 [45]. Increased activity as compared to Ru/Al_2O_3 was observed for Ru/TiO_2-Al_2O_3, which was attributed to the interaction of TiO and Ru, that reduces the average Ru particle size and impedes Ru particle agglomeration [47].

Supported Ni is the most often investigated due to its price, availability and also high activity in CO_2 methanation and selectivity towards CH_4. Several support materials such as Al_2O_3 [19, 48–52], SiO_2 [53–55], TiO_2 [56, 57], CeO_2 [58, 59], ZrO_2 [60, 61] and Ce-Zr oxides [59, 62] have been investigated with regard to their influence on the performance of supported Ni catalysts. Vance and Bartholomew [54] reported that the specific activity and the CH_4 selectivity, respectively, increase in the order $Ni/SiO_2 < Ni/Al_2O_3 < Ni/TiO_2$, whereas Pandey et al. [63] found that the CH_4 yield increases in the order $Ni/SiO_2 < Ni/TiO_2 < Ni/ZrO_2 < Ni/Al_2O_3$ for catalyst with a Ni loading of 10 wt-%. In the latter case, the increasing activity was attributed to a rising CO_2 adsorption capacity in the same order. Ni supported on CeO_2, ZrO_2 or Ce-Zr mixed oxides as support material have been reported to exhibit good catalytic performance due to their high oxygen storage capacity, their basic character and ability to highly disperse Ni as well as an improved reducibility [21, 59, 64–66]. Muroyama et al. [67] also examined more exotic materials such as Y_2O_3, Sm_2O_3 and La_2O_3 and found that the CH_4 yield at 523 K decreases in the order $Ni/Y_2O_3 > Ni/Sm_2O_3 > Ni/ZrO_2 > Ni/CeO_2 > Ni/Al_2O_3 > Ni/La_2O_3$.

The influence of the Ni loading of Ni/Al_2O_3 catalysts on the CO_2 methanation activity and CH_4 selectivity was studied by several groups [48, 51, 52, 68]. The CO_2 conversion was reported to increase when the Ni content rises from 10 to 20 wt-%, before it decreases again at higher loadings. This effect was attributed to a decreasing Ni dispersion at high Ni loadings. Moreover, higher Ni loadings also improve the reducibility, hence increasing the amount of metallic Ni and in this way the catalytic activity [68]. Interestingly, studies of Aksoylu and Önsan revealed that the Ni surface specific activity increases with Ni loading for catalysts where the Ni content is below 15 wt-% [52]. Garbarino et al. could show, that the CO selectivity increases with rising Ni content and Ni particle diameter, respectively. It is proposed, that in large Ni crystallites, plain faces, active for reverse water gas-shift reaction, are largely exposed, whereas edges of

the Ni crystallites, facilitating methanation, predominate in smaller Ni particles [48].
Wu et al. [69] investigated CO_2 hydrogenation over a 0.5 wt-% and a 10 wt-% Ni/SiO_2 catalyst. Their results indicate, that the catalytic activity decreases with increasing Ni loading, whereas the CH_4 selectivity increases with rising Ni content. Formate, which is formed as intermediate, is proposed to be competitively hydrogenated to CO or CH_4, whereupon larger Ni clusters favor the CH_4 formation. Schüler et al. [70] applied chemical vapor deposition (CVD) for the synthesis of Ni/SiO_2 catalysts. The influence of pressure, deposition time and temperature on the specific Ni surface area was investigated in a design of experiment (DoE) approach. An interaction of time and temperature was found, which influences the results of the CVD process, whereas interactions between time and pressure as well as pressure and temperature are negligible. Moreover, the catalytic activity of a 10 wt-% Ni/SiO_2 catalyst synthesized by an optimized CVD technique, was shown to outperform a conventional Ni/SiO_2 system synthesized by incipient wetness impregnation. Several studies also employed mesostructured silica nanoparticles (MSN) [71–74] and zeolites [75, 76] as support material. MSN exhibits beneficial features for catalysts, such as a large pore volume and a very high surface area [77]. The catalytic activity of Ni based zeolites was reported to increase with rising Si/Al ratio, most likely due to a high hydrophobicity of catalysts with large Si/Al ratios. Water, which has an inhibiting effect on CO_2 methanation [78, 79], is adsorbed on the catalyst, hence increasing activity [76]. Aziz et al. compared several oxidic, MSN and zeolite materials. The catalytic activity in CO_2 methanation at atmospheric pressure within the range from 423 - 723 K was reported to increase within the order $Ni/Al_2O_3 < Ni/SiO_2 < Ni/HY < Ni/MCM\text{-}41 < Ni/MSN$. The superior performance of Ni/MSN was proposed to originate from an increased concentration of basic sites and/or oxygen vacancy site density [12, 72].
Next to classic metal-support systems also Ni-Al hydrotalcite-like catalysts have been investigated [19, 52, 79–86]. Abello et al. systematically varied the Ni loading in those systems and found the highest activity and selectivity at a Ni/Al ratio of 2 [81]. He at al. found a significantly improved performance of a hydrotalcite derived Ni-Al system as compared to Ni/Al_2O_3 due to an increased Ni dispersion and basicity [84]. This is in line with studies of Abate et al. [82] and the work of Aksoylu and Önsan [52]. However, a conclusive statement about the optimal catalyst composition is difficult, as the metallic Ni content and dispersion highly depend on the degree of reduction and the reducibility, respectively. Also Gabrovska et al. [85] varied the Ni loading of Ni-Al hydrotalcite and could demonstrate that the systems with a Ni/Al ratio of 3 exhibits an optimal performance upon reduction at 673 - 723 K, whereas a Ni/Al ratio of 0.5 performs best when increasing the reduction temperature to 803 - 873 K. It is well known, that the composition and the synthesis conditions strongly influence the reducibility of the catalyst [87–90]. Doping e.g. with La, Fe or Mn can further improve catalytic performance [18, 63, 86].
A more detailed description of catalyst systems would go beyond the scope of this work but can be found in recent reviews [12, 15, 24, 27, 91].

2.3 Mechanistic aspects of CO_2 methanation

Governing reaction mechanisms are intensively discussed in literature. Proposed mechanisms be divided into two groups. The first group proposes CO as intermediate in two possible reaction pathways. Both pathways assume dissociative adsorption of CO_2 and H_2. For the unassisted pathway, subsequent carbon-oxygen bond cleavage occurs, forming adsorbed carbon and oxygen. Both species are then hydrogenated to CH_4 and H_2O, respectively. In the hydrogen-assisted route, the adsorbed carbonyl species is hydrogenated to COH and formyl, respectively. Then the second carbon-oxygen bond cleavage takes place forming a CH-species which is then further hydrogenated to CH_4. Also the formation of CH_nO species as intermediates in the hydrogen-assisted pathway were reported [30, 33, 92–94]. Mechanisms belonging to the second category

Table 2.1: Proposed mechanisms for CO_2 methanation considering CO as intermediate.

Hydrogen-assisted CO dissociation				Unassisted CO dissociation			
1:	$CO_2 + 2^*$	$\rightleftharpoons$	$CO^* + O^*$	1:	$CO_2 + 2^*$	$\rightleftharpoons$	$CO^* + O^*$
2:	$H_2 + 2^*$	$\rightleftharpoons$	$2H^*$	2:	$H_2 + 2^*$	$\rightleftharpoons$	$2H^*$
3:	$CO^* + H^*$	$\rightleftharpoons$	$CHO^* + ^*$	3:	$CO^* + ^*$	$\rightleftharpoons$	$C^* + O^*$
4:	$CHO^* + ^*$	$\rightleftharpoons$	$CH^* + O^*$	4:	$C^* + H^*$	$\rightleftharpoons$	$CH^* + ^*$
5:	$CH^* + 3H^*$	$\rightleftharpoons$	$CH_4{}^* + 3^*$	5:	$O^* + H^*$	$\rightleftharpoons$	$OH^* + ^*$
6:	$CH_4{}^*$	$\rightleftharpoons$	$CH_4 + *$	6:	$OH^* + H^*$	$\rightleftharpoons$	$H_2O^* + ^*$
7:	$O^* + H^*$	$\rightleftharpoons$	$OH^* + ^*$	7:	H_2O^*	$\rightleftharpoons$	$H_2O + ^*$
8:	$OH^* + H^*$	$\rightleftharpoons$	$H_2O^* + ^*$	8:	$CH^* + 3H^*$	$\rightleftharpoons$	$CH_4{}^* + 3^*$
9:	H_2O^*	$\rightleftharpoons$	$H_2O + ^*$	9:	$CH_4{}^*$	$\rightleftharpoons$	$CH_4 + ^*$

propose hydrogenation of formate species without forming CO as intermediate. Herein, CO_2 is adsorbed on the support forming carbonate species. Carbonate on the metal-support interface is then hydrogenated to formate, which is then further hydrogenated to methoxy species and finally to CH_4. Hydrogen atoms required for these steps are provided by the metal phase where H_2 is dissociatively adsorbed [20, 21, 40]. Formate species, which diffuse from the support to the metal-support interface, were also reported to act as precursor for the formation of CO intermediates on the active metal surface, where CO is then further hydrogenated to methane [95, 96].

The presence of various intermediate species also depends on the catalyst composition and structure as well as on the reaction conditions and surface coverages. Carbonate and formate intermediates often have been observed on support materials of high basicity, where CO_2 is adsorbed on basic sites, such as surface hydroxyl and oxygen groups [97], and the resulting carbonate species is stabilized. Park et al., for example, could show that increasing the basicity of Pd/SiO_2 systems by Mg, significantly increases the CO_2 methanation rate as compared to pure Pd/SiO_2. In the Pd-Mg/SiO_2 system, Mg carbonates are formed as intermediates that are further hydrogenated to methane. CO_2 methanation over Pd/SiO_2 on the other hand, proceeds via dissociative CO_2 adsorption, whereupon most of the CO formed desorbs before further

hydrogenation [40]. Theoretical studies of Kim et al. support these results [41]. Similarly, Falconer and Zagli found that CO and CO_2 methanation follow the same reaction mechanism on Ni/SiO_2 [53], whereas Pan et al. [20] as well as Abello et al. [80, 81] proposed hydrogenation of carbonate intermediates on Ni/Al_2O_3 and Ni-Al catalysts, respectively. In contrast to this, formation and hydrogenation of carbonyl intermediates were reported on both Rh/TiO_2 [33, 98], Rh/SiO and Rh/Al_2O_3 [32, 99]. Carbonaceous intermediates on the catalyst support were also found on Ni-based ceria-zirconia catalysts [20, 21, 100]. Thereby, also oxygen vacancy sites have been proposed to be active sites for CO_2 adsorption, leading to carbonate formation [100]. In Ni-promoted mesostructured silica nanoparticles (Ni/MSN), on the other hand, oxygen vacancies have been reported to stabilize oxygen originating from carbon-oxygen bond cleavage of CO_2 on the Ni phase. The stabilized oxygen atom is then hydrogenated to water. CO as well as hydrogen atoms, formed on the Ni phase, migrate to the support, forming carbonyl and formate species which are further hydrogenated to CH_4 [71].
It is also possible that several mechanisms and pathways occur at the same time. Vesselli at al. [101, 102] proposed that hydrogen-assisted CO_2 activation with subsequent carboxyl-intermediate formation and conversion to CH_4, takes place over Ni(110) and polycrystalline Ni, respectively. At the same time, also formate is formed in a parallel pathway but is hydrogenated at a significantly slower rate and accumulates on the surface. Formate-derivates were therefore described to be spectator species. Formate-spectator species were also observed for supported Rh catalysts [33, 103].

2.4 Catalyst deactivation

2.4.1 General aspects of catalyst deactivation

Causes for catalyst deactivation can be of chemical, mechanical and thermal origin, whereas intrinsic deactivation mechanisms can be classified into six different types, namely attrition/crushing, poisoning, fouling, thermal degradation, vapor compound formation accompanied by transport as well as vapor/solid and solid/solid reactions. Predominant deactivation mechanisms among other factors are dependent on the type of active metal and the type of reaction. With regard to the scope of this thesis, the discussion of common deactivation mechanisms, therefore, is mainly focused on supported Ni catalysts in methanation reactions.

2.4.2 Thermal degradation and sintering

Thermal degradation and sintering have been described as main causes for Ni catalyst deactivation in methanation reactions. Sinter phenomena are generally temperature dependent and require the mobility of atoms and clusters. As a rule of thumb, atoms located around defects become mobile at temperatures higher than the Hüttig temperature, T_H, which can be calculated with equation 2.5:

$$T_H = 0.3 \cdot T_{melt}. \tag{2.5}$$

At temperatures exceeding the Tamman temperature, T_T (equation 2.6), the mobility of bulk atoms and small clusters increases [104]:

$$T_T = 0.5 \cdot T_{melt}. \tag{2.6}$$

T_{melt} is the melting point of the respective species. With the melting point of Ni being 1725 K, T_H is 518 K and T_T is 863 K [104]. In contrast to this, T_H and T_T of Al_2O_3 are 695 and 1159 K, respectively. This shows, why Al_2O_3 is considered a thermostable support material.
Sintering is generally considered to follow two mechanisms, namely particle migration with subsequent coalescence and Ostwald ripening. In the first mechanism, particles of the active phase migrate over the support and coalesce. Thereby, particle migration is a result of mobile Ni atoms on the Ni surface (Ni adatoms) that diffuse from one side of the Ni particle to the other [105]. Ostwald ripening describes atom and vapor migration from one crystallite over the support and/or the gas phase to another crystallite were it is incorporated [104–108]. Upon sintering, large particles grow on expense of small ones. Empirically, particle sintering can be fitted with equation 2.7:

$$\frac{d_\mathrm{i}}{d_\mathrm{i}^0} = (1 + k_\mathrm{S} \cdot t)^j . \tag{2.7}$$

In equation 2.7, d_i is the particle size of species i after a certain reaction time t. The initial particle diameter of species i is represented by d_i^0, k_S is the sintering constant and j is the order. In case of particle migration and coalescence, n = 1/7 is obtained, whereas sintering according to Ostwald ripening exhibits n = 1/3 [108]. However, it has to be considered, that all of these processes can occur at the same time and are coupled with each other [106].
Next to the temperature also the support material (including its structure and interaction with the active phase), promoters, metal type and the gas atmosphere influence sintering effects. The carrier and structural promoters may inhibit particle migration in a way that they form "valley positions", where the active metal particle is "trapped" [104]. Also support surface defects as well as micro- and macropores with pore diameters close to the metal particle size

impede surface migration and sintering [106]. With regard to metal-support interactions in co-precipitated Ni-Al catalysts, it was reported that nickel-aluminate like structures are formed upon reduction, in which metallic Ni crystallites are partially covered or embedded, increasing sintering resistance [90, 109–111]. In contrast to this, the presence of water vapor has been shown to significantly accelerate Ni particle sintering [105, 112–114]. In steam atmosphere Ni_2-OH complexes are formed on the Ni surface, which exhibit a lower energy of formation and diffusion as compared to Ni adatoms [113]. Water can also weaken and destroy strong metal-support interactions and accelerate Ni particle sintering in this way [115].
Another critical component accelerating Ni particle sintering is CO due to the formation of carbonyl species [116–120]. Thereby, Ni metal atoms react with CO forming volatile $Ni(CO)_4$ or mobile subsurface carbonyl species, which diffuse from small crystallites over the surface to larger ones where they are decomposed, increasing the particle size [106, 116]. The sintering process can be modeled according to Ostwald ripening [118, 119]. Carbonyl formation is generally favored at low temperatures and high CO partial pressures [106, 116]. Under conditions where the Ni carbonyl formation rate exceeds its decomposition rate, Ni carbonyl vapor is stabilized and can be removed from the catalyst bed by the product gas stream, leading to a loss of active Ni. At high temperature and low CO partial pressures the decomposition rate exceeds the formation rate and Ni carbonyl is decomposed onto the Ni particle again before it can be transported out of the system [106].
Not only the active Ni phase is prone to sintering, but also the catalyst carrier. Sintering can proceed via surface diffusion, solid-state diffusion, formation of volatile species, grain boundary diffusion and phase transformation [106]. Accordingly, the gas atmosphere has a significant influence on sintering. In oxidizing milieu, silica and alumina are most stable, whereas carbon is more stable in reducing atmosphere. Similar to the Ni phase, steam significantly accelerates carrier sintering.

2.4.3 Carbon formation

Coke and carbon formation, as a form of fouling, is another predominant deactivation mechanism for Ni catalysts. Coke is a product of hydrocarbon decomposition, whereas carbon is formed upon disproportion of CO. The mechanisms for carbon formation are illustrated in Figure 2.3A [106, 121]. CO dissociation at temperatures between 473 and 773 K leads to the formation of adsorbed atomic carbon, C_α, which can be dissolved in Ni (C_d) or further converted to polymeric, amorphous species (C_β) and Ni_3C. At higher temperatures (573 - 1273 K), graphitic, crystalline carbon, C_c, and vermicular filaments, fibers and whiskers, C_v, can be formed. For whisker and graphene formation, carbon migrates to the rear of the Ni particle through surface and subsurface diffusion where nucleation and formation of whiskers and graphene layers take place. Ni atoms migrate in the opposite direction to allow for continuous fiber growth with the Ni particle on top (Figure 2.3) [105, 122, 123]. Metallic Ni, in this way, is still accessible

for reactant species and consequently, whisker formation does not necessarily lead to catalyst deactivation, unless pores of the support get blocked [106]. For coke- and carbon-insensitive

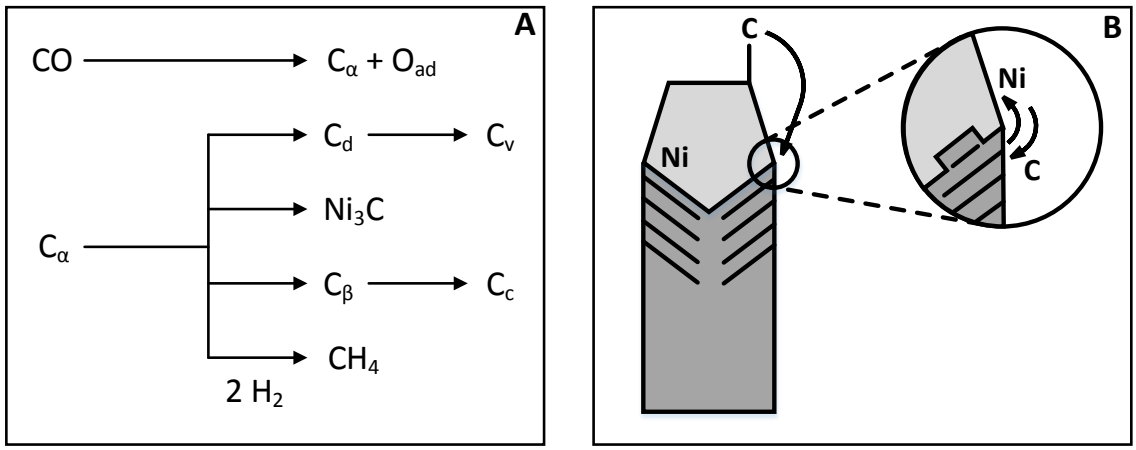

Figure 2.3: Mechanisms of (A) carbon and (B) whisker formation (adapted from [106, 121, 123]).

reactions, to which also methanation of CO belongs, carbon deposits can be removed in H_2, as shown in Figure 2.3. Catalyst deactivation in this case highly depends on the interplay of carbon formation and gasification rate. Carbon formation is circumvented under conditions where the gasification rate exceeds the rate of carbon formation. For CO methanation, as a rule of thumb, this regime is achieved at temperatures below 600 and above 700 K, but also depends on the reactant concentration and the catalyst activity [106]. Also the catalyst composition, structure and morphology influence carbon formation. For example, Ni step-edge sites are preferred nucleation centers for whisker and graphene layer formation. However, nucleation only starts above a minimum Ni particle diameter of 6 to 7 nm [41, 124]. Also the shape of the growing filament depends on the Ni particle size [122].
For Ni catalysts in CO_2 methanation under stoichiometric feed gas composition carbon formation was not observed [23, 66, 82, 125]. However, thermodynamic calculation revealed that at CO_2/H_2 of 2 or lower leads to carbon formation [23].

2.4.4 Poisoning

Poisoning occurs due to species (reactants, products or feed gas impurities) that chemisorb strongly on the catalyst. Poisoning can involve blocking of active sites, access blocking of adsorbed reactant species to each other, impeding surface diffusion, changes of the electronic properties of the metal atoms as well as geometrical changes and surface restructuring. Alteration of the surface geometry is especially critical in structure-sensitive reactions [104, 106]. Impurities in the feed gas such as As, P and S compounds as well as halides were reported to be critical for Ni in hydrogenation reactions [106]. Arsenic and phosphorous components lead

to deactivation due to alloy formation with Ni [126, 127]. Also alkali metals are strong poisons and can lead to deactivation due to blockage of active Ni sites. For a Ni/MgO system, an almost tenfold reduction of activity was reported at a sodium content of 0.07 wt-%, whereas adding 0.5 wt-% potassium reduced the activity by four decades [128]. Moreover, alkali can react with alumina supports forming β-alumina, which drastically reduces the mechanical strength of the support [127]. The majority of poisoning studies, however, concentrate on sulfur components, mainly H_2S, as they are common impurities in feedstocks for methanation. Also sulfur was reported to block active sites. A strong non-linear correlation between the catalyst activity and sulfur coverage was observed [129, 130]. Rostrup-Nielsen et al. described the activity decrease with the correlation given in equation 2.8 [108]:

$$\frac{r}{r^0} = \left(1 - \Theta_S\right)^l, \tag{2.8}$$

where r is the catalyst activity at a certain sulfur coverage, Θ_S, and r^0 is the initial activity of the non-poisoned catalyst. From the exponent l one can calculate the number of atoms forming an active site for reaction. However, it has to be mentioned, that the structure and stoichiometry of adsorbed sulfur is determined by a complex interplay of reaction temperature, reactant concentration, sulfur coverage and gas atmosphere [106, 129, 131–133]. For CO methanation, pre-sulfidation, for example, leads to a significantly more severe deactivation than in situ poisoning [129]. Under in situ conditions, CO adsorbs on the most active sites for methanation, whereas sulfur is chemisorbed on Ni terraces. When pre-sulfiding, sulfur species also adsorb on the most active sites [132]. At high CO partial pressures, chemisorbed sulfur can be removed as COS [106]. Regeneration can also be achieved in H_2O/H_2 atmospheres [134]. Also the catalyst composition influences deactivation due to poisoning [131]. Additives such as Mo were reported to selectively adsorb sulfur increasing the sulfur resistance of Ni catalysts [106].
Poisoning does not necessarily have to be disadvantageous. For example, sulfur as well as potassium preferentially adsorb on Ni step sites and can impede graphene and whisker formation in this way [105, 123]. Also the catalyst selectivity can be tuned by selectively poisoning active sites [106].

2.4.5 Solid/solid and gas/solid reactions

H_2O was described to be capable of re-oxidizing metallic Ni [135]. High CO and CO_2 conversions in methanation reactions lead to a high H_2O partial pressure, which might favor re-oxidation. Despite this, metallic Ni was reported to be stable up to a H_2O/H_2 ratio of 50 [136]. However, there is also evidence that steam induces spinel-formation [137] and structural changes were also observed under CO_2 methanation conditions [80, 81].

2.4.6 Kinetic modeling of deactivation

As explained above, catalyst deactivation can be a complex interplay of several mechanisms. This complicates the kinetic modeling of deactivation. In the simple case, in which deactivation occurs through sintering and structural modifications, the activity loss is traditionally described with a simple power-law model, shown in equation 2.9 [138]:

$$-\frac{\mathrm{d}a_{\mathrm{rel}}}{\mathrm{d}t} = k_{\mathrm{d}} \cdot a_{\mathrm{rel}}(t)^{m}. \tag{2.9}$$

Herein, m is the order of deactivation and a_{rel} (relative activity) is the catalyst activity after a specific time on stream, t, per initial activity. The rate constant of deactivation, k_d, can be described with the Arrhenius-type correlation given in equation 2.10, with $k_{d,0}$ being the pre-exponential factor, T being the reaction temperature and E_d being the activation energy of deactivation:

$$k_{\mathrm{d}} = k_{\mathrm{d},0} \cdot \exp\left(\frac{-E_d}{R \cdot T}\right). \tag{2.10}$$

A major drawback of the simple model, given in equation 2.9, is the assumption that activity ultimately approaches zero. However, in most cases, the activity levels off at a residual value at infinite time on stream. Therefore, the results obtained from the simple power law model often indicate physically not meaningful phenomena such as changing deactivation orders with increasing reaction time [139]. A generalized power law equation (equation 2.11), taking into consideration a residual relative activity $a_{\mathrm{rel,eq}}$, allows for a more consistent description of catalyst deactivation:

$$-\frac{\mathrm{d}a_{\mathrm{rel}}}{\mathrm{d}t} = k_{\mathrm{d}} \cdot \left(a_{\mathrm{rel}}(t) - a_{\mathrm{rel,eq}}\right)^{m}, \tag{2.11}$$

However, for the application of the generalized model, it is essential to accurately determine $a_{\mathrm{rel,eq}}$, which requires long measurement times.

3 Experimental Background

3.1 Catalyst synthesis

In this work, Ni-Al catalysts were synthesized via co-precipitation and incipient wetness impregnation. Co-precipitation is the simultaneous precipitation of the catalyst components. Thereby, a solid is formed upon supersaturation of a homogeneous mixture of the corresponding metal salts solutions. Supersaturation, for example, can be achieved by adjusting the precipitation temperature, evaporation of the solvent or adding a precipitation agent, the latter of which, can change the pH.
There are several ways in which co-precipitation using a precipitation agent can be performed. In a common approach, the metal solution is filled in a stirred tank and precipitated by continuously adding the precipitation agent. Alternatively, the mixture of metal salt solutions can be added to the precipitation agent. Another, more complex, technique is co-precipitation at a constant pH. Thereby, the metal solutions and the precipitating agent are added simultaneously to the vessel in a way that the pH, needed for precipitation, is kept constant [9, 140, 141]. The latter is applied in this work. The corresponding setup is depicted in Figure 3.1. After precipitation, the precipitate is calcined and/or reduced, whereupon the counter ions to the metal cations are decomposed and the final catalyst is obtained. Therefore, it is important to select counter ions that can be decomposed during calcination/reduction. Examples of favorable ions are nitrates, hydroxides or carbonates [142].
Incipient wetness impregnation is one of the simplest methods for catalyst synthesis. Herein, an aqueous or non-aqueous solution, containing the desired active component, is added dropwise to the dried support material. Upon impregnation, the liquid fills the pores of the support material due to capillary forces. The total volume of the added solution corresponds to the pore volume of the support material. Similarly to the precipitation route, the precursors after impregnation are dried in vacuum, inert gas or air and subsequently calcined [9, 141].
The synthesis procedure for the catalysts applied in this work is described in greater detail in the corresponding sections in the subsequent chapters.

Figure 3.1: Setup for co-precipitation of Ni-Al catalysts.

3.2 Elemental analysis

Elemental analysis was conducted in the microanalytic laboratory of the Technical University of Munich. For the determination of the Ni content in the samples, photometry or atom absorption spectroscopy were applied, depending on the estimated Ni loading.

For photometry, the solid sample is solubilized. Subsequently, a coloring agent is added, which reacts with Ni, forming a color complex. The color complex absorbs light of a characteristic wavelength. The concentration of Ni can be determined from the intensity decrease.

For atom absorption spectroscopy, the solubilized sample is dispersed in a mixing chamber, forming an aerosol. Subsequently, the aerosol is dried, mixed with an oxidizing gas and atomized. Similarly to photometry, the Ni species absorbs light of a characteristic wavelength and its concentration can be determined from the light intensity decrease.

For the analysis of carbon, hydrogen and nitrogen species, the sample is treated in O_2 at a temperature of 1273 K. CO_2, H_2O and N_2 formed are separated via gas chromatography and analyzed quantitatively using a thermal conductivity detector.

3.3 N_2 physisorption

The knowledge of the exposed surface area and the porosity of catalytic materials is essential in heterogeneous catalysis. For their characterization, N_2 physisorption is commonly applied. For this, N_2 is dosed into a cell, which contains the sample and is held under vacuum at 77 K. Adsorption takes place until equilibrium pressure, p, is established. The N_2 uptake is calculated from the difference of the gas amount admitted into the cell and the amount of gas required to fill the volume around the sample. This is repeated point by point up to a relative pressure, p/p_0, close to 1, with p_0 being the saturation pressure of the probe gas at the operating temperature. In this way, an adsorption isotherm is obtained [143]. Subsequently, the sample is commonly evacuated point by point to obtain the desorption branch of the isotherm. Depending on the sample porosity and texture, different isotherm shapes are observed. Literature differentiates between six types of isotherms, which are depicted in Figure 3.2. Microporous materials (pore

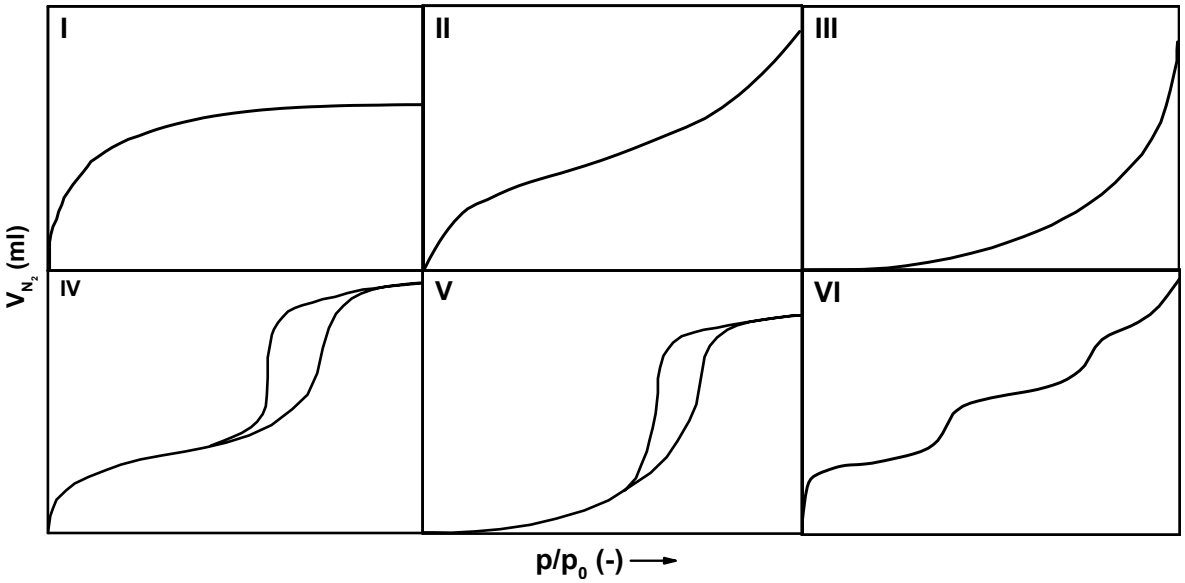

Figure 3.2: Isotherm types obtained upon N_2 physisorption (adapted from [143]).

diameter $d_p < 2$ nm) typically exhibit isotherms of **Type I**. A high N_2 uptake is observed at low pressures due to micropore filling and with increasing p/p_0, the isotherm reaches a limiting value, indicating that all surface sites are filled. **Type II** isotherms are obtained with non-porous or macroporous ($d_p > 50$ nm) materials, where next to monolayer also multilayer adsorption takes place. At low adsorption pressures, the isotherm follows the same trend as a **Type I** isotherm until monolayer coverage is reached at the inflection point B. With increasing p/p_0, multilayer adsorption starts and the isotherm rises. **Type III** isotherms are of convex shape due to a weak interaction of the adsorbate with the adsorbent. **Type IV** isotherms also exhibit an inflection point B and are of a similar shape as **Type II** isotherms. The characteristic of **Type IV** isotherms is the hysteresis between the adsorption and desorption branch. This is caused by N_2 condensation in mesopores (2 nm $< d_p <$ 50 nm). **Type V** isotherms are similar to

Type III isotherms at low relative pressures but exhibit a hysteresis upon desorption. A stepwise multilayer adsorption on non-porous surfaces results in a **Type VI** isotherm. The hysteresis

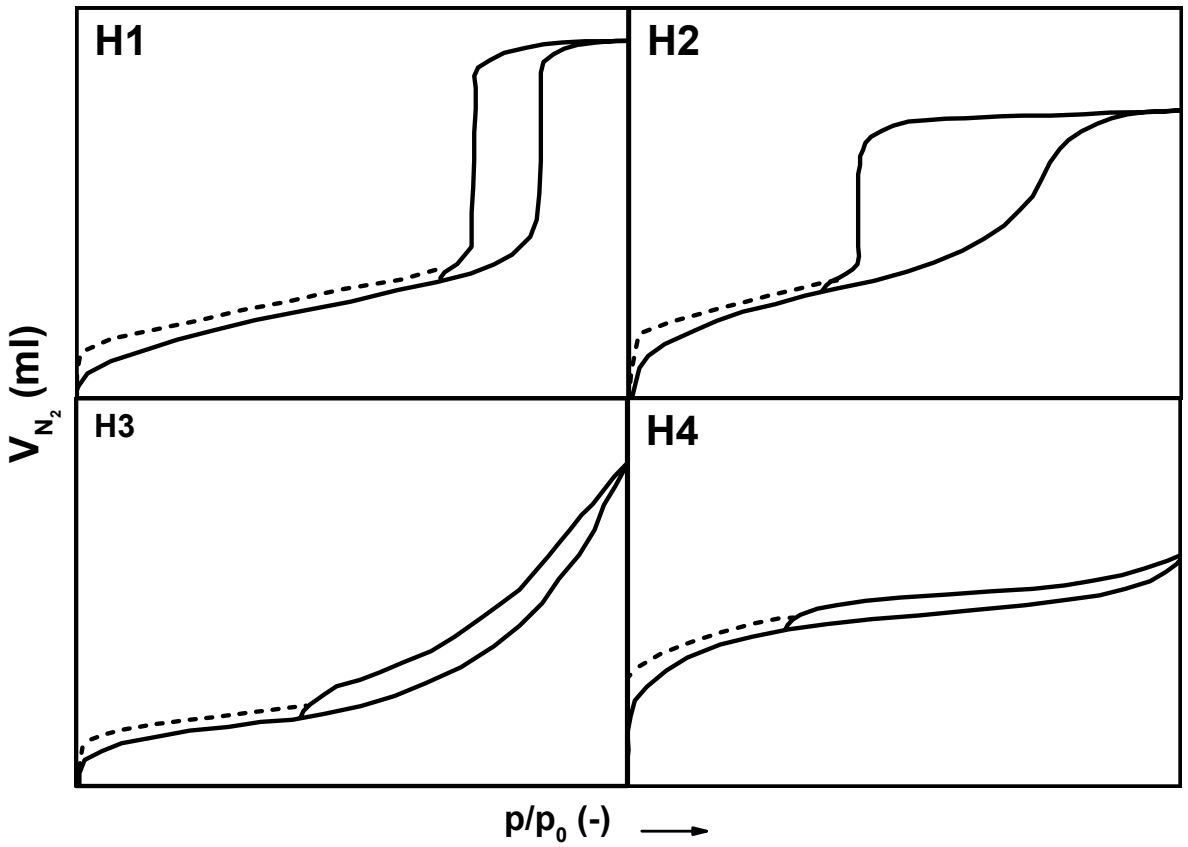

Figure 3.3: Types of hystereses loops upon N_2 physisorption (adapted from [143]).

shape is dependent on the pore structure and geometry and can be classified in four groups, shown in Figure 3.3. **Type H1** is obtained in the case of well-defined cylindrical pores and agglomerates of uniform spheres, whereas, **Type H2** hystereses are observed for disordered and not well-defined pore structures. The characteristic feature of a **Type H3** hysteresis is a vertical rise of the isotherm at high relative pressures. This shape is commonly observed in the case of aggregates of non-rigid plate like particles forming slit-shaped pores. Similarly, hystereses of **Type H4** indicate narrow slit-shaped pores but in the microporosity range. A common feature of the hystereses is the closure point of the adsorption and desorption branch at a relative pressure around $p/p_0 = 0.4$. This point is independent from the material being investigated. Low pressure hystereses, that do not exhibit a closure point at this relative pressure, most likely indicates swelling of non-rigid pores and/or an irreversible N_2 uptake in pores that are about the same size as a N_2 molecule. In this case, a reliable isotherm interpretation and pore size analysis are no longer possible [143].

The N_2 monolayer uptake, $V_{N_2,ML}$, is commonly determined with the BET method, named after Brunauer, Emmett and Teller [144]. Applying Langmuir assumptions, the physisorption

isotherm can be described with the BET equation, which is depicted in equation 3.1 in its linearized form:

$$\frac{1}{V_{N_2}\left(\left(p/p_0\right)-1\right)} = \frac{1}{V_{N_2,ML}\cdot C} + \frac{C-1}{V_{N_2,ML}\cdot C}\cdot\left(\frac{p}{p_0}\right). \tag{3.1}$$

In equation 3.1, V_{N_2} is the volume of adsorbed N_2. The BET constant C is an indicator for the adsorbent/adsorbate interaction. For $C \approx 100$, a sharp point B is observed in the isotherm. For $C < 20$, point B is not clearly discerned. Plotting $\left(V_{N_2}\left(\left(p/p_0\right)-1\right)\right)^{-1}$ against p/p_0 allows for the determination of $V_{N_2,ML}$. It has to be noted, that equation 3.1 is usually valid only in the range of $0.05 < p/p_0 < 0.30$ [143, 144]. The specific total surface area, S_{BET}, can be calculated from $V_{N_2,ML}$ according to equation 3.2 [143]:

$$S_{BET} = \frac{V_{N_2,ML}\cdot N_A \cdot A_{N_2}}{V_M \cdot m_{cat}}, \tag{3.2}$$

with N_A being Avogadro´s constant and A_{N_2} being the cross-sectional area of a N_2 molecule ($0.162\,nm^2$ [143, 144]). The sampled mass used for analysis is represented by m_{cat}. The total pore volume, V_P, is calculated from the mass of adsorbed N_2, m_{N_2}, at p/p_0 close to unity assuming that the pores are filled with adsorbate in its liquid state [145]:

$$V_P = \frac{m_{N_2}}{\rho_{N_2,l}\cdot m_{cat}}. \tag{3.3}$$

In equation 3.3, $\rho_{N_2,l}$ is the density of liquid N_2 ($0.808\,g\,cm^{-3}$ [146]). From V_P and S_{BET}, the average pore diameter, d_P, can be calculated assuming cylindrical pore geometry [143]:

$$d_P = \frac{4\cdot V_P}{S_{BET}}. \tag{3.4}$$

A clean catalyst surface prior to analysis is an important prerequisite for reliable and reproducible results. This is commonly achieved by heating the sample under vacuum. Thereby, the conditions have to be chosen depending on the catalyst structure and compositions, since thermally induced structural and morphological changes should be avoided. Also heating in inert gas flow is possible [143].

3.4 Static chemisorption measurements

Static chemisorption measurements allow to determine the amount of gaseous probe molecules that are chemisorbed on the surface of the material investigated. In contrast to physisorption,

strong chemical bonds between the adsorbens and the adsorbate are established upon adsorption. Thereby, it is also possible, that intermolecular bond breakage of the adsorptive molecule occurs (dissociative chemisorption). Chemisorption is generally an exothermic process with higher values for the adsorption enthalpy as compared to physisorption. For the determination of the chemisorbed gas amount, portions of the probe gas are dosed onto the sample at a selected pressure and temperature until equilibrium is obtained. This procedure is repeated for several adsorption pressures at a constant temperature. Plotting the adsorbed amount of probe gas in each measurement against the respective adsorption pressure gives an adsorption isotherm. The isotherm represents both strongly and weakly chemisorbed species as well as physisorbed species ("combined" curve in Figure 3.4). In order to discriminate between these species, the sample is evacuated again. Upon evacuation, only those species remain adsorbed, which are strongly bond to the sample surface. Subsequently, probe gas is dosed onto the sample again in the same matter as described earlier. A second isotherm is obtained, which describes weakly chemisorbed as well as physisorbed species ("weak" curve in Figure 3.4). In cases, where exclusively strong chemisorption occurs, the second isotherm corresponds to physisorbed species. The isotherm representing strong chemisorption ("strong" curve in Figure 3.4) is obtained by subtracting the "weak" isotherm from the "combined" isotherm [147]. As for physisorption measurements, a clean sample surface is essential for a reliable analysis. The monolayer uptake

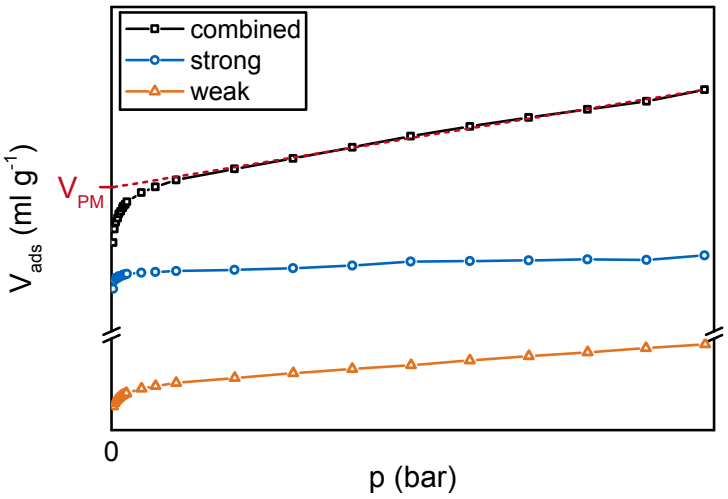

Figure 3.4: Example of isotherms obtained upon static chemisorption.

of chemisorbed species can be determined by back-extrapolating the low slope region of the "combined" isotherm to $p = 0\,\text{bar}$ (indicated by the dashed line in Figure 3.4). Thereby, it is assumed that at high adsorption pressures, the surface is saturated with chemisorbed species and the increase of adsorbed gas originates from physisorption. As physisorption generally increases linearly with adsorption pressure, its contribution to the total gas uptake can be assumed to be insignificant at $p = 0\,\text{bar}$ [147, 148]. In cases where only the amount of strongly chemisorbed species is needed, the "strong" isotherm can be back-interpolated to $p = 0\,\text{bar}$.

From the monolayer uptake of chemisorbed probe molecules, V_{PM}, also the active metal surface area of supported metal catalysts, S_{Me}, can be determined according to equation 3.5:

$$S_{\mathrm{Me}} = \frac{V_{\mathrm{PM}} \cdot N_A \cdot z}{V_{\mathrm{M}} \cdot m_{\mathrm{S}} \cdot \sigma_{\mathrm{Me}}}. \tag{3.5}$$

In equation 3.5, N_A is Avogadro´s constant. V_M and m_{S} are the molar volume and the sample mass, respectively. The stoichiometry factor, z, describes how many metal atoms are needed for chemisorption of one adsorptive molecule. The number of surface metal atoms per unit area is represented by σ_{Me}. When determining S_{Me}, interaction of the probe molecules with the catalyst support as well as gas diffusion into the bulk of the metal phase have to be avoided. For Ni as active metal phase ($\sigma_{\mathrm{Ni}} = 1.54 \cdot 10^{19}\,\mathrm{m}^{-2}$ [149]), H_2 is commonly applied. In this case, z has a value of 2, since H_2 is dissociatively chemisorbed on Ni with one hydrogen atom bond to one Ni atom [150]. Next to the active metal surface area, also the dispersion, D_{Me}, as well as the average metal particle diameter, d_{Me}, can be calculated using equation 3.6 and equation 3.7 [79, 147]:

$$D_{\mathrm{Me}} = \frac{N_{\mathrm{PM}} \cdot z \cdot M_{\mathrm{Me}}}{m_{\mathrm{S}} \cdot w_{Me}}, \tag{3.6}$$

$$d_{\mathrm{Me}} = \frac{w_{\mathrm{Me}} \cdot f}{S_{\mathrm{Me}} \cdot \rho_{\mathrm{Me}}}. \tag{3.7}$$

In equation 3.6 and 3.7, M_{Me} is the molar weight of the active metal and w_{Me} is the weight fraction of the active metal in the sample. The shape factor, f, has a value of 6 for spherical particles and ρ_{Me} is the density of the active metal ($8.9\,\mathrm{kg\,m}^{-3}$ for Ni [79]).

3.5 X-ray diffractometry (XRD)

A standard technique to elucidate the structure of solid materials is X-ray diffractometry (XRD). X-rays of wavelengths corresponding to the distances between atoms in crystals are passed through the sample, where they are scattered at the electrons of the atoms. The scattering strength depends on the number of electrons surrounding the atom. Constructive interference upon scattering (diffraction) only occurs if Bragg´s law is fulfilled [151]:

$$\lambda \cdot n = 2 \cdot d_{hkl} \cdot \sin\Theta. \tag{3.8}$$

In equation 3.8, λ is the wavelength of the incident beam, n the diffraction order and d_{hkl} is the interplanar distance (d-spacing) of the crystallographic planes, leading to diffraction. For $n = 1$, the index hkl corresponds to the Miller indices. Θ is the diffraction angle according

to scheme 3.5. Recording the intensity of the scattered X-rays as a function of 2Θ results in

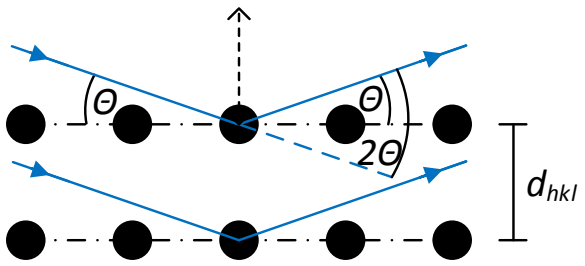

Figure 3.5: Illustration of Bragg´s law.

the corresponding diffractogram. For diffraction angles where Bragg´s law is fulfilled, a signal (reflection) is observed. However, sharp peaks are only obtained for highly crystalline materials with a long-range order of the unit cells. Amorphous materials exhibit very broad and not well defined signals [151, 152].
Based on the position of the reflection and the *d*-spacing, respectively, the unit cell parameters can be calculated. For the hydrotalcite-structure, the lattice parameters *a* and *c* can be calculated according to equation 3.9 [151]:

$$\sin^2\Theta = \frac{\lambda^2}{4a^2}\left[\frac{4}{3}\left(h^2+k^2+hk\right)+\left(\frac{4}{c}\right)^2 l^2\right]. \tag{3.9}$$

For cubic systems, typically obtained for NiO, γ-Al_2O_3 and $NiAl_2O_4$, the cell parameters can be calculated with equation 3.10 [151]:

$$\sin^2\Theta = \frac{\lambda^2}{4a^2}\left[h^2+k^2+l^2\right]. \tag{3.10}$$

From line broadening of the diffraction signal, the crystallite size, d_c, can be calculated using the Scherrer equation [147]:

$$d_c = \frac{K\cdot\lambda}{W(\Theta)\cdot\cos\Theta}. \tag{3.11}$$

For the width of the diffraction peak, *W*, the full width at half maximum (FWHM) is used. The Scherrer constant, *K*, depends on the particle shape. In this work, a Scherrer constant of 0.9 was applied, assuming spherical particles. As indicated in equation 3.11, *W* is a function of the diffraction angle. If using a single peak for crystallite size determination, diffraction peaks between $2\Theta = 30-50^\circ$ should be used.
Next to d_c, also microstrains in the crystallite and the instrument itsself lead to line broadening.

Microstrains interrupt the long-range order and therefore can bias the crystallite size calculation [151]. For highly nanocrystalline materials, the specimen dominates over instrumental broadening. Otherwise, instrument and sample contributions to peak broadening have to be deconvoluted through calibration. On the other hand, a minimum amount of repeating atomic planes have to be present in order to create a peak in the diffraction pattern. The minimum crystallite size that still can be calculated from peak broadening is between 3 and 5 nm.
X-ray diffractometer are commonly operated in Bragg-Brentano geometry. Thereby, the detector and X-ray source are positioned on the goniometer circle around the sample. In $\Theta - \Theta$ motion, both the detector and the beam source rotate around the sample. In $\Theta - 2\Theta$ operation, the X-ray source is stationary and the sample holder and detector are moving. In Debye-Scherrer geometry, the sample (fixed for example in a glass capillary) as well as the X-ray beam source are stationary. The detector rotates around the sample to cover the full 2Θ range. In all cases, spinning of the sample increases the number of crystallite orientations exposed to the X-ray beam [151].
For the production of X-rays, electrons are accelerated and targeted at an anode. Upon the impact, an electron is ejected from an inner shell of the atom. Electron transfer form a higher shell to the vacant shell results in the emission of on X-ray photon of a characteristic wavelength. Radiation due to electron transition from the M- or L- shell to the empty K-shell is called Kβ and Kα radiation, respectively. Electron fine structure causes the occurrence of Kα radiation of slightly different energy, namely Kα_1 and Kα_2 radiation, with an intensity ratio of 2/1. Next to this characteristic radiation, also Bremsstrahlung is observed, which originates from deceleration of striking electrons within the anode. For analysis, mostly Kα radiation is applied. X-rays of unwanted wavelengths as well as Bremsstrahlung can be removed by filters (e.g. Ni in the case of a Cu anode) or by a monochromator [151, 153].

3.6 X-ray photoelectron spectroscopy (XPS)

X-ray photoelectron spectroscopy is based on the photoelectric effect. Thereby, soft photons, typically emitted from a Mg Kα or Al Kα source (see also chapter 3.5), interact with the sample in UHV. The penetration depth of the X-rays lies within 1 - 10 µm. The impinging photons cause an electron of the sample atoms to be emitted. Thereby, only electrons originating from the surface and a few angstrom below can leave the sample, since their interaction probability with the solid exceeds by far the corresponding value for incoming photons. The emitted electrons are recorded according to their kinetic energy, E_{kin}, which depend on the photon energy, E_p, the spectrometer work function, ϕ_S, and the binding energy of the electron, E_b:

$$E_{kin} = E_p - E_b - \phi_S. \tag{3.12}$$

Based on equation 3.12, E_b of the emitted electron can be determined. The binding energy is dependent on the orbital, the photoelectron originates from and the electron spin orientation. Every element has a unique set of binding energies depending on its oxidation state. In this way, the surface species of a sample can be determined by means of XPS. Shifts of the binding energy obtained from a sample in comparison to pure reference materials allow to draw conclusions on the chemical state of the surface species.
In addition to photoelectrons also Auger electrons can be emitted from the sample. In these cases, an electron from an outer orbital fills the vacancy in an inner shell after the photoelectron has been emitted. The released energy can cause a second electron, an Auger electron, to emit [154, 155].

3.7 FT-IR spectroscopy

Infra-red (IR) spectroscopy is based on the interaction of molecules and atomic groups with electromagnetic radiation between 400 and 4000 cm^{-1}. Electromagnetic radiation is absorbed and induces vibrations of atom groups. Thereby, the energy of the impinging radiation has to match the difference between the energetic state of the molecule before, E', and after E'' absorption:

$$E'' - E' = h \cdot \tilde{\nu} \cdot c. \tag{3.13}$$

In equation 3.13, h is Planck´s constant, $\tilde{\nu}$ is the wavenumber of the impinging electromagnetic radiation and c is the speed of light. The energy difference has discrete values, which are characterized by quantum numbers. Moreover, absorption is only possible, if a dipole moment is induced or changed upon vibration. Diatomic molecules such as H_2 or N_2, therefore, are not IR active. With regard to the linear CO_2 molecule, the asymmetric stretching vibration induces a change of the dipole moment, whereas the symmetric stretching vibration does not.
The required energy for exciting a vibration ($E'' - E'$) increases with the binding strength of the corresponding atoms. Consequently, also the wavenumber of the absorbable electromagnetic radiation increases as indicated in equation 3.13. As various functional groups exhibit different binding energies depending on their atomic composition, their absorbance behavior is an intrinsic characteristic and can be used for their identification.
When conducting Fourier-Transform-Infra-red (FT-IR) spectroscopy, electromagnetic radiation is emitted from an IR source and passed through the sample exciting vibrations. A detector records time dependent intensity changes due to absorption as an interferrogram. Subsequently, the interferrogram is converted into a wavenumber dependent absorbance spectrum by means of Fourier-transformation [156–158].

3.8 Thermogravimetry and temperature programmed reduction (TPR) measurements

In the calcined catalysts, Ni is present in its oxidic form. Therefore, the catalysts have to be reduced prior to measurements in order to obtain metallic Ni:

$$NiO + H_2 \rightleftharpoons Ni + H_2O. \tag{3.14}$$

Reduction processes can be more complicated than described in equation 3.14. Different oxidic Ni phases have been reported depending on the catalyst composition and synthesis procedure [80, 81, 109, 110]. Those species can vary in reducibility requiring different reduction temperatures. Also other gases than H_2O can be released upon reduction depending on the catalyst composition. Thermogravimetric analysis coupled with mass spectrometry is a powerful tool to follow and elucidate the complex processes during reduction. Thereby, the sample is placed in a crucible that is heated linearly in reductive atmosphere, mostly H_2 that is diluted in inert gas such as Ar or N_2. The crucible is connected to a microbalance to follow the mass loss of the sample. The evolving gas species are analyzed by means of a mass spectrometer. If side reactions consuming H_2 can be excluded, the quantity of reduced Ni and the degree of reduction at a certain temperature can be determined from the amount of H_2 consumed or the amount of H_2O produced.
It is well known that specimens in a thermobalance exhibit weight changes upon heating, which do not originate from physical or chemical changes of the sample. This is due to buoyancy effects upon heating, that originate for example from density changes of the gas. In order to compensate these effects, a blank measurement has to be performed which is used to correct the raw data of the run with a sample [159].

3.9 Setup for deactivation experiments

Deactivation studies were conducted in the setup illustrated in Figure 3.6. The reactor unit consists of four U-shaped tubular fixed bed reactors (inner diameter of 4 mm) in an convection oven with a maximum operation temperature of 753 K. The inner wall of the reactors is coated with glass to ensure an inert behavior. The reactors can be operated in parallel and the gas flow to each reactor can be adjusted individually within the range from 5 to 500 $Nml\,min^{-1}$ by means of four mass flow controllers (model 5850TR from Brooks Instrument®). The catalyst material to be investigated is fixed in the reactors in between two plugs of silica wool. For kinetic measurements, a thermocouple is inserted into each reactor and brought in contact with the catalyst to measure the bed temperature during operation. Alternatively, each reactor can be

equipped with two shut-off valves, to remove the samples from the setup without being exposed to air. Feed gas is supplied from gas bottles. A gas mixing unit allows to vary the composition of CO_2, H_2, Ar and N_2 in the feed gas, which is fed to a storage tank at a maximum pressure of 30 bar. Upstream of the mass flow controllers, the feed gas pressure is reduced to 15 bar, which is to the maximum operating pressure of the setup. The operating pressure itself is adjusted by four back pressure regulators (one for each reactor), which are operated simultaneously and heated in an oven at 425 K. Product gas analysis is performed with an Agilent® 7820A gas chromatograph equipped with two thermal conductivity detectors. A Porapack-N column from Sigma-Aldrich® allows for the separation of CO_2 and H_2O. H_2, Ar, N_2, CH_4 and CO are separated by a Molsieve 5A column (Sigma-Aldrich®). A multi-position valve allows for the selection of the desired reactor line to be analyzed. The feed gas composition can be analyzed separately via an additional line bypassing the reactor unit. All piping downstream of the reactors is heated to prevent condensation of product gases.

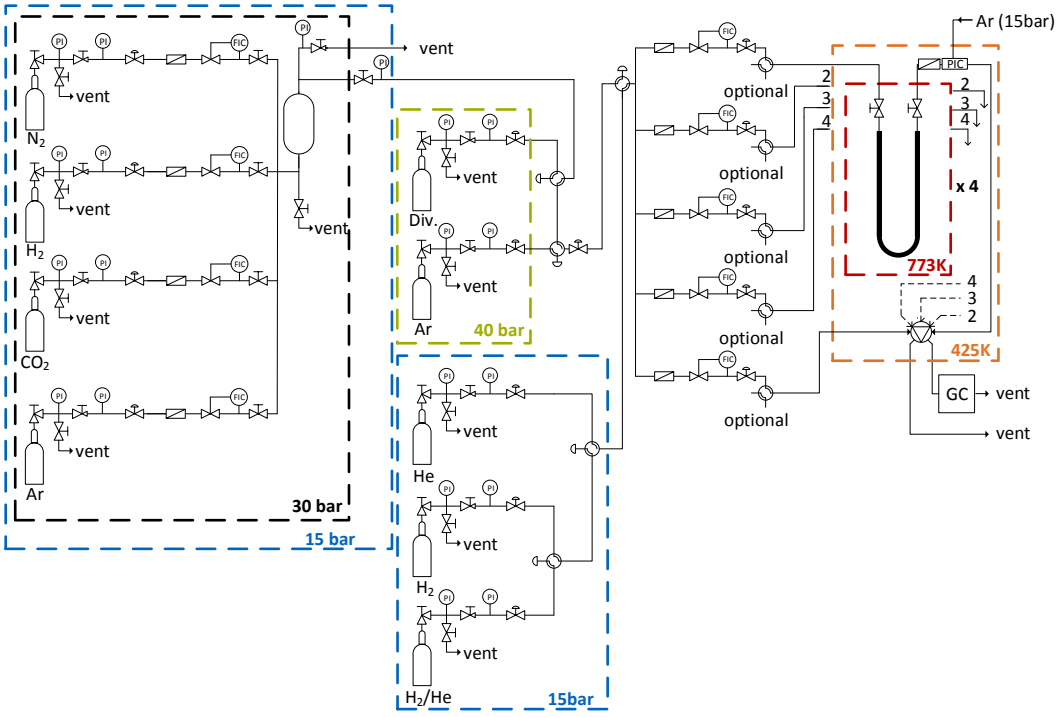

Figure 3.6: Flow diagram of the setup for deactivation studies where the reactors are equipped with shut-off valves [160].

3.10 Determination of kinetic parameters

CO_2 conversion, X_{CO_2}, CH_4 yield, Y_{CH_4} and CH_4, selectivity, S_{CH_4} are important parameters in order to compare different catalyst systems with regard to their performance in CO_2

methanation. For continuously operated reactors, CO_2 conversion is defined as the amount of CO_2 converted in relation to the CO_2 amount fed to the reactor. The converted CO_2 amount is calculated from the difference of the molar CO_2 stream entering ($\dot{n}_{CO_2,in}$) and leaving ($\dot{n}_{CO_2,out}$) the reactor:

$$X_{CO_2} = \frac{\dot{n}_{CO_2,in} - \dot{n}_{CO_2,out}}{\dot{n}_{CO_2,in}}. \tag{3.15}$$

The CH_4 yield is defined as the amount of CH_4 produced per amount of CO_2 in the feed stream according to equation 3.16. The produced CH_4 amount is determined from the difference between the molar flow of CH_4 in the feed, $\dot{n}_{CH_4,in}$ and in the product gas, $\dot{n}_{CH_4,out}$, with ν_{CO_2} and ν_{CH_4} being the stoichiometric coefficient of CO_2 and CH_4, respectively:

$$Y_{CH_4} = \frac{|\nu_{CO_2}|}{|\nu_{CH_4}|} \cdot \frac{\dot{n}_{CH_4,out} - \dot{n}_{CH_4,in}}{\dot{n}_{CO_2,in}}. \tag{3.16}$$

The CH_4 selectivity describes the fraction of CO_2 that is converted to CH_4:

$$S_{CH_4} = \frac{|\nu_{CO_2}|}{|\nu_{CH_4}|} \cdot \frac{\dot{n}_{CH_4,out} - \dot{n}_{CH_4,in}}{\dot{n}_{CO_2,in} - \dot{n}_{CO_2,out}} = \frac{Y_{CH_4}}{X_{CO_2}}. \tag{3.17}$$

Another important parameter is the reaction rate, r. The differential reaction rate, which cannot be determined through measurements, is defined as the amount of reactant per unit time at a specific point in the reactor. The integral reaction rate, r_{CH_4}, in contrast, is the average value of the production rate over the reactor and can be determined according to equation 3.18:

$$r_{CH_4} = \frac{1}{|\nu_{CH_4}|} \cdot \left(\dot{n}_{CH_4,out} - \dot{n}_{CH_4,in}\right). \tag{3.18}$$

From equation 3.18, the weight time yield , *WTY*, can be calculated according to:

$$WTY = \frac{r_{CH_4}}{m_{cat}} = \frac{\frac{1}{|\nu_{CH_4}|} \cdot \left(\dot{n}_{CH_4,out} - \dot{n}_{CH_4,in}\right)}{m_{cat}}. \tag{3.19}$$

The reaction rate is also a function of the reaction orders of the reactants, m_{CO_2} and m_{H_2}, as well as their partial pressures, p_{CO_2} and p_{H_2}:

$$r = k \cdot p_{CO_2}^{m_{CO_2}} \cdot p_{H_2}^{m_{H_2}}. \tag{3.20}$$

The reaction rate constant, k, is a function of the reaction temperature, T and the activation energy of the reaction, E_A. It can be described with Arrhenius´s law:

$$k = k_0 \cdot e^{\left(-\frac{E_A}{R \cdot T}\right)}. \tag{3.21}$$

Equation 3.21 in its logarithmic form gives:

$$\ln(k) = \ln\left(k_0\right) - \frac{E_A}{R} \cdot \frac{1}{T}. \tag{3.22}$$

Under differential conditions (CO_2 conversions between 5 and 10 %), the differential reaction rate can be approximated with the integral reaction rate. Moreover, the reaction can be assumed to be irreversible. Consequently, the reaction rate can be determined according to:

$$r_{CH_4} = \frac{1}{\left|\nu_{CH_4}\right|} \cdot \left(\dot{n}_{CH_4,out} - \dot{n}_{CH_4,in}\right) = k \cdot p_{CO_2,in}^{m_{CO_2}} \cdot p_{H_2,in}^{m_{H_2}}. \tag{3.23}$$

Logarithmizing equation 3.23 using equation 3.22 yields:

$$\ln\left(r_{CH_4}\right) = \ln\left(k_0\right) - \frac{E_A}{R} \cdot \frac{1}{T} + m_{CO_2} \cdot \ln\left(p_{CO_2,in}\right) + m_{H_2} \cdot \ln\left(p_{H_2,in}\right). \tag{3.24}$$

Varying the partial pressure of one reactant, i, in the feed while keeping the partial pressure of the other reactant constant allows to determine the corresponding reaction order m_i from the slope of the linear correlation obtained when plotting $\ln\left(r_{CH_4}\right)$ against $\ln\left(p_{i,in}\right)$. The reaction order of the second reactant can be determined accordingly. Repeating this procedure at different reaction temperatures, allows for the determination of E_A from the slope of the linear correlation obtained upon plotting $\ln\left(r_{CH_4}\right)$ against T^{-1}.
The reaction orders of CO_2 and H_2 have been shown to be nearly constant within the temperature range from 448 - 533 K [79]. In this case, E_A in equation 3.24 can be determined directly from plotting $\ln\left(r_{CH_4}\right)$ against T^{-1}. The calculated values for E_A allow conclusions on the presence of mass transport limitations. Values between 5 and 10 kJ mol^{-1} are obtained for pore diffusion limitation. For film diffusion limitation, the calculated activation energy is only about 50 % of the corresponding value in kinetic regime.

3.11 Setup for transient measurements

Transient measurements were conducted in a single-pass setup (Figure 3.7) of reduced dead volume and no-flow regions. The setup is equipped with a U-shaped tubular reactor, which is identical to those of the setup for deactivation studies (see section 3.9). Operating temperatures up to a maximum of 773 K are realized by two heated metal plates in between which the reactor is inserted together with a type K thermocouple for recording the oven temperature. The oven can be actively cooled with pressurized air. The catalyst material is placed in the isothermal zone of the bracket situated on the reactor outlet and secured in between two plugs of silica wool. The bed is contacted with a type K thermocouple on its top end to measure and control the bed temperature. Feed gas is brought to reaction temperature in the empty

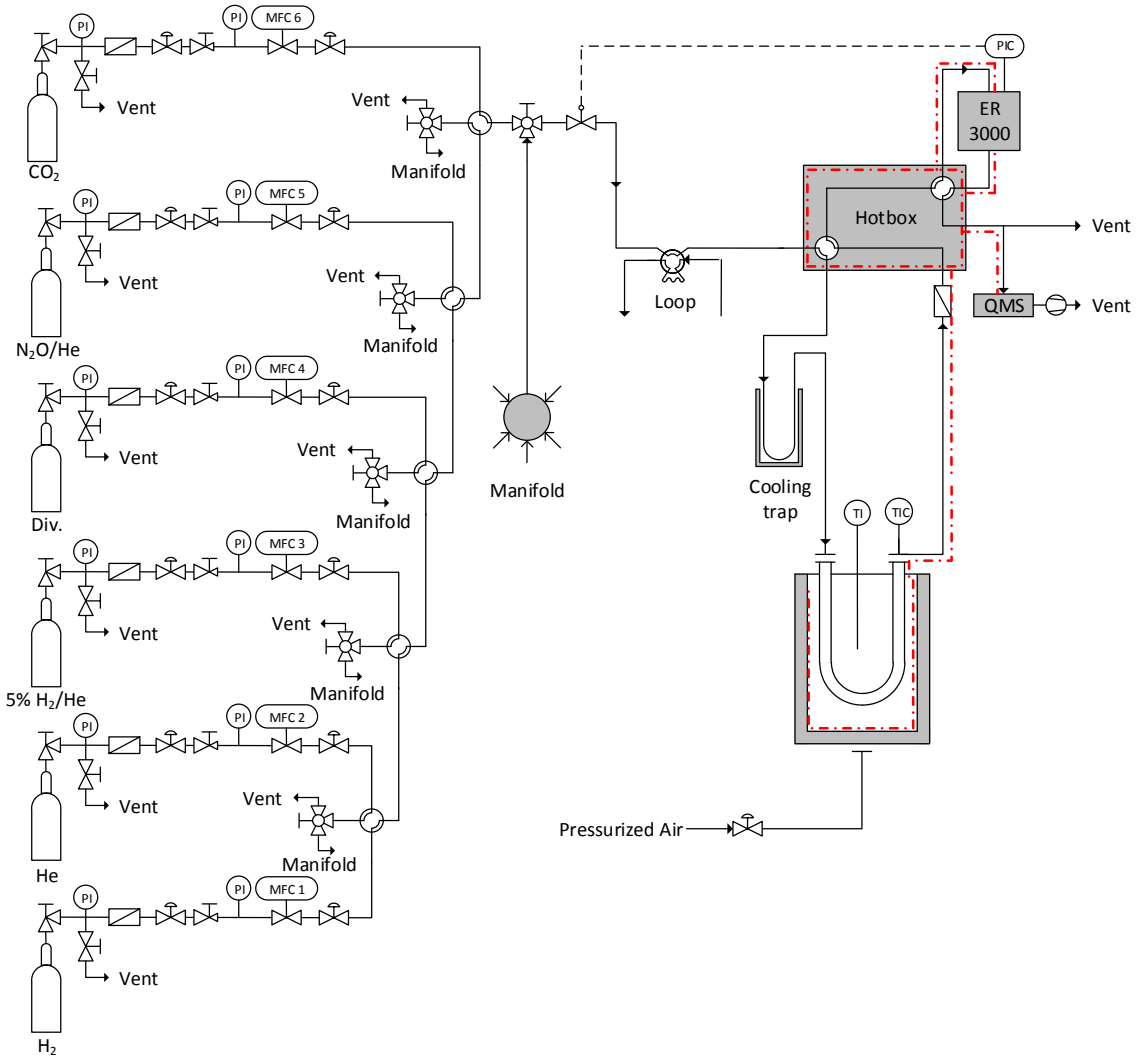

Figure 3.7: Flow diagram of the setup for transient measurements [161].

bracket on the inlet side of the reactor. The whole reactor unit can be inserted in a insulated drum and immersed in liquid N_2 so that operating temperatures as low as 84 K on the reactor inside can be achieved. Feed gas is supplied from gas bottles. Calibrated mass flow controllers (model 5850TR from Brooks Instrument®) in each line allow to adjust the respective flow rate individually. The interconnection of 4-way valves in the gas supply line allows for only one type of feed gas being fed to the reactor. Mixing different feed gases can be realized with a mixing unit connected to the setup through a manifold. Sample loops for pulsed experiments can be connected to a 6-port injection valve upstream of the reactor. Residual feed gas impurities can be removed with an additional cooling trap. An Omnistar GSD 301 quadrupole mass spectrometer (QMS) from Pfeiffer Vacuum® is applied for time resolved product gas analysis. All piping downstream of the reactor is heated to prevent condensation of product gas. A filter prevents blockage of the QMS capillary with catalyst material and silica wool. The operating pressure up to a maximum of 28 bar is adjusted by a pressure regulator (ER3000 from Tescom®). Both

the pressure regulator and the reactor itself can be brought into a bypass position by switching a 4-port valve.
Reactors with shut-off valves containing activated samples (see chapter 3.9) can be mounted into the setup under inert conditions. For this, a 3-way valve connected to a rotary vane pump is inserted into the feed gas supply line in front of the reactor inlet (Figure 3.8). The piping between the shut-off valve and the 3-way valve are periodically evacuated and flushed with He (1) before the shut-off valve at the reactor inlet is opened and the reactor is connected to the analysis unit under He flow (2). For removal of samples from the setup under inert conditions, the reactor outlet is disconnected from the setup under He flow before a shut-off valve is installed. Subsequently, both the shut-off valve on the inlet and outlet are closed and the rector is removed from the setup.

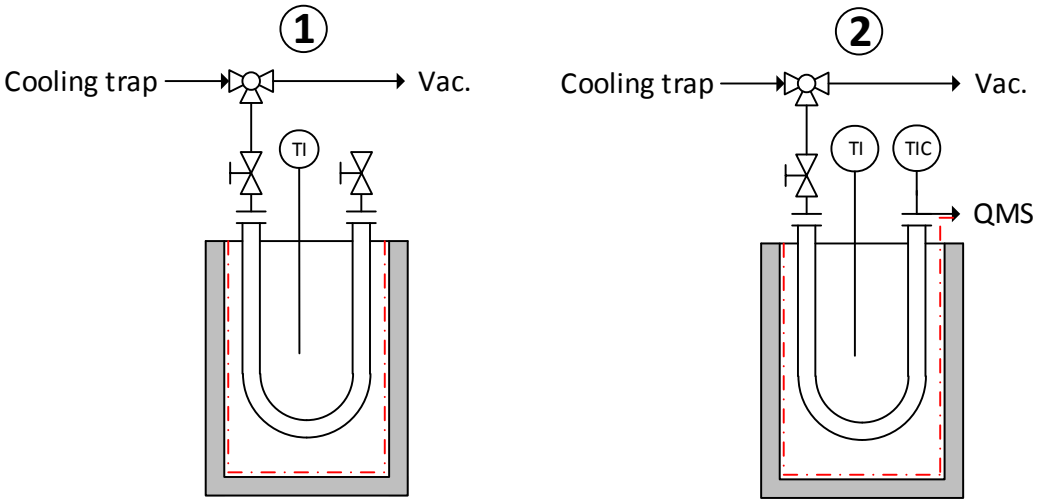

Figure 3.8: Reactor configuration for analysis of activated samples.

3.12 Temperature programmed desorption (TPD)

Temperature programmed desorption (TPD) belongs to transient measurement techniques, where the operating temperature is linearly increased. The changes of the product gas are recorded time resolved at high resolution, e.g. by mass spectrometry. Commonly, TPD is applied in ultra high vacuum (UHV) to investigate single crystal surfaces. Herein, probe gas is adsorbed on the clean surface below its desorption temperature. After dosing, UHV is established and the sample temperature is increased linearly. The changes of the partial pressure of the desorbing gas allow for the determination of the desorption parameters such as the activation energy of desorption, $E_{A,\mathrm{des}}$, the pre-exponential factor $k_{0,\mathrm{des}}$ and the desorption order. However, results obtained from single crystal surfaces in UVH often are barely transferable to real, more complex

catalysts under industrial process conditions. This is referred to as "material gap" and "pressure gap", respectively.

Amenomiya and Cvetanović were the first to develop a method to investigate real catalysts at ambient pressure by means of TPD [162]. Herein, the catalyst material is analyzed as powder in a fixed bed reactor. Also here, probe gas is adsorbed on the clean catalyst surface. After adsorption, the catalyst bed is flushed with inert gas to remove not adsorbed probe gas. Then, the catalyst bed temperature is linearly increased under inert gas flow and the changes in the effluent gas composition is recorded time resolved by means of a mass spectrometer. The concentration profile of the desorbing gas for first and second order desorption are schematically depicted in Figure 3.9. The signal position is dependent on the $E_{A,\mathrm{des}}$, the pre-exponential factor and

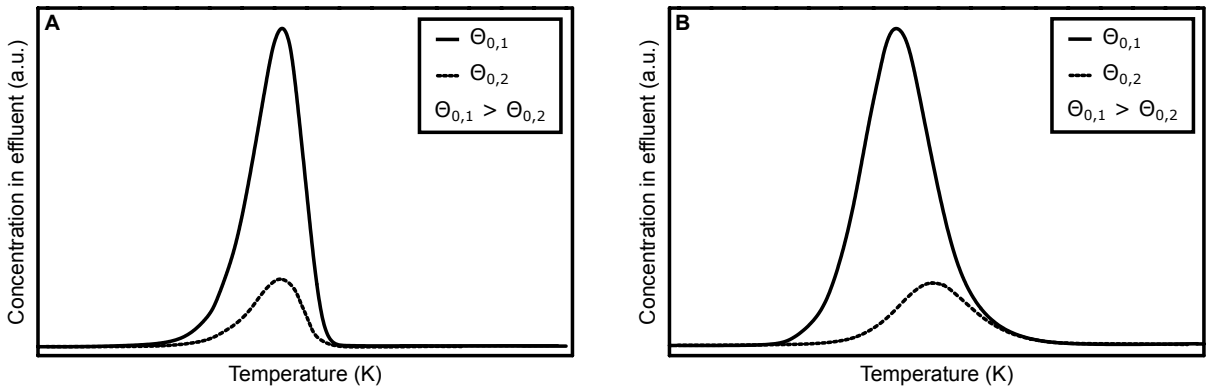

Figure 3.9: Schematic concentration profiles of desorbing gas upon (A) first order desorption and (B) second order desorption at varying initial coverages, Θ_0 (adapted from [163]).

the initial coverage, Θ_0. For first order desorption, typically, an asymmetric profile shape is obtained with a steep decrease at temperatures higher than the peak maximum. No signal shift is obtained when changing the initial coverage. For a second order desorption, which is typical for associative desorption of a two-atomic gas, a symmetric profile is obtained with the peak maximum shifting to higher temperatures when the initial coverage is decreased.

Next to the determination of kinetic parameters also the calculation of the active metal surface area is possible [164, 165]. Additionally, information about the nature of exposed surfaces and adsorption sites can be obtained [165, 166]. A proper determination of kinetic desorption parameters is only achievable if the partial pressure of the desorbing species reflects the desorption kinetics. However, several phenomena can bias the calculation. For example, pore diffusion limitation and readsorption can lead to signal broadening and significant peak shifts [163, 167, 168]. For a proper design of TPD experiments in the absence of limitations both in a CSTR configuration and in a packed bed, Demmin and Gorte derived six dimensionless parameters [168, 169]. These parameters are listed in Table 3.1.

In Table 3.1, ε_b, L_b, d_b and m_cat are the porosity, the length, the diameter and the mass of catalyst bed, respectively. The heating rate, the initial and final temperature are represented by β, T_0 and T_f. R_p is the particle radius and Q is the carrier gas flow rate. D_e and D_a are the effective diffusion coefficient and the axial dispersion coefficient, respectively. S denotes the active surface area capable of adsorbing gas per volume of the catalyst and ρ_cat is the

Table 3.1: Criteria for TPD measurements in the absence of limitations (adapted from [168, 170]).

Dimensionless parameter	Definition	Requirement
DG1: $\frac{\varepsilon_b \cdot L_b \cdot \pi \cdot d_b^2 \cdot \beta}{4 \cdot Q \cdot (T_f - T_0)}$	carrier gas residence time/experiment time	< 0.01
DG2: $\frac{\varepsilon_b \cdot R_p^2 \cdot \beta}{D_e \cdot (T_f - T_0)}$	diffusion time constant/experiment time	< 0.01
DG3: $\frac{\rho_p \cdot R_p^2 \cdot Q}{3 \cdot m_{cat} \cdot D_e}$	carrier gas flow rate/diffusion rate	< 0.05
DG4: $\frac{4 \cdot Q \cdot L_b}{\pi \cdot d_b^2 \cdot D_a}$	carrier gas flow rate/axial mixing	< 0.05
DG5: $\frac{S \cdot \rho_{cat} \cdot s \cdot F \cdot R_p^2}{3 \cdot D_e}$	adsorption rate/diffusion rate	< 1
DG4: $\frac{S \cdot \rho_{cat} \cdot s \cdot F \cdot \pi \cdot d_b^2 \cdot L_b \cdot (1-\varepsilon_b)}{4 \cdot Q}$	adsorption rate/carrier gas flow rate	< 1

catalyst density. The sticking coefficient is represented by s. The factor, F, is dependent on the temperature, T, the universal gas constant, R and the molar mass of the desorbing species, M, according to equation 3.25 [168]:

$$F = \left(\frac{R \cdot T}{2 \cdot \pi \cdot M} \right)^{0.5}. \tag{3.25}$$

The dimensionless parameter DG1 describes the ratio of the average residence time of the carrier gas to the overall time needed for the experiment. Gas species desorbing simultaneously from different points of the catalyst bed are detected at different times if the carrier gas flow rate is too slow in comparison to the temperature range and heating rate applied. Accordingly, DG2 correlates the time needed for intraparticle diffusion and the measurement time. DG2 should fall below 0.01 for negligible diffusion time lags. In a typical design of a TPD setup, this these criteria are normally fulfilled [168]. DG3 represents the ratio of carrier gas flow rate to the diffusion rate and is indicative of particle concentration gradients. Gradients can be considered negligible if DG3 falls below 0.05. Kanervo et al. [170] derived a similar correlation for evaluating intraparticle diffusion limitations in systems where intraparticle mass transport follows Knudsen diffusion:

$$\frac{Q \cdot R_p^2 \cdot \rho_p \cdot \left(1 - \varepsilon_b\right)}{D_e \cdot m_{cat} \cdot \varepsilon_b} < 0.16. \tag{3.26}$$

Parameter DG4 is the Peclet number [168, 170]. It represents the ratio of the carrier gas flow rate to axial mixing and describes the extent of back-mixing in the packed-bed. For values below 0.1 the packed bed can be adequately described with a CSTR model [168]. However, Kanervo et al. [170] found that perfect mixing is practically not achievable under typical experimental conditions and presented a PFR model for kinetic analysis of TPD. DG5 and DG6 evaluate the influence of readsorption at a very high and a very low carrier gas volume flow, respectively. DG5 correlates the adsorption and desorption rate, whereas DG6 measures the

ratio of the adsorption rate to the carrier gas flow rate. However, very high flow rates resulting in values for DG3 above 10 should be avoided [168]. Also here, Kanervo et al. [170] could show that readsorption cannot be avoided in plug flow reactor operation under typical operating conditions, when adsorption is non- or slightly activated. Consequently, only information about the quasi-equilibrium but not desorption kinetics can be obtained.
Even though the criteria by Demmin and Gorte are commonly applied, also other correlations can be found in literature [171, 172].

3.13 Pulse and frontal chromatography

Pulse and frontal chromatography belong to the group of transient measurements where the partial pressure of a probe gas species is changed. In pulsed measurements, the probe gas is dosed into an inert gas flowing over the catalyst bed, whereas frontal chromatography implies switching between gas streams. Reactive gas species applied in these measurements interact with the sample. Conclusions on the nature of interaction can be drawn from variations of the pulse/front form or the amount of reaction products. If adsorption of the probe gas takes place the amount of adsorbed gas, for example, can be determined from the difference of applied and detected pulses upon pulse chromatography. A common probe gas applied in frontal chromatography for characterization of the active metal surface area is N_2O [173–176]. Herein, an inert gas stream flowing over the activated catalyst is switched to an N_2O stream. Once N_2O reaches the catalyst bed, it is dissociatively decomposed, with the metallic phase being oxidized and N_2 being formed. Once the oxidation is complete, N_2 formation is slowing down and N_2O is detected in the effluent gas. From the amount of N_2 formed, N_N (which corresponds to the amount of oxygen that oxidized the sample) the active metal surface area can be determined if subsurface/bulk oxidation and side reactions can be excluded:

$$S_{Me} = \frac{N_N \cdot N_A \cdot z}{m_{cat} \cdot \sigma_{Me}}. \tag{3.27}$$

The factor, z, represents the stoichiometry of the metal oxide layer. Equation 3.27 also can be applied when N_2O is pulsed onto the catalyst.

4 Synthesis and characterization of Ni-Al catalysts for CO_2 methanation

Part of this chapter was published in:

S. Ewald, M. Kolbeck, T. Kratky, M. Wolf, O. Hinrichsen, *On the deactivation of Ni-Al catalysts in CO_2 methanation*, Applied Catalysis A: General, **2019**, *570*, 376-386.

Part was also published in:

S. Ewald, O. Hinrichsen, *On the interaction of CO_2 with Ni-Al catalysts*, Applied Catalysis A: General, **2019**, *580*, 71-80.

4.1 Introduction

The methanation of CO_2 is an exothermic reaction and thermodynamically favored at low temperatures. Under industrially relevant process conditions, however, the reaction is kinetically controlled and catalysts have to be applied to obtain high conversions and product yields. Among a broad range of group VIII transition metals which are capable of catalyzing the CO_2 methanation reaction, Ni is of high economic importance. Commercial Ni catalysts for hydrogenation reactions are commonly synthesized via precipitation with subsequent calcination and are activated in situ. Precipitated systems are often mistaken as supported catalysts, however, the composition and microstructure can significantly differ from this conception. Moreover, the microstructure of the precursors influence the physico-chemical properties and hence, the performance of the final catalyst [81, 87–89, 177, 178]. The catalyst, so to speak, has a "chemical memory" of its synthesis history, similar to copper catalysts for methanol synthesis [179]. The understanding of structure-activity relations, therefore, starts with the elucidation of the catalyst´s material chemistry already in the precursor and calcined state.

For the studies in this work, Ni-Al catalysts with varying Ni loading are synthesized via co-precipitation in order to obtain catalysts typically applied industrially. For the sake of comparison, also classic metal-support systems, namely Ni/γ-Al_2O_3, are synthesized by an impregnation technique. Selected precursors and calcined samples are characterized by means of XRD, N_2 physisorption and TPR coupled with TG-MS.

4.2 Experimental

4.2.1 Catalyst synthesis

For co-precipitation, 1 l of bidistilled water was heated to 303 K in a stirred glass tank. An equimolar mixture of 0.5 M NaOH (Merck®) and 0.5 M Na_2CO_3 (Sigma-Aldrich®) was applied as precipitating agent which was added by an Titrino Autotitrator 716DMS from Methrom® to obtain a pH of 9. Subsequently, an aqueous solutions of $Ni(NO_3)_2 \cdot 6H_2O$ (1 M, Merck®) was mixed with an aqueous solution of $Al(NO_3)_3 \cdot 9H_2O$ (1 M, Sigma-Aldrich®) and added dropwise into the vessel by a peristaltic pump. The Ni/Al ratio was varied between 0/1, 1/5, 1/3, 1/2, 1/1, 3/1, 5/1 and 1/0. Flow beaker were inserted for efficient mixing conditions. Throughout precipitation, the pH was kept constant by adding precipitating agent when needed. The resulting slurry was aged for 18 h in the mother liquor at 303 K. After aging, the precipitate was filtered and washed until pH 7 before it was dried over night in air at 353 K. The precursors were calcined in flowing air at a heating rate of 5 K min^{-1}. They were kept at the desired calcination temperature for 6 h. The maximum calcination temperature was 723 K for all precursors, except for the one with a Ni/Al ratio of 1/2, which was calcined at 1173 K. The resulting calcined systems are denoted as PC01, PC15, PC13, PC12, PC11, PC31, PC51 and PC01 according to their Ni/Al ratio. Calcined catalyst material was pressed, grinded and sieved prior to analysis.

For incipient wetness impregnation, γ-Al_2O_3 (Sasol®) with a pore volume of $V_p = 0.5\,cm^3\,g^{-1}$ was impregnated with $Ni(NO_3)_2 \cdot 6H_2O$ (1 M, Merck®). The samples were calcined under the same conditions as precipitated catalysts. The desired Ni loading of the impregnated samples after calcination was 9 and 17 wt-%. The corresponding catalysts are denoted as IC9 and IC17, respectively.

The Ni/Al ratio in the precursors after precipitation as well as the Ni loading of the calcined catalysts was determined by atom absorption spectroscopy using a AA280FS from Varian® and photometry using a Shimadzu® UV-160. The results are given in Table 4.1.

Table 4.1: Results from elemental analysis.

Catalyst	PC10	PC51	PC31	PC11	PC12	PC13	PC15	PC01	IC17	IC9
Ni/Al[a] (-)	-	4.87	2.97	1.04	0.49	0.36	0.21	-	n. d.	n. d.
Ni loading[b] (wt-%)	79.0	64.4	58.3	38.1	n. d.	22.5	15.3	-	16.7	9.1

[a] in the precursors after precipitation
[b] calcined samples

4.2.2 Catalyst Characterization

XRD analysis was performed with a Stadi P diffractometer from STOE® equipped with a Ge(111) monochromator. The diffractometer was operated at 50 kV and 30 mA in Debye-Scherrer geometry. Measurements were conducted within $2\theta = 5 - 90\,^\circ$ at $0.86\,^\circ\mathrm{min}^{-1}$ and a stepsize of $0.5\,^\circ$. For analysis, sample material was sealed in a glass capillary with an inner diameter of 0.5 mm.

N_2 physisorption measurements at the boiling point of liquid N_2 were conducted on a Novatouch from Quantachrome®. Both the adsorption and desorption isotherms were recorded. The BET surface area, S_{BET}, was calculated from the adsorption branch within $p/p_0 = 0.05 - 0.3$. The pore volume and average pore diameter were determined from S_{BET} and the N_2 uptake at p/p_0 close to 1 assuming cylindrical pores. For measurements, 100 mg of sample material were used and degassed under vacuum at 393 K for 3 h prior to analysis.

Thermogravimetric (TG) analysis was applied to investigate the reduction behavior of the calcined catalysts. Measurements were conducted with a Netzsch® STA 409 thermobalance. For product gas analysis, an Omnistar GSD 301 quadrupole mass spectrometer from Pfeiffer Vacuum® was applied. For analysis, 25 to 50 mg of calcined catalyst material were loaded into the balance. Subsequently, the samples were heated in Ar ($Q_{Ar} = 60\,\mathrm{Nml\,min}^{-1}$) to 623 K at a heating rate of $3\,\mathrm{K\,min}^{-1}$ to remove adsorbed surface species. The samples were held at this temperature for 1 h before they were cooled down to room temperature. Then, the gas flow was switched to 5% H_2 in Ar and temperature programmed reduction (TPR) was performed up to a maximum temperature of 1173 K at a gas flow rate of $75\,\mathrm{Nml\,min}^{-1}$.

4.3 Results and discussion

4.3.1 Catalyst structure

Figure 4.1A depicts XRD patterns of the catalyst precursors. PC31 shows the characteristic reflections of takovite (JCPDS 15-0087). The reflections at $2\Theta = 11.3\,^\circ$ and $2\Theta = 22.9\,^\circ$ can

be attributed to the (003) and the (006) plane, respectively. The (110) and (113) planes exhibit reflections at $2\Theta = 60.8°$ and $2\Theta = 62.0°$. The (012), (015) and (018) reflections at $2\Theta = 35.0°$, 39.1° and 46.8°, show significant asymmetries, indicating stacking faults [87, 178]. Takovite belongs to the hydrotalcite group and consists of brucite-like layers containing layered double hydroxides, where cations occupy the center of an octahedron surrounded by six hydroxyl ions in the corners of the octahedron. For charge compensation, CO_3^{2-} is found in the interlayer between the hydroxides together with H_2O [180]. The characteristic takovite reflections are

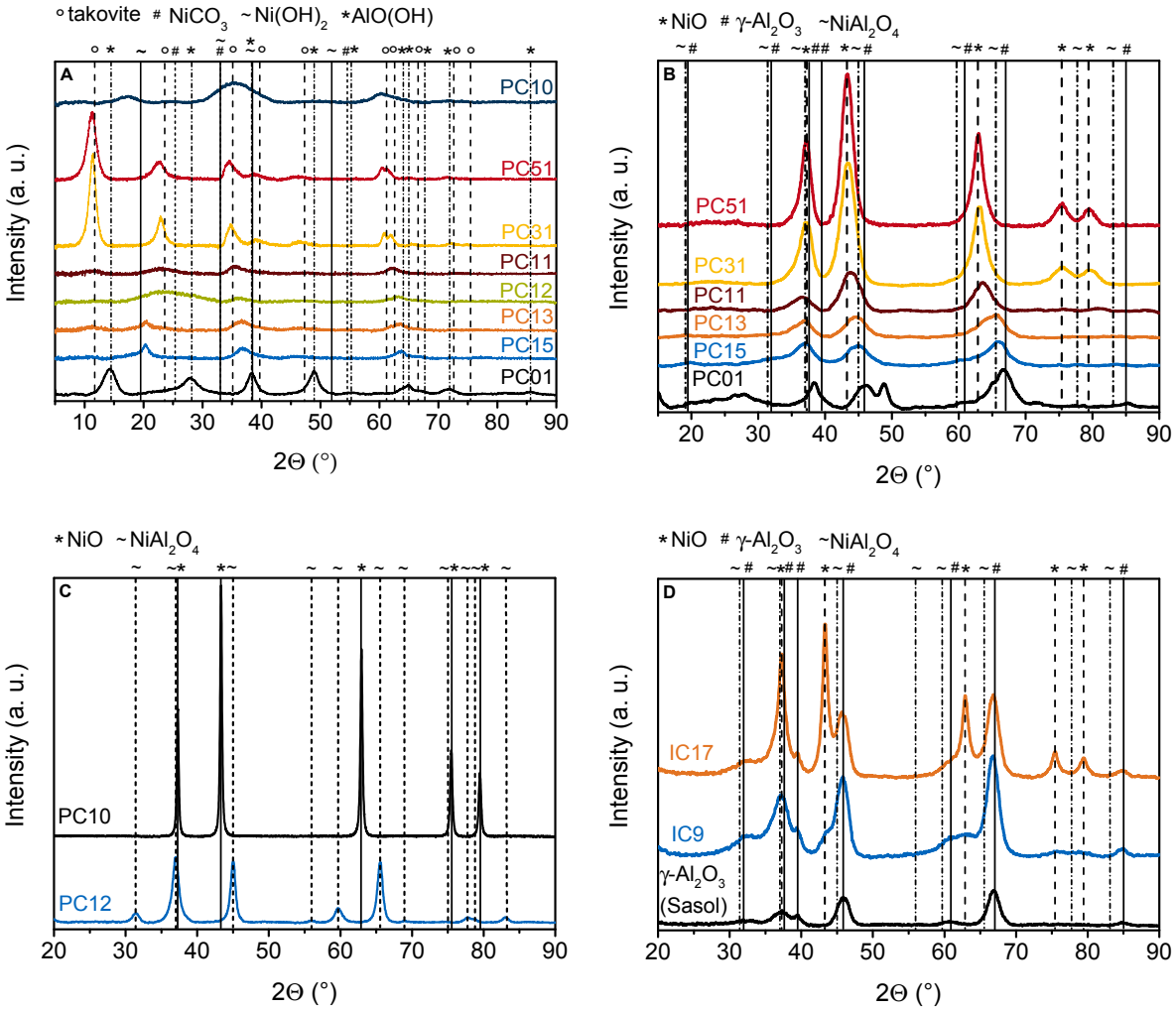

Figure 4.1: XRD pattern of (A) the catalyst precursors after precipitation and (B-D) catalyst samples after calcination (JCPDS: takovite 15-008, $Ni(OH)_2$ 1-074-2075, $NiCO_3$ 1-078-0210, NiO 78-0429, γ-Al_2O_3 10-0425, $NiAl_2O_4$ 10-0339, AlO(OH) 21-1307).

shifted to higher diffraction angles with declining Ni loading. In PC11 the (110) and (113) reflections cannot be distinguished anymore. For the calculation of the lattice parameters *c* and *a*, we used the (006) and the (012) reflection, respectively. We abstained from the calculation of *c* by averaging the positions of the reflections of the (003) and the (006) plane as suggested by Abate et al. [82], since sample PC11 shows poor crystallinity and the reflection of the (003) plane at $2\Theta = 10.7°$ in this case is barely detectable. The lattice parameter *a* decreases from 3.037 Å in PC31 to 2.988 Å in PC11, indicating substitution of Ni^{2+} by Al^{3+} forming a mixed

basic carbonate. The Al^{3+} cation has a *smaller* ionic radius than Ni^{2+}, so that substitution *decreases* the average distance between two cations, which is represented by *a*. The lattice parameter *c* decreases from 23.27 to 23.02 Å, which can be explained by an increasing electrostatic interaction between the brucite layer and the anion containing interlayer with increasing Al^{3+} substitution [85, 178, 181]. In reverse, the higher content of Ni^{2+}, in sample PC51 as compared to takovite causes an *increase* in the cation distance and *a decrease in* electrostatic interaction, and shifts the reflections to lower diffraction angles.[1] The corresponding values for the lattice parameters *a* and *c* in this case are 3.061 and 23.57 Å, respectively. The lattice parameters of the samples PC13 and PC15 were not calculated due to poor crystallinity of those samples. A closer inspection of the pattern in Figure 4.1 reveals, that already the reflections of PC31 are shifted (even though to lower diffraction angles) compared to pure takovite. The calculations of the lattice parameters results in an increase of *c* from 22.60 Å in takovite to 23.27 Å in PC31. Parameter *a* increases slightly from 3.025 to 3.037 Å. Deviations might be explained by a poor ordering in the synthesized samples. Also compensating anions other than carbonate have to be considered leading to changes in the interaction of the brucite layer and the interlayer. In this context, the precipitation conditions have been reported to have significant influence [87, 178]. The crystallinity increases form PC51 to PC31 and then decreases again with decreasing Ni content. No additional crystalline phase was observed for the sample with the highest Ni loading, PC51, whereas samples PC13 and PC15 exhibits an additional phase with a strong reflection at $2\Theta = 20.3°$. For co-precipitated samples with low Ni loadings the formation of crystalline boehmite [85, 178] and gibbsite [85] was reported, but not observed here. Also bayerite, which might transform to gibbsite during precipitation is not observed, which is in accordance with previous work [79]. Puxley at al. [87] reported on the formation of nitrate containing mixed oxides when applying a Ni/Al ratio equal to spinel stoichiometry during precipitation. However, elemental analysis revealed a nitrogen content below the detection limit in all precursors so that the formation of this phase can be ruled out. However, boehmite is the only detectable phase in sample PC01. For sample PC10, which does not contain any Al species, no crystalline $Ni(OH)_2$ or $NiCO_3$ is observed.

XRD pattern of calcined samples are depicted in Figure 4.1B-D. The signals observed in calcined PC51 and PC31 match the positions of bunsenite reflections. The peak intensity decreases with declining Ni content due to a reduction of crystallinity and a decreasing NiO particle size. Moreover, the reflections are shifted to higher diffraction angles with decreasing Ni content. The reflection in sample PC11, which is located between the signal of the (200) plane of bunsenite and $2\Theta = 65.5°$ for the (440) plane of $NiAl_2O_4$, indicates the presence of Al^{3+}-containing NiO. For precipitated samples with a Ni loading below 23 wt-%, the reflection situated between the signal for the (440) of $NiAl_2O_4$ and $2\Theta = 67.0°$ for the (440) plane of Al_2O_3, suggests Ni^{2+}-containing alumina [87, 89, 177]. No additional crystalline phase is observed in samples PC51,

[1] The content marked in italic deviates from the corresponding sections of the articles this chapter was published in. This is due an error that occurred upon citing from literature references given there.

PC31, PC11 and PC13. One might speculate whether spinel is present in PC15, the poor crystallinity of which complicates a distinct analysis. In sample PC01, the reflections of γ-Al_2O_3 are observed. The additional signal at $2\Theta = 48.8\,^\circ$ might be attributed to some boehmite, indicating that the sample was not fully calcined under the experimental conditions chosen. Figure 4.1C depicts XRD pattern of calcined PC10 and PC12. Pure bunsenite is obtained in the case of PC10. The characteristic reflections at $2\Theta = 37.3\,^\circ$, $43.3\,^\circ$, $62.9\,^\circ$, $75.5\,^\circ$, and $79.5\,^\circ$ correspond to the (111), (200), (220), (311) and (222) plane, respectively. The respective values for the *d*-spacing are 2.410, 2.087, 1.476, 1.258 and 1.205 Å. The high calcination temperature of 1173 K results in the formation of the spinel phase $NiAl_2O_4$. The three main reflections at $2\Theta = 36.7\,^\circ$, $44.5\,^\circ$, and $65.5\,^\circ$ correspond to the (311), (400) and (440) with values for the *d*-spacing of 2.431, 2.015, and 1.425 Å. In the impregnated samples (Figure 4.1D), all reflections can be attributed to bunsenite and γ-Al_2O_3. The signal intensity rises with increasing Ni loading which is in line with the growth of NiO crystallites. The structures of selected samples are further analyzed by means of XPS measurements and discussed in greater detail in chapter 6.

Table 4.2: Results from N_2 physisorption measurements of calcined samples.

Catalyst	PC10	PC51	PC31	PC11	PC12	PC13	PC15	PC01	IC17	IC9	γ-Al_2O_3
S_{BET} ($m^2\,g_{cat}^{-1}$)	15.2	118.4	130.3	180.2	98.1	196.8	211.6	223.0	142.8	166.2	195.7
V_P ($cm^3\,g_{cat}^{-1}$)	0.06	0.47	0.41	0.51	0.45	0.31	0.35	0.73	0.30	0.39	0.45
d_P (nm)	15.4	15.8	12.7	11.4	18.4	6.4	6.6	6.5	8.4	9.3	9.3

Table 4.2 and Figure 4.2 summarize characterization data from N_2 physisorption measurements of calcined samples. All samples investigated exhibit a type IV isotherm with a hysteresis, indicating the presence of mesopores. Pure NiO (sample PC10) as well as precipitated samples of low Ni loadings up to 22.5 wt-% show a type H2 hysteresis, implying that the pore structure is not well-defined. A type H3 hysteresis, typical for non-rigid aggregates of plate-like particles forming slit-shaped pores, is observed for precipitated samples of higher loadings. The hystereses of sample PC10 and PC12 are barely observable, which indicates a low porosity of those samples. PC01 exhibits characteristic features of a type H1 hysteresis, which is typically obtained in the case of cylindrical pores and agglomerates of uniform spheres. A type IV isotherm with a type H2 hysteresis is observed for γ-Al_2O_3. The pore structure does not change upon impregnation within the range of Ni loadings applied in this study. The BET surface area, S_{BET}, decreases with rising Ni content, whereas the average pore diameter increases for precipitated samples. No clear trend is observable for the total pore volume. The low value for the BET surface area and the total pore volume in sample PC10 underlines a poor porosity as mentioned before. Sample PC12 exhibits a lower BET surface area but an increased average pore diameter as compared to the other precipitated samples, which can be attributed to sintering effects induced by the significantly higher calcination temperature of 1173 K. The BET surface area and the total pore volume of impregnated samples decrease with rising Ni content, indicating pore blockage by Ni species. The average pore diameter of IC9 is the same

as for pure γ-Al_2O_3 and decreases when the Ni content is increased to 17 wt-%. One might expect that the average pore diameter initially increases with rising Ni content since small pores are blocked first. However, a Ni content of 9 wt-% might already be high enough that this effect is compensated by partial blockage of larger pores.

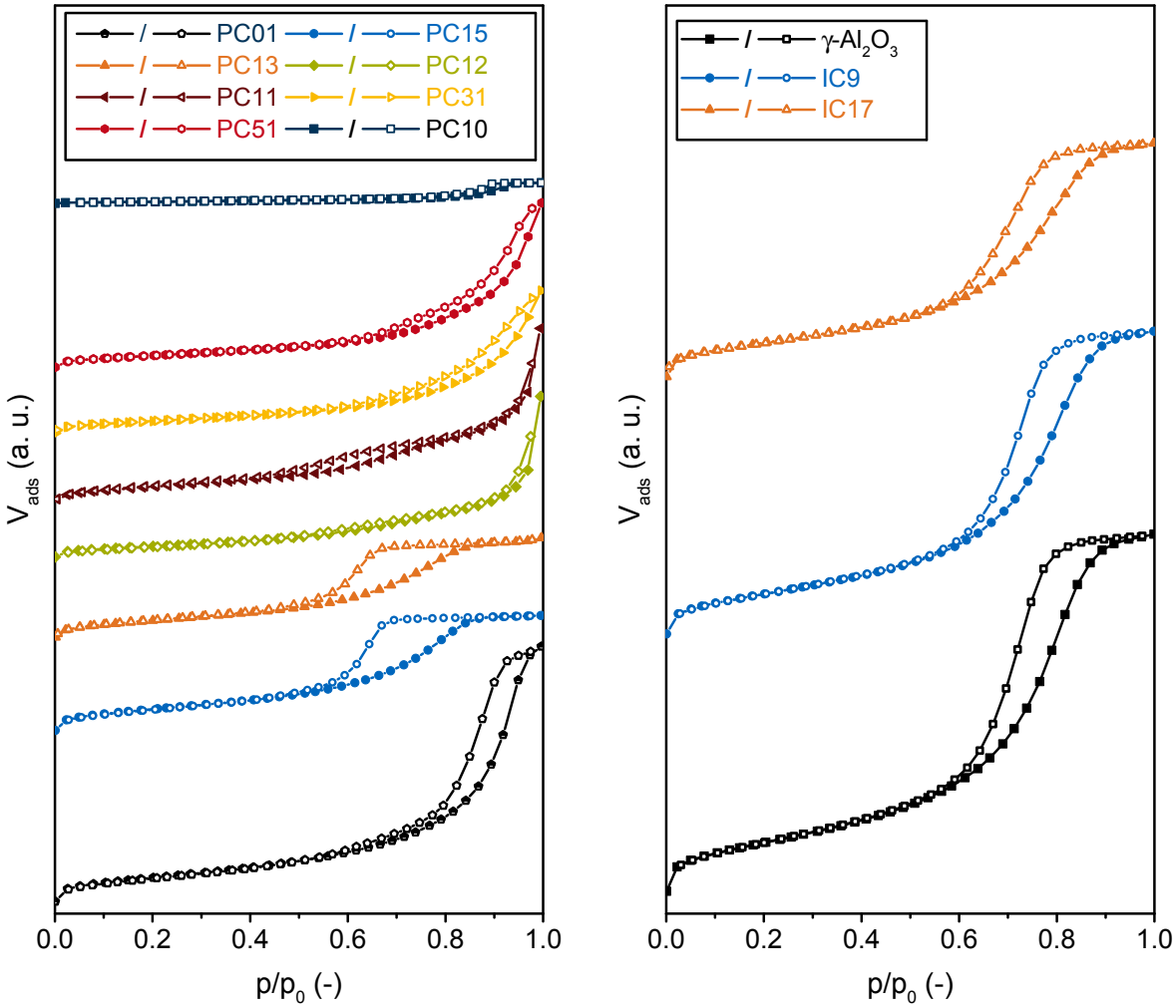

Figure 4.2: N_2 adsorption/desorption isotherms of calcined samples

4.3.2 Reduction behavior

Figure 4.3 depicts TPR results of the synthesized samples and pure γ-Al_2O_3. The trend of the weight loss determined from TG analysis matches the reduction profiles (Figure A.1). Pure NiO and $NiAl_2O_4$ reveal a reduction signal at 620 and 1055 K, respectively, which is in good agreement with literature [182–185]. A very weak reduction signal is also observed for γ-Al_2O_3 and PC01. This might be attributed to the elimination of surface hydroxyl groups and in the case of PC01 also to the conversion of boehmite residues. The mass loss during reduction is 1.8 % for γ-Al_2O_3 and 3.5 % for PC01. For precipitated samples, a broad pattern between the reduction

signal of NiO and $NiAl_2O_4$ is observed, which is continuously shifted to higher temperatures with declining Ni content. This reflects well the gradual change from a NiO-like to a spinel-like structure as revealed by XRD. Interestingly, the reduction temperature of PC51, the structure of which, according to XRD results, corresponds to NiO (Figure 4.1B), is shifted to higher temperatures as well. The intimate contact of NiO to an amorphous Al-containing structure, not detectable by XRD, might lead to a strong interaction decreasing the reducibility of the Ni species. Zieliński interpreted this interaction on a way that water induces the formation of a surface nickel aluminate retarding the reduction [90, 110]. This mechanism was proposed especially but not exclusively for highly loaded Ni-Al catalysts [137]. It is also possible that small amounts of Al^{3+} are incorporated into the NiO lattice impeding reduction but the changes are too marginal to be detected by XRD. On the other hand, the reduction profile of PC15, in which case XRD analysis gave some indication of spinel, does not match the position of $NiAl_2O_4$, excluding the presence of bulk spinel. However, surface spinel was reported to be reducible at lower temperatures as compared to bulk nickel aluminate [109, 185, 186]. The profile shapes of samples PC51, PC31 and PC11 reveal two overlapping signals, which strongly indicates the existence of an additional mixed oxide phase of amorphous character, which is not resolved by XRD. Also Zieliński reported on the simultaneous presence of a crystalline NiO-rich and an amorphous Al-rich phase in co-precipitated systems [90, 110]. One might speculate whether the signals of PC13 and PC15 between 800 and 1050 K also consist of overlapping signals. In addition to the broad feature, a small signal centered around 700 K is observed in PC15. This signal might be a result of surface hydroxyl elimination, revealed by a comparison with the pattern of γ-Al_2O_3, or indicates the presence of small NiO crystallites which exhibit low nucleation rates during reduction impeding reducibility [185]. Zieliński, however, proposed that small and large Ni crystallites are reduced with the same ease [109].

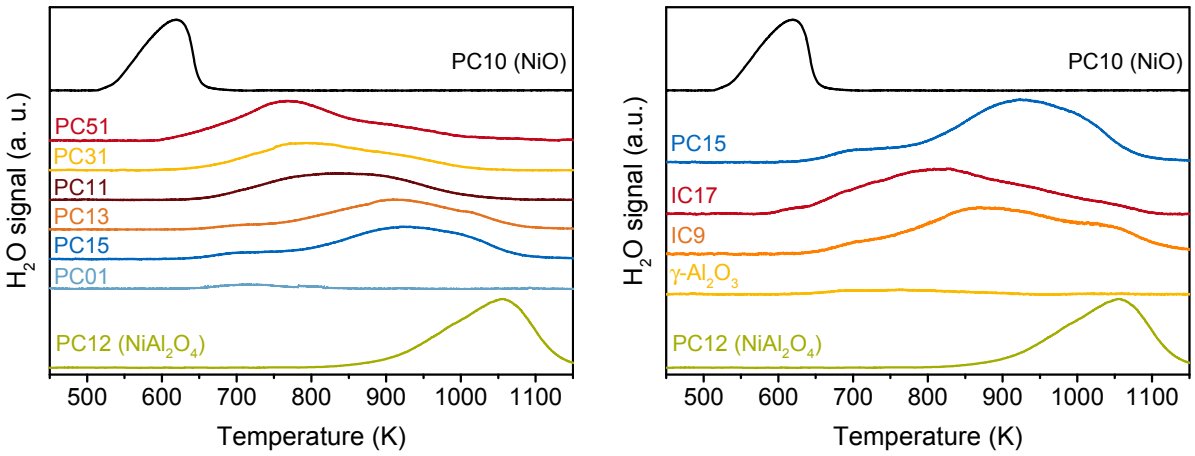

Figure 4.3: Results from temperature programmed reduction.

Also for impregnated samples, a broad reduction signal at significantly higher temperatures as for pure NiO is observed. As for precipitated samples, the reduction signal is shifted to higher temperatures with decreasing Ni loading. This is somewhat surprising as NiO is detected as the only Ni-containing phase by means of XRD. Also here, water induced formation of a

spinel-like surface layer might impede the reduction [137]. Zieliński also reported on "free" and "fixed" NiO in impregnated systems with the content of each phase depending on the Ni loading [109]. "Free" NiO coincides with phase pure bunsenite, whereas "fixed" NiO, requiring significantly higher temperatures for reduction, comprises nickel aluminate-like species as well as NiO crystallites covered by this spinel-like layer. The latter is detected as bunsenite in XRD but exhibits a significantly lower reducibility as pure NiO. Nickel aluminate-like structures and covered NiO species were also observed in other studies [109, 111, 185, 187, 188]. Also decreased nucleation rates due to small Ni particle sizes have to be taken in consideration, similar to precipitated samples. With regard to the pattern of IC9, it can be speculated whether amorphous bulk spinel is present as a peak at about 1050 K is observed, coinciding with the profile of the $NiAl_2O_4$ reference. A comparison of PC15 and IC17, which exhibit similar Ni loadings, reveals that precipitated samples are more difficult to reduce than impregnated systems.

All samples are completely reduced at a maximum temperature of 1173 K as summarized in Table 4.3. For all samples, the expected mass loss was calculated on the assumption that metallic Ni is formed due to reduction of NiO and $NiAl_2O_4$, respectively. The experimental result for pure NiO (PC10) and $NiAl_2O_4$ (PC12) agrees well with the calculated value. The mass loss determined from thermogravimetric measurements of supported samples, however, is higher than the theoretical mass loss. The discrepancy rises with decreasing Ni loading and increasing BET surface area. In samples with higher BET surface areas more surface hydroxyl groups are exposed to H_2 that can be eliminated increasing the mass loss upon reduction.

Table 4.3: Comparison of calculated and measured mass loss upon reduction.

Catalyst	PC10	PC51	PC31	PC11	PC12	PC13	PC15	IC17	IC9
theoretical mass loss (%)	21.0	17.5	15.9	10.4	9.1	6.1	4.2	4.6	2.5
measured mass loss (%)	21.5	20.6	19.9	15.7	9.4	9.6	7.7	7.7	4.3

4.4 Conclusion

Ni-Al catalysts with varying Ni loadings as well as pure NiO and $NiAl_2O_4$ were synthesized via co-precipitation and incipient wetness impregnation. The precursors and calcined samples were characterized by means of XRD and N_2 physisorption measurements. The reduction behavior was characterized by TPR experiments in a TG-MS setup. Precipitated precursors consist of mixed basic carbonates the structures of which depend on the Ni/Al ratio in sample. For a Ni/Al ratio of 3/1 a takovite-like structure is observed. Upon calcination at 723 K, Ni-Al mixed oxides of varying stoichiometry are formed, whereas calcination of the precursor with a Ni/Al ratio of 1/2 at 1173 K results in $NiAl_2O_4$. Pore structure analysis revealed a mesoporous character of all

samples, whereat the porosity of pure NiO and $NiAl_2O_4$ is significantly lower as compared to the other samples. For precipitated samples the pore structure is dependent on the Ni loading. For impregnated samples, pore blockage is observed upon impregnation with the overall pore structure remaining unchanged. TPR experiments revealed multiple Ni species in the catalyst samples. At least two Ni species of varying crystallinity are observed in precipitated samples, the reducibility of which decreases with increasing Al content and calcination temperature. Also for impregnated samples the reducibility is impeded as compared to pure NiO.

5 Characterization of nickel catalysts with transient methods

This chapter was published in:

S. Ewald, S. Standl, O. Hinrichsen, *Characterization of nickel catalysts with transient methods*, Applied Catalysis A: General, **2018**, *549*, 93-101.

5.1 Abstract

The Ni surface area is a key factor in catalytic performance of supported Ni catalysts employed in heterogeneously catalyzed reactions. For its characterization, transient measurement techniques are powerful but need a proper experimental design and a high level of accuracy. In this study, several transient methods, namely temperature programmed desorption of H_2 (H_2-TPD), pulsed H_2 chemisorption and N_2O chemisorption, were applied and evaluated for the characterization of Ni catalysts. Results were compared with those from static H_2 chemisorption. Ni powder, as well as $NiAlO_x$ and Ni/γ-Al_2O_3 with varying Ni loadings, synthesized via precipitation and incipient wetness impregnation, respectively, were used as model catalysts. H_2-TPD within in the temperature range from 84 - 753 K is able to completely describe the interaction of H_2 with supported Ni. However, a quantitative analysis of the specific Ni surface area based on H_2-TPD is difficult whereas pulsed H_2 chemisorption leads to comparable results as obtained from static measurements. Adsorption and pre-treatment conditions have a strong impact on the desorption spectra. Reversible morphologic changes of the Ni surface were revealed by H_2-TPD when changing the gas atmosphere during pre-treatment. N_2O chemisorption occurs in three steps including fast oxygen uptake, growth of the oxide layer and subsequent layer thickening due to subsurface and bulk oxidation. A separation of surface and subsurface/bulk oxidation of $NiAlO_x$ and Ni/γ-Al_2O_3, both of which are readily oxidized even under mild conditions, is only achievable at temperatures between 190 and 195 K. In this temperature range, the ratio of adsorbed oxygen atoms, O, and the number of Ni surface atoms, Ni_S, (O/Ni_S) is 0.38 ± 0.07, which can be applied for specific Ni surface area determination. The experimental mode of N_2O

chemisorption (flow or titration mode) does not influence the extent of subsurface oxidation. The separation of surface and subsurface/bulk oxidation is more feasible in the case of Ni powder. Here, a suitable temperature for Ni surface area determination lies within 265 and 285 K with an O/Ni_S ratio of 0.96 ± 0.05.

5.2 Introduction

Supported Ni catalysts are widely applied in various reactions, like hydrogenation of CO [120, 189–191] and CO_2 [48, 52, 54, 78–81, 192–194]. These reactions are catalyzed by group VIII transition metals with supported Ni being the most often investigated due to its price and availability. In contrast to the hydrogenation of CO, CO_2 methanation is less intensively studied and information about catalyst deactivation is scarce. However, in order to develop highly active and efficient catalysts the understanding of predominant deactivation phenomena is of great importance. Herein, the characterization of the active metal surface area is essential. For this purpose the static chemisorption of H_2 and CO are widely applied [184, 195–197] despite CO having major drawbacks such as multiple adsorption states as well as the formation of toxic carbonyl species. Static methods allow the quantification of both strongly and weakly bound gas but require a high vacuum and measurements take up a significant amount of time. Moreover, the catalyst properties under vacuum can differ from those under working conditions at higher pressures. Therefore, it is critical to correlate the activity of catalysts with characterization results from low pressure experiments.

Within the last decades also transient methods have been developed for the characterization of supported Ni catalysts, particularly the temperature programmed desorption of H_2 (H_2-TPD) and pulsed H_2 chemisorption. However, most H_2-TPD studies, especially those found in older literature, apply UHV conditions, and thus show the same disadvantages as static methods. Amenomiya and Cvetanović were the first to apply the temperature programmed desorption technique under flow conditions [162]. Those conditions allow for the study of the catalyst much closer to working conditions. Additionally, measurements are much faster and easier to conduct. It is also possible to apply them for in situ characterization which has great potential for elucidating deactivation phenomena [198]. Moreover, H_2-TPD, when designed properly, allows for the assessment of H_2 interaction with the metal surface making it a powerful tool in microkinetic analysis of hydrogenation reactions [166, 199–203].

One major drawback with regard to H_2-TPD on Ni catalysts is that supported Ni is prone to H_2 spillover. Also pre-treatment conditions and the mode of H_2 adsorption prior to TPD have a significant impact on the desorption signal which makes a careful design of the TPD experiment essential. However, most studies in literature choose pre-adsorption parameters more or less arbitrarily. Only a few studies correlate results from different characterization techniques [166, 203]. Znak and Zieliński [204, 205] systematically investigated the influence of

H_2 pre-adsorption and concluded that a full picture of the H_2 interaction with alumina-supported Ni catalysts can only be obtained when starting H_2-TPD experiments at temperatures as low as 100 K. However, their studies were more of qualitative nature.
Another transient method to determine the active metal surface area is N_2O chemisorption where N_2O is decomposed into gaseous N_2 and oxygen that is adsorbed on the metal surface. N_2O chemisorption is widely applied to determine copper surface areas [173, 174, 206, 207]. With regard to the calculation of Ni surface areas, there is controversy in literature. Rudajevova and Pour as well as Kuijpers et al. stated that N_2O is not a suitable probe molecule for Ni surface area determination since oxygen uptake can exceed a monolayer and N_2O readily oxidizes subsurface and bulk Ni [208, 209]. Ho and Yeh conducted microgravimetric studies of the N_2O chemisorption on Ni powder and concluded that Ni surface area determination is possible at temperatures between 195 - 232 K with a stoichiometric ratio of $O/Ni_S = 0.6$ [210]. Recently, Tada et al. introduced the pulse titration of N_2O at elevated temperatures as a reliable method to characterize Ni supported on α-Al_2O_3 [149]. It is known that catalyst properties can change depending on the support, synthesis procedure and the crystallite size, making it difficult to compare the results in those studies. Differences in the measurement procedure can also impede a comparison.
In this study we present a comprehensive investigation of H_2-TPD for the characterization of nickel-aluminum catalysts. The influence of catalyst pre-treatment and H_2 adsorption is systematically examined and the results are compared with static H_2 chemisorption as standard characterization technique. In addition, N_2O chemisorption for the determination of the specific Ni surface area is applied and evaluated using both pulsed and flow conditions. Also Ni powder is examined in order to elucidate the influence of the support on N_2O chemisorption.

5.3 Experimental

5.3.1 Catalyst synthesis

Nickel-aluminum catalysts with varying Ni loadings were synthesized via co-precipitation of the corresponding metal nitrate solutions at constant pH, in accordance with literature [79, 80]. For this, 1 l of bidistilled water was placed in a glass vessel with flow beakers and heated to 303 K under stirring. An equimolar mixture of 0.5 M NaOH (Merck®) and 0.5 M Na_2CO_3 (Sigma-Aldrich®) was used as the precipitating agent and added by an automatic titrator (Titrino Autotitrator 716DMS by Methrom®) to obtain a constant pH of 9. Subsequently, the aqueous solutions of $Ni(NO_3)_2 \cdot 6H_2O$ (1 M, Merck®) and $Al(NO_3)_3 \cdot 9H_2O$ (1 M, Sigma-Aldrich®) were mixed and added dropwise by a peristaltic pump. The molar Ni/Al ratios applied were 1/5, 1/3, 1/1, 3/1 and 5/1. The samples are denoted as PC15, PC13, PC11, PC31 and PC51,

respectively. Also a sample containing only Ni was synthesized, denoted as PC10 in the following. The precipitate was aged in the mother liquor at 303 K for 18 h under stirring. Afterwards, the precipitate was washed until constant pH was achieved and dried at 353 K. The resulting precursor was calcined in flowing air at a linearly increasing temperature up to 723 K at 5 K min^{-1}. Calcination was continued at this temperature for 6 h. The calcined precursor was pressed, grinded and sieved. The sieve fraction of 150 - 250 µm was used for further analysis.
Additionally, alumina-supported catalysts with Ni loadings of 9 wt-% and 17 wt-% were synthesized by incipient wetness impregnation of γ-Al_2O_3 (Sasol®) with an aqueous solution of $Ni(NO_3)_2 \cdot 6H_2O$ (1 M, Merck®). The catalyst samples are denoted as IC9 for the sample with the desired 9 wt-% of Ni and IC17 for the desired 17 wt-% of Ni. For γ-Al_2O_3, a sieve fraction of 150 - 250 µm was used. After impregnation the catalyst precursors were dried and calcined under the same conditions as for precipitated catalysts.

5.3.2 Catalyst characterization with standard techniques

The Ni content in the calcined catalyst samples was determined via atom absorption spectrometry using an AA280FS from (VARIAN®). X-ray diffraction (XRD) was performed with a PANalytical® Empyrean using Cu-Kα radiation, operating at 45 kV and 40 mA. Measurements were carried out within the range from $2\theta = 5 - 90^\circ$ with a stepsize of 0.013° and a scanning rate of $3.42^\circ min^{-1}$.
The specific Ni surface area of the supported catalyst systems was determined by static H_2 chemisorption with an Autosorb 1C from Quantachrome®. For analysis, roughly 100 mg of calcined catalyst were placed in the sample cell and heated to 753 K under 5 % H_2 in He at 3 K min^{-1}. The sample was reduced at this temperature for 5 h. Afterwards the sample cell was evacuated at reduction temperature and held under vacuum for another 60 min before it was cooled down to room temperature. For the calculation of the specific Ni surface area, an adsorption isotherm was recorded at 308 K. An equilibration time of 2 min was applied for every data point of the isotherm. The specific Ni surface area was determined according to equation 5.1 assuming dissociative H_2 adsorption on Ni:

$$S_{Ni} = \frac{N_H \cdot N_A \cdot z}{m_{cat} \cdot \sigma_{Ni}} \tag{5.1}$$

S_{Ni} is the Ni surface area per gram calcined sample (specific Ni surface area), N_A is Avogadro's constant and N_H is the amount of adsorbed H_2 molecules obtained from extrapolating the adsorption isotherm to zero pressure. The stoichiometry factor z is 2 for dissociative chemisorption of H_2 on Ni [150], m_{cat} is the mass of calcined catalyst and σ_{Ni} is the number of Ni atoms per unit area ($1.54 \cdot 10^{19} m^{-2}$ [149]). The Ni dispersion D_{Ni} was calculated according to equation 5.2

with M being the molecular weight of Ni and w being the weight fraction of Ni in the calcined sample:

$$D_{\mathrm{Ni}} = \frac{N_{\mathrm{H}} \cdot z \cdot M}{m_{\mathrm{cat}} \cdot w}. \tag{5.2}$$

5.3.3 Experimental setup for transient measurements

Transient experiments were conducted in a single-pass setup equipped with a glass-lined fixed bed reactor. The reactor has an inner diameter of 4 mm and can be operated up to 773 K (Figure 3.7). The reactor unit can be immersed in liquid nitrogen so that temperatures as low as 84 K can be applied. Gas is fed to the reactor by a gas supply line, the dead volume and no-flow regions of which are reduced to a minimum. All gases were of high purity (6.0 for H_2 and He, 5.0 for N_2O). A cooling trap operated at liquid nitrogen temperature removes remaining water impurities from the feed gas. A calibrated sample loop connected to a 6-port injection valve in the gas supply line allows for pulsed experiments. By switching a 4-port valve the reactor can be brought into a bypass position. Product gas analysis is conducted using an Omnistar GSD 301 quadrupole mass spectrometer (QMS) from Pfeiffer Vacuum® for time resolved analysis.

5.3.4 Temperature programmed desorption of H_2

For H_2-TPD, 50 - 100 mg of calcined catalyst were placed in the isothermal zone of the reactor and secured by means of two plugs of silica wool. The catalyst bed was contacted with a thermocouple to measure the temperature of the bed. Reduction was performed under similar conditions as for static H_2 chemisorption. After reduction, the catalyst was flushed with He and cooled down to room temperature. Prior to desorption, the reactor was heated or cooled to the desired adsorption temperature in He. Then, H_2 was adsorbed at atmospheric pressure in a continuous flow of 60 Nml min^{-1}. Afterwards, the catalyst was flushed with He for at least 30 min before temperature programmed desorption (TPD) in He was performed at 6 K min^{-1}. Alternatively, H_2 adsorption was conducted in a three step program similarly described in literature [204, 205]. First, H_2 was adsorbed at the desired adsorption temperature and atmospheric pressure for 30 min. Next, the catalyst bed was cooled down to 84 K and H_2 was adsorbed at this temperature for another 30 min. Then, the catalyst was flushed with He (100 Nml min^{-1}) for 30 min before TPD. The maximum temperature during TPD did not exceed reduction temperature to avoid temperature induced morphologic changes of the catalyst. After TPD the catalyst was held at the final temperature until a constant baseline of the H_2 signal was obtained. Finally, the system was calibrated and the catalyst was cooled down to room temperature. The amount of desorbed H_2 during TPD was determined from the area under the H_2 signal.

In general, H_2-TPD measurements were conducted in a sequence on a sample. Two different pre-treatment procedures were applied in between TPD experiments. In the first procedure, the catalyst was treated with 2 % H_2 in He at reduction temperature for 15 min followed by flushing with He and cooling to room temperature. In the second pre-treatment procedure, the catalyst was not treated with H_2 but cooled to room temperature under He after calibration.

5.3.5 Pulsed H_2 chemisorption

Pulsed H_2 chemisorption was performed with supported and unsupported Ni. Supported Ni was reduced as mentioned earlier. 150 mg of unsupported Ni was reduced at 673 K for 2 h (5 % H_2 in He, $\beta = 3\,\mathrm{K\,min^{-1}}$). This step was followed by flushing with He at reduction temperature for 60 min and cooling to room temperature. Experiments were conducted at 308 K by injecting 2 % H_2 in He into a He stream ($13\,\mathrm{Nml\,min^{-1}}$) flowing over the reduced catalyst bed. Pulses were injected by means of a calibrated sample loop ($V_{loop} = 1$ ml). After adsorption, the catalyst was flushed with He ($100\,\mathrm{Nml\,min^{-1}}$) and TPD was conducted under the same conditions as previously described. The adsorbed amount of H_2 and the resulting specific Ni surface area were calculated from the number of adsorbed pulses and equation 5.1.

5.3.6 N_2O chemisorption

For N_2O chemisorption experiments 25 – 150 mg of calcined catalyst were reduced in situ as previously described. After reduction, chemisorption of N_2O was either conducted in a flow or titration experiment. Flow experiments were performed similarly to literature [174]. The sample was cooled to the desired start temperature under He. Subsequently, the reactor was switched into the bypass position and the gas was changed to 1 % N_2O in He. Once a constant N_2O signal was obtained, the reactor was switched online and N_2O was fed to the reactor at constant temperature. After this isothermal treatment, the temperature was linearly increased with $\beta = 6\,\mathrm{K\,min^{-1}}$ to a temperature not exceeding 753 K and calibration of the system was performed. Titration experiments were conducted by dosing pulses of 1 % N_2O in He onto the catalyst bed using a calibrated sample loop ($V_{loop} = 1$ ml) and He as carrier gas with a flow rate of $13\,\mathrm{Nml\,min^{-1}}$.

5.4 Results and discussion

5.4.1 Catalyst characterization with standard techniques

Results from elemental analysis and static H_2 chemisorption are depicted in Table 5.1. The specific Ni surface area of the precipitated catalysts rises with increasing Ni loading and reaches a maximum at a Ni/Al ratio of 3. Impregnated catalysts show similar Ni surface areas at lower Ni loadings as compared to precipitated catalysts. The observed trend in the case of the precipitated samples seems contradictory to results published earlier where a linear correlation of the specific Ni surface area and the Ni loading up to a Ni/Al ratio of 5 was obtained [79]. It has been shown that the applied conditions during precipitation and calcination have a strong impact on the resulting catalyst structure and Ni particle size [82, 88, 178]. Already small deviations in the synthesis conditions can result in structural differences which impedes the reproducibility of the specific Ni surface area and explains the observed discrepancy.

Table 5.1: Characterization results of precipitated and impregnated Ni catalysts.

	PC10	PC15	PC13	PC11	PC31	PC51	IC9	IC17
Ni loading (wt-%)	79.0	15.3	22.5	38.1	58.3	64.4	9.1	16.7
S_{Ni} ($m^2\ g_{cat}^{-1}$)	n. d.	3.6	9.4	17.1	32.9	30.1	3.8	9.2
Ni dispersion (%)	n.d.	3.5	6.3	6.7	8.5	7.0	6.3	8.3

XRD results of the calcined catalysts are depicted in Figure 5.11. The crystalline phases were identified with the PDF database. PC10 reveals the typical pattern of NiO. In the aluminum containing precipitated catalysts mixed oxides, $NiAlO_x$, are present, the structure of which strongly depends on the Ni/Al ratio (Figure 5.11A). Neither a crystalline Al_2O_3 nor a $NiAl_2O_4$ phase are observed. A detailed description of Ni/Al mixed oxides typically obtained through precipitation can be found elsewhere [80, 81, 88, 178, 211]. In the impregnated catalysts, all phases can be assigned to NiO and γ-Al_2O_3, as revealed by the comparison with the pattern of the pure support material (Figure 5.11B). This is the typical pattern of unreduced Ni/γ-Al_2O_3 catalysts.

5.4.2 Temperature programmed desorption of H_2

Znak and Zieliński have shown that H_2-TPD is independent of the synthesis procedure and the Ni loading [204]. Therefore PC11 was chosen as representative sample to study the interaction of H_2 with supported Ni catalysts by means of H_2-TPD. Figure 5.1 shows a typical result after H_2 adsorption at 308 K for 30 min. A broad desorption signal with overlapping peaks is detected

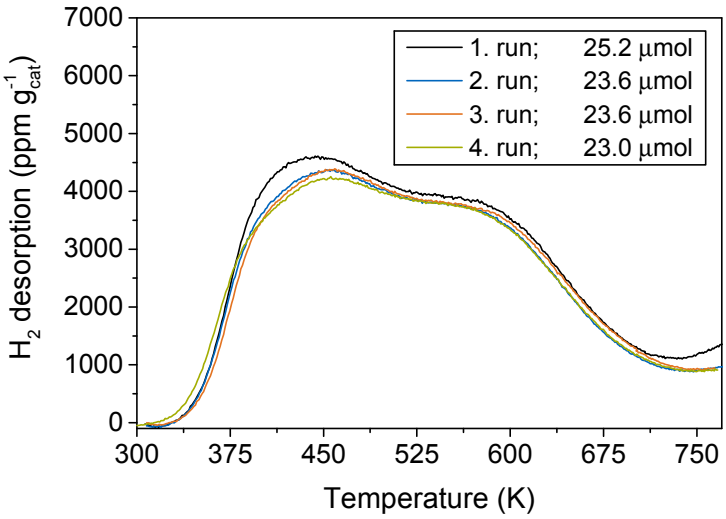

Figure 5.1: Reproduction experiment of H_2-TPD when adsorbing H_2 at 308 K for 30 min (PC11, $m_{cat} = 75\,mg$, $Q_{He} = 34\,Nml\,min^{-1}$).

between 350 and 700 K. These desorption signals can be attributed to H_2 adsorbed on the Ni surface [166, 203–205]. The onset of a desorption signal at 750 K may come from H_2 spillover and/or reoxidation of Ni by water inherent on the sample after reduction [135, 212]. However, when reproducing the experiment with the same catalyst sample the area under the TPD curve decreases from the first to the second run and remains constant during the subsequent runs. This implies that particle sintering is not an issue during TPD and also reoxidation of Ni can be ruled out since the latter would decrease the amount of reduced surface Ni, resulting in a further decrease of the TPD signal in each run. The slightly higher intensity in the first run was also observed by other research groups [213]. This effect could be explained by H_2 storage on the support during reduction followed by reverse spillover to the Ni phase and desorption during TPD. Variations of the purging time after reduction did not influence this trend (not shown here). The decrease of the desorbed H_2 amount between the first and the subsequent TPD runs is less than 9 %. Variation of the catalyst mass revealed essentially the same desorption pattern (Figure 5.12). Moreover, when conducting TPD with 50 mg of calcined catalyst the experimental conditions correlate with those reported by Znak and Zieliński for which transport limitations could be ruled out [204]. Therefore, we also exclude the presence of transport limitations under the experimental conditions chosen here.

A more complete picture of the H_2 interaction is obtained when adsorbing H_2 also at temperatures as low as 84 K. Results depicted in Figure 5.2 reveal multiple signals over the whole temperature range. In addition to the two overlapping peaks between 350 and 700 K, which are derived from H_2 chemisorbed on the Ni surface (α_1-peak and α_2-peak), two more distinct signals can be observed. The signal centered around 150 K reflects H_2 adsorbed in the subsurface region of the Ni crystallites (γ-peak) and the H_2 evolving around 300 K (β-peak) can be attributed to multilayer adsorption and H_2 adsorbed on edges and corners of the Ni crystallites [204, 205]. In the temperature range from 450 – 750 K, the TPD curve obtained after the three step adsorption process resembles the one after adsorption at 308 K.

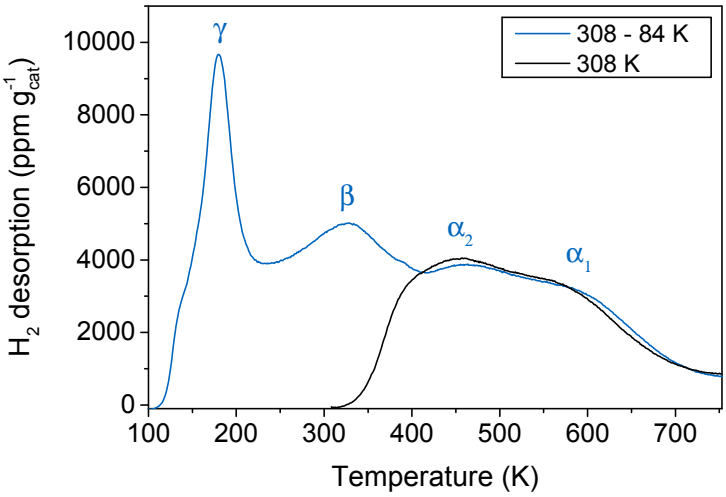

Figure 5.2: Influence of adsorption procedure on H_2-TPD (PC11, $m_{cat} = 75\,mg$, $Q_{He} = 34\,Nml\,min^{-1}$).

When the initial adsorption temperature in the three step adsorption process is increased up to 308 K the intensity of the γ-signal and β-signal is rising (Figure 5.3). Those observations are in good agreement with the work of Znak and Zieliński and indicate that the adsorption on those sites is an activated process [205]. The intensity of the α_2-signal is also slightly increased when the initial adsorption temperature is raised from 90 – 308 K, suggesting that H_2 chemisorption on the Ni surface is a somewhat activated process. However, overlapping desorption peaks make it difficult to clearly discern single signals and the higher intensity around 450 K might be due to a partial overlap of the β-Signal and the α_2-signal. At initial adsorption temperatures higher

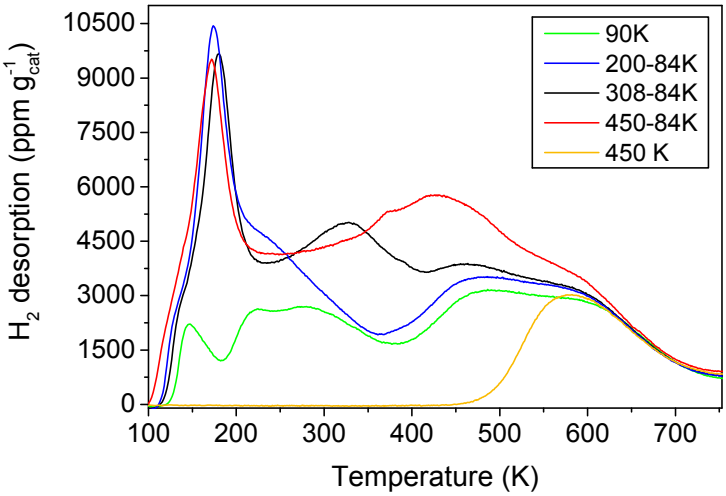

Figure 5.3: Influence of adsorption temperature on H_2-TPD (PC11, $m_{cat} = 75\,mg$, $Q_{He} = 34\,Nml\,min^{-1}$).

than 308 K the amount of H_2 adsorbed in the β position is slightly reduced but still present whereas the intensity of the two α-signals is significantly increased. This supports findings by Znak and Zieliński that higher adsorption temperatures cause morphologic changes of the Ni surface or a restructuring of the adsorbed H_2 layer [205]. Similar effects were observed on Ru single crystals, where a reduction of repulsive adsorbate-adsorbate interactions at higher

temperatures allows the adsorption on additional sites [214]. Our results also show an increase of desorbing H_2 when the initial adsorption temperature is increased. In similar studies, this effect was ascribed to chemisorption being an activated process where more H_2 can be adsorbed at higher temperatures [166, 215]. However, when adsorbing H_2 solely at 450 K the resulting signal is significantly lower and resembles the curve obtained after adsorption at 308 K. At higher adsorption temperatures weaker adsorption sites are hardly populated and the species adsorbed on those sites might be removed when flushing with He prior to desorption resulting in a lower signal intensity as compared to the spectrum obtained after the three step adsorption process. The additional H_2 desorbing after the three step adsorption process might be also explained by reverse spillover of H_2. Cooling down from adsorption temperatures to 84 K takes longer for higher initial adsorption temperatures, allowing for more H_2 being stored on the support. When the coverage of H_2 is reduced during the TPD measurement, H_2 stored on the support migrates back to the Ni surface and desorbs, which increases the desorption signal at this temperature. Already adsorption at 308 K for 24 h significantly increases the desorption signal (Figure 5.4). When H_2 is adsorbed in a pulsed manner, where the H_2 partial pressure

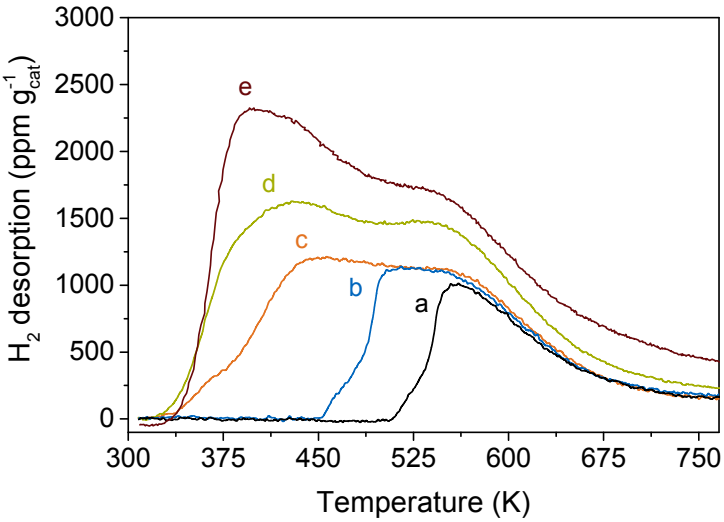

Figure 5.4: Effect of time and H_2 partial pressure during adsorption at 308 K on H_2-TPD. Adsorption of (a) 10 pulses, (b) 15 pulses, (c) 40 pulses; Adsorption for (d) 30 min and (e) 24 h in a continuous H_2 flow (m_{cat} = 75 mg, Q_{He} = 100 Nml min^{-1}).

is reduced, strong adsorption sites are occupied first and weaker sites are filled in succession. The same trend was also observed by other research groups for alumina- [205] and silica [213]-supported catalysts. Once a breakthrough of the H_2 pulses is observed (pulsed adsorption prior to curve (c) in Figure 5.4), the signal in the following TPD remains constant with an increasing number of pulses. Variation of the He flow, sample loop size and H_2 concentration per injection gave essentially the same pattern in the following TPD (not shown here). The adsorbed amount of H_2 and the resulting Ni surface area correlate with results from static H_2 chemisorption (Table 5.2 and Figure 5.5). This is also the case when varying the Ni loading and the synthesis procedure. The amount of H_2 desorbed from the catalysts PC11, PC31 and PC51 after pulsed adsorption is lower than the H_2 uptake. A reason for this might be that part of the H_2 adsorbed

migrates to the support where it is too strongly bound to desorb during the following TPD. It is also possible, that the maximum temperature of 753 K is too low to completely include the strongest adsorption site. The desorption signals of the catalysts PC15, PC13, IC9 and IC17 were too weak for the calculation of the desorbing H_2 amount.

Table 5.2: Comparison of characterization results from static H_2 chemisorption and transient characterization techniques.

	PC10	PC15	PC13	PC11	PC31	PC51	IC9	IC17
H_2 uptake ($\mu mol\, g_{cat}^{-1}$)	17.5	45.6	119.2	257.7	426.8	338.2	60.2	101.8
H_2 desorption ($\mu mol\, g_{cat}^{-1}$)	n. d.	n. d.	n. d.	212.4	356.1	292.2	n.d.	n.d.
H_2 monolayer uptake ($\mu mol\, g_{cat}^{-1}$)	n.d.	45.7	120	218.9	420.2	385.1	48.5	118.1

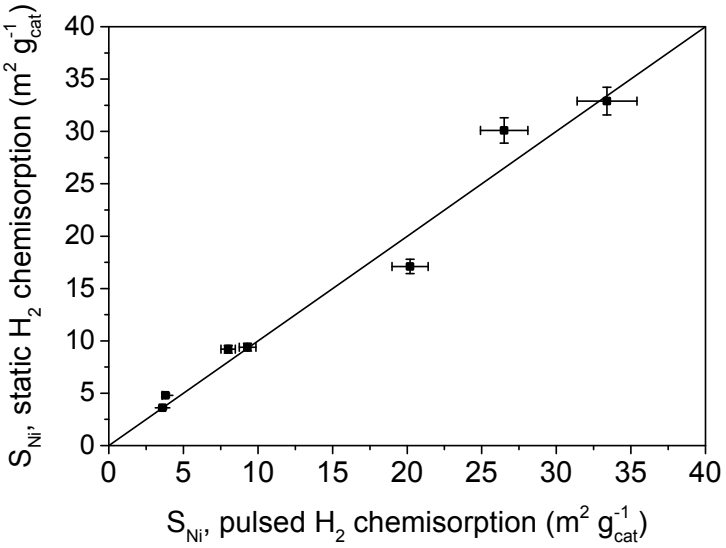

Figure 5.5: Comparison of static and pulsed H_2 chemisorption for the calculation of the specific Ni surface area.

It must be noted at this point that the TPD results presented in Figure 5.4 and Table 5.2 were recorded with a higher He flow rate as compared to those shown earlier. Preliminary experiments reveal that an increase of the He flow rate shifts the desorption signal to lower temperatures (Figure 5.12B). Increasing the flow rate of the carrier gas reduces the H_2 partial pressure in the gas phase and the desorption signal approaches typical profiles as recorded in vacuum [204]. Nevertheless, the desorbed H_2 amount remains constant.

The spectra depicted in Figure 5.6 show the influence of different pre-treatment procedures on TPD. When treating the catalyst bed with diluted H_2 at reduction temperature, the following TPD signal reveals the typical pattern of two overlapping but discernable desorption signals in the temperature range from 350 – 753 K (1. run in Figure 5.6A and Figure 5.6B). When the catalyst is pre-treated solely with He in between H_2-TPD measurements, a signal shift and a slight increase of the signal intensity are observed (2. run in Figure 5.6A and 5.6B). The differences in applied pre-treatment conditions seem to only influence desorption signals at

temperatures higher than 350 K. Moreover, the observed changes are shown to be reversible when switching back to 5% H_2 in He during pre-treatment (3. run Figure 5.6B). Kanervo et

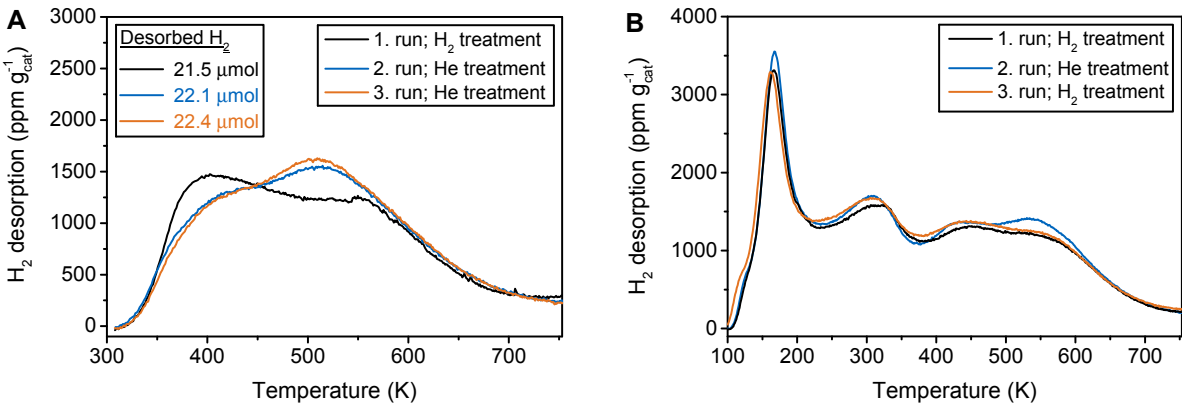

Figure 5.6: Influence of catalyst pre-treatment at reduction temperature on H_2 interaction with PC11 (m_{cat} = 50 mg, Q_{He} = 100 Nml min^{-1}): (A) Sequence of H_2-TPD measurements after H_2 adsorption at 308 K for 30 min. The pre-treatment conditions were kept constant from the second to the third run. (B) Sequence of H_2-TPD measurements after H_2 adsorption at 308 K followed by 84 K for 30 min. The pre-treatment conditions were alternated.

al. conducted similar sequences of H_2-TPD experiments with a 17 wt-% Ni/Al_2O_3 catalyst and studied the influence of the gas atmosphere on the desorption signal, which mirrors the findings of this study [166]. Cooling down in He in between TPD measurements leads to a broad desorption signal with one maximum whereas cooling down in H_2 results in two distinct desorption peaks. It could be shown by means of kinetic analysis that the spectrum is made up of two overlapping signals regardless of the pre-treatment conditions. Differences in the signal shape were deduced to a shift of the adsorption state with the higher enthalpy whereas the other adsorption site remains unchanged [166]. The nature of the shift is not yet known but it is possible that the gaseous environment influences the ratio of the interface energy and the energy of the free surfaces, which leads to changes of the wetting behavior of the support by the active metal [216]. This in turn results in different particle shapes and facet distributions with different strength of H_2 chemisorption. Such a dynamical wetting/non-wetting behavior was reported for Cu/ZnO systems, where changes of the oxygen content in the ZnO phase, induced by reversible switching of the oxidation potential of the gas atmosphere, caused dynamical changes of the contact surface energy [216, 217]. For the study presented here, the gas atmosphere during catalyst pre-treatment did not contain any oxygen containing species, which means that changes of the surfaces by oxidation can be ruled out. It is more likely that H_2 adsorption on the surfaces changes the energy of the free surfaces.

In summary, our results show that the interaction of H_2 and the Ni surface is complex and strongly depends on the adsorption conditions applied. It is therefore difficult to quantify the Ni surface area solely by H_2-TPD. A combination with pulsed H_2 chemisorption allows the calculation of the specific Ni surface area. The dynamic nature of the Ni phase emphasizes how important it is to keep pre-treatment conditions constant when comparing characterization results from different characterization techniques. Moreover, the presented results demonstrate

the strength of H_2-TPD as characterization technique and the high data quality that can be obtained with the equipment applied in this study. In a subsequent study H_2-TPD will be applied to elucidate morphologic changes of Ni catalysts during CO_2 methanation.

5.4.3 Chemisorption of N_2O

A typical N_2O flow experiment started at 308 K is displayed in Figure 5.7. 12 min after the start of the measurement the reactor is switched online. After a time delay of 30 s, which is caused by the dead volume of the setup, N_2O is quantitatively decomposed to N_2 and oxygen, which chemisorbs on the catalyst surface. After roughly 22 min, no more N_2O is converted and N_2O breaks through as a front while the N_2 signal is decreasing. Heating of the sample in the subsequent temperature programmed treatment, releases small amounts of N_2O shortly after the beginning of the temperature ramp followed by further oxidation of Ni until at temperatures higher than 500 K N_2O is catalytically decomposed into gaseous N_2 and O_2. The increase of N_2O at the beginning of the temperature ramp indicates that part of the N_2O is non-dissociatively adsorbed on the catalyst surface. In UHV studies it was shown that N_2O molecularly adsorbs on Ni(111) but desorbs at temperatures higher than 100 K [218], which makes it unlikely that those species cause the observed N_2O peak in Figure 5.7. N_2O readily decomposes on Ni(110) within 323 – 873 K [219] and on Ni(100) between 200 and 800 K [220] where in the latter case also molecularly adsorbed N_2O was detected. It might be that the same species is also observed here.

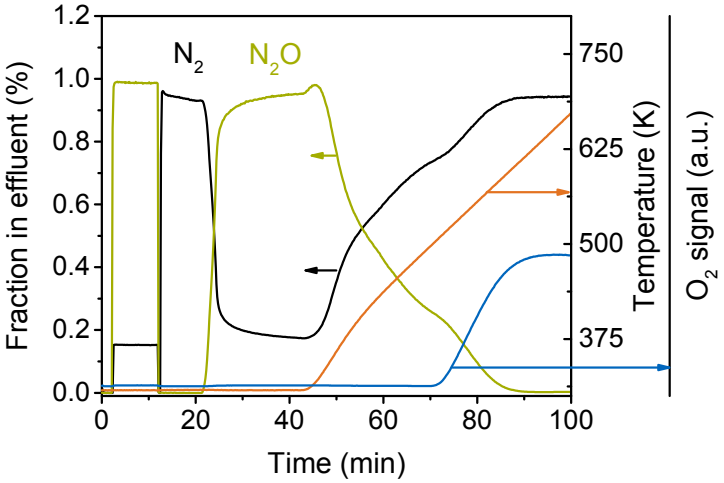

Figure 5.7: Temperature programmed N_2O chemisorption experiment with the catalyst PC11 (m_{cat} = 75 mg, 1 % N_2O in He, Q_{gas} = 25 Nml min^{-1}, β = 6 K min^{-1}).

The amount of produced N_2 during the isothermal part was calculated from the area under the N_2 curve between its onset and its intersection with the N_2O signal [174]. From the calculated number of released N_2 molecules, N_N, the specific Ni surface area, S_{Ni}, was determined

according to equation 5.3 assuming that one oxygen atom is adsorbed per Ni surface atom ($O/Ni_S = 1$) [149]:

$$S_{Ni} = \frac{N_N \cdot N_A}{m_{cat} \cdot \sigma_{Ni}} \tag{5.3}$$

The resulting specific Ni surface area for PC11 is 60.7 $m^2\,g_{cat}^{-1}$, which is higher than the corresponding result from static H_2 chemisorption by a factor of 2.5. This implies that under the conditions chosen, consecutive reactions like subsurface and bulk oxidation of Ni might be present to a significant extent. Such undesired consecutive reactions could be reduced when decreasing the residence time. However, a reduction of the catalyst mass down to 25 mg, giving a reduction of the residence time by a factor of 3, yields essentially the same specific Ni surface area (results not shown here). To decrease the N_2O partial pressure during the experiment, in order to suppress subsurface and bulk Ni oxidation, pulse titration of N_2O was applied as suggested by Tada et al. [149] but at a somewhat lower N_2O partial pressure per pulse and a lower temperature. The results are displayed in Figure 5.8. A total of 164 pulses of

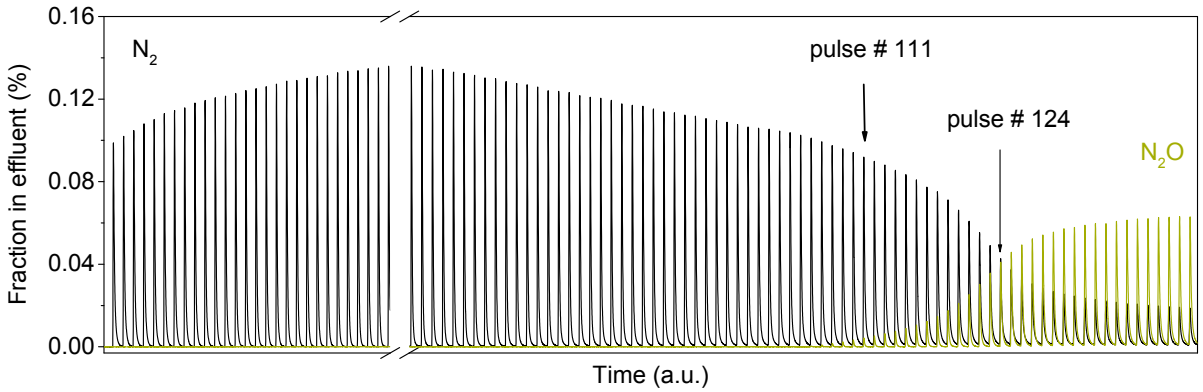

Figure 5.8: Pulse titration of N_2O onto the catalyst sample PC11 (m_{cat} = 25 mg, T = 308 K, 1 % N_2O in He, Q_{He} = 13 Nml min^{-1}).

1 % N_2O in He were injected into a He stream flowing over the catalyst. Once the pulses reach the catalyst bed N_2O is decomposed and N_2 is the only product detected in the effluent. Within the first pulses the intensity of the N_2 response signal increases. At the same time no N_2O is detected supporting the findings in Figure 5.7 that parts of the N_2O pulsed onto the catalyst is non-dissociatively adsorbed on the catalyst surface. The increase of the N_2 responses might be also explained in a way that N_2O is decomposed and N_2 produced is adsorbed on the surface. Also Van Hardeveld and Van Montfoort observed N_2 adsorption on supported Ni at room temperature [221]. By increasing the number of pulses, the N_2 peak intensity reaches a constant level and the amount of N_2 per pulse leaving the reactor corresponds well with the N_2O volume per injection fed to the reactor, implying that N_2O is quantitatively decomposed. After 111 pulses N_2O is detected in the effluent gas and the N_2 signal intensity is decreasing. However, no sharp N_2O breakthrough is observed and the area of a stable N_2O peak after the breakthrough is 12 % lower than that of an input pulse combined with peak broadening. The total amount of N_2

produced during the titration experiment was calculated from the area under the N_2 signal until pulse number 124 which corresponds to the point where the enveloped lines of the N_2 and the N_2O curve intersect. The resulting specific Ni surface area is 68.7 $m^2\ g_{cat}^{-1}$, which corresponds to the results from the temperature programmed experiment in Figure 5.7 but is significantly higher than 17.1 $m^2\ g_{cat}^{-1}$ as determined by static H_2 chemisorption. The point of the intersection of the enveloped line strongly depends on the intensity of the N_2 and the N_2O peaks. Since the latter do not reach the same intensity as the N_2 peaks, the point of intersection is detected later than it would be when the N_2O and N_2 peaks were equally high. This explains the higher specific Ni surface area determined in the titration experiment as compared to the flow experiment. The observations strongly indicate that for the catalytic system studied here consecutive reactions take place even under milder conditions as suggested by Tada et al. [149]. The difference might arise from the different support material and synthesis procedure applied here. Moreover, the results demonstrate that the experimental mode (flow or titration experiment) has no influence on the N_2O chemisorption behavior of the catalyst.

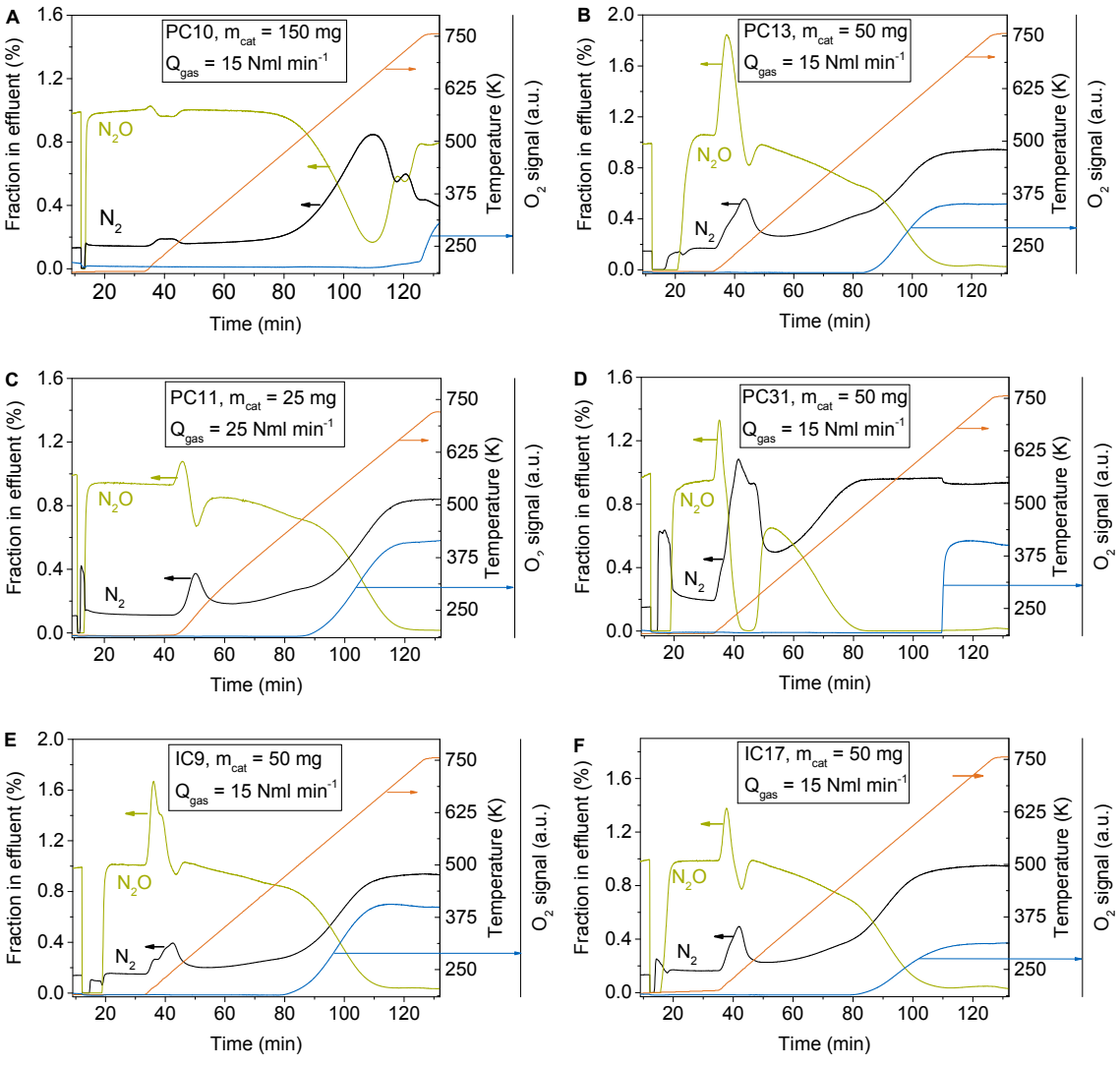

Figure 5.9: Influence of reaction temperature and support material on N_2O chemisorption (1 % N_2O in He, $\beta = 6\,K\,min^{-1}$).

Flow experiments with an initial temperature of 190 – 195 K were conducted to further investigate the temperature dependence and the influence of the catalyst support and structure on consecutive reactions. Results are depicted in Figure 5.9. For the supported systems (Figure 5.9B – F), initially, only part of the N_2O fed to the reactor is decomposed. The rest is weakly adsorbed and desorbs as soon as the temperature increases. N_2 formation further rises with temperature. A strong N_2 peak is observed between 220 and 350 K independent from the synthesis procedure and the Ni loading. The integration of the N_2 signal in Figure 5.9C up to 308 K gives a specific Ni surface area of 58.5 $m^2\ g_{cat}^{-1}$ which agrees with the results from the flow experiment at 308 K (Figure 5.7). The results obtained from Ni powder (Figure 5.9A) can be interpreted in a way that surface Ni is oxidized at 220 – 250 K. With increasing temperature the N_2 signal only slightly increases, indicating subsurface oxidation to a small extent. At temperatures as high as 650 K bulk Ni is oxidized until N_2O is catalytically decomposed at temperatures higher than 750 K. Obviously, Ni oxidation occurs at lower temperature in $NiAlO_x$ and Ni/γ-Al_2O_3 systems as compared to Ni powder.

From the results in Figure 5.9, the O/Ni_S ratio can be calculated for the different reaction temperatures. Results are depicted in Figure 5.10. Ni_S is the number of Ni surface atoms as determined from pulsed H_2 chemisorption. The amount of adsorbed oxygen atoms, O, is determined through integration of the N_2 signal from its onset during the isothermal treatment until the temperature of interest. For the calculation of the O/Ni_S ratio at around 190 K the N_2 signal was integrated up to its intersection with the N_2O curve.

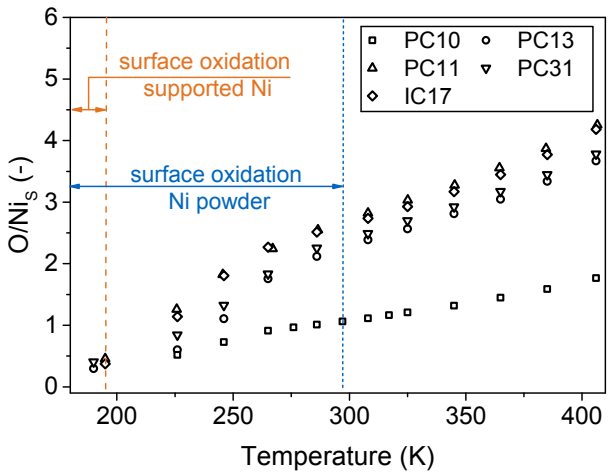

Figure 5.10: Influence of reaction temperature on the O/Ni_S ratio obtained from N_2O chemisorption on Ni.

For supported catalysts, the O/Ni_S ratio is 0.38 ± 0.07 at 190 – 195 K regardless of the Ni loading and synthesis procedure. In the case of pure Ni (PC10), the intensity of the N_2-signal in this temperature range was too weak for a proper calculation. Similar values of 0.3 – 0.6 obtained from gravimetric and pulsed experiments in the same temperature range were reported for Ni powder [210, 222] and supported Ni [222]. With increasing temperature a steep increase of the O/Ni_S is observed until the curves flatten out at O/Ni_S = 0.9 for unsupported and 1.75 – 2.3 for supported Ni. The slope of the increase is higher for supported catalysts which is in accordance

with the increased oxidizability mentioned earlier. The O/Ni_S ratio of the supported samples still noticeably rises after the flattening of the curve. The observations can be interpreted in a way that N_2O chemisorption follows a three step process, which was also observed by Zieliński [222]. First fast oxygen chemisorption takes place up to $O/Ni_S = 0.3 – 0.4$. Then moderate decomposition leads to the growth of the oxide layer followed by subsequent thickening of the layer due to subsurface and bulk oxidation. It is not easy to separate subsurface from bulk oxidation in the supported systems investigated. Only at temperatures around 190 – 195 K oxidation is limited to the Ni surface. This temperature range seems suitable for specific Ni surface area of these catalysts. The corresponding O/Ni_S ratio is 0.38 ± 0.07 as mentioned earlier. In contrast to this, subsurface and bulk oxidation of Ni powder occur at elevated temperatures. The O/Ni_S ratio of pure Ni only slightly increases within the temperature range from 265 – 285 K. The corresponding O/Ni_S ratio in this temperature range is 0.96 ± 0.05 indicating surface oxidation with the formation of an oxygen monolayer. Those conditions might be applied for Ni surface area determination of Ni powder.

5.5 Conclusion

Results show that for nickel-aluminum catalysts H_2-TPD within the temperature range from 84 - 753 K is a suitable method to obtain a complete picture of the interaction of H_2 with Ni. Variations of the adsorption and pre-treatment conditions have a significant impact on TPD. Switching the gas atmosphere between He and H_2 during pre-treatment at 753 K prior to TPD results in reversible morphologic changes of the Ni phase. H_2 spillover and multiple overlapping peaks make a quantitative characterization of the Ni surface area difficult. A proper selection of H_2 adsorption conditions is crucial for the calculation of the Ni surface area. It is recommended to apply pulsed H_2 chemisorption for Ni surface area determination.
N_2O chemisorption experiments reveal that N_2O is decomposed in a three step process comprising fast oxygen uptake and formation of an oxide layer followed by thickening of the oxide layer due to subsurface and bulk oxidation. The extent of subsurface and bulk oxidation depends on the reaction temperature but not on the experimental mode (flow or titration experiment). In the case of $NiAlO_x$ and $Ni/\gamma\text{-}Al_2O_3$ subsurface and bulk oxidation can be sufficiently suppressed at temperatures as low as 190 - 195 K. The corresponding O/Ni_S ratio is 0.38 ± 0.07 which might be applied for surface area determination. At higher temperatures those catalysts are readily oxidized impeding a separation of surface from subsurface and bulk oxidation. Bulk oxidation of Ni powder in contrast, only occurs at elevated temperatures. The O/Ni_S ratio remains somewhat constant at a value of 0.96 ± 0.05 within 265 - 285 K, suggesting the formation of an oxygen monolayer. Those conditions seem suitable for the Ni surface area determination of Ni powder.

5.6 Supporting Information

5.6.1 XRD pattern of the calcined catalysts

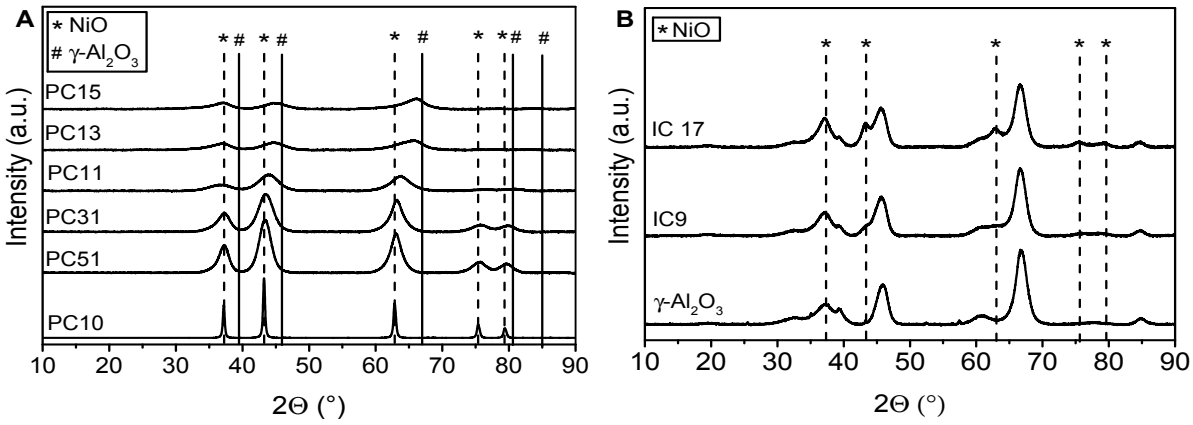

Figure 5.11: XRD pattern of the precipitated (A) and impregnated (B) catalysts (PDF-Numbers: NiO 96-101-0094, γ-Al_2O_3 96-101-0462). The XRD pattern of the support material used for incipient wetness impregnation (γ-Al_2O_3) is displayed in (B) for comparison.

5.6.2 Influence of catalyst mass and carrier gas flow on H_2-TPD

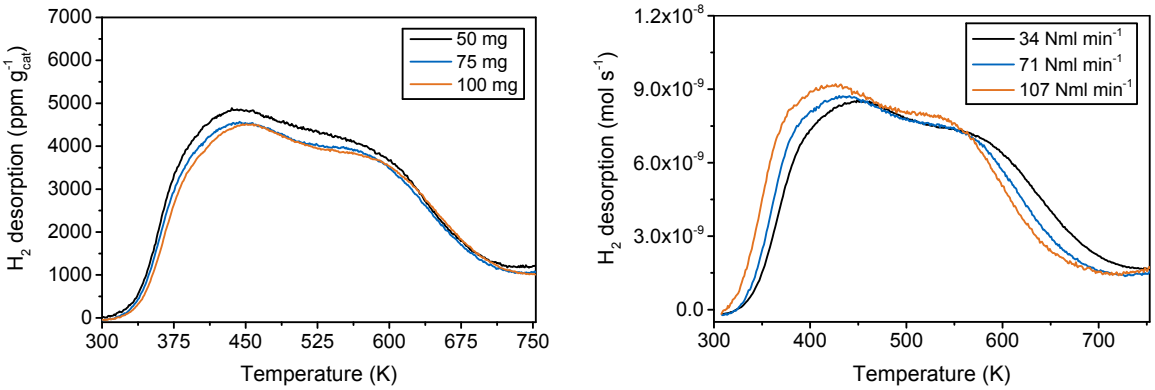

Figure 5.12: Influence of the catalyst mass on H_2-TPD after adsorption at 308 K for 30 min (PC11, $Q_{He} = 34\,\mathrm{Nml\,min^{-1}}$, $\beta = 6\,\mathrm{K\,min^{-1}}$).

6 Catalyst deactivation in CO_2 methanation

This chapter was published in:

S. Ewald, M. Kolbeck, T. Kratky, M. Wolf, O. Hinrichsen, *On the deactivation of Ni-Al catalysts in CO_2 methanation*, Applied Catalysis A: General, **2019**, *570*, 376-386.

6.1 Abstract

This work provides detailed knowledge of long-term deactivation of Ni catalysts in CO_2 methanation. $NiAlO_x$ mixed oxides with varying Ni loading as well as a 17 wt-% Ni/γ-Al_2O_3 catalyst were synthesized via co-precipitation and incipient wetness impregnation, respectively. The catalysts were aged at 523, 573 and 623 K under equilibrium conditions up to 165 h. Periodic activity measurements under differential conditions reveal severe deactivation. The stability of co-precipitated systems increases with decreasing Ni content on the expense of catalyst activity. Ni/γ-Al_2O_3 exhibits a lower stability as a comparable mixed oxide. A power law model is applied for the kinetic description of deactivation. Catalyst samples are characterized by means of temperature programmed desorption of H_2 (H_2-TPD) and CO_2 (CO_2-TPD), pulsed H_2 chemisorption, XRD, FT-IR spectroscopy, XPS and N_2 physisorption. Fresh and deactivated catalyst samples are characterized by means of temperature programmed desorption of H_2 (H_2-TPD) and CO_2 (CO_2-TPD), pulsed H_2 chemisorption, XRD and N_2 physisorption. Main deactivation mechanisms in the co-precipitated samples are found to be Ni particle sintering, a loss of BET surface area as well as a reduction of CO_2 adsorption capacity and medium basic sites, along with structural changes of the mixed oxide phase. Ni particle growth and a decrease in BET surface area lead to deactivation of the impregnated sample. Structure-activity correlations imply a complex interplay of governing deactivation phenomena as well as structure sensitivity.

6.2 Introduction

Depleting fossil fuels and climate change combined with a global increase of energy demand make the development of a sustainable energy supply an urgent issue. Therein, energy production from renewables and efficient storage technologies play a key role. In this context, the production of synthetic natural gas (SNG) through the methanation of CO_2 with H_2, which is derived from water electrolysis using surplus energy from renewables, has gained great interest. SNG can easily be stored and transported in the already existing gas grid and can be reconverted for energy production when needed [11, 223, 224].
The methanation of CO_2 was first described by Sabatier and Senderens in 1902 [22]. It is an exothermic reaction that is favored at low temperatures and elevated pressures.

$$CO_2 + 4H_2 \rightleftharpoons CH_4 + 2H_2O \quad \Delta H_R^0 = -165\,\mathrm{kJ\,mol^{-1}} \tag{6.1}$$

Under industrially relevant process conditions, however, the reaction is kinetically hindered, which necessitates the development and application of suitable catalysts. Group VIII transition metals have shown to be highly active for CO_2 methanation [27]. In the last years, intensive research has been conducted on supported metals such as Ru [28, 225–227], Pd [40, 228] or Ni [18, 20, 21, 48–50, 53, 54, 58, 59, 63, 65–67, 75, 76, 79–82, 86, 125, 229–231], with Ni being the most often investigated due to its low price and availability. Also a broad variety of support materials has been applied such as SiO_2 [53, 54], Al_2O_3 [49, 50, 229], CeO_2 [58, 67], ZrO_2 [67, 230] as well as Ce-Zr [21, 66, 231]. Ceria as support material is of great interest due to its oxygen storage capacities and redox properties [58, 91]. In recent literature, also zeolites as support materials have been investigated [75, 76]. Promoting those catalysts, for example with Fe, Co or Mn [18, 50, 63, 231] has shown to further improve the catalyst activity and stability. An overview can be found in recent reviews [12, 24, 91].
For the development of active and stable catalysts, also a deep knowledge of governing deactivation mechanisms is essential. With regard to CO_2 methanation, however, detailed studies about catalyst deactivation are scarce. Abello et al. [80, 81] conducted lifetime testing at different temperatures up to 600 h using co-precipitated, highly loaded Ni-Al catalysts. The applied catalysts have shown to maintain their high catalytic performance due to negligible Ni particle sintering, which became evident by XRD analysis. Measurement were conducted under constant reaction conditions with initial CO_2 conversions, ranging from 66 to 92.4 %. However, to exclude equilibrium effects, catalyst activity should be tested under less severe conditions at low conversions to track changes of the intrinsic catalyst activity. Koschany et al. [79] aged a co-precipitated Ni-Al catalyst (Ni/Al = 1) at 653 K under equilibrium conditions for 320 h with water already dosed into the feed gas. A strong activity decrease of 40 % was observed by decoupling catalyst aging and activity measurements. Mutz et al. [125, 232] investigated catalyst deactivation under fluctuating reaction conditions.
Unfortunately, most of the studies found in literature do not couple activity measurements with

catalyst characterization, making the elucidation of deactivation mechanisms and structure-activity relations difficult. Moreover, a kinetic description of deactivation, to our best knowledge, is not available. In this work, therefore, a systematic deactivation study, comprising both a kinetic description of deactivation and a detailed characterization, is presented. Co-precipitated and impregnated Ni-Al catalysts with a broad range of Ni loadings are applied.

6.3 Experimental

6.3.1 Catalyst Synthesis

Aqueous solutions of $Ni(NO_3)_2 \cdot 6H_2O$ (1 M, Merck®) and $Al(NO_3)_3 \cdot 9H_2O$ (1 M, Sigma-Aldrich®) were co-precipitated at 303 K and a constant pH of 9 using an equimolar mixture of 0.5 M NaOH (Merck®) and 0.5 M Na_2CO_3 (Sigma-Aldrich®) as precipitating agent. The synthesis procedure is described in greater detail in [161]. The Ni/Al ratio varied between 1/0, 1/3, 1/2, 1/1 and 3/1. Accordingly, the co-precipitated catalysts are denoted as PC10, PC13, PC12, PC11 and PC31 in the following. The precursors of catalyst PC10, PC13, PC11 and PC31 were calcined in flowing air at 723 K for 6 h at a heating rate of 5 K min^{-1}. The precursor of sample PC12 was calcined at 1173 K under otherwise identical conditions. After calcination, the catalysts were pelletized, grinded and sieved. Measurements were conducted with the sieve fraction of 150 - 200 µm. A 17 wt-% Ni/γ-Al_2O_3 catalyst (IC17) was synthesized via incipient wetness impregnation of γ-Al_2O_3 (Sasol®, 150 - 200 µm) with $Ni(NO_3)_2 \cdot 6H_2O$ (1 M, Merck®) and subsequent calcination under the conditions mentioned earlier. Elemental analysis was conducted via photometry using a Shimadzu® UV-160 and atom absorption spectroscopy (AAS) using an AA280FS from Varian®. The obtained Ni/Al ratios in the precursors as well as the Ni content in the calcined samples are summarized in Table 4.1.

6.3.2 Deactivation experiments and activity measurements

Deactivation studies were conducted with sample PC13, PC11, PC31 and IC17. The setup applied, is equipped with four U-shaped, glass-lined fixed bed reactors that can be operated in parallel (Figure 3.6). The reactors have an inner diameter of 4 mm. Feed gas, containing a mixture of $H_2/CO_2/Ar/N_2$ = 8/2/9/1, is supplied by a gas mixing unit. The gas flow is controlled individually for each reactor by means of calibrated mass flow controllers. Product gas is analyzed with an Agilent® 7820A gas chromatograph equipped with a Porapack-N column (Sigma-Aldrich®) for the quantification of CO_2, H_2O, and a packed Molsieve 5A column (Sigma-Aldrich®) for the quantification of H_2, Ar, N_2, CH_4 and CO. N_2 was used as internal

standard for quantitative analysis. All gases were of high purity (He and 5 % H_2 in He 6.0, rest 5.0). For the studies, 50 mg of calcined catalyst material, which were further diluted with 450 mg of purified SiC, were loaded in each reactor, secured in between two plugs of silica wool and contacted with a thermocouple. Prior to deactivation, the samples were reduced in 5 % H_2 in He at 753 K for 5 h ($\beta = 1\,\mathrm{K\,min^{-1}}$), flushed with He and cooled down to room temperature. After reduction, the samples were heated in He to 523 K, flushed with feed gas ($H_2/CO_2/Ar/N_2$ = 8/2/9/1) and pressurized to 8 bar before an initial activity test was performed. Afterwards, the catalyst samples were heated to 623 K where they were aged up to 165 h with a feed gas flow rate of 15 Nml $\mathrm{min^{-1}}$ (GHSV = 23 873.2 $\mathrm{m^3\,g_{cat}^{-3}\,h^{-1}}$, WHSV = 19.3 $\mathrm{g_{Feed}\,g_{cat}^{-1}\,h^{-1}}$). This low feed gas flow rate was chosen to ensure a fast deactivation by stressing the catalyst under high conversions and a high partial pressure of H_2O. Selected samples were also aged at 523 and 573 K. In a separate run, catalyst PC31 was treated solely in Ar at 623 K and 8 bar. After 2, 5, 8, 10, 15 h and then every 10 h the reactors were cooled down to 523 K for activity measurements. All activity tests were performed under differential conditions using a feed gas flow rate of 500 Nml $\mathrm{min^{-1}}$ ($H_2/CO_2/Ar/N_2$ = 8/2/9/1, p = 8 bar, GHSV = 795 774.7 $\mathrm{m^3\,g_{cat}^{-3}\,h^{-1}}$, WHSV = 657.9 $\mathrm{g_{Feed}\,g_{cat}^{-1}\,h^{-1}}$). The CO_2 conversion, X_{CO_2}, CH_4 yield, Y_{CH_2}, CH_4 selectivity, S_{CH_4}, and the corresponding weight time yield, *WTY*, were determined according to the following equations with $x_{i,\mathrm{in}}$ being the fraction of species i in the feed and $x_{i,\mathrm{out}}$ being the fraction of species i in the product gas:

$$X_{CO_2} = \left(1 - \frac{x_{CO_2,\mathrm{out}} \cdot x_{N_2,\mathrm{in}}}{x_{CO_2,\mathrm{in}} \cdot x_{N_2,\mathrm{out}}}\right) \tag{6.2}$$

$$Y_{CH_4} = \left(\frac{x_{CH_4,\mathrm{out}} \cdot x_{N_2,\mathrm{in}}}{x_{CO_2,\mathrm{in}} \cdot x_{N_2,\mathrm{out}}}\right) \tag{6.3}$$

$$S_{CH_4} = \frac{Y_{CH_4}}{X_{CO_2}} \tag{6.4}$$

$$WTY = \left(\frac{Q_{\mathrm{Feed}} \cdot x_{CH_4,\mathrm{out}} \cdot x_{N_2,\mathrm{in}}}{V_M \cdot x_{N_2,\mathrm{out}} \cdot m_{\mathrm{cat}}}\right) \tag{6.5}$$

Q_{Feed} denotes the feed gas volume flow, V_M the molar volume and m_{cat} the mass of calcined catalyst used in a run. The deactivation behavior of the different catalysts is described with a power law model [138, 233]:

$$\frac{\mathrm{d}a_{\mathrm{rel}}}{\mathrm{d}t} = -k_d \cdot a_{\mathrm{rel}}(t)^m \tag{6.6}$$

$$a_{\mathrm{rel}} = \frac{WTY(t)}{WTY(t = 0\,\mathrm{h})} \tag{6.7}$$

In equation 6.6 and 6.7, a_{rel} is the relative activity, k_d is the rate constant and m is the reaction order of deactivation.

For a detailed characterization study, each reactor was equipped with shut-off valves and loaded with the same kind and amount of catalyst. After reduction, one sample was removed for characterization, whereas the other samples were reheated and aged at 623 K under the same conditions as mentioned above. Following the activity measurement after 25, 95 and 165 h, the catalyst samples were depressurized, flushed with Ar for 30 min and cooled down to room temperature. One sample was removed from the setup for characterization, whereas the other samples were reheated and further aged.

6.3.3 Catalyst characterization

6.3.3.1 Temperature programmed measurements

Temperature programmed measurements for catalyst characterization were conducted in a setup described elsewhere [161]. Fresh and deactivated samples were transferred into the setup for transient measurements under inert conditions. For temperature programmed desorption of H_2 (H_2-TPD), H_2 was adsorbed in a three step program, comprising adsorption at 308 K for 30 min (60 Nml min^{-1}), gradual cooling to 84 K under H_2 and adsorption at this temperature for another 30 min. Subsequently, the catalyst sample was flushed with He (100 Nml min^{-1}) to remove weakly adsorbed H_2 before temperature programmed desorption was performed under He (100 Nml min^{-1}, $\beta = 6\,\mathrm{K\,min}^{-1}$) up to a maximum temperature of 753 K. After calibration of the mass spectrometer, the sample was cooled down to room temperature. Aged samples were treated with 5 % H_2 in He at 753 K for 30 min, flushed with He for 60 min and cooled down to room temperature in order to obtain a clean catalyst surface prior to H_2 adsorption.

After H_2-TPD, the specific Ni surface area, S_{Ni}, was determined via pulsed H_2 adsorption using a calibrated sample loop (V_{loop} = 1 ml). A total of 40 pulses of 2 % H_2 in He were injected at 308 K into a He stream (13 Nml min^{-1}) flowing over the catalyst bed. S_{Ni} was determined from the number of adsorbed pulses and equation 5.1. After adsorption, the catalyst was flushed with He and H_2 was desorbed under the same conditions as mentioned earlier.

In a next step, temperature programmed desorption of CO_2 (CO_2-TPD) was conducted. Prior to TPD, 2 % CO_2 in He was pulsed onto the catalyst under the same conditions as for pulsed H_2 adsorption. After flushing, TPD was conducted in He (100 Nml min^{-1}, $\beta = 6\,\mathrm{K\,min}$) up to 753 K and calibration of the mass spectrometer was performed. The CO_2 uptake, U_{CO_2}, was

calculated from the number of adsorbed pulses as well as from the area under the TPD curve. After CO_2-TPD, the sample was again treated in 5 % H_2 in He at 753 K and flushed with He to restore a clean catalyst surface. Subsequently, the sample was removed from the setup under inert atmosphere and transferred into a glovebox, where the catalyst material was separated from SiC and silica wool for further analysis. The purity was 5.0 or higher for CO_2 and 6.0 for H_2 and He.

For the determination of the degree of reduction, 60 - 130 mg of calcined catalyst were loaded into the setup and heated in He at 673 K for 45 min (100 Nml min^{-1}, $\beta = 6\,K\,min^{-1}$) and cooled down to room temperature. Subsequently, the sample was reduced in 5 % H_2 in He under the same conditions as applied prior to deactivation measurements. Product gas leaving the reactor was passed through a cooling trap operated at liquid N_2 temperature to remove evolving CO_2 and H_2O. The degree of reduction was calculated from the H_2 consumption and the Ni content in the sample.

6.3.3.2 X-ray diffraction (XRD)

For analysis, samples were sealed in glass capillaries (∅ 0.5 mm). X-ray diffraction (XRD) was performed with a STOE® Stadi P diffractometer (Ge(111) monochromator, Cu-Kα radiation, $\lambda = 1.540\,56$ Å) operating at 50 kV and 30 mA in Debye-Scherrer geometry. Measurements were carried out within the range from $2\Theta = 5 - 90^\circ$ with a stepsize of 0.5 ° and a scanning rate of 0.86 °min^{-1}. Particle sizes were determined applying the Scherrer equation and interplanar distances were calculated according to Bragg´s law. A proper separation of the catalyst material from SiC was difficult to achieve in some cases (especially for samples with low Ni loadings) and resulted in sporadic reflections attributed to SiC in the XRD pattern. In those cases, the XRD data was smoothed for presentation using a percentile filter. Also noisy data was smoothed for presentation using the same procedure.

6.3.3.3 N_2 physisorption

N_2 physisorption measurements were performed at the boiling point of liquid N_2 using a NOVAtouch from Quantachrome®. The catalyst BET surface area, S_{BET}, was determined from the adsorption branch of the isotherm within the p/p_0 range from 0.05 to 0.3, assuming that one N_2 molecule covers 0.162 nm^2. The total pore volume, V_P, and the average pore diameter, d_P, were determined from the amount of adsorbed N_2 at p/p0 = 0.994. For the measurement, the aged catalysts were handled in the glovebox and transferred to the setup under inert gas. Since the samples were already heated in He after characterization by means of transient techniques, the analysis of those samples did not require any additional pretreatment.

6.3.3.4 Combined FT-IR and CO_2-TPD measurements

FT-IR and CO_2-TPD measurements were combined to investigate the CO_2 interaction with Ni-Al catalysts in greater detail. For this purpose, 50 mg of catalyst sample PC11 were loaded into the setup for transient measurements. Reduction was performed in 5% H_2 in He (purities: 6.0 each) at a heating rate of 3 K min^{-1} up to 753 K where the catalyst was held for 5 h. Subsequently, the sample was flushed with He at reduction temperature for 60 min and cooled down to 308 K. Then, CO_2 was adsorbed either in a pulsed manner as described above (6% CO_2 in He, V_{loop} = 1 ml, Q_{He} = 13 Nml min^{-1}) or in a continuous flow (Q_{CO_2} = 50 Nml min^{-1}) for 30 min. After flushing with He, TPD was conducted at 6 K min^{-1} (Q_{He} = 100 Nml min^{-1}) and calibration of the mass spectrometer was performed.
FT-IR measurements were conducted in a Bruker® Vertex 70. Calcined PC11 was pressed into a self-supporting waver, which was mounted in a high temperature chamber equipped with CaF_2 windows. Reduction was performed under identical conditions as for CO_2-TPD measurements. A background spectrum was recorded before CO_2 adsorption was conducted for 30 min at 303 K using a continuous stream of 6% CO_2 in He (purities: 5.5 forCO_2, 6.0 for He). Then, the waver was flushed with He and TPD was performed at 3 K min^{-1} in a He flow of 100 Nml min^{-1}. IR spectra were recorded at a resolution of 4 cm^{-1} and noisy data was smoothed prior to presentation.

6.3.3.5 X-ray photoelectron spectroscopy (XPS)

XPS studies of the calcined catalysts were conducted with a Leybold-Heraeus® LHS 10 spectrometer using a non-monochromatized Al-K_α source (1486.7 eV). The powder samples were pressed into cavities and measured as pellets. In order to remove adsorbates and impurities originating from handling in air, all samples were degassed in vacuum at 673 K for 2 h before the XPS measurements. In addition, PC10 was annealed at 1273 K for 30 min in O_2 at a pressure of $1 \cdot 10^{-6}$ mbar following a literature-known preparation technique [234]. The analyzer was operated at a constant pass energy of 100 eV, leading to an energy resolution with a full width at half-maximum (FWHM) of about 1.1 eV. The energy scale of the spectra was corrected for sample charging by using the O 1s signal (531 eV, Al_2O_3). All spectra were recorded in an ultra-high vacuum (UHV) chamber at a pressure below $5 \cdot 10^{-8}$ mbar. Core level spectra were fitted by using Voigt functions and linear background subtraction. The Ni 3s/Al 2s region was deconvoluted using five components. For Ni 3s, two components account for the main peak as well as a known satellite [235]. Al 2s signals generated by Al-$K_{\alpha 3}$ (1496.5 eV) and Al-$K_{\alpha 4}$ (1498.5 eV) radiation overlap with the Ni 3s main peak and were, hence, considered in two further components [155]. The parameters for each secondary component (FWHM, relative intensities and differences in binding energies with respect to the main peak) were obtained

from reference samples measured under the same conditions. The calculated Ni/Al atomic ratio obtained from the peak areas of Ni 3s and Al 2s were verified by using the peak areas of Ni 2p and Al 2s. The difference in escape depths of the Ni 2p and Al 2s photoelectrons was accounted for by a factor of 1.8 determined with the TPP-2M model [236].

6.4 Results and discussion

6.4.1 Catalyst deactivation

Results from the deactivation experiment at 623 K are depicted in Figure 6.1A. The CO_2 conversion during activity measurements is below 17 % so that differential conditions can be assumed. A reduction of the aging time between two activity measurements yielded essentially the same deactivation pattern, which indicates a good reproducibility of the results and proves, that the activity measurements as well as heating and cooling do not bias the deactivation behavior

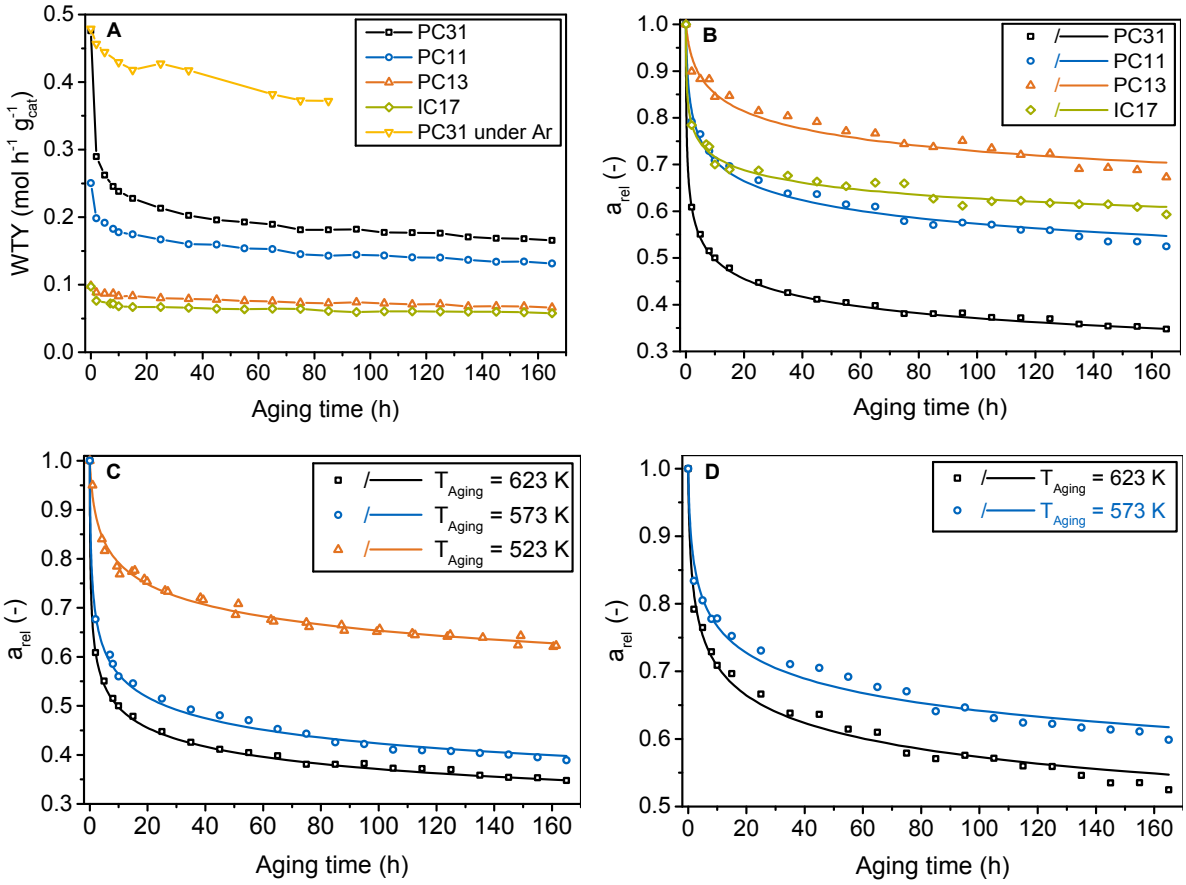

Figure 6.1: Deactivation behavior of the synthesized catalysts. The straight lines represent results from the PLM fit (Feed: $H_2/CO_2/Ar/N_2$ = 8/2/9/1 if not stated otherwise); (A-B) T_{Aging} = 623 K; (C) catalyst PC31; (D) catalyst PC11.

(Figure 6.8). Upon aging under reaction conditions, the activity of all catalysts significantly decreases within the first 25 h of aging. The activity of catalyst PC31 decreases by roughly 55 % of its initial value within this time span, whereas catalyst PC11 and PC13 lose 34 % and 19 %, respectively. The stability of co-precipitated catalysts increases with decreasing Ni content and is higher at a comparable initial activity than that of impregnated systems. Aging of catalyst PC31 under inert gas results in a significantly slower deactivation. The activity only drops about 20 %.

Results from the PLM fit according to equations 6.6 and 6.7 at various aging temperatures are shown in Figure 6.1B-D. The corresponding values for the rate constant and the reaction order are given in Table 6.1. The results match the experimental data with rate constants between 0.05 and 3.08 h^{-1} and orders ranging from 8.90 to 18.21. Catalyst deactivation is faster at higher temperatures. In all measurements, the CO_2 conversion under aging conditions is beyond 93 % which is close to equilibrium conversion resulting in a water partial pressure of about 2.3 bar. The CH_4 selectivity is beyond 91 % and the carbon mass balance is closed within 5 % taking into consideration CO_2, CO and CH_4. Variation of the catalyst bed length revealed that after 20 % of the bed length the CO_2 conversion exceeds 87 %. Taking into account errors occurring due to bypass of the feed gas at such low catalyst loadings, it can be assumed, that the catalyst bed is aged under an equilibrated gas atmosphere over the whole bed length. Therefore, the catalyst samples are representative for characterization. Data of catalyst deactivation for PC11 and PC13 at 573 and 523 K are not reported, since equilibrium conversion was not achieved under these conditions and consequently a uniform aging of the catalyst bed could not be ensured.

Table 6.1: Deactivation rate constants and reaction orders according to the PLM fit.

	$T_{Aging} = 523\,K$		$T_{Aging} = 573\,K$		$T_{Aging} = 623\,K$	
	$k_d\left(h^{-1}\right)$	$m(-)$	$k_d\left(h^{-1}\right)$	$m(-)$	$k_d\left(h^{-1}\right)$	$m(-)$
PC31	0.12 ± 0.02	12.68 ± 0.67	1.20 ± 0.30	8.99 ± 0.40	3.08 ± 0.41	8.90 ± 0.18
PC11	n. d.	n. d.	0.22 ± 0.10	13.78 ± 1.42	0.31 ± 0.10	11.30 ± 0.87
PC13	n. d.	n. d.	n. d.	n. d.	0.05 ± 0.02	14.30 ± 2.18
IC17	n. d.	n. d.	n. d.	n. d.	1.78 ± 1.13	18.21 ± 1.78

At this point, we would like to emphasize, that the kinetic description of the deactivation behavior is a pure empiric one. Therefore, the results should not be over-interpreted. Moreover, the selected aging conditions were especially chosen to achieve severe conditions for a fast deactivation and do not represent conditions typically present in plant operation.

Since samples were removed from the setup and pre-treated in H_2 prior to characterization, the samples may change. In order to elucidate to what extent changes in the deactivation behavior take place upon this treatment, we conducted a deactivation run with the precipitated samples at an aging temperature of 623 K and performed temperature programmed hydrogenation (TPH) after 95 and 165 h on stream. For this, the aged samples were depressurized, flushed with Ar and cooled down to room temperature. Subsequently, TPH was performed at 753 K for 30 min

at a rate of 1 K min^{-1}. Afterwards, an activity test was performed under differential conditions at 8 bar before the samples were reheated and further aged. Results are depicted in Figure 6.9A. Upon TPH, a small increase of the catalyst activity is observed, which might be caused by adsorbates on the catalyst surface. However, the observed trend is close to the detection limit, especially in the case of sample PC13. Therefore, it is concluded that the influence of intermittent TPH on the overall deactivation behavior is insignificant and it is reassured that samples after H_2 treatment are representative. Nevertheless, the observed effects underline the importance to thoroughly investigate the effect of pre-treatment procedures if catalyst characterization is not conducted in situ.

6.4.2 Activation energy

The activation energy was calculated before and after deactivation. The results are summarized in Table 6.2. The corresponding Arrhenius plots for fresh and aged catalysts are depicted in Figure 6.2. Arrhenius plots for the determination of the activation energy after deactivation at various aging temperatures are summarized in Figure 6.10. Results for the activation energy lie between 84 and 94 kJ mol^{-1}, which is in good agreement with values between 69 and 109 kJ mol^{-1} reported in literature [54, 79, 237, 238]. This also shows that the periodic activity measurements were conducted in the kinetically controlled regime and mass transport limitations can be ruled out. Only minor changes in the activation energy are observed upon aging.

Table 6.2: Activation energy before ($E_{A,0\,h}$) and after deactivation at various temperatures.

	PC31	PC11	PC13	IC17
$E_{A,\,0\,h}\left(\mathrm{kJ\,mol^{-1}}\right)$	90.4 ± 1.6	84.6 ± 1.9	86.3 ± 1.0	85.9 ± 0.1
$E_{A,\,523\,K,\,165\,h}\left(\mathrm{kJ\,mol^{-1}}\right)$	82.9 ± 2.2	n. d.	n. d.	n. d.
$E_{A,\,573\,K,\,165\,h}\left(\mathrm{kJ\,mol^{-1}}\right)$	92.6 ± 0.7	90.4 ± 0.9	n. d.	n. d.
$E_{A,\,623\,K,\,165\,h}\left(\mathrm{kJ\,mol^{-1}}\right)$	84.4 ± 1.0	91.8 ± 1.1	93.7 ± 2.1	89.5 ± 5.2

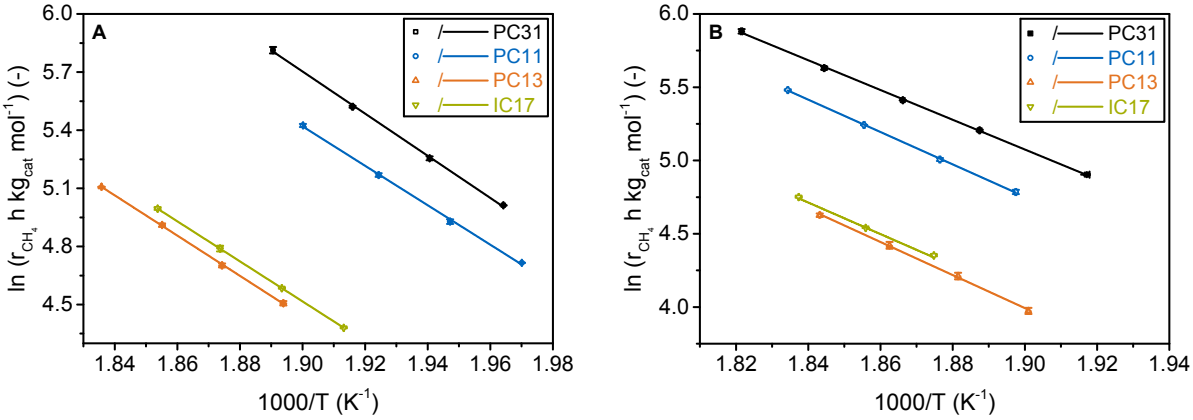

Figure 6.2: Arrhenius plot for the calculation of the apparent activation energy (A) before and (B) after aging at 623 K for 165 h.

6.4.3 Catalyst characterization

6.4.3.1 Carbon formation and the influence of water on deactivation

A common deactivation mechanism during CO methanation is the formation of carbon deposits blocking active sites [190, 239]. In CO_2 methanation, however, carbon formation has been reported to be not an issue [48, 66, 82, 125]. To provide experimental proof, that also in this study carbon formation is unlikely, we, at random, checked for carbon depositions using catalyst PC31. After aging at 623 K for 165 h, the sample was heated in He at 753 K for 30 min ($\beta = 6\,\mathrm{K\,min^{-1}}$) to remove weakly adsorbed species, followed by temperature programmed hydrogenation (TPH) from room temperature to 753 K in 5 % H_2 in He at $6\,\mathrm{K\,min^{-1}}$. CH_4 could not be detected in the effluent gas during TPH, indicating the absence of carbon deposits. In order to check for carbon residues still present after TPH, the carbon content of the treated sample was determined by CHNS analysis. With a result of 0.35 wt-%, which is insignificantly higher than 0.20 wt-% for a fresh sample, carbon depositions can be considered to have a negligible influence on deactivation.

Since carbon formation can be excluded, the significantly more severe deactivation under reaction conditions compared to inert gas (Figure 6.1) may be attributed to water formed during reaction. Consequently, the chosen reaction conditions represent hydrothermal aging conditions. It is well known, that hydrothermal conditions significantly accelerate Ni particle sintering due to the formation of Ni_2-OH complexes [113, 240], leading to deactivation.

6.4.3.2 X-ray diffraction

Upon precipitation, mixed basic carbonates are formed, the structure of which highly depends on the Ni/Al ratio in the sample. For catalyst PC31 a XRD pattern similar to that of takovite is observed while characteristic takovite reflections are shifted to higher diffraction angles when the Ni/Al ratio decreases. The XRD pattern of the catalyst precursors after precipitation are depicted and discussed in greater detail in section 4.3.1 and Figure 4.1.

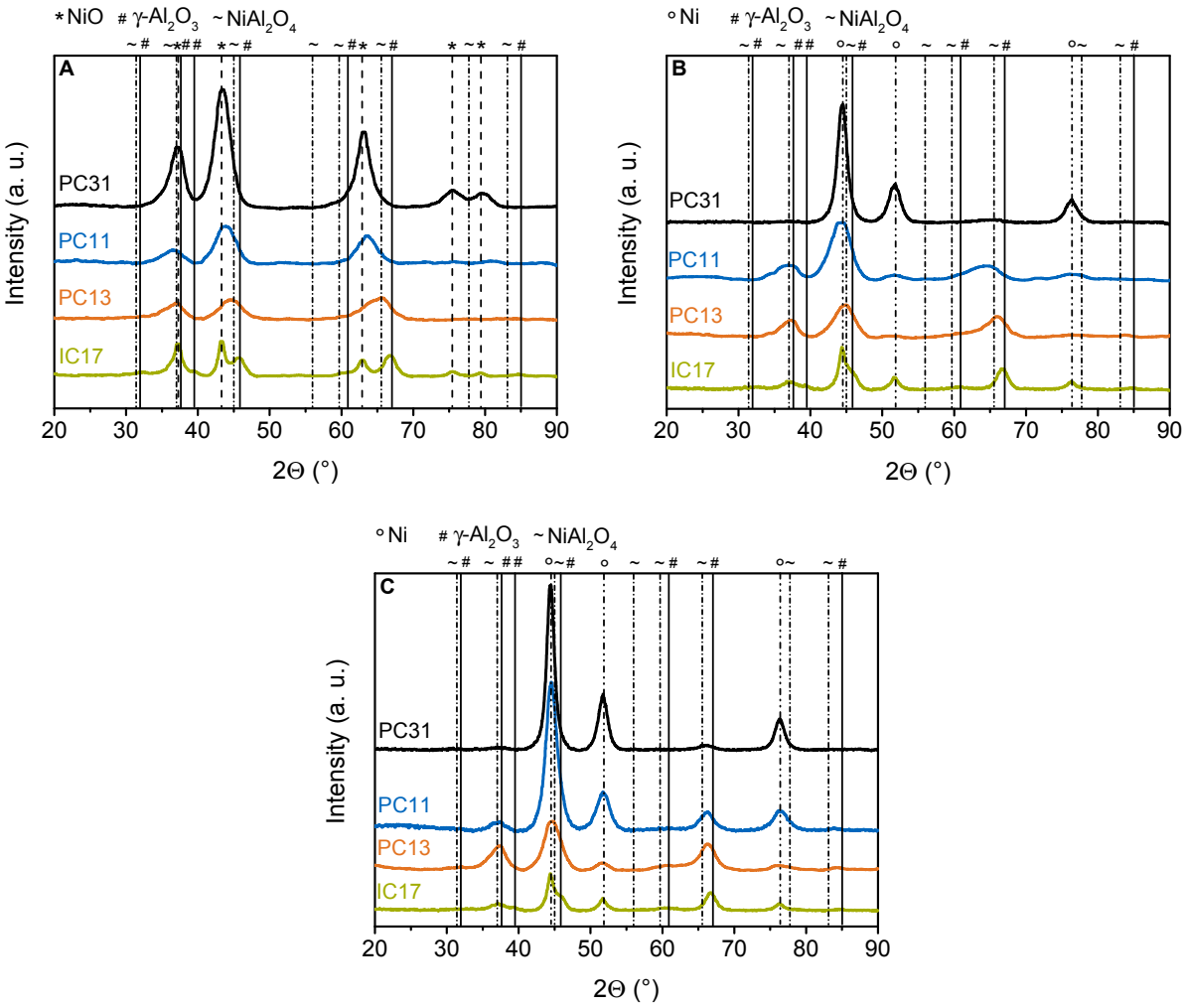

Figure 6.3: XRD patterns of the catalysts after (A) calcination, (B) reduction and (C) 165 h of aging at 623 K (JCPDS: NiO 78-0429, Ni 87-0712, γ-Al_2O_3 10-0425, $NiAl_2O_4$ 10-0339).

Figure 6.3 shows XRD pattern of catalysts PC31, PC11, PC13 and IC17 after calcination, reduction and aging. The pattern of calcined PC10 and PC12 are shown and discussed in section 4.3.1 and Figure 4.1C. The calcined PC31 exhibits the typical pattern of bunsenite (JCPDS 78-0429). The peak intensity decreases with decreasing Ni content. The reflections corresponding to the (311) and (222) plane in bunsenite are barely detectable in the samples PC11 and PC13 due to the small NiO particles. Moreover, the reflections are shifted to higher diffraction angles with decreasing Ni content, indicating the formation of a mixed oxide phase $NiAlO_x$, which

is typical of mixed basic carbonates calcined at temperatures lower than 873 K [88, 177]. The mixed oxide phase can consist of alumina containing Ni^{2+} ions and NiO containing Al^{3+} [87, 88, 177]. The Ni^{2+}/Al^{3+} ratio in the catalyst determines the formation and concentration of each phase [87, 177]. The d-spacing of the reflection at $2\Theta = 63.1°$ in sample PC31 and $2\Theta = 63.5°$ in sample PC11 with 1.473 and 1.463 Å, respectively, lie between 1.476 Å for the (220) plane in bunsenite and 1.425 Å for the (440) plane in $NiAl_2O_4$, indicating the presence of the latter mixed oxide. The d-spacing calculated from the reflection at $2\Theta = 65.6°$ in PC13 is 1.422 Å, which is between the corresponding values for the (440) plane of $NiAl_2O_4$ and the (440) plane of γ-Al_2O_3 (d-spacing 1.395 Å), indicating alumina containing nickel [177]. However, it is also possible, that both phases are present in a sample but differ in the degree of crystallinity or are of low concentration, so that the one or the other might not be observed in the XRD pattern [81, 90, 110, 177]. Neither a crystalline γ-Al_2O_3 nor $NiAl_2O_4$ phase is observed in the co-precipitated samples, although Abello et al. could show the presence of a spinel phase in similar catalysts by means of Rietveld refinement [81]. XPS analysis, the results of which are summarized and discussed in section 6.6.4, revealed no observable differences in the chemical state of the sample surfaces and therefore is not conclusive in clarifying the catalyst structure.

Upon reduction, metallic Ni is formed with reflections of the (111), (200) and (220) plane at $2\Theta = 44.5°, 51.9°$ and $76.4°$, respectively. The reflections of $NiAlO_x$ in the co-precipitated samples are shifted to higher diffraction angles compared to calcined samples, indicating a depletion of Ni^{2+} in the mixed oxide phase due to reduction. However, the shifted signals do not match the positions of γ-alumina, indicating that the catalyst systems studied are not completely reduced under the experimental conditions applied. No further shift was observed when increasing the reduction time (not shown here). The calculated degree of reduction is 27, 57 and 79% for catalyst PC13, PC11 and PC31, respectively, which additionally proves that the samples are only partially reduced. Ni particle diameters, d_{Ni}, were determined from peak broadening of the Ni (200) reflection at $2\Theta = 51.9°$. The Ni particle sizes of freshly reduced catalysts lie within 2.3 and 5.3 nm, which is in good agreement with literature values [80, 81] but is close to the detection limit. The particle size decreases with decreasing Ni content for the co-precipitated samples. The small particle size might be ascribed to the reduction mechanism in co-precipitated samples. It is proposed, that Ni particles start to nucleate on the surface of the nickel oxide-rich phase and particle growth takes place, which is limited by the presence of Al^{3+} ions [88]. Zieliński reported on aluminate species being formed on edges and corners of the particle upon aging, impeding a further growth of the Ni particles [90]. Also microstrains and paracrystallinity have to be taken into consideration to explain the small particle sizes [87, 211].

Upon aging, the reflection of the mixed oxide centered around $2\Theta = 65.0°$ is again shifted to higher diffraction angles, indicating structural changes during aging for all co-precipitated catalysts. The structural changes are most pronounced within the first 25 h of aging (Figure 6.13).The shift might be attributed to structural changes in the alumina phase or indicates additional Ni^{2+} depletion of the mixed oxide phase due to a further reduction upon aging, as

it was observed by Abello et al. [81]. However, even upon the observed modifications, the reflections do not match the pattern of γ-Al_2O_3. Interestingly, the reflection of the mixed oxide in all samples lie between the (440) plane of $NiAl_2O_4$ and γ-Al_2O_3, respectively. Results for the *d*-spacing are close together around 1.41 Å. A closer inspection reveals a small reflection around $2\Theta = 60.4\,^{\circ}$, which is more pronounced at lower Ni/Al ratios, suggesting, that, to a small extent, phase separation might have taken place. The reflections of metallic Ni are increasing with aging time for all co-precipitated samples, indicating Ni particle growth or increasing crystallinity of the Ni particles. Results for the Ni particle diameter are given in Table 6.3. The most pronounced change regarding the Ni particle diameter also occurs within the first 25 h of aging, which mirrors the trend of the catalytic activity. Also here, the influence of TPH after aging on the catalyst structure was investigated and could be ruled out (Figure 6.9B).

In the impregnated sample, two clearly distinguishable phases, namely bunsenite and γ-Al_2O_3, are present after calcination. Also here, no crystalline $NiAl_2O_4$ spinel phase is observed. However, there is evidence, that next to "free" NiO situated on the γ-Al_2O_3 surface, also "fixed" NiO exists in the form of a spinel-like structure on the alumina support ("surface spinel") or as particles encapsulated by this spinel-like phase [87, 110, 188]. The spinel structure is assumed to be too poorly crystallized to be detected by XRD [110]. XPS analysis revealed that the Ni^{2+} surface species in the impregnated sample exhibits a similar feature as in pure NiO, which is in agreement with XRD results. XPS pattern of the Al^{3+} surface species do not match those of pure γ-Al_2O_3, $NiAl_2O_4$ or Ni-Al mixed oxides. This might be due to the inhomogeneous character of the surface in IC17 (section 6.6.4). After activation, all reflections can be attributed to Ni and γ-Al_2O_3. No NiO is detected. It is discussed in literature, that first "free" NiO is reduced followed by the reduction of the spinel-like structure resulting in both small Ni particles, which are unlikely to be detected by XRD and Ni particles encapsulated by Ni-containing alumina. Ni-containing alumina is also formed on the support [110]. The encapsulating alumina phase might prevent Ni particle sintering during reduction, resulting in the small particle size of 6 nm observed here. A degree of reduction of 82%, again, reveals incomplete reduction and supports the formation of a Ni-containing alumina phase.

Upon aging, no structural changes are observed. The Ni particle diameter remains unchanged during aging around 6 nm, which is somewhat contradictory to the trend of the catalyst activity.

Table 6.3: Results from characterization of fresh and deactivated catalyst samples. For deactivation the samples were aged at 623 K.

Catalyst	Ni loading (wt-%)	Aging time (h)	S^{a}_{Ni} $\left(m^2\,g^{-1}_{cat}\right)$	D_{Ni} (%)	$U^{b}_{CO_2}$ $\left(\mu mol\,g^{-1}_{cat}\right)$	$U^{c}_{CO_2}$ $\left(\mu mol\,g^{-1}_{cat}\right)$	d^{d}_{Ni} (nm)	S^{e}_{BET} $\left(m^2\,g^{-1}_{cat}\right)$	V^{e}_{P} $\left(cm^3\,g^{-1}_{cat}\right)$	d_P (nm)
PC31	58.3	0	25.3	7.3	141.4	91.3	4.1	158	0.53	13.2
		25	21.8	5.6	93.1	53.2	4.7	100.2	0.48	19
		95	19.9	5.1	71.6	42.2	5.1	97.6	0.49	20
		165	19.7	5.1	n.d.	n.d.	5.3	95	0.49	20.6
PC11	38.1	0	21.5	8.5	128.3	65.5	2.8	261.6	0.54	8.4
		25	16	6.3	94.8	43.7	3.2	148.5	0.49	13.2
		95	14.3	5.6	80.5	35.6	3.4	134.8	0.5	14.8
		165	13.4	5.3	63.9	32.6	3.7	147.2	0.52	14
PC13	22.5	0	7.4	4.9	92	43.7	2.3	163.6	0.25	6
		25	6.8	4.5	77.2	38.5	2.9	n. d.	n. d.	n. d.
		95	6.3	4.2	62	29.1	3.3	n. d.	n. d.	n. d.
		165	5.4	3.6	61.8	29.3	3.5	145	0.35	9.7
IC17	16.7	0	8.6	5.7	82.1	49.7	6	150.4	0.36	9.5
		25	6.7	4.4	79.7	46.7	5.9	141.7	0.37	10.4
		95	6.2	4.1	72.9	41.7	6.1	131.7	0.33	9.9
		165	6.1	4.0	63.5	n.d.	6.4	133.4	0.35	10.4

[a] results are per gram of calcined sample

[b] determined from pulsed CO_2 adsorption; results are per gram of calcined sample initially loaded into the reactor

[c] determined from TPD; results are per gram of calcined sample initially loaded into the reactor

[d] determined from peak broadening of the Ni (200) reflection

[e] results are per gram of activated sample

6.4.3.3 Temperature programmed desorption of H_2

Results from H_2-TPD are depicted in Figure 6.14 and Figure 6.4. The patterns exhibit overlapping desorption signals centered around 170, 294, 427 and 530 K. The first peak around 170 K can be attributed to H_2 adsorbed in the subsurface region of Ni. The second peak centered around 308 K originates from H_2 adsorbed in the second layer and on edges and corners of Ni particles. The overlapping peaks in the temperature range from 350 - 700 K represents H_2 adsorbed on the Ni surface [204, 205]. The pattern is independent of the Ni loading and the synthesis procedure, which is in agreement with literature [205]. Deviations in the maximum temperature of the desorption signal centered around 170 K most likely originate from small non-linearities of the temperature ramp in this range, which is very close to the starting point of the heating procedure.

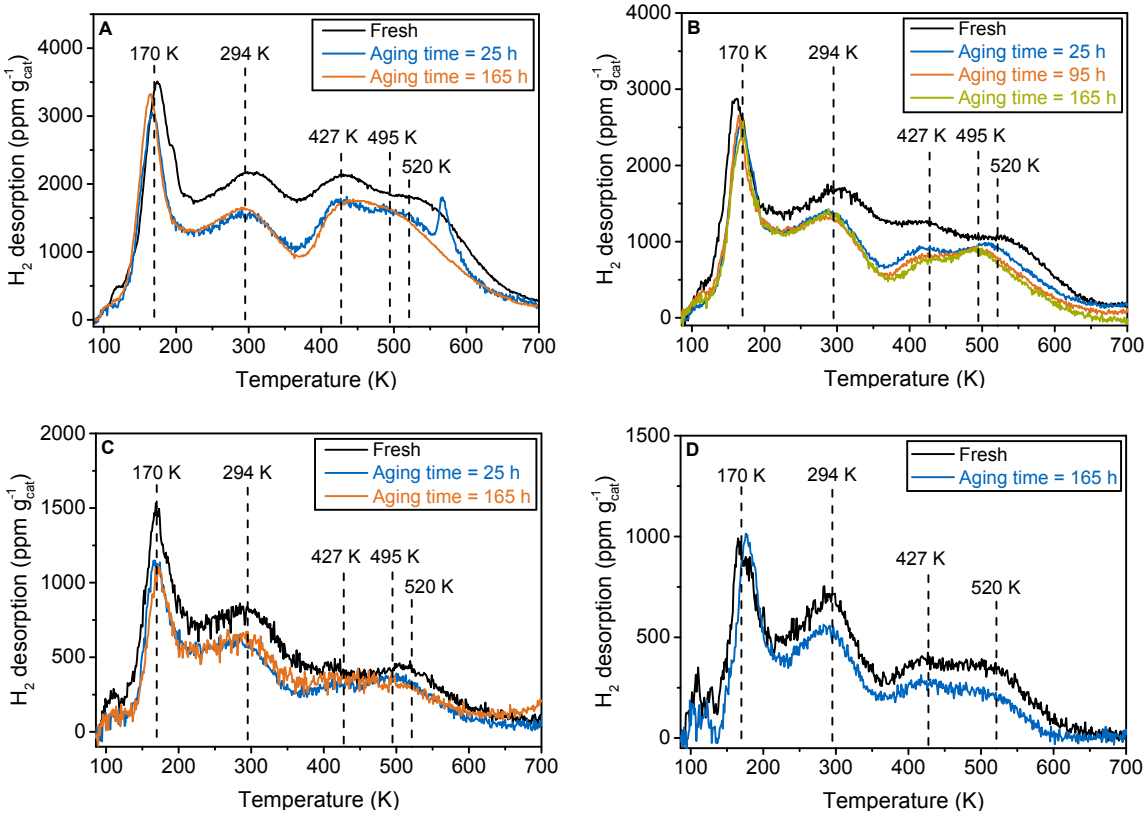

Figure 6.4: Influence of catalyst aging at 623 K on H_2 interaction with (A) catalyst PC31, (B) catalyst PC11, (C) catalyst PC13 and (D) catalyst IC17.

With aging time, the signal intensity and the area under the desorption curve decreases, indicating a loss of Ni surface area and sintering of the Ni particles, respectively (Figure 6.4). As indicated by the pattern of sample PC31 and PC11 (Figure 6.4A and B), the decrease is most pronounced within the first 25 h, which is in accordance with the trend of the catalyst activity in Figure 6.1A. A pronounced signal shift is not observed in the case of the impregnated sample IC17 (Figure 6.4D). In the case of the co-precipitated samples, a shift of the signal centered

around 520 K to lower temperatures is observed, which might originate from the annealing of defects in the Ni phase [205]. Also the gas atmosphere, which the catalyst is exposed to, can induce morphological changes of the Ni phase, leading to shifts in the desorption signals as shown in a previous study [161] as well as in the work of Kanervo et al. [166]. However, multiple overlapping peaks make the identification of single peaks difficult. Already changes in intensity of overlapping signals can lead to peak shifts in the cumulative curve. Deconvolution of the TPD pattern might reveal single desorption peaks. However, for a sophisticated evaluation, knowledge about the desorption kinetics is essential. Since the kinetics of desorption from sites leading to low temperature signals is not trivial, we abstained from a deconvolution. The additional signal at 567 K for PC31 could be attributed to water impurities in the He stream, oxidizing the catalyst surface.

6.4.3.4 Specific Ni surface area

The trend of the specific Ni surface area over aging time is depicted in Figure 6.5 and summarized in Table 6.3. The specific Ni surface area of the freshly reduced co-precipitated samples increases with rising Ni content, which is in line with the improved catalyst activity with increasing Ni content. The specific Ni surface area of the reduced impregnated sample is similar to that of PC13. The specific Ni surface area decreases over aging time, which is in accordance with the results obtained from H_2-TPD. The loss of Ni surface area is most pronounced within the first 25 h of aging. Catalysts PC31, PC11 and IC17 lose about 23, 26 and 22 % of their specific Ni surface area, whereas catalyst PC13 is more stable and loses only about 8 % of its initial Ni surface area. Interestingly, the activity of PC13 is higher with increasing aging time as compared to catalyst IC17 (Figure 6.1A and B), although the specific surface area of both systems is similar. This will be discussed later in greater detail.

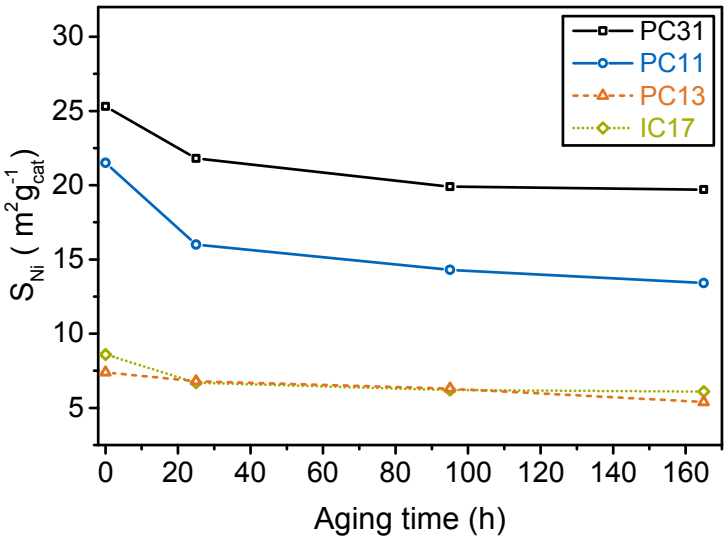

Figure 6.5: Development of the specific Ni surface area, S_{Ni}, upon aging at 623 K.

6.4.3.5 Temperature programmed desorption of CO_2

The TPD results after pulsed CO_2 adsorption on freshly reduced catalyst samples are shown in Figure 6.15A and Figure 6.6. The corresponding values for the CO_2 uptake are given in Table 6.3. Four overlapping desorption signals are detected within the temperature range from

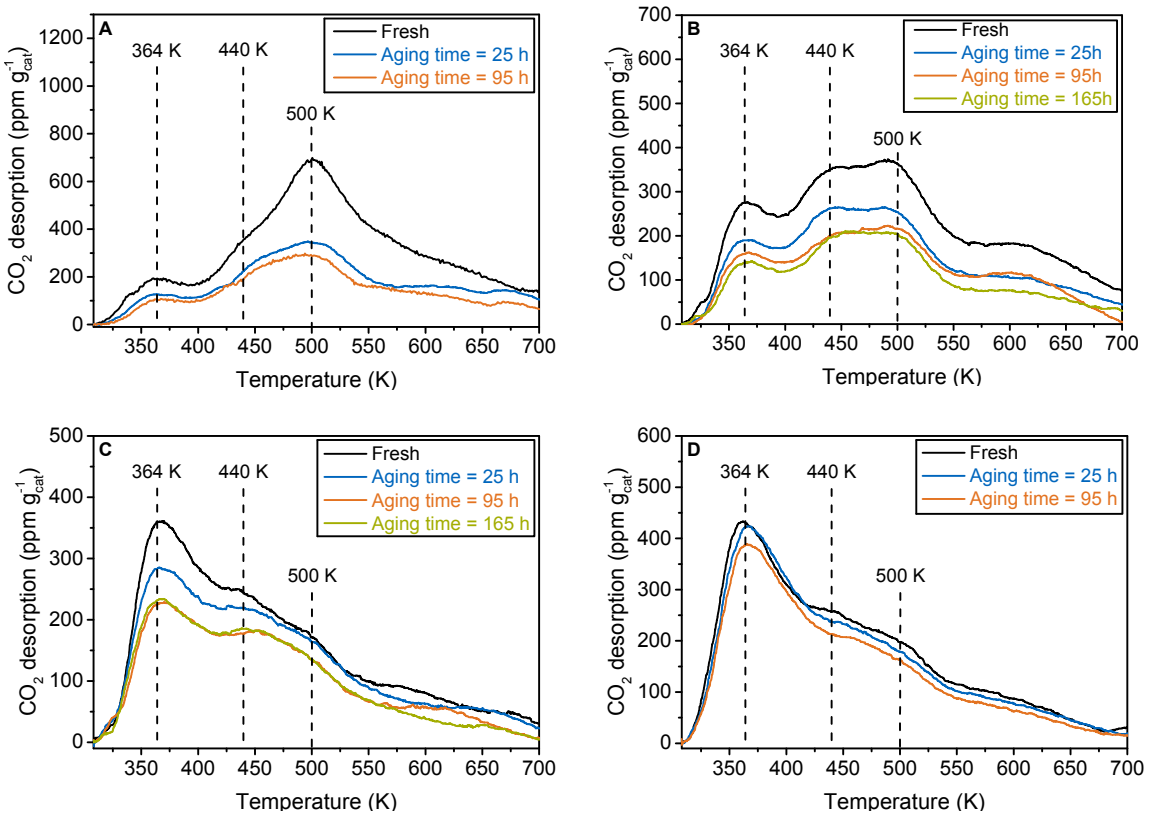

Figure 6.6: Influence of catalyst aging at 623 K on CO_2 interaction with (A) catalyst PC31, (B) catalyst PC11, (C) catalyst PC13 and (D) catalyst IC17.

308 to 700 K. The positions of the signals are independent of the Ni loading and the synthesis procedure, indicating that the kind of adsorption sites for CO_2 is the same in each catalyst system studied. For hydrotalcite-derived materials, Di Cosimo et al. [241] and Wierzbicki et al. [86] found three desorption peaks within the temperature range investigated, while Wang et al. [242] identified four signals when conducting CO_2-TPD from γ-Al_2O_3. Combining TPD and FT-IR measurements allows to assign the observed desorption signals in this study to several carbonate species on the catalyst surface (section 6.6.7 and Figure 6.15).The signal centered around 364 K can be attributed to weakly bound bicarbonate followed by the desorption of bidentate carbonate (signal centered around 440 K) and monodentate carbonate (signal centered around 500 K). The broad desorption signal between 550 and 700 K might be attributed to bridged/"organic-like" carbonate species [242]. This assignment is in good agreement with results of Wang et al. [242]. With increasing Ni loading, the overall CO_2 adsorption capacity in co-precipitated samples is enhanced. The amount of weakly bound bicarbonate decreases, whereas the amount

of bidentate and monodentate carbonates as well as strongly bound bridged/"organic-like" carbonate species increases with rising Ni content. Our results are in accordance with findings in literature, where the basicity was reported to increase with the M^{2+}/M^{3+} ratio in hydrotalcite-derived materials up to $M^{2+}/M^{3+} \sim 3$ [243, 244]. However, a discrepancy between adsorbed and desorbed amount of CO_2 is observed. It might be that part of the weakly adsorbed species is removed from the catalyst surface already during purging after adsorption. Also CO detected at higher temperatures (not shown here) biases the calculation of the desorbed CO_2 amount. A more detailed investigation of the CO_2 interaction with Ni-Al catalysts is currently in progress. Since CO_2 desorption mechanisms and kinetics are unknown, we also here abstained from a deconvolution of the desorption pattern.
Over aging time, the CO_2 adsorption capacity of the co-precipitated catalysts decreases significantly with the strongest loss of adsorption capacity taking place, again, within the first 25 h of aging (Figure 6.6). The decline is less pronounced with decreasing Ni content. The reduction of medium/strong and weak basic sites occurs more intensely in catalyst PC31 and PC13, respectively, whereas the density of all basic sites decreases similarly in the case of PC11. The decrease of basicity is also in line with structural changes accompanied by a potential depletion of Ni^{2+} from the mixed oxide as revealed by XRD analysis, reducing the M^{2+}/M^{3+} ratio. Only minor changes in CO_2 adsorption capacity and TPD signal intensity, respectively, were observed in catalyst IC17. No signal shifts are observed in any of the catalysts studied, indicating that the kind of active sites for CO_2 adsorption remains unchanged during aging but the site density decreases.

6.4.3.6 N_2 physisorption measurements

Results from N_2 physisorption are summarized in Figure 6.16 and Table 6.3. The catalyst samples PC31 and PC11 exhibit type IV isotherms with type H3 hysteresis loops that show no limiting gas adsorption at high p/p_0. Such a hysteresis loop is typical of aggregates of plate-like particles with slit-shaped pores [143], which are also observed for Ni/Al hydrotalcite-type materials in literature [245]. The catalyst samples PC13 and IC17 feature type IV isotherms and a type H2 hysteresis with a limiting nitrogen uptake at high p/p_0. The pore structure of solids exhibiting a H2 hysteresis is often not well defined and an interpretation of the hysteresis is difficult [143]. Upon aging, the pore structure remains unchanged regardless of the catalyst composition and the Ni loading (Figure 6.16), while the BET surface area of all catalysts investigated is decreasing. It is well known that alumina is prone to sintering under hydrothermal conditions, contributing to the decrease of BET surface area [246, 247]. For the co-precipitated samples, the average pore diameter increases with aging time while the total pore volume remains constant. Therefore, the decrease in BET surface area, to a large extent, may be attributed to the increase of larger pores while smaller ones are blocked due to Ni particle growth. A larger pore size increases the effective diffusion coefficient of the reactants enhancing

internal mass transport [248]. Consequently, internal mass transport limitations are not induced upon aging and can be ruled out as cause for the activity loss. With regard to the total pore volume of catalyst PC13, the results indicate a volume increase over aging time. However, a proper separation of the catalyst material from SiC and silica wool turned out to be difficult in this case, so that the available sample mass for N_2 physisorption was rather low for pore size determination. Therefore those values should not be over-interpreted. Also for the impregnated sample, a decrease in BET surface area is observed upon aging, however, the total pore volume as well as the average pore diameter remain constant within the error margin.

6.4.4 Structure-activity correlation

Figure 6.7 depicts the correlation between the Ni surface area and the catalyst activity. A somewhat linear correlation is obtained for catalyst IC17, PC13 and PC11, whereas a strong deviation from linearity is observed for catalyst sample PC31. These observations are in line with results

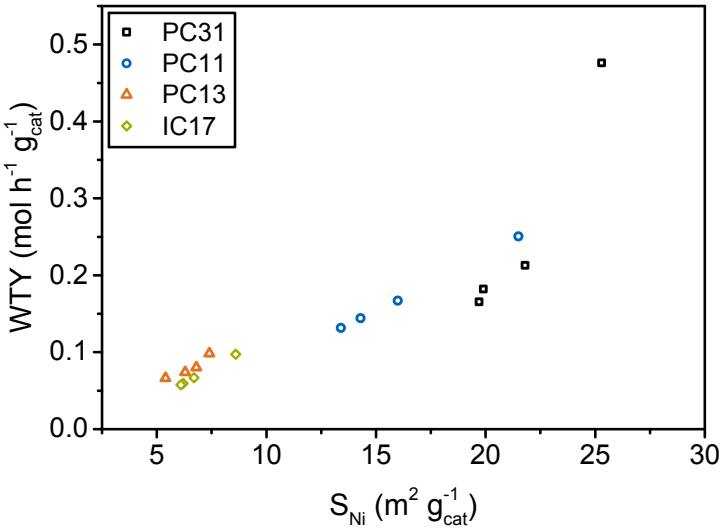

Figure 6.7: Correlation between S_{Ni} and WTY.

for the specific activity, shown in Figure 6.17. A strong initial decrease is observed in the case of PC31. Also the other samples show a slight decrease of specific activity in the first 25 h, indicating that the activity also here does not depend solely on the Ni surface area. However, the observed deviations are certainly within the limits of measurements accuracy, especially when determining small Ni surface areas in the case of IC17 and PC11. The findings might be explained by the decreasing CO_2 adsorption capacity with aging time, which is observed for each catalyst system. CO_2 stored on the support may reverse spillover to the Ni phase, where it then reacts with H_2 [19], increasing the activity. In reverse, a reduction of CO_2 storage capacity leads to a loss of activity. This would also explain the lower activity of PC31 after 25 h compared to fresh PC11, both of which have a similar Ni surface area. A distinct correlation between CO_2

uptake and catalyst activity is not observed but CO_2 adsorption, in contrast to the results shown in [19], seems to have more influence at higher Ni surface areas. For catalysts with small Ni surface areas, it is likely that CO_2 is abundantly stored on the support and the Ni surface area itself is limiting. Increasing the Ni surface area, therefore, directly increases the activity. At higher Ni surface areas also the stored amount of CO_2 gains importance. A distinct correlation between BET surface area and activity could not be established either.

There is also evidence that monodentate carbonate on medium basic sites is hydrogenated fastest and therefore, medium basic sites are proposed to be essential for high catalytic activity [20]. As evident from the desorption signal at 500 K in Figure 6.15A, the amount of medium basic sites forming monodentate carbonate are most abundant in sample PC31, which also shows the highest activity, and declines with decreasing Ni content. The medium basic site density decreases significantly within the first 25 h of aging in the case of PC31 (Figure 6.6A), which is in line with a strong initial decrease of activity and specific WTY. In contrast, the decrease of medium basic site density is less pronounced at lower Ni loadings for co-precipitated samples and basically no change in basicity is observed for sample IC17. More medium basic sites are also observed in fresh PC11 compared to PC31 after 25 h of aging as depicted in Figure 6.15D, which is an alternative explanation for the higher activity despite a similar Ni surface area.

Considering the trend of the specific activity, especially for sample PC31, also structure sensitivity has to be taken into account [108]. It is well known that step sites are most active in the hydrogenation of CO [108, 249], which is purportedly an intermediate step in CO_2 methanation. Also for CO_2 methanation, these sites were reported to be very active [48]. Step sites are dependent on the Ni particle size more than the Ni surface area and decrease with increasing Ni particle size. Also in this study, the trend of the activity of co-precipitated samples follows the development of the Ni particle size (Table 6.3). A comparison of particle sizes of a fresh PC11 sample and a PC31 sample aged for 25 h reveals smaller particle sizes in the PC11 sample, so that the higher activity of the fresh PC11 sample can also be explained in the context of structure sensitivity. Structure sensitivity would also explain the better performance of PC13 compared to IC17 upon aging, which shows similar values for the Ni surface area, even higher CO_2 adsorption capacities and more medium basic sites but larger Ni particles. Surprisingly, however, the activity right after reduction is similar despite larger Ni particles in sample IC17.

When interpreting correlations of particle size and activity in this study, one should keep in mind that the average Ni particle diameter was calculated from peak broadening in XRD, which is often underestimating particle sizes due to defects in the crystalline phase. This is especially the case in co-precipitated samples that exhibit a high degree of paracrystallinity [87, 211]. An increase of Ni particle size, therefore, can be caused by particle growth and/or a reduction of defects. In this context, one might speculate to what extent the reduction of defects, which were found to enhance both activity and stability in Ni nanoparticles [250], contribute to deactivation.

With regard to the impregnated sample, the constant particle diameters, despite a decreasing Ni surface area, might be explained by highly defective Ni crystals. This would be also in accordance with results from H_2-TPD. Besides, changes of the Ni particle diameter might not be

observable if most of the Ni species is present in an encapsulated form, where particle sintering is impeded as mentioned before. We abstained from the calculation of the Ni particle diameters from H_2 chemisorption results, since the degree of reduction of co-precipitated samples might change during aging. TEM imaging as another method to determine the particle size is impeded due to the ferromagnetic character of activated samples and sensitivity to air. A direct quantification of step sites and their correlation with activity might provide a deeper understanding of the nature of active sites for CO_2 methanation. Edges and corners of the Ni particles can be revealed by H_2-TPD as mentioned earlier. The results presented in Figure 6.4, however, do not allow a quantification, since desorbing H_2 in the relevant temperature range does not only originate from the Ni phase but also from the second adsorption layer. Next to step sites also the metal-support interface was attributed importance in the methanation of CO and CO_2 [21, 48, 244]. For the calculation of the metal-support interface, Tada et al. [251] and Mebrahtu et al. [244] applied a hemispherical model. The applicability of the model seems questionable in our case, again, due to the paracrystallinity and incomplete reduction of the co-precipitated samples.

Finally, it is also possible that different reaction mechanisms and active sites are present simultaneously, where the one or the other dominates, depending on Ni loading, catalyst morphology and structure [48, 51, 252, 253]. For impregnated Ni/Al_2O_3 systems with a metal loading < 15 wt-% Hu et al. [252] found three different active sites, exhibiting different activity and mechanism in CO_2 methanation, whereas Kester at al. [51] reported on two different active sites, one of which is made up by Ni species surrounded by oxygen, whereas the other is located on Ni particles. Only the latter were reported to be present in catalysts with Ni loadings exceeding 15 wt-% [51]. As summarized in Table 6.2, the calculated activation energies are similar for each catalyst system studied and remain constant within the error margin. Therefore, it is likely that the type of active site does not change but the site density decreases upon aging. Also the reaction mechanism, the rate-determining step and the concentration of the reactant species on the catalyst surface seem to be the same before and after aging. This is the case for each catalyst sample investigated independent from the Ni loading and structure. Furthermore, constant activation energies additionally prove that transport limitations do not occur upon aging and all measurements were conducted under kinetically controlled conditions.

6.5 Conclusion

The long-term deactivation of co-precipitated $NiAlO_x$ and an impregnated 17 wt-% Ni/γ-Al_2O_3 catalyst in CO_2 methanation under hydrothermal conditions was investigated and predominant deactivation mechanisms were revealed. The stability of mixed oxide catalysts increases with decreasing Ni content on the expense of activity. The impregnated catalyst reveals a lower stability than a comparable co-precipitated sample. The deactivation behavior could be kinetically

described with a power law model. Main causes of deactivation in co-precipitated samples were found to be Ni particle growth as well as the decrease of medium basic sites and the overall CO_2 adsorption capacity, which are accompanied or induced by structural changes and a loss of BET surface area. Ni particle sintering and a decline of BET surface area are possible causes for deactivation in the impregnated sample. The pore structure of each catalyst system investigated remains constant. A distinct correlation between a single deactivation phenomena and the activity could not be established, so that a complex interplay of several deactivation phenomena and/or structure sensitivity have to be considered.

6.6 Supporting Information

6.6.1 Influence of activity measurements on deactivation behavior

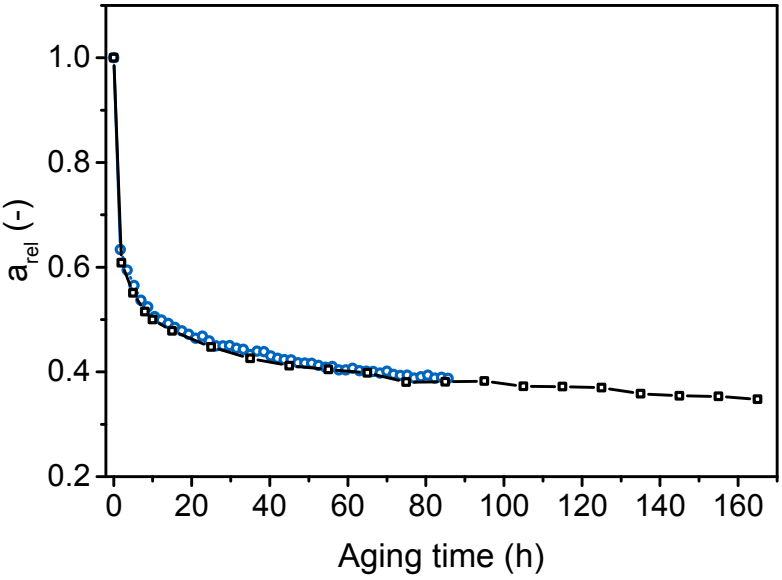

Figure 6.8: Catalyst activity a_{rel} over aging time; (blue circles) activity measurements every 1.75 h; (black squares) activity measurement after 2, 5, 8, 10, 15 h and then every 10 h (T_{Aging} = 623 K, catalyst PC31).

6.6.2 Influence of TPH on deactivation and catalyst structure

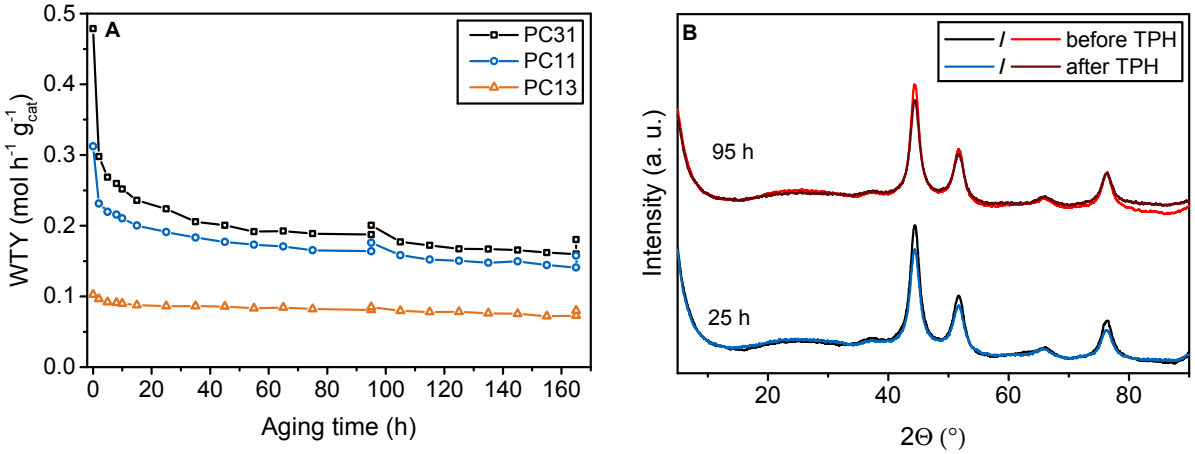

Figure 6.9: (A) Influence of temperature programmed hydrogenation after 95 and 165 h on stream on the deactivation behavior ($H_2/CO_2/Ar/N_2$ = 8/2/9/1, Q_{Feed} = 500 Nml min^{-1}, m_{cat} = 50 mg, p = 8 bar, T_{Aging} = 623 K); (B) influence of temperature programmed hydrogenation after 25 and 95 h of aging on the XRD pattern of PC31.

6.6.3 Determination of the apparent activation energy after aging

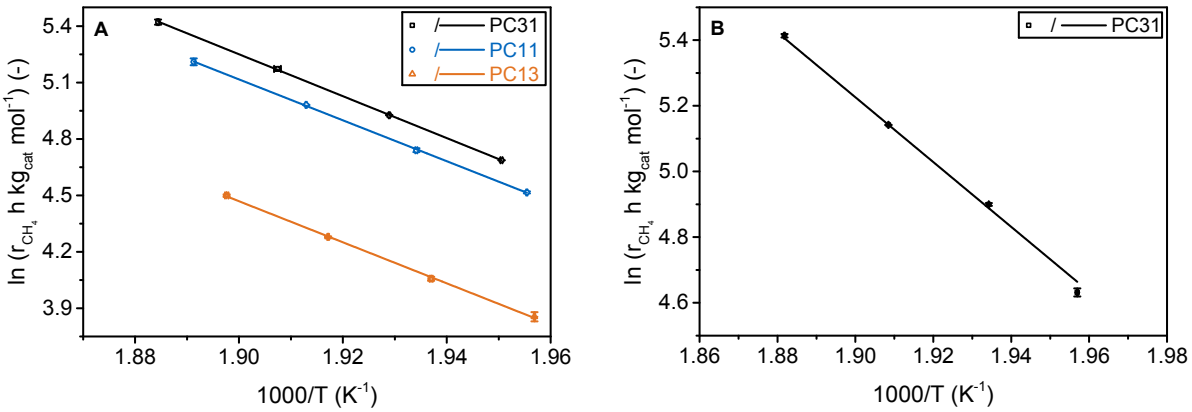

Figure 6.10: Arrhenius plot for the calculation of the apparent activation energy after 165 h on stream at (A) 573 K and (B) 523 K ($H_2/CO_2/Ar/N_2$ = 8/2/9/1, Q_{Feed} = 500 Nml min^{-1}, m_{cat} = 50 mg, p = 8 bar).

6.6.4 XPS analysis

Results of a detailed XPS analysis of the calcined catalyst samples as well as reference materials are presented in this section. Figure 4.1C reveals pure bunsenite and $NiAl_2O_4$ as the only crystalline phase in calcined PC10 and PC12, respectively. Therefore, these samples are used as reference materials NiO and $NiAl_2O_4$ in the following. XPS results for co-precipitated and

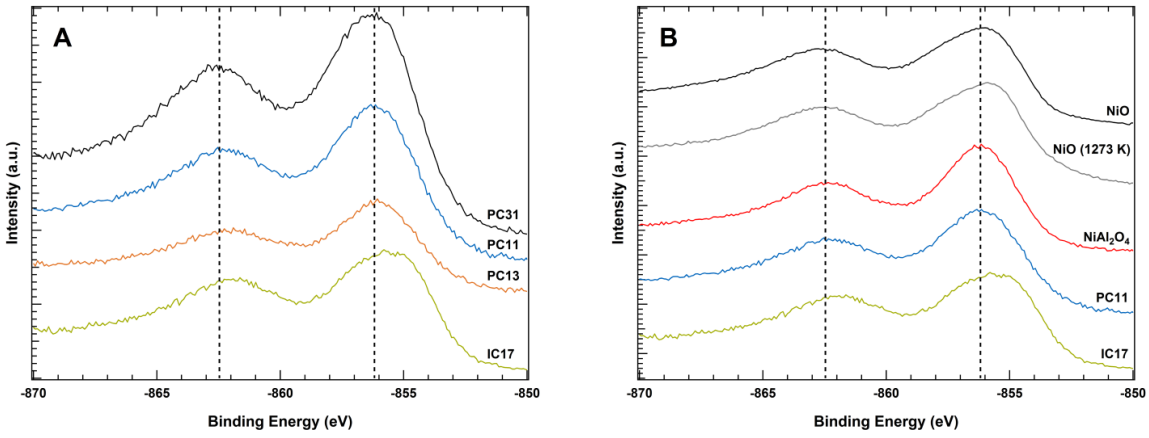

Figure 6.11: (A) Comparison of the Ni 2p3/2 region of precipitated and impregnated samples. (B) XPS results of the Ni 2p3/2 region in relation to reference materials.

impregnated samples are shown and compared in Figure 6.11. For sample PC13, PC11 and PC31, the recorded binding energies (BE) of the Ni $2p_{3/2}$ main signal (Figure 6.11A) and its satellite are independent from the Ni loading and centered around 856.0 eV and 862.5 eV, respectively. Also the peak shapes are identical. The differences in signal intensity originate

from the increase of the Ni loading in the order PC13 < PC11 < PC31 (Table 4.1 and Table 6.3). In contrast, the impregnated catalyst exhibits peak broadening of the main signal and a decrease in binding energy to about 855.5 eV. This might indicate that Ni^{2+} components are situated in a different chemical environment as compared to the co-precipitated samples.
In Figure S.7B, the Ni $2p_{3/2}$ of PC11 and IC17 are compared with corresponding patterns of NiO and $NiAl_2O_4$. Next to the standard degassing at 673 K, NiO was also pre-treated in O_2 at 1273 K (sample NiO (1273 K) in the following) since this procedure is known to produce clean NiO surfaces [234]. Both pre-treatments lead to identical spectra, as the Ni $2p_{3/2}$ main feature around 856.0 eV and its satellite at 862.5 eV do not differ in energy position and peak shape. This strongly suggests, that the chemical state of the NiO surface is the same in both cases and that already degassing at 673 K results in a clean surface. Comparing the spectra of NiO and PC11, a slight shift of the peak maxima to lower binding energies as well as peak broadening is observed for NiO. The pattern of IC17, on the other hand, corresponds well to the one of NiO which implies that the chemical state of the Ni^{2+} surface species in the impregnated sample is very similar to the one of pure NiO. The signals of PC11 reveal identical binding energies and peak shapes as $NiAl_2O_4$ within measurement accuracy. This implies that $NiAl_2O_4$ is present on the surface of the mixed oxide samples investigated. However, essentially the same spectrum is obtained independent of the Ni loading (Figure 6.11A) which contradicts the assumption of $NiAl_2O_4$ on the surface, as spinel requires a Ni/Al ratio of 1/2. It is more likely that the differences in the chemical state of the surface species in $NiAl_2O_4$ and mixed oxides of different Ni/Al ratios are very small and cannot be revealed by means of XPS analysis. In

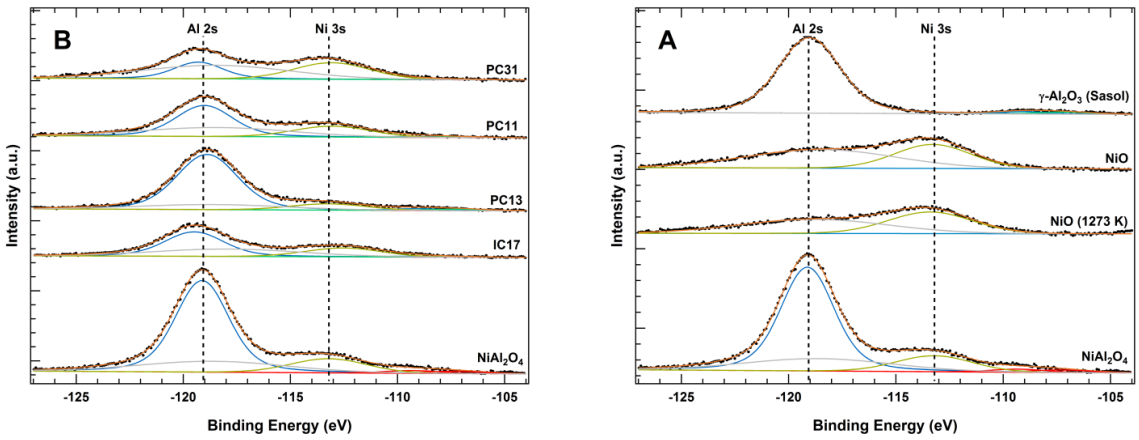

Figure 6.12: (A) XPS results for the Al 2s and the Ni 3s region of reference materials. (B) comparison of Al 2s and Ni 3s signals of co-precipitated and impregnated catalyst samples.

Figure 6.12, the Al 2s/Ni 3s region of the catalysts and reference materials is shown. The spectra obtained for Al_2O_3 and NiO, reveal the intrinsic shape and position of the Al 2s and Ni 3s signal, respectively. NiO typically exhibits a satellite structure [235] leading to a broad signal in the same region where also the Al 2s signal is observed. Determining the intrinsic peak parameters (relative binding energies, number of components and peak widths) for Al 2s and Ni 3s in pure

γ-Al_2O_3 and NiO, respectively, allows for the deconvolution of the overlapping signals in Ni-Al mixed oxides. On this basis, a comparison of the binding energies, peak shapes and peak areas was conducted. No significant differences in the peak shape are observed. Concerning the binding energies, similar trends were obtained as for the Ni $2p_{3/2}$ region. All co-precipitated samples reveal a constant binding energy of approx. 119.0 eV for the Al 2s signal. A comparison with the pattern obtained for γ-Al_2O_3 and $NiAl_2O_4$ demonstrates that the chemical state of the surface Al^{3+} species is very similar in the precipitated samples, γ-Al_2O_3 and $NiAl_2O_4$. In addition, the calculation of the difference in binding energy (Δ BE) of the Ni $2p_{3/2}$ and Al 2s signal results in a similar value of 737.1 ± 0.1 eV (Table 6.4), which is within the spectral resolution limit of the instrument (± 0.1 eV). This additionally proves that a decisive elucidation of the exact surface composition in precipitated samples is not possible by means of XPS. The pattern of IC17, however, reveals a different trend. The binding energy of the Al 2s signal is shifted to a higher value by 0.5 eV as compared to the other samples. The difference might arise from the inhomogeneous character of the surface in the impregnated sample.

Our results seem contradictory to a comparable study by Shalvoy et al. [254]. There, substantial differences were reported for the binding energy of the Ni $2p_{3/2}$ in NiO (854.6 eV), $NiAl_2O_4$ (856.1 eV) and co-precipitated Ni-Al samples (856.8 ± 0.4 eV). However, the calculated values for Δ BE of the Ni $2p_{3/2}$ and Al 2s signal, on average 737.1 ± 0.45 eV, are in good agreement with corresponding results in this work. We assume that the discrepancy in binding energies arises from an inaccurate correction for sample charging in [254], as the C 1s signal originating from adventitious carbon was used. In the study presented here, only insignificant amounts of carbon species were observed after pre-treatment and the O 1s peak as an intrinsic signal was used for correction. Calculated values for the Ni/Al ratio on the catalyst surface are summarized

Table 6.4: XPS results.

Catalyst	PC31	PC11	PC13	IC17	$NiAl_2O_4$ (PC12)
Δ BE[a] (eV)	737.07	737.06	737.17	736.40	737.05
Ni/Al[b] (wt-%)	2.98 ± 0.60	0.93 ± 0.19	0.28 ± 0.06	0.93 ± 0.19	0.41 ± 0.08

[a] difference in binding energy of Ni $2p_{3/2}$ and Al 2s
[b] on the catalyst surface calculated from XPS results.

in Table 6.4. For co-precipitated systems, the surface composition in the calcined samples agrees well with the bulk Ni/Al ratio obtained in the corresponding precursors after precipitation. The rather high experimental error of 20% is induced by the broad Ni 3s signals.

6.6.5 XRD analysis of fresh and aged catalyst samples

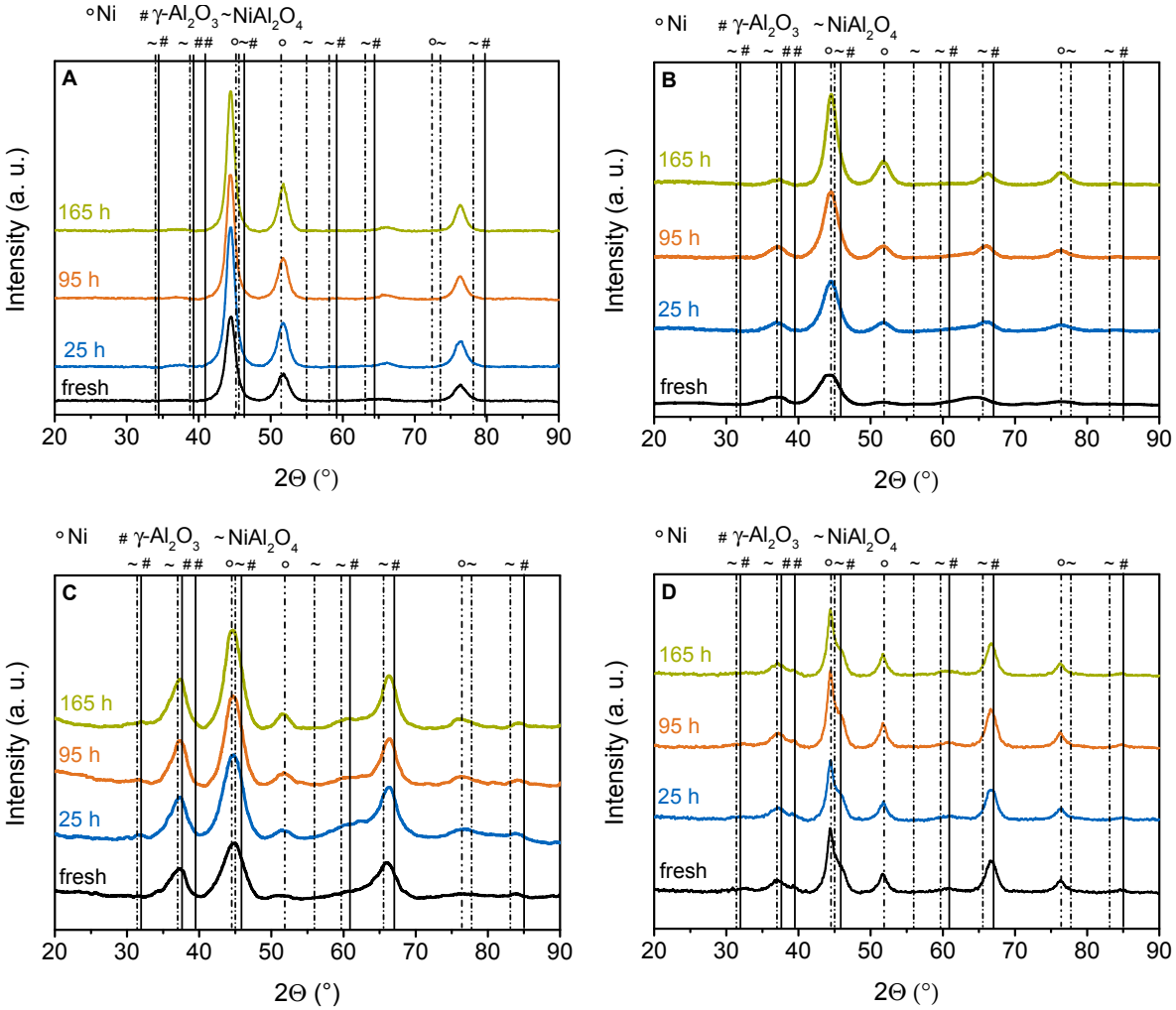

Figure 6.13: XRD analysis upon aging of (A) PC31, (B) PC11, (C) PC13 and (D) IC17 at 623 K (JCPDS: NiO 78-0429, Ni 87-0712, γ-Al_2O_3 10-0425, $NiAl_2O_4$ 10-0339).

6.6.6 H_2-TPD results of fresh catalyst samples

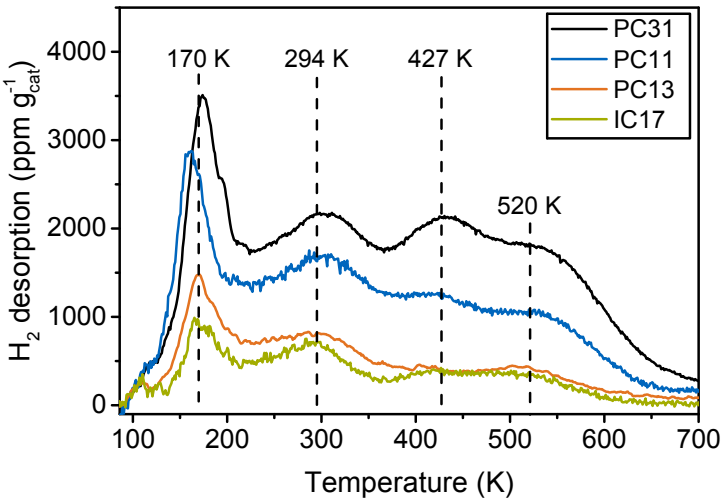

Figure 6.14: Influence of Ni loading on H_2-TPD.

6.6.7 CO_2-TPD and FT-IR results

Results from CO_2-TPD and FT-IR measurements are depicted in Figure 6.15. For all catalyst systems studied, desorption signals at 364, 440 and 500 K as well as a broad feature between 550 and 700 K are observed. Additionally, CO was observed at temperatures higher than 600 K (not shown here). CO_2 adsorption in a pulsed manner results in significantly lower signal intensities as compared to adsorption under flow (Figure 6.15B). This is most pronounced in the case of desorption from weak basic sites exhibiting the desorption signal at 364 K. However, the peak temperature of each signal does not change, indicating that the same kind of adsorption sites are occupied independent from the CO_2 partial pressure. Consequently, the FT-IT measurements in Figure 6.15C, recorded upon adsorption under flow, can be applied to interpret the desorption patterns in Figure 6.15A. Results reveal multiple absorption bands between 1100 and 1900 cm^{-1}. No bands related to CO species on metallic Ni or $Ni(CO)_4$ are observed. This implies, that CO detected above 600 K originates from dissociation of desorbing CO_2, forming CO and oxygen, the latter of which is retained on the catalyst surface. The adsorption bands at 1670, 1410 as well as 1259 cm^{-1} are the first to vanish during TPD and are not observable anymore at temperatures higher than 419 K. Consequently, those bands can be attributed to bicarbonate, which is well known to be formed upon interaction of CO_2 with Al^{IV} and/or Al^{IV}-OH sites and are only weakly bound to the catalyst surface [242, 255, 256]. Adsorption bands at 1649 and 1346 cm^{-1}, that can be assigned to bidentate carbonate, vanish at temperature higher than 440 K followed by bands at 1548 and 1441 cm^{-1}, originating from monodentate carbonate, that are stable until 514 K [256, 257]. The absorption band at 1225 cm^{-1} and an additionally formed band at 1200 cm^{-1} are stable up to the maximum temperature of 753 K. Also the small pattern between 1700 and 1900 cm^{-1} is still present at those temperatures. Absorption bands

in these regions can be attributed to strongly bound bridged/"organic-like" species, which typically exhibit complex bands above 1700 and below 1200 cm^{-1} [242, 255]. The signal at 1301 cm^{-1} has been ascribed to an additional form of bridged/"organic-like" species by Wang et al. [242]. However, the band disappears at temperatures higher than 514 K which makes its assignment to strongly disputable. In this context, one might also take into consideration bands due to minor amounts of Ni carboxylate [255], since next to Al also Ni is present in the mixed oxide. The assignment of observed absorption bands and a comparison with literature is often not straight forward due to the significant influence of the catalyst structure and electronic properties, respectively. This, to some extent, also explains the deviations of the observed bands compared to literature [242, 255–257]. Nevertheless, the FT-IR results are sufficient to assign the desorption signals during TPD in Figure 6.15A to the different carbonate species on the catalyst surface. Consequently, the desorption signal at 364 K can be ascribed to bicarbonate followed by bidentate and monodentate carbonate with desorption peaks at 440 and 500 K. Desorption of bridged/"organic-like" species cause a broad desorption pattern between 550 and 700 K.

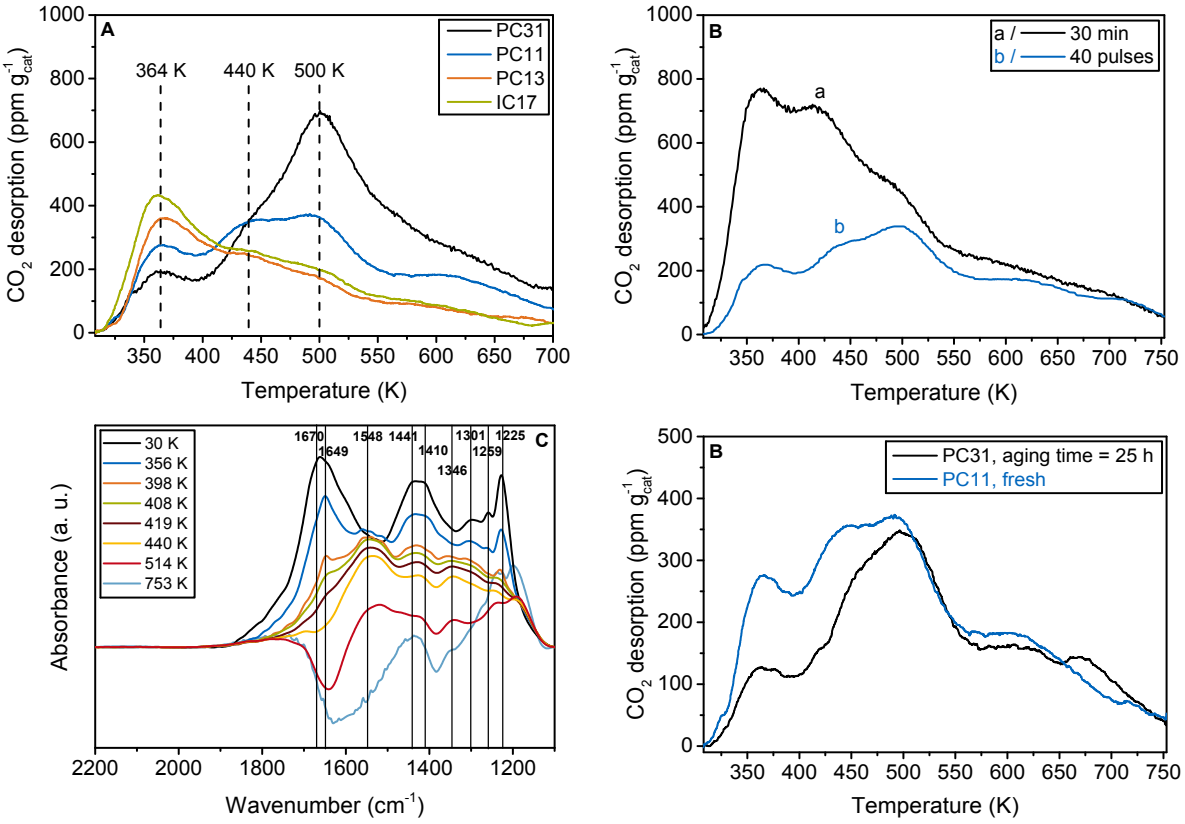

Figure 6.15: TPD and FT-IR results from activated samples. (A) TPD patterns after pulsed CO_2 adsorption. (B) comparison of TPD patterns after CO_2 adsorption in a continuous mode and in a pulsed manner [160]. (C) FT-IR results during TPD after adsorption of 6 % CO_2 in He for 30 min [160]. (D) comparison of a fresh PC11 and a deactivated PC31 sample.

6.6.8 N_2 physisorption measurements

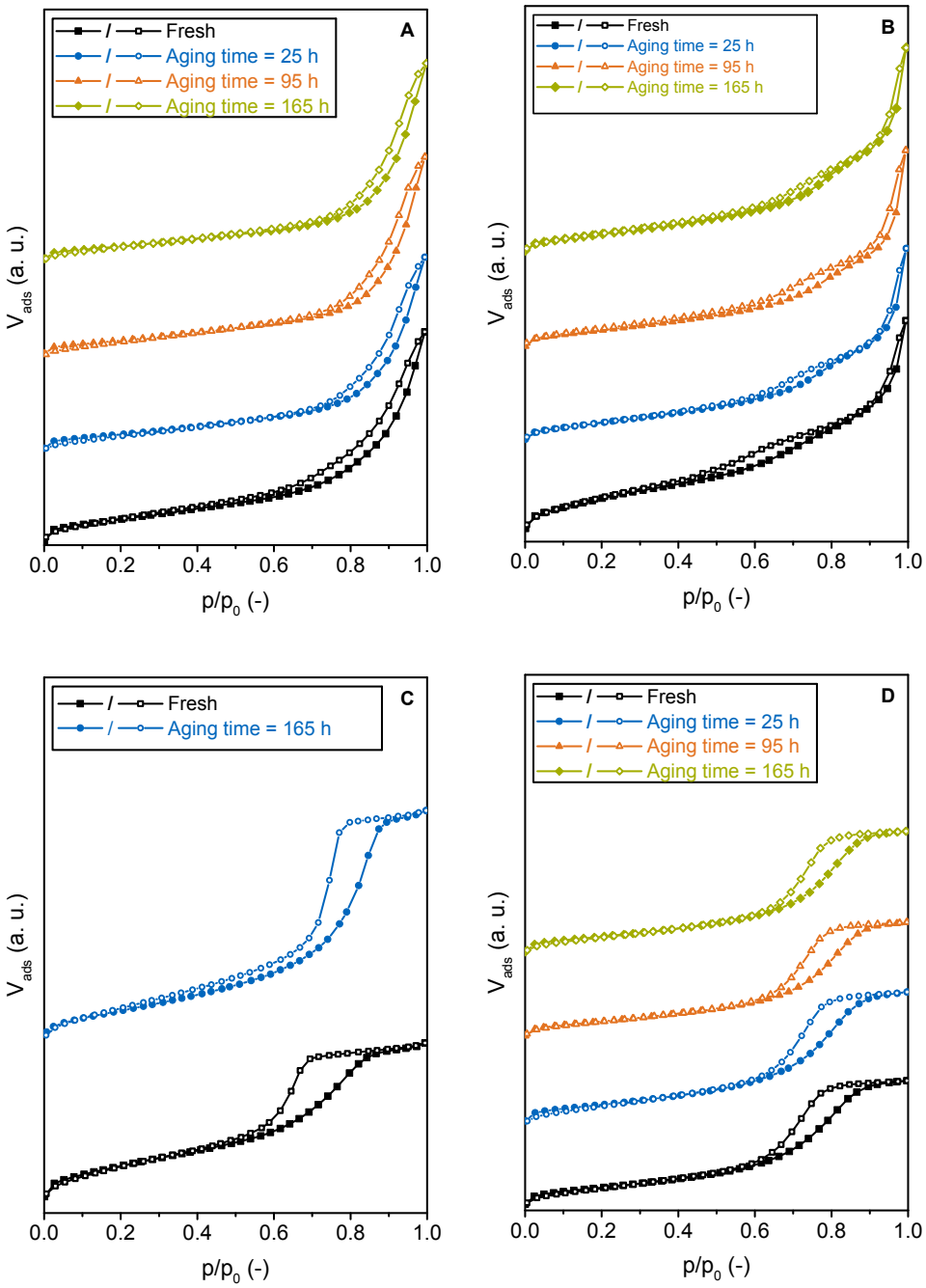

Figure 6.16: N_2 adsorption/desorption isotherms of fresh and deactivated samples of catalyst (A) PC31, (B) PC11, (C) PC13 and (D) IC17 (T_{Aging} = 623 K).

6.6.9 Development of the specific activity upon aging

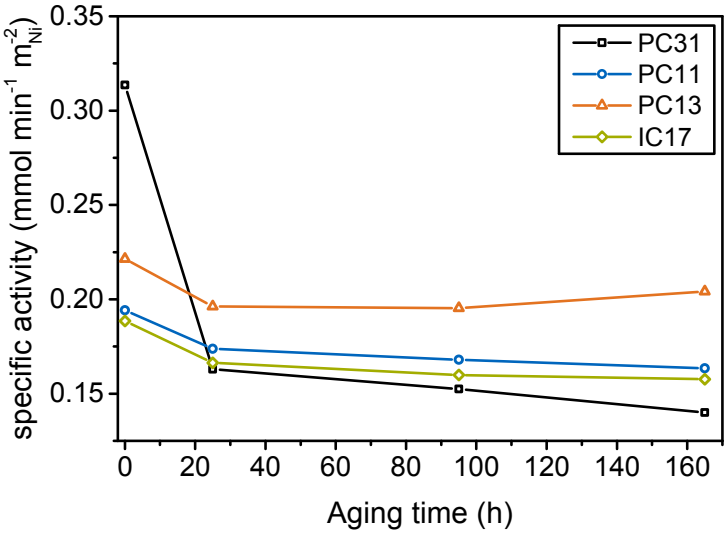

Figure 6.17: Development of the specific activity (WTY per specific Ni surface area) upon aging at 623 K.

7 On the interaction of CO_2 with Ni-Al catalysts

This chapter was published in:

S. Ewald, O. Hinrichsen, *On the interaction of CO_2 with Ni-Al catalysts*,
Applied Catalysis A: General, **2019**, *580*, 71-80.

7.1 Abstract

Knowledge of the CO_2 interaction with the catalyst material is of great importance in the development of efficient catalysts for the methanation of CO_2. In this study, the CO_2 adsorption modes on and interaction with Ni-Al catalysts are systematically investigated by coupling FT-IR and CO_2-TPD measurements next to pulsed and static CO_2 chemisorption. The knowledge that is derived allows for a concise characterization of the CO_2 interaction with Ni-Al catalyst by means of CO_2-TPD. The strength of this technique in elucidating structure-activity relations of Ni-Al catalysts for CO_2 methanation is demonstrated. For the study, catalysts with varying Ni loading are synthesized via co-precipitation and incipient wetness impregnation. CO_2 adsorption under flow conditions close to room temperature leads to the formation of carbonate species on the catalyst. After elongated exposure of the catalyst to CO_2, typically present under static conditions, Ni-CO species are also formed. The density of weak basic sites forming bicarbonate decreases with increasing Ni content for precipitated catalysts, while medium and strong basic sites forming bidentate, monodentate and bridged/"organic"-like species increase. Bicarbonate is the most abundant species on impregnated samples upon CO_2 adsorption under flow conditions. Only a minor influence of the Ni loading on the catalyst basicity is observed for the impregnated samples. TPD results also indicate that CO_2 adsorption on Ni-Al catalysts is an activated process. A more complete picture of the CO_2 interaction with Ni-Al catalysts is obtained when starting TPD measurements at temperatures as low as 218 K. Bicarbonate, bidentate and monodentate carbonate exhibit desorption signals at 325, 416 and 500 K, respectively, while bridged/"organic"-like species show a broad desorption pattern between 550 and 750 K.

An additional desorption signal is observed at 260 K. Pulsed CO_2 chemisorption reveals that strong adsorption sites are filled first. The uptake of strongly chemisorbed CO_2 determined from pulsed adsorption is significantly lower than corresponding values from static chemisorption.

7.2 Introduction

The hydrogenation of CO_2 was first described by Sabatier and Senderens in 1902 [22], but only recently came back into the focus of research as a promising technology to store energy from renewables [10]. Since its "rediscovery" a broad range of catalytic materials has been investigated for their applicability. Group VIII transition metals like Ni, Rh or Ru supported on SiO_2, Al_2O_3, ZrO_2 or CeO_2 have been reported to be active for CO_2 hydrogenation. A comprehensive overview of catalytic systems studied can be found in recent reviews [12, 24, 258]. Supported Ni is probably the most often investigated due to its price and availability. Also Ni-containing mixed oxides gained attention [18, 79–81] in part due to their higher stability as compared to classic metal-support systems [112].

For a good catalytic performance, a high active metal surface area is essential. However, studies have also supplied evidence that the CO_2 adsorption capacity as well as the basicity of the catalyst are important [18, 20, 21, 52]. In order to investigate the interaction of CO_2 with catalytic materials and their basicity, infra-red (IR) spectroscopy is widely applied [20, 21, 81, 86, 255, 256, 259–262]. While this technique is predestined to elucidate adsorbed CO_2 species on the surface, a quantitative analysis of CO_2 adsorption is often not straight-forward. Temperature programmed desorption (TPD) on the other hand is capable of more easily quantifying CO_2 adsorption on different sites. However, it is not possible to determine adsorption modes a priori. Moreover, TPD also allows the study of CO_2 interaction at elevated pressures much closer to working conditions, while IR measurements are commonly conducted under vacuum or atmospheric pressure. CO_2 adsorption and desorption enthalpies can also be determined by TPD, making it a powerful tool in evaluating the catalyst performance in CO_2 conversion reactions. It is reasonable to combine IR and TPR measurements to obtain both qualitative and quantitative information about the CO_2 interaction with catalytic materials. However, only some studies so far have applied those techniques for the characterization of CO_2 interaction with Ni-containing mixed oxides [20, 21, 81, 86, 262]. Moreover, experimental conditions are mostly chosen arbitrarily, although adsorption conditions can have a significant influence on the interaction of the probe gas with the catalyst material, as proven in our previous study [161]. This makes a comparison of experimental results and the attribution of desorption signals to weakly, moderately or strongly adsorbed species difficult. For example, Pan et al. [100] conducted CO_2-TPD measurements with activated Ni/γ-Al_2O_3 and Ni/$Ce_{0.5}Zr_{0.5}O_2$ within the temperature range from 323 to 1173 K. In this range they found three signals and attributed the pattern between 323 and 523 K to weakly adsorbed species, the pattern between 523 and

973 K to species in medium basic sites and the desorption signal at higher temperatures to strongly adsorbed species. In contrast, Muroyama et al. [67] found three distinct desorption signals within the temperature range from 298 and 798 K and attributed the signal between 598 and 798 K to strongly adsorbed species. Mebrahtu et al. [244] correlated performance data of activated Ni-Fe/(Mg, Al)Ox with CO_2-TPD pattern, the latter of which, were recorded on catalysts in their calcined state. However, it is known that structural changes of these catalysts take place upon reduction, which might alter their basicity [18].
A systematic investigation of the CO_2 interaction with Ni-Al catalysts, to our best knowledge, is lacking. In this study, therefore, we present a detailed study of the CO_2 interaction with Ni-Al catalysts by means of FT-IR measurements, temperature programmed desorption of CO_2 (CO_2-TPD) as well as pulsed and static CO_2 chemisorption. The influence of adsorption modes and conditions on CO_2 interaction is evaluated. The influence of the Ni loading, the catalyst synthesis procedure and the catalyst state (calcined or activated) on the basicity are investigated. Adsorbed species are identified and quantified by coupling FT-IR and CO_2-TPD measurements.

7.3 Experimental

7.3.1 Catalyst synthesis and elemental analysis

Ni-Al catalysts were synthesized via co-precipitation and incipient wetness impregnation. For co-precipitation, aqueous solutions of $Ni(NO_3)_2 \cdot 6H_2O$ (1 M, Merck®) and $Al(NO_3)_3 \cdot 9H_2O$ (1 M, Sigma-Aldrich®) were mixed and precipitated at 303 K and a constant pH of 9. An equimolar mixture of 0.5 M NaOH (Merck®) and 0.5 M Na_2CO_3 (Sigma-Aldrich®) was used as precipitating agent. Details can be found in [79, 80]. The Ni loading of the precipitated samples was adjusted by varying the Ni/Al ratio between 1/5, 1/3, 1/2, 1/1, 3/1 and 5/1 (samples donated as PC15, PC13, PC12, PC11, PC31 and PC51 in the following). Also samples just containing Al (PC01) or Ni (PC10), were synthesized in the same way. After precipitation, the precursors were dried at 353 K overnight. Subsequently, the dried precursors, except for PC12, were calcined in flowing air at 723 K for 6 h (5 K min^{-1}). The dried PC12 precursor was calcined at 1173 K in order to obtain $NiAl_2O_4$ as reference material. After calcination, the catalyst material was pressed, ground and sieved. The sieve fraction of 150 – 250 µm was used for measurements. 9 and 17 wt-% Ni/γAl_2O_3 (denoted as IC9 and IC17 in the following) were synthesized via incipient wetness impregnation of γ-Al_2O_3 from Sasol® (PURALOX SCCa150/200, S_{BET} = 196 $m^2\,g_{cat}^{-1}$, 150 – 200 µm) with an aqueous solution of $Ni(NO_3)_2 \cdot 6H_2O$ (1 M, Merck®). After impregnation, the precursors were dried and calcined under the same

conditions as the precipitated samples. The actual Ni content was determined via AAS using a Varian® AA280FS and photometry using a Shimadzu® UV-160.

7.3.2 N_2 physisorption and temperature programmed reduction (TPR)

N_2 physisorption measurements were performed at the boiling point of liquid N_2 using a Novatouch from Quantachrome®. For the measurements, roughly 100 mg of calcined catalyst material were placed in the sample cell and degassed under vacuum at 393 K for 3 h prior to analysis. The BET surface area was determined from the adsorption branch of the isotherm within $p/p_0 = 0.05 - 0.3$. The average pore diameter and volume were calculated assuming spherical pore geometry.
TPR measurements and the mass loss during reduction were recorded with a STA thermobalance from Netzsch®. For analysis 25 – 50 mg of calcined catalyst were loaded into the crucible and heated in Ar ($Q_{Ar} = 60\,Nml\,min^{-1}$) at 623 K for 1 h ($\beta = 3\,K\,min^{-1}$). After cooling down to room temperature, TPR was performed in 5% H_2 in Ar at a flowrate of 75 Nml min^{-1} up to a maximum temperature of 1173 K. Product gas analysis was performed with an Omnistar GSD 301 quadrupole mass spectrometer from Pfeiffer®.

7.3.3 Temperature programmed desorption of CO_2 (CO_2-TPD)

CO_2-TPD was studied in greater detail using a setup described elsewhere [161]. All gases were of high purity (5.0 or higher for CO_2, 6.0 for He and H_2). For analysis, 50 - 150 mg of catalyst material were fixed in the isothermal zone of the reactor with two plugs of silica wool and a thermocouple was placed in the catalyst bed. For reduction, Ni-Al samples were heated to 753 K in 5 % H_2 in He at a heating rate of $3\,K\,min^{-1}$. The samples were kept at reduction temperature for 5 h. PC10, which does not contain Al, was reduced at 673 K for 2 h (5 % H_2 in He, $\beta = 3\,K\,min^{-1}$). After reduction, the catalysts were purged with He and cooled down to 308 K. Subsequently, the setup was brought to the desired adsorption temperature and CO_2 was introduced either in a continuous flow or in a pulsed manner. For adsorption in a continuous mode, a stream of pure CO_2 was fed to the reactor for 30 to 90 min at a flow rate of 50 Nml min^{-1}. Pulsed CO_2 adsorption was achieved by injecting 2 % CO_2 in He into a He stream flowing over the catalyst using of a calibrated sample loop ($Q_{He} = 13\,Nml\,min^{-1}$, $V_{loop} =$ 1 ml). After adsorption, the catalyst was flushed with He to remove any weakly adsorbed CO_2 and TPD was performed up to 753 K under flowing He ($Q_{He} = 100\,Nml\,min^{-1}$, $\beta = 6\,K\,min^{-1}$). Alternatively, CO_2 was adsorbed in a three step process. First, CO_2 was fed at 308 K for 30 min. Subsequently, the sample was carefully cooled down to 218 K under flowing CO_2 where adsorption for another 30 min was conducted. Then, the sample was purged with He and TPD

was performed under the same conditions as mentioned before. Adsorption was not conducted at temperatures lower than 218 K to avoid resublimation of CO_2. Noisy data was smoothed for presentation. The reactor used in this study was equipped with a shut-off valve at the inlet so that samples could be removed from the setup under inert conditions.

7.3.4 Ni surface area determination and XRD analysis

The specific Ni surface area of activated samples was determined through pulsed H_2 adsorption using the same setup as for CO_2-TPD experiments. In total, 20 - 40 pulses of 5 % H_2 in He (purity 6.0 each) were used. Details can be found in [161].
XRD analysis was performed with a STOE® Stadi P diffractometer operated at 50 kV and 30 mA (Ge(111) monochromator, Cu-Kα radiation, λ = 0.154 056 Å). The diffractogram was recorded within $2\Theta = 5 - 90^\circ$ at step size of 0.5 ° (scanning rate: 0.86 °min^{-1}). For analysis, the catalyst material was sealed in glass capillaries with an inner diameter of 0.5 mm. Selected activated catalysts were removed from the setup for CO_2-TPD measurements under inert conditions and separated from silica wool in a glovebox prior to analysis. Also here, noisy data was smoothed for presentation.

7.3.5 FT-IR measurements

FT-IR spectra at atmospheric pressure were recorded with a BioRad® FTS 575 C equipped with a high temperature chamber with ZnSe windows. For analysis, selected catalyst samples (150 – 250 µm) were reduced in the setup for CO_2-TPD measurements under the same conditions as mentioned above. After reduction, the catalyst material was removed from the setup and transferred into a glovebox under inert conditions where it was separated from silica wool. The pure catalyst material was pressed into a self-supporting wafer, which was mounted into the spectrometer without being exposed to air. PC10, PC01, PC12 and γ-Al_2O_3 were not reduced prior to IR measurements but directly pressed into wafers. The wafer and chamber were conditioned by heating to 523 K in He (60 Nml min^{-1}) at a rate of 5 K min^{-1}. Then, the wafer was cooled down to 313 K and background spectra were recorded. Subsequently, CO_2 was adsorbed for 30 min at 313 K using 6 % CO_2 in He with a flow rate of 40 Nml min^{-1}. After adsorption, the wafer was purged and TPD up to 523 K was conducted in flowing He (Q_{He} = 60 Nml min^{-1}) at a constant heating rate of 5 K min^{-1}. Spectra were recorded within the range from 900 to 4000 cm^{-1} at a resolution of 4 cm^{-1}.
Alternatively, FT-IR measurements were conducted with a Vertex 70 from Bruker®, equipped with a high temperature chamber with CaF_2 windows. For the measurements, 50 to 100 mg of calcined catalyst material (150 – 250 µm) were pressed into a self-supporting wafer and

reduced under the same conditions as for CO_2-TPD. After reduction, the sample was degassed at reduction temperature for 60 min and cooled down to 303 K under He. Subsequently, a background spectrum was collected. Then, CO_2 was adsorbed either in a continuous flow using 6 % CO_2 in He at a flow rate of 100 Nml min^{-1} or under static conditions at a reduced pressure of 2.2 mbar. For the latter, the reduced wafer was evacuated and kept at $1 \cdot 10^{-5}$mbar for 2 h after reduction. After cooling to 303 K, 6 % CO_2 in He was dosed into the chamber until a constant pressure of 2.2 mbar was achieved. Subsequently, the wafer was evacuated again to $1 \cdot 10^{-5}$mbar. Also here, measurements were conducted during adsorption and evacuation. Spectra were recorded within the range of 1100 to 4000 cm^{-1} at a resolution of 4 cm^{-1}. Noisy data was also smoothed for presentation in this case.

7.3.6 Static CO_2 chemisorption

Static CO_2 chemisorption measurements were conducted in a Quantachrome® Autosorb 1C. 100 mg of calcined catalyst material were placed in the sample cell and reduced at 753 K in 5 % H_2 in N_2 for 5 h (β = 3 K min^{-1}). After reduction, the catalyst was evacuated at 753 K for 60 min and subsequently cooled down to room temperature under vacuum. CO_2 was fed at 308 K and an adsorption isotherm was recorded with an equilibration time of 10 min. The total amount of CO_2 adsorbed and the reversible CO_2 uptake was obtained by extrapolating the corresponding adsorption isotherm to zero pressure. The amount of strongly adsorbed CO_2 was obtained by subtracting the reversible from the total CO_2 uptake. An increase of the equilibrium time has shown to have no influence on the CO_2 uptake. The purity was 5.0 for all gases used.

7.4 Results and discussion

7.4.1 Elemental analysis and catalyst characterization

Results from elemental analysis and metallic Ni surface area determination are summarized in Table 7.1 and 4.1. XRD analysis, which is discussed in greater detail in chapter 4.3.1, reveals a takovite-like structure in PC51 and PC31 after precipitation and mixed basic carbonates in Ni-containing precursors. Calcination of these precursors leads to the formation of a crystalline bunsenite and a Ni-Al mixed oxide phase. The structure of these phases depends on the Ni content in the sample. Impregnated samples exhibit a crystalline bunsenite and a γ-Al_2O_3 phase after calcination independent of the Ni loading. $NiAl_2O_4$ is the only crystalline phase in sample PC12 and NiO is observed in sample PC10. These samples, therefore, can be referred to as

$NiAl_2O_4$ and NiO reference, respectively. Results obtained from N_2 physisorption and TPR measurements are discussed in chapter 4.3.1 and 4.3.2, respectively.

Table 7.1: Characterization results (partly taken from [161]).

	PC01	PC15	PC13	PC11	PC31	PC51	PC10	IC9	IC17	γ-Al_2O_3
S_{Ni} ($m^2\,g_{cat}^{-1}$)	-	3.6	9.4	17.1/19.2[e]	32.9	30.1	1.4	3.8	9.2	-
$U(CO_2)^{a}_{total}$ ($\mu mol\,g_{cat}^{-1}$)	382.6	350.2	283.9	238.7	194.0	178.0	n. d.	269.8	248.3	257.5
$U(CO_2)^{b}_{irrev.}$ ($\mu mol\,g_{cat}^{-1}$)	230.0	194.6	142.2	142.8	157.8	160.2	n. d.	167.4	160.2	172.8
$U(CO_2)^{c}_{pulse}$ ($\mu mol\,g_{cat}^{-1}$)	85.4	88.8	74.2	116.8	124.4	124.2	< 2	83.8	89.8	49.0
CO_2 desorption[d] ($\mu mol\,g_{cat}^{-1}$)	50.2	51.5	38.6	61.2	70.8	67.1	n. d.	45.1	48.5	33.9

[a] total CO_2 uptake determined from static chemisorption
[b] irreversible CO_2 uptake determined from static chemisorption
[c] determined from pulsed adsorption with a total of 40 pulses
[d] determined from TPD subsequent to pulsed adsorption
[e] reproduction measurement

7.4.2 FT-IR measurements upon CO_2 adsorption under flow

Results from FT-IR measurements upon CO_2 adsorption under flow at room temperature, followed by He purging and TPD are depicted in Figure 7.1 and Table 7.2. Also the spectra of CO_2 adsorption on NiO (PC10) and $NiAl_2O_4$ (PC12) are presented for reference purposes in Figure 7.2. Multiple adsorption bands between 900 and 1800 cm^{-1} are observed, which are typical of carbonate-like species. For γ-Al_2O_3 (Figure 7.1A-C), the absorbance bands at 1647 and 1435 cm^{-1} can be ascribed to the asymmetric and symmetric O-C-O stretching mode of bicarbonate, respectively. The corresponding δ(OH) band is observed at 1229 cm^{-1}. Bicarbonates are formed due to the interaction of CO_2 with Al^{IV} and/or Al^{IV}-OH sites of weak basicity [242, 257, 263]. These bands are formed fast within the first minutes of adsorption and only slightly gain intensity with increasing adsorption time. These observations are in good agreement with results of Wang et al. [242]. The signal centered at 1389 cm^{-1} can be attributed to the symmetric O-C-O stretching mode of monodentate carbonate. The corresponding band of the asymmetric O-C-O stretching mode is observed as a shoulder at 1535 cm^{-1}. The shoulder between 1312 and 1352 cm^{-1} originates from the symmetric O-C-O stretching mode of bidentate carbonate. The signal of the corresponding symmetric O-C-O stretching mode is strongly overlapped by the signal at 1647 cm^{-1} but can be discerned at 1628 cm^{-1} upon purging with He (Figure 7.1B).

Moreover, a broad feature between 1000 and 1200 cm^{-1} is observed. Purging with He after CO_2 adsorption reduces the intensity of signals at wavenumbers higher than 1200 cm^{-1}. The intensity decrease is most pronounced for bicarbonate indicating that those species are weakly bound to the surface, which is in good agreement with literature [242]. The signal intensity of the broad pattern between 1000 and 1200 cm^{-1} remains unchanged upon He purging, implying that those bands represent strongly bound species, which have been described as bridged/"organic"-like carbonate in literature [242, 255]. Upon TPD, bands attributed to bicarbonate are the first to disappear at temperatures higher than 393 K (Figure 7.1C). This, again, reflects the weak basic character of adsorption sites forming bicarbonate. Bidentate and monodentate carbonate bands vanish at temperatures higher than 433 K, whereas bridged/"organic"-like species are observed until 514 K. Consequently, bi- and monodentate carbonate are formed on basic sites of medium strength and bridged/"organic"-like species arise from CO_2 adsorption on strong basic sites.

The shape of the spectrum obtained after CO_2 adsorption on PC10 (Figure 7.2) agrees well with the one of γ-Al_2O_3, indicating the formation of carbonates. However, the bands are shifted to lower wavenumbers and a clearly discerned band at 1016 cm^{-1} is observed. In literature, the absorbance band at 1215 cm^{-1} is ascribed to bicarbonate [255]. The absorbance bands centered around 1626 and 1385 cm^{-1} exhibit the same behavior, which strongly indicates that these bands can be attributed to bicarbonate as well. Interestingly, these absorbance bands are established fast within the first minute of adsorption but decrease in intensity with increasing adsorption time, which implies restructuring and rearrangement of the adsorbed carbonate species. An additional signal at 1261 cm^{-1} is observed. Ueno at al. ascribed this signal, which was observed at 1276 cm^{-1} in their study, to Ni carboxylate [264]. A corresponding band observed at 1545 cm^{-1} in literature might not be discerned here due to a strong overlap with the broad signal at 1626 cm^{-1}.

The signal positions between 1200 and 1800 cm^{-1} upon CO_2 adsorption on $NiAl_2O_4$ (PC12) (Figure 7.2) coincide with the band positions in the case of γ-Al_2O_3, indicating that essentially the same bicarbonate, monodentate carbonate, and bidentate carbonate species are observed. No additional signals pointing at Ni carboxylate formation are detected. In comparison with γ-Al_2O_3, an additional absorbance band at 1018 cm^{-1} is obtained which coincides with the signal at 1016 cm^{-1} in NiO (PC10). Also here, the absorbance bands at wavenumbers below 1200 cm^{-1} are stable upon He purging and are the last to disappear at temperatures higher than 473 K (Figure 7.10). This indicates that those bands arise form strongly bound species such as bridged/"organic"-like species.

The spectra obtained after CO_2 adsorption on PC01 (Figure 7.1D-F) reveal essentially the same species as for γ-Al_2O_3. However, the fraction of bidentate carbonate (in this case with an absorbance band between 1318 and 1367 cm^{-1}) is increased, whereas the amount of strongly bound CO_2 exhibiting bands below 1200 cm^{-1} is decreased.

CO_2 adsorption on IC17 (Figure 7.1G-I) leads to the same pattern as for pure γ-Al_2O_3. The intensity of bands originating from monodentate carbonate increases in comparison to the signal intensity of bicarbonate. The absorbance band of the symmetric O-C-O stretching mode

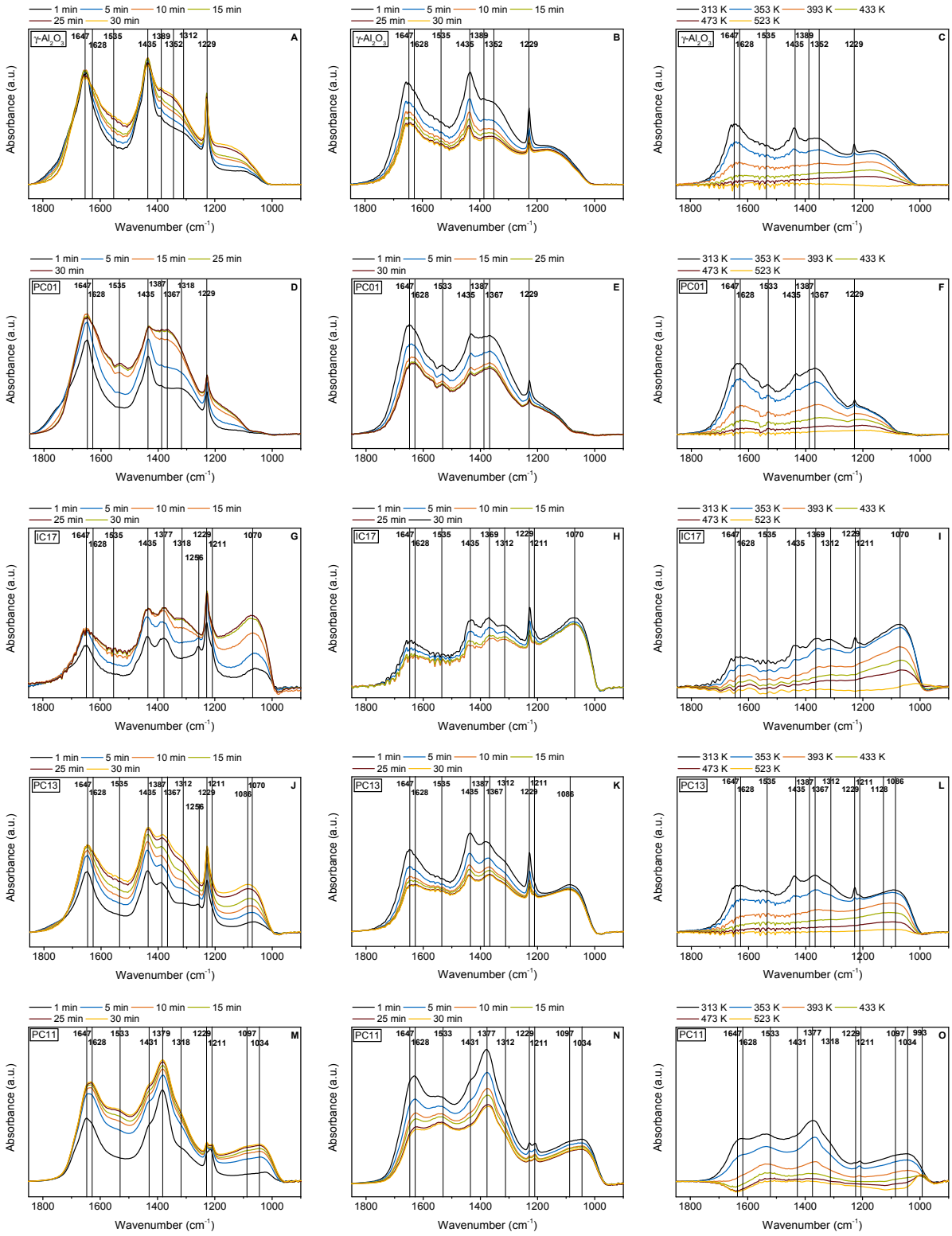

Figure 7.1: Results from FT-IR measurements during CO_2 adsorption at 1 bar and 313 K (left column), He purging after adsorption (middle column) and TPD (right column).

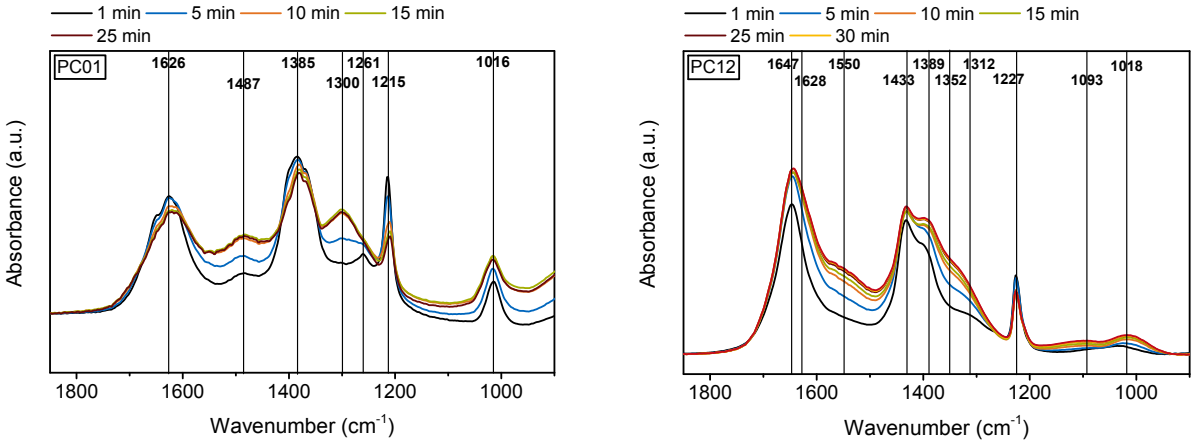

Figure 7.2: Results from FT-IR measurements during CO_2 adsorption under flow at 1 bar and 313 K on NiO (PC10) and $NiAl_2O_4$ (PC12).

of monodentate carbonate is slightly shifted to a lower wavenumber of 1377 cm^{-1}. However, already intensity changes of strongly overlapping signals can lead to apparent shifts in the signal position. Additionally, a distinct absorbance band is observed at 1070 cm^{-1}, which most likely originates from CO_2 adsorbed on strong basic sites, e.g. in a bridged mode, as is does not decrease upon He purging (Figure 7.1H) and is stable up to a temperature of 473 K (Figure 7.1I). In the pattern obtained after CO_2 adsorption for 1 and 5 min, an additional signal at 1256 cm^{-1} is observed together with a weak shoulder at 1211 cm^{-1}. A comparison with the spectra obtained for pure NiO (Figure 7.2) reveals that these bands might originate from carboxylate species and bicarbonate due to CO_2 interaction with NiO-like structures. TPR measurements revealed that IC17 is not completely reduced under the chosen reduction conditions (see chapter 4.3.2). Therefore, NiO-like structures might still be present in the sample, leading to the observed bands. The pattern obtained after CO_2 adsorption on PC13 (Figure 7.1J-L), the sample which reveals a similar Ni content as sample IC17, coincides with the corresponding spectra of the impregnated sample. Moreover, the band positions in the range between 1200 and 1800 cm^{-1} do not change with increasing Ni content of the precipitated mixed oxide samples. This indicates that neither the synthesis procedure nor the Ni loading of the Ni-Al systems in this study influence the vibration mode of surface species adsorbed on weak and medium basic sites. With increasing Ni loading of precipitated systems, the density of medium and strong basic sites increases as compared to weak basic sites, which form bicarbonate. In all precipitated samples investigated, the shoulder at 1211 cm^{-1} is present. The band centered at 1258 cm^{-1}, which is observed in sample IC17 and PC13, is not discerned in sample PC11 (Figure 7.1M-O), which might be due to a strong overlap by bands at higher wavenumbers. Also the reducibility increases with higher Ni loading and consequently, the amount of NiO-like structures that form species, which exhibit bands at these wavenumbers, declines. In sample PC11, two distinct bands at 1097 and 1034 cm^{-1} are observed, whereas one broad band centered between 1070 and 1086 cm^{-1} is observed on samples of lower Ni loading. This might indicate, that two different strongly adsorbed species are formed on the catalyst PC11. In all samples, bands attributed

to bicarbonate significantly decrease upon purging with He. Upon TPD, they are also the first to vanish at temperatures higher than 393 K, followed by bidentate carbonate, monodentate carbonate and strongly bound species, the latter of which exhibit bands at wavenumbers below 1200 cm^{-1}. In the case of PC11, a negative band between 1550 and 1700 cm^{-1} is observed, which could be attributed to structural changes of the catalyst surface, altering the IR absorption behavior of the wafer. As absorption of the wafer contributes to the background spectra, which are subtracted from each measurement, changes of the wafer absorption behavior become manifest in the corrected spectra. In this context, one might take elimination of surface hydroxyl groups into consideration [257]. Next to a negative band, a new absorbance band is detected at 993 cm^{-1}, which is stable even at temperatures up to 523 K. This again, could be attributed to changes of the catalyst surface properties or to restructuring and transformation of the adsorbed species. Carbonate transformation was observed in literature upon CO_2 adsorption and desorption from hydrotalcite-like materials [259]. Further studies are needed to clarify the observed pheno-mena.

7.4.3 FT-IR measurements upon CO_2 adsorption under static conditions

Results from static CO_2 adsorption on sample PC11 under static conditions at room temperature and 2.2 mbar leads to additional signals between 1700 and 2100 cm^{-1} next to absorption bands in the carbonate region (Figure 7.3 and Table 7.3). Those bands can be attributed to Ni-CO species formed upon dissociative adsorption of CO_2 on metallic Ni. The absorption bands at 2006 and 1894 cm^{-1} can be ascribed to linearly bound and bridged CO, respectively [67, 262, 265–268], while the band at 1807 cm^{-1} most likely originates from CO bound to three Ni atoms [268]. The shoulder between 1800 and 1700 cm^{-1} might be attributed to an overlap with bands at lower wavenumber. Upon evacuation to $1 \cdot 10^{-5}$mbar (Figure 7.3B), no significant decrease of the band intensity is observed for Ni-CO species whereas carbonate absorption bands loose intensity. In contrast to this, no bands related to Ni-CO species are detected upon adsorption under flow conditions, which is in agreement with studies of Abello et al. [81] and Pan et al. [20]. However, dissociation, which is thermodynamically favored as compared to chemisorption on Ni [269], is observed in literature when adsorbing CO_2 on Ni-Al catalysts at elevated temperatures [67, 262, 268]. It is possible that dissociative CO_2 adsorption is kinetically hindered at room temperature so that very low residence times, which are typically obtained under flow conditions, do not allow for the formation of Ni-CO species. Activated CO_2 dissociation also has been observed on some clean Ni surfaces and reported in literature [270]. At this point, we would like to mention again, that IR measurements under static conditions were conducted with a different setup as compared to measurements, the results of which are depicted in Figure 7.1. In order to exclude systematic errors, we also conducted flow experiments in the

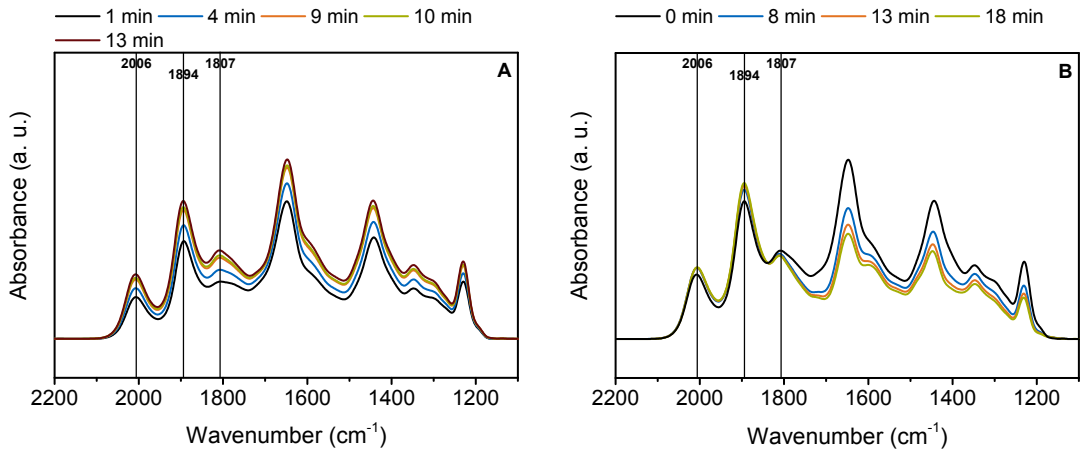

Figure 7.3: Results from FT-IR measurements with sample PC11. (A) CO_2 adsorption at 2.2 mbar under static conditions and (B) subsequent evacuation to $1 \cdot 10^{-5}$mbar.

second setup. Also here, no Ni-CO bands were observed, which further confirms that Ni-CO bands are formed upon static CO_2 adsorption at room temperature. No bands related to $Ni(CO)_4$ were observed in our experiments.

Table 7.2: Comparison of observed absorption bands (cm^{-1}) in the carbonate region with literature.

	Bicarbonates			Bidentates		Monodentates		Bridged/"organic"-like		Carboxylate	
	ν_{as} (OCO)	ν_s (OCO)	δ (OH)	ν_{as} (OCO)	ν_s (OCO)	ν_{as} (OCO)	ν_s (OCO)				
$\gamma-Al_2O_3$	1647	1435	1229	1628	1352-1312	1535	1389	1200-1000			
PC01	1647	1435	1229	1628	1367-1318	1535	1387	1200-1100			
PC13	1647	1435	1229-1211	1628	1312	1535	1387-1367	1128-1070			1256
PC12 ($NiAl_2O_4$)	1647	1433	1227	1628	1330-1312	1535	1387	1093-1018			
PC11	1647	1431	1229-1211	1628	1318-1312	1535	1377-1379	1097-1034			
IC17	1647	1431	1229-1211	1628	1318-1312	1535	1377-1369	1070			1256
PC10 (NiO)	1626	1385	1215								1261
$\gamma-Al_2O_3$ [242]	1645	1445-1435	1230	1675-1670	1350	1550	1392-1385	1310-1304	1000		
$\gamma-Al_2O_3$ [255]	1650-1639	1490-1440	1236-1225	1730-1660	1270-1230	1530	1370	1900-1750	1180		
Al_2O_3 [256, 257]	1650	1480-1440	1230-1220	1630-1610	1340-1320	1560-1510	1400-1360	1900-1700	1200-1100		
Al_2O_3 [260]	1647	1476	1233	1704	1265			1756	1204		
$Ni/\gamma-Al_2O_3$ [20]	1653	1434	1227			1566	1361				
Ni/Al_2O_3 [67]	1653	1534	1230								
NiO [255]			1215	1670-1620		1640	1390	1730	1160	1560-1545	1410-1276
HTlc[a] [260]	1658-1650	1420-1400				1591-1574	1386-1365				
HTlc[a] [259]				1600	1347	1510	1385	1700	1310		

[a]HTlc: hydrotalcite

Table 7.3: Comparison of observed absorption bands (cm^{-1}) of Ni-CO species with literature.

	Linear bonded CO	Bridged bonded CO	Threefold bonded CO
PC11	2006	1894	1807
Ni/Al_2O_3 [265]	2053	1927	
Ni/Al_2O_3 [266]	2015	1910-1830	
Ni/Al_2O_3 [67]	2021	1851	
Ni/Al_2O_3 [268]	2058	1930	1887
Ni-Al oxide [262]	2014	1844	

7.4.4 Temperature programmed desorption of CO_2

TPD results for catalyst PC11 after CO_2 adsorption at 308 K for 30 min are depicted in Figure 7.4. CO_2 desorption from weak basic sites exhibits a desorption signal at 364 K, whereas desorption from medium basic sites results in signals centered around 416 and 500 K. In addition, a broad feature between 550 and 750 K is observed, originating from CO_2 desorbing from strong basic sites. A comparison of the patterns in Figure 7.4 with the FT-IR results in Figure 7.1

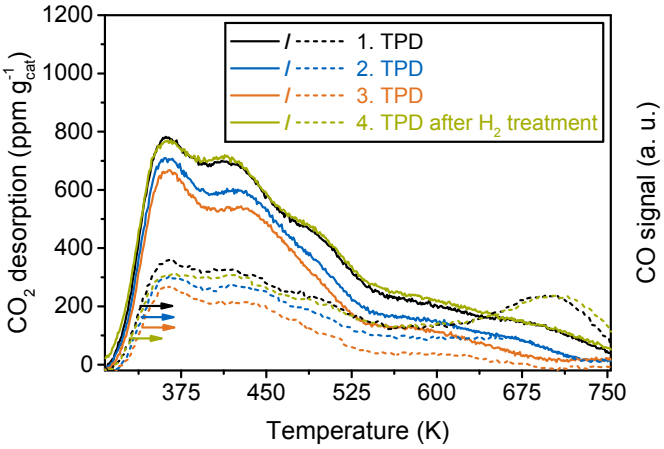

Figure 7.4: Reproduction of TPD measurements subsequent to CO_2 adsorption on reduced PC11 at 308 K for 30 min. The first three TPD measurements were recorded sequentially. The fourth measurement was conducted after treatment in 5 % H_2 in He at 753 K for 30 min ($\beta = 3\,\mathrm{K\,min^{-1}}$).

allows for the assignment of the desorption signals to different species. The desorption signal at 364 K can be attributed to bicarbonate desorbing from weak basic sites. The signal at 416 K originates from bidentate carbonate. The desorption peaks at 500 K and between 550 and 750 K can be ascribed to monodentate carbonate and bridged/"organic"-like species, respectively. The assignment is in very good agreement with results of Wang et al. [242]. At temperatures higher than 550 K next to CO_2 also substantial amounts of CO are detected (a quantitative analysis is presented below). FT-IR results show that no Ni-CO species are formed during adsorption under flow conditions at 303 K. Therefore, it is likely that CO is detected due to dissociation of desorbing CO_2 at elevated temperatures with oxygen staying on the Ni surface. This is further supported by CO formation upon pulsing of CO_2 onto a reduced PC11 sample at 700 K (Figure 7.11). Besides, the Ni surface area does not change upon CO_2 exposure at 308 K which is shown by a value of 19.2 $m^2\,g_{cat}^{-1}$ before and 19.9 $m^2\,g_{cat}^{-1}$ after CO_2 adsorption. This additionally proves that, under the chosen conditions, CO_2 dissociates on metallic Ni at elevated temperatures but not close to room temperature. When reproducing TPD measurements on the same sample, a decrease of CO_2 desorption is observed, indicating a reduction of basic sites. This is in line with results from FT-IR measurements, which also indicated structural changes of the catalyst surface. No structural changes of the catalyst bulk material are observed upon CO_2-TPD as revealed by XRD analysis (Figure 7.12). The amount of CO also declines from one TPD experiment to the other. It is likely, that oxygen on the Ni surface, formed during the

first TPD run, impedes dissociative CO_2 adsorption in the subsequent runs. Upon H_2 treatment at 753 K for 30 min (5 % H_2 in He, $\beta = 3\,\mathrm{K\,min^{-1}}$), the original state of the catalyst surface is restored. Also the detected amount of CO increases again and reaches its original level.

Figure 7.5 depicts the influence of adsorption time and temperature on adsorption. Increasing the adsorption time at 308 K slightly enhances adsorption on weak basic sites forming bicarbonate. The amount of monodentate carbonate and the density of strong basic sites is reduced, in compliance with results depicted in Figure 7.4, since curve (a) and curve (b) were recorded successively. Adsorption at 373 K (curve (c) and (d)) increases desorption from weak and medium basic sites, indicating that adsorption on Ni-Al catalysts is an activated process. An increase of adsorption time at 373 K slightly further improves adsorption on medium basic sites (not indicated in Figure 7.5). Species on medium basic sites are flushed from the catalyst surface at 373 K, which explains the lower signal intensity of curve (d) as compared to curve (c). CO_2 adsorption in a three step process including adsorption at 308 as well as 218 K leads to an intensity increase of the signals attributed to weak and medium basic sites (curve (e)). The onset of an additional desorption signal is observed around 260 K. The signal attributed to bicarbonate is shifted to lower temperatures by approximately 10 K and becomes more symmetrical. This indicates that weak basic sites are only partially occupied at 308 K and that part of the adsorbed CO_2 is removed when flushing prior to TPD. This is in line with FT-IR results depicted in Figure 7.1.

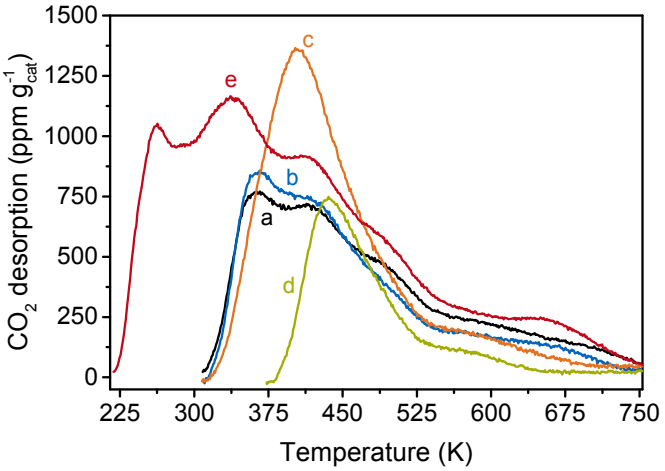

Figure 7.5: Influence of adsorption time and temperature on CO_2 interaction with reduced PC11. CO_2 was adsorbed at (a) 308 K for 30 min, (b) 308 K for 90 min, (c) 373 K for 30 min followed by cooling to 308 K in CO_2, (d) 373 K for 30 min and (e) 308 K for 30 min followed by cooling down to 218 K and adsorption at 218 K for another 30 min.

The influence of the Ni loading and the synthesis procedure on CO_2 desorption is depicted in Figure 7.6. Sample PC01 exhibits a board desorption signal between 225 and 375 K, indicating a high density of weak basic sites, as well as a broad shoulder at higher temperatures. In comparison, the density of weak basic sites in the Ni-containing sample PC15 is decreased. It further declines with increasing Ni loading of the precipitated samples, whereas the amount of bidentate and monodentate carbonate as well as strongly adsorbed species rises. No significant

differences in basicity are observed between PC31 and PC51. However, clear distinguishable signals related to bidentate, monodentate and strongly bound species cannot be detected for sample PC15 and PC13. This might be attributed to the strong desorption signal originating from bicarbonate overlapping smaller peaks as evident by the shoulder at higher temperatures. No signal shifts are observed, which means that the same kind of adsorbed CO_2 species are observed in each catalyst. These observations are also in line with FT-IR results depicted in Figure 7.1. When varying the Ni loading of impregnated systems, no significant change of the CO_2 adsorption behavior is observed. The obtained TPD patterns coincide with the one of γ-Al_2O_3 with a slightly increased CO_2 desorption from medium and strong basic sites. However, also here, the strong desorption signal attributed to bicarbonate might superimpose less intense peaks at higher temperatures. Comparing the pattern of sample PC01 and γ-Al_2O_3 reveals that the density of weak basic sites is significantly higher in sample PC01.

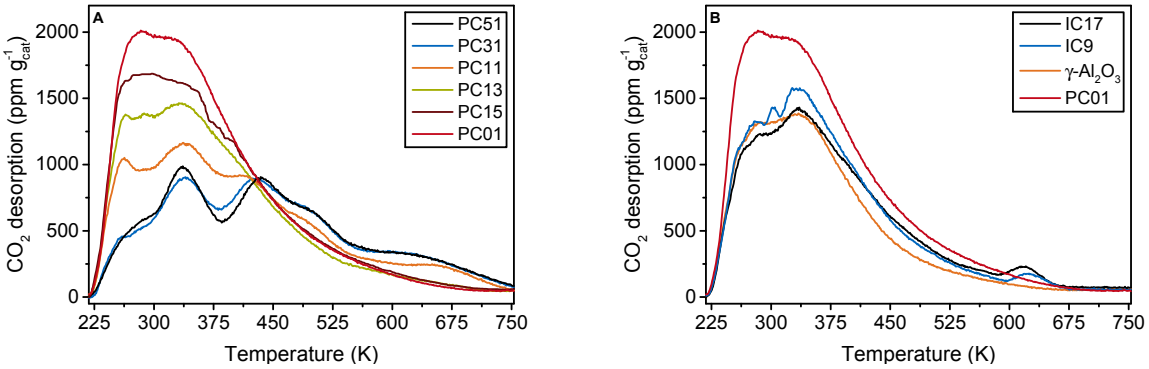

Figure 7.6: Influence of the Ni loading and synthesis procedure on basicity and CO_2 adsorption of activated samples. CO_2 was adsorbed in a three step process comprising adsorption at 308 K for 30 min, subsequent cooling to 218 K under CO_2 and adsorption at 218 K for another 30 min.

Results from TPD after pulsed CO_2 adsorption are depicted in Figure 7.7. Adsorption of limited CO_2 amounts by varying the number of pulses reveals that strong adsorption sites are occupied first and subsequently weaker sites are filled. Once CO_2 pulses break through and reach a constant intensity, the subsequent TPD pattern remains constant (pulsed adsorption prior to curve (d) and (e) in Figure 7.7A). The signal intensity declines from curve (a) to (e), which again might originate from structural changes of the catalyst surface upon TPD, as mentioned earlier, since the measurements were conducted sequentially on the same catalyst sample. This also explains the higher intensity of the desorption signals after pulsed adsorption on a fresh catalyst sample (Figure 7.7B). The desorption signal intensity after adsorption of 40 pulses at a dosing temperature of 308 K is significantly lower as compared to the TPD pattern obtained after CO_2 adsorption at 308 K using a continuous gas stream (Figure 7.7B).

The TPD pattern obtained after pulsed adsorption in Figure 7.8 reveals that mostly weak basic sites are present on calcined PC11. Upon reduction, medium and strong basic sites are formed, while the weak basic site density is reduced. It is well known, that structural changes take place during the reduction of precipitated catalysts [79–81, 88, 112], which very likely changes

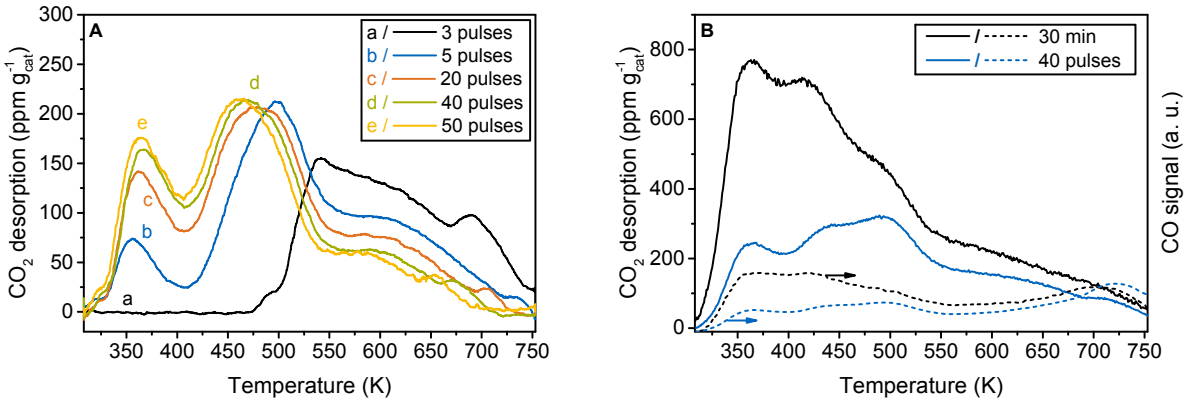

Figure 7.7: (A) Influence of limited CO_2 amounts on adsorption and (B) comparison of TPD results after pulsed adsorption and adsorption under CO_2 flow. The experiments were conducted with reduced sample PC11 at a dosing temperature of 308 K.

the basicity. Next to structural changes, surface hydroxyl groups, which are essential for the formation of bicarbonate, are eliminated during reduction [135], decreasing the density of weak basic sites. These results also point out the importance of characterizing catalyst materials in their active state. Results of TPD measurements subsequent to CO_2 adsorption on γ-Al_2O_3 before and after reduction are depicted in Figure 7.13. Heating in H_2 leads to a significant reduction of weak basic sites, most likely due to elimination of surface hydroxyl groups as indicated by TPR results (chapter 4.3.2). No significant changes are observed with regard to the density of medium and strong basic sites.

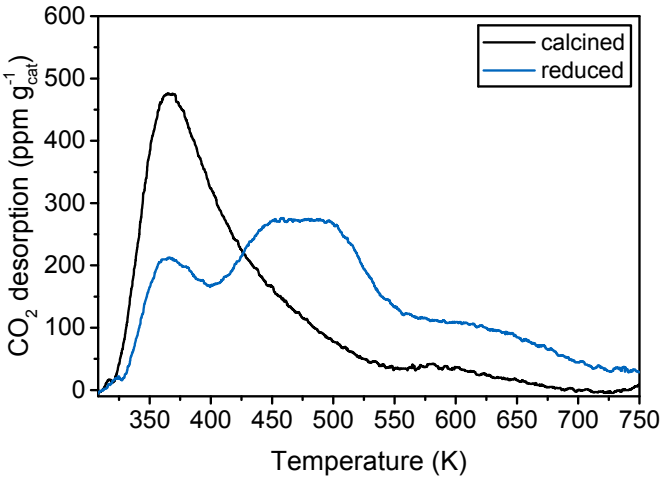

Figure 7.8: TPD results after adsorption of 40 CO_2 pulses at 308 K on calcined and reduced PC11. The measurements were conducted sequentially on the same sample.

A quantitative analysis of the pulsed experiments in Figure 7.7 reveals that only 40 to 55 % of the CO_2 adsorbed on the reduced catalyst sample desorb during TPD (Table 7.4). As evident from FT-IR measurements, part of the CO_2 adsorbed is flushed from the catalyst surface during purging prior to TPD. Moreover, the maximum temperature of 753 K might not be high enough to completely desorb strongly adsorbed CO_2 species, which is shown by TPD coupled with FT-IR measurements in Figure 7.1O. Furthermore, a part of the CO_2 desorbing is converted to CO

at temperatures higher than 550 K, as mentioned earlier and shown in Figure 7.4 and 7.7B. This further explains the observed discrepancy between adsorbed and desorbed CO_2. Correcting the CO signal in Figure 7.7B for CO_2 fragmentation allowed for the quantification of the detected CO. A total CO amount of 12.0 µmol g_{cat}^{-1} is released, which is 11.4 % of the CO_2 retained by the catalyst upon pulsing.

Table 7.4: Comparison of adsorbed and desorbed amounts of CO_2 during pulsed adsorption and subsequent TPD for PC11. Corresponding TPD pattern are depicted in Figure 7.7.

Pulses	3[a]	5	20	40	50	40[a]
$U(CO_2)^{b}_{pulse}$ (µmol g_{cat}^{-1})	46.4	n. d.	61.7	58.3	53.1	105.4
CO_2 desorption[c] (µmol g_{cat}^{-1})	19.4	25.6	27.8	30.4	27.5	58.2
Fraction of CO_2 desorbed (%)	41.9	n. d.	45.0	52.1	51.8	55.2

[a] experiment conducted with a fresh catalyst sample
[b] determined from pulsed adsorption
[c] determined from TPD subsequent to pulsed adsorption

Results from static CO_2 chemisorption and a comparison with pulsed CO_2 adsorption and TPD are summarized in Table 7.1. In the case of γ-Al_2O_3, the adsorbed CO_2 amount upon pulsing is only 28 % of the irreversible CO_2 uptake calculated from static measurements. As indicated in Figure 7.6 γ-Al_2O_3 mostly exhibits weak basic sites, which are only partially occupied at low CO_2 partial pressures and residence times typically present in pulsed experiments. Static conditions, in contrast, allow for more sites to be filled, which explains the higher value obtained. The same discrepancy is observed for PC01 where 22 % of the irreversible CO_2 uptake determined from static chemisorption are adsorbed upon CO_2 pulsing. Also for Ni-containing samples, deviations between static and pulsed experiments are observed. However, the deviations decrease with increasing Ni loading. This is in line with the density increase of medium and strong basic sites at higher Ni content (Figure 7.6), on which the adsorption is less strongly influenced by the CO_2 partial pressure. Also the formation of Ni-CO species under static conditions (Figure 7.3) has to be taken into consideration as an additional reason for the observed deviations. As mentioned earlier, dissociative CO_2 adsorption on metallic Ni is likely to be kinetically hindered close to room temperature. Low residence times, typically obtained in pulsed experiments, therefore, impede dissociation. In contrast, long equilibration times in static chemisorption measurements allow for Ni-CO formation.

The total CO_2 adsorption capacity of Ni-containing samples, determined from static chemisorption, decreases with increasing Ni content. Contrary to this, the irreversible CO_2 uptake and the amount of adsorbed CO_2 determined from pulsed experiments and TPD initially decreases for precipitated samples with rising Ni content and reaches a minimum at a Ni loading between 22.5 and 38.1 wt-%. At higher loadings, the adsorbed amount of CO_2 rises again. The contradictory trend of total and reversible CO_2 uptake is in agreement with the increasing density of weak basic sites with rising Al content. The initial decrease from sample PC15 to PC13, which exhibit similar densities of medium basic sites, could be attributed to the significantly higher weak basic

site density of sample PC15 (Figure 7.6A). More CO_2 can be adsorbed on those sites even upon evacuation in the case of PC15. The irreversible CO_2 uptake slightly decreases with increasing Ni loading for the impregnated samples. Pulsing of CO_2 onto unsupported metallic Ni (reduced PC10) revealed an insignificant CO_2 uptake. This again supports that CO_2 does not dissociate on metallic Ni at room temperature under transient conditions.

7.4.5 Catalyst performance in CO_2 methanation

Recently, we investigated the catalytic performance as well as the deactivation behavior of catalyst PC31, PC11, PC13 and IC17 in CO_2 methanation in great detail [112]. The activity per Ni surface area (specific activity) was shown to vary for the samples investigated, as indicated in Figure 7.9. This suggests structure sensitivity as well as additional factors which influence the activity. In this context, the CO_2 adsorption capacity and the basicity of the catalyst material was reported to be important [19–21]. As shown in Figure 7.6 and as discussed in our previous study [112], the density of medium basic sites forming monodentate formate rises with increasing Ni loading of precipitated samples. Pan et al. [20] proposed that medium basic sites forming monodentate formate species promote CO_2 methanation as monodentate formate is hydrogenated faster than other formate species. This is in line with a higher specific activity of sample PC31 as compared to samples of a lower Ni content. Moreover, the results nicely demonstrate the strength of CO_2-TPD measurements in evaluating and elucidating structure-activity relations.

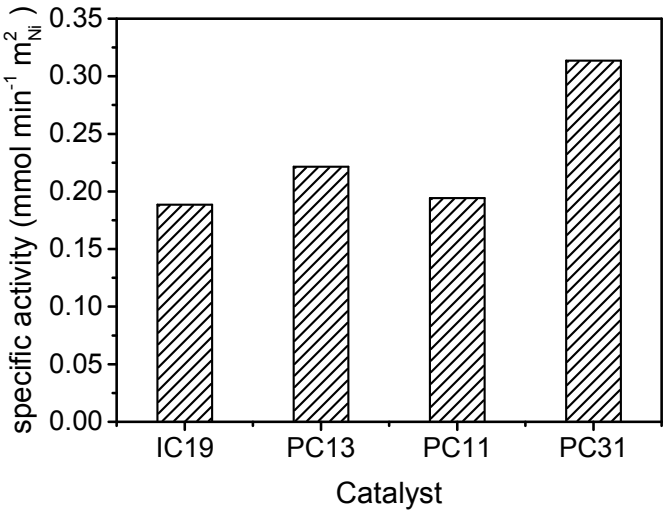

Figure 7.9: Specific activity of freshly activated samples in CO_2 methanation (m_{cat} = 50 mg, T = 523 K, p = 8 bar, Feed: $H_2/CO_2/Ar/N_2$ = 8/2/9/1, Q_{Feed} = 500 Nml min^{-1}, data taken from [112]).

7.5 Conclusion

Adsorption modes and the interaction of CO_2 with co-precipitated and impregnated Ni-Al catalysts were elucidated using FT-IR spectroscopy, CO_2-TPD as well as pulsed and static CO_2 chemisorption. Adsorption close to room temperature under flow conditions leads to the formation of four different species on the surface, namely bicarbonates (adsorbed on weak basic sites), bidentate carbonates, monodentate carbonates (adsorbed on medium basic sites) and bridged/"organic"-like species (adsorbed on strong basic sites). The density of medium and strong basic sites increases with increasing Ni loading, whereas the amount of bicarbonate decreases. Bicarbonate is the most abundant species on impregnated samples and γ-Al_2O_3. In the subsequent TPD run, bidentate, monodentate and bridged/"organic"-like species exhibit a desorption signal at 416 and 500 K as well as a broad desorption pattern between 550 and 750 K, respectively. An additional CO signal at temperatures higher than 550 K originates from dissociation of desorbing CO_2. Close to room temperature, dissociative CO_2 adsorption on Ni is not observed under flow conditions, but is observed under static conditions forming Ni-CO species. Variation of the adsorption time and temperature implies that CO_2 adsorption on Ni-Al-catalysts is an activated process. Adsorption of CO_2 at temperatures as low as 218 K leads to a more complete adsorption on weak basic sites, forming bicarbonate with a corresponding desorption signal at 325 K and an additional desorption signal at 260 K. Pulsed CO_2 adsorption reveals that strong adsorption sites are filled first. The amount of adsorbed CO_2 is significantly lower than under flow or static conditions, which demonstrates that the experimental design has a strong influence on the CO_2 interaction and adsorption modes on Ni-Al catalysts. The results provide the necessary knowledge to concisely characterize the CO_2 interaction with Ni-Al catalyst by means of CO_2-TPD. The strength of this technique in elucidating structure-activity relations of Ni-Al catalysts in CO_2 methanation was shown.

7.6 Supporting Information

7.6.1 FT-IR measurements

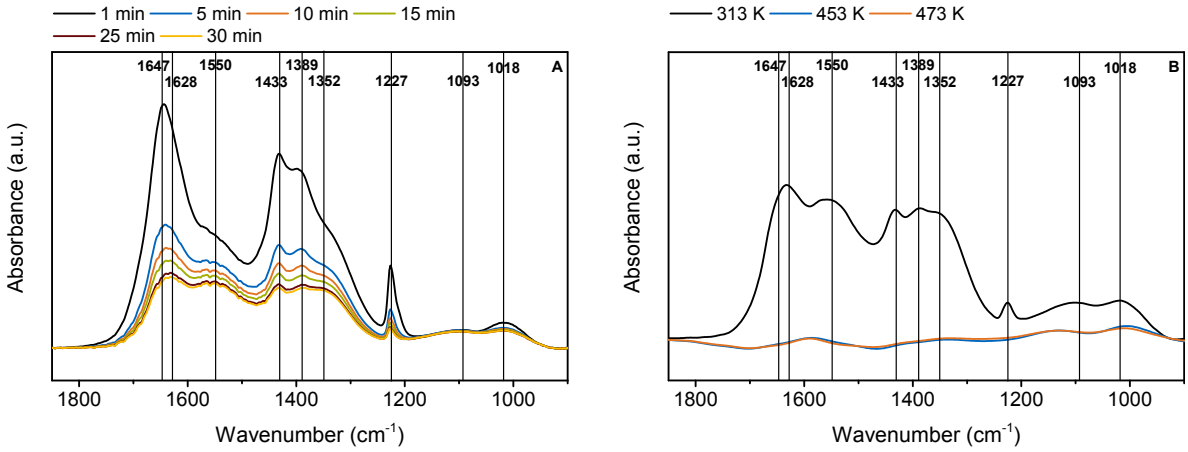

Figure 7.10: Results from FT-IR measurements with $NiAl_2O_4$ (PC12) upon (A) He purging after CO_2 adsorption under flow and (B) subsequent TPD.

7.6.2 CO_2 pulse experiment at 700 K

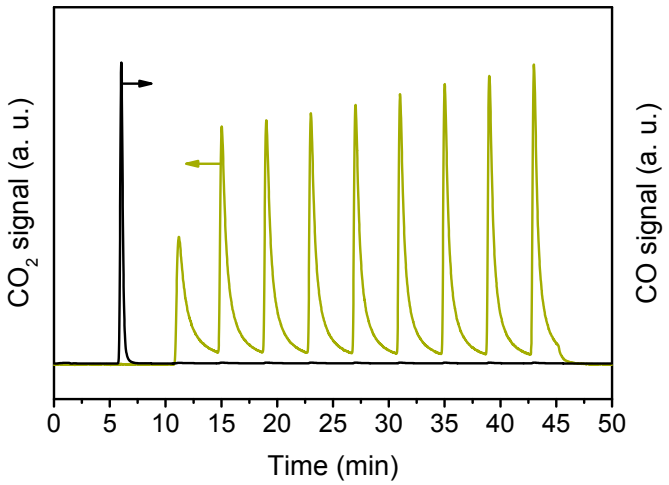

Figure 7.11: CO and CO_2 in the effluent gas upon pulsing 6 % CO_2 in He onto a reduced PC11 sample at 700 K (10 pulses).

7.6.3 XRD results

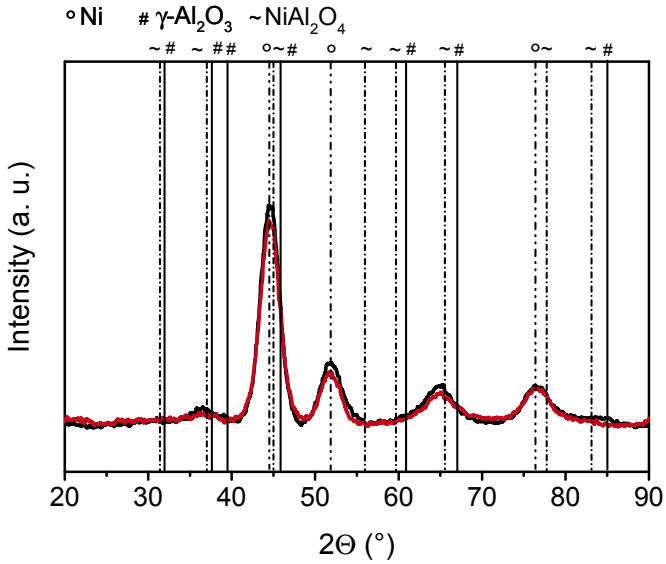

Figure 7.12: XRD pattern of PC11 after (black) reduction and (red) CO_2-TPD (JCPDS: Ni 78-0712, γ-Al_2O_3 10-0425, $NiAl_2O_4$ 10-0339).

7.6.4 CO_2-TPD measurements with alumina

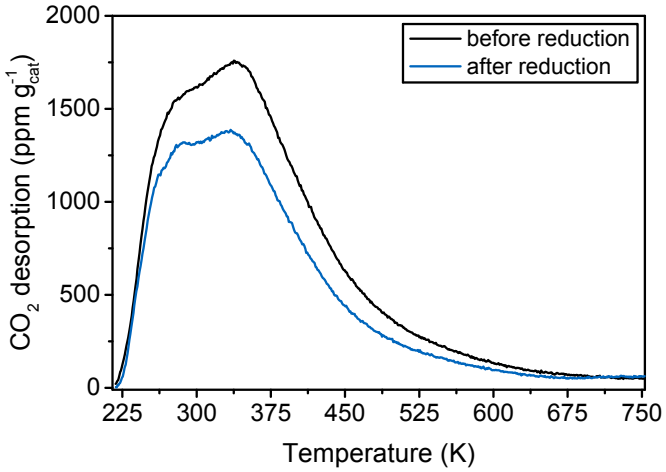

Figure 7.13: TPD results after CO_2 adsorption on γ-Al_2O_3 before and after reduction. CO_2 adsorption was conducted in a three step process comprising adsorption at 308 K, gradual cooling to 218 K under CO_2 and adsorption at 218 K for another 30 min.

8 Conclusion and Outlook

8.1 Conclusion

Methanation of CO_2 is a promising technology to efficiently store renewable energy within the Power-to-Gas (PtG) concept [10]. Therein, H_2, derived from water hydrolysis using a surplus of renewable energy, is converted with CO_2 to synthetic natural gas (SNG). SNG can be stored and transported within the natural gas grid and is reconverted for energy production when needed. Highly selective and stable catalysts are required to meet the requirements of SNG purity and to cope with the exothermal character of the reaction. Industrially, supported Ni catalysts are of great importance as they combine low cost and high selectivity but suffer from deactivation under severe reaction conditions. In order to design both active and thermostable catalysts, the knowledge of deactivation mechanisms and their interplay are essential. However, deactivation phenomena occurring in CO_2 methanation have only been scarcely investigated, although the reaction has been known for more than 100 years [22]. In this work, therefore, Ni catalysts for CO_2 methanation are investigated in greater detail.

For the measurements, Ni-Al catalysts with varying Ni loadings were synthesized via co-precipitation and incipient wetness impregnation. The structure of the precursors and calcined catalyst material was investigated by means of XRD, XPS, TPR and N_2 physisorption. The catalyst precursors after precipitation consist of mixed basic carbonates, the structure of which is highly dependent on the Ni content. Within this study, a takovite-like structure is observed as the only crystalline phase for Ni/Al ratios of 3 and higher. Upon calcination, crystalline Ni-Al mixed oxides are formed which consist of a NiO lattice with Al^{3+} being inserted as well as a Ni-containing spinel-like structure. The content of each phase is determined by the Ni/Al ratio of the catalyst. Higher Al contents give rise to the Ni-containing alumina in accordance with a decreasing reducibility. In impregnated samples, next to crystalline NiO supported on γ-Al_2O_3, an amorphous Ni-Al mixed oxide phase of decreased reducibility is also present, which partly encapsulates NiO. Also for impregnated samples, the reducibility declines with rising Al content. Impregnated samples are easier to reduce than precipitated samples at a comparable Ni loading. Metal-support interactions require higher temperatures to reduce free NiO as compares to pure NiO. All samples are mesoporous. In precipitated samples with Ni loadings beyond 38 wt-% agglomerates of plate like particles form slit-shaped pores, whereas

the pore structure in samples of lower Ni content is not well defined. The BET surface area decreases with increasing Ni content while the average pore diameter increases. Pore blockage, decreasing the pore volume and surface area, is observed in impregnated samples with Ni loadings exceeding 16 wt-%.

The interaction of H_2, a reactant in CO_2 methanation, was thoroughly investigated by means of H_2-TPD. The studies were coupled with a thorough investigation and elucidation of N_2O chemisorption as a fast and facile in situ technique to determine the active Ni surface area of activated samples. H_2-TPD within the temperature range from 84 to 753 K allows for a complete characterization of the H_2 interaction with supported Ni-Al catalysts. For hydrogen located in the subsurface region of Ni, a desorption signal at 150 K is observed, whereas H_2 adsorbed in the second layer on edges and cornes of the crystallites exhibits a broad pattern centered around 308 K. Two overlapping peaks between 300 and 750 K quantify H_2 adsorbed on the Ni surface. The H_2 interaction is also highly dependent on the experimental conditions applied. Elevated adsorption temperatures cause morphologic changes and a restructuring of the adsorbed hydrogen layer. A dynamic behavior of the Ni morphology is also observed when altering the gas atmosphere, the catalyst is exposed to prior to the measurement. From a quantitative analysis, it is evident that spillover effects bias the calculation of the Ni surface area, whereas values obtained from the H_2 uptake upon pulsed adsorption are in good agreement with static measurements.

N_2O chemisorption on the supported systems was shown to readily oxidize metallic Ni at room temperature. Oxidation proceeds in a three step process. Initially, a fast oxygen uptake takes place with formation of an oxide layer at a more moderate rate. Subsequent thickening of the oxide layer leads to subsurface and bulk oxidation. The oxidation process is independent from the N_2O partial pressure in the gas phase. For supported systems, the decoupling of surface from subsurface and bulk oxidation can be obtained at reaction temperatures between 190 and 195 K with a O/Ni_S ratio of 0.38 ± 0.07. The metallic surface area of Ni powder, on the contrary, can be reliably determined at chemisorption temperatures of 265 – 285 K at a O/Ni_S ratio of 0.96 ± 0.05. However, the low reaction temperatures, necessary to suppress subsurface and bulk oxidation, impede the application of N_2O chemisorption as an easy in situ technique for the metallic Ni surface area determination of the catalysts systems applied in this study.

In a second part, the deactivation of precipitated and impregnated Ni-Al catalysts under CO_2 methanation conditions was thoroughly investigated. The catalysts were aged evenly over the whole bed length at 8 bar and 523, 573 as well as 623 K under thermodynamic equilibrium using a stoichiometric feed gas composition. Periodic activity measurements under kinetically controlled conditions allowed for the obtainment of time dependent activity data. The water content in the gas atmosphere has shown to significantly accelerate deactivation, indicating hydrothermal sintering. For precipitated Ni-Al systems, the catalyst stability increases with rising Al content, whereas the catalyst activity decreases in the same order. The deactivation behavior can be described with a power law model. The activation energy is similar for each catalyst system studied and remains constant upon aging within the experimental error. This

suggests that the kind of active site, the reaction mechanism and the rate determining step, respectively, is the same for each catalytic system applied and is not changing upon aging.
Governing deactivation phenomena and structure-activity relationships were elucidated by means of a detailed characterization study. Fresh as well as samples aged for 25, 95 and 165 h were removed from the aging setup under inert conditions and characterized with standard and transient techniques. Upon reduction at 753 K, metallic Ni is formed with the Ni content in the mixed oxide phase decreasing. Complete reduction, however, cannot be achieved. Ni particle growth due to hydrothermal sintering is a main cause of deactivation next to an overall decrease of CO_2 adsorption capacity and the reduction of medium basic sites in particular. These phenomena are accompanied or induced by a decrease of the BET surface area and structural modifications due to Ni^{2+} depletion of the mixed oxide phase. A reduction of defects in the Ni phase became evident from H_2-TPD results as well as X-ray diffraction. The analysis of structure-activity relations indicates a complex interplay of deactivation mechanisms and/or structure sensitivity. Carbon deposition could be ruled out as a cause of deactivation.
Furthermore, the interaction of CO_2 with Ni-Al catalysts was studied in greater detail by FT-IR spectroscopy, CO_2-TPD as well as pulsed and static CO_2 chemisorption. CO_2 adsorption is highly sensitive to the adsorption mode applied. Adsorption under flow results in carbonate species on the oxide phase. Bicarbonate and bridged/"organic"-like species are formed on weak and strong basic sites, respectively, whereas monodentate and bidentate carbonate are observed on medium basic sites. The bond strength to the oxide increases in the order bicarbonate < bidentate carbonate < monodentate carbonate < bridged/"organic"-like species. Moreover, CO_2 adsorption was revealed to be an activated process, where weak basic sites forming bicarbonate are only partially filled at room temperature. An additional very weak adsorption site, which is not occupied at room temperature, is observed upon CO_2 adsorption at temperatures as low as 260 K. At temperatures higher than 600 K, oxidation of metallic Ni most likely takes place, forming gaseous CO. In addition to the formation of carbonates on the oxide phase, dissociative CO_2 adsorption on metallic Ni and formation of Ni-CO species are observed under static conditions at room temperature.

8.2 Outlook

The deactivation of Ni-Al catalysts under CO_2 methanation conditions has been shown to be a complicated process, giving rise to both a complex interplay of several deactivation mechanisms and structure sensitivity. To obtain a deeper understanding of deactivation, it is essential to decouple these effects.
To unravel structure sensitivity, the correlation between the catalyst activity and Ni particle size is essential, excluding support effects other than influencing the size and shape of the Ni particles. For a reliable determination of the Ni particle size, electron microscopy such as TEM

is advantageous, as Ni crystallite size determination by XRD and chemisorption techniques is impeded due to paracrystallinity and a changing degree of reduction during aging. TEM analysis would also facilitate the determination of particle size distributions as a function of aging time and temperature, allowing access to the modeling of Ni particle sintering. A key point, however, is the transfer between setups under inert conditions or the development of effective procedures for sample passivation, which is not straight forward due to the high oxophilic character of metallic Ni. Complementary EDX mapping and XPS studies would allow a more sophisticated elucidation of the catalyst structure and its alteration during aging, as amorphous phases are not detectable by means of X-ray diffraction. Also here, the problem of transferring fresh and deactivated samples between setups has to be overcome.

Individual adsorption sites, representing basic sites of variable strength and potentially different Ni facets are accessible by means of H_2- and CO_2-TPD. The differentiation between those sites on a quantitative basis holds great potential to investigate their individual influence on the catalyst performance by correlating their abundance with catalytic data. This necessitates a deconvolution of the corresponding TPD pattern based on an adequate kinetic model that has been tested against experimental data.

With regard to the results from CO_2-TPD and IR spectroscopy, the expansion of TPD/IR studies to promoted systems, also within a detailed deactivation study, is conceivable, since electronic promoter effects on the active Ni phase would become manifest in signal shifts in the desorption pattern and could be characterized by TPD.

Next to catalyst deactivation phenomena, also the reaction mechanism is still under debate and may alter depending on the catalyst composition. For its elucidation, operando IR and EXAFS measurements can be applied. The studies can be completed with transient measurements comprising temperature programmed surface reaction and switching experiments, which proved to be capable in clarifying reaction mechanisms [163, 271].

From an industrial point of view, biogenic and fossil feedstocks have great potential but generally contain poisoning compounds, such as H_2S, leading to severe catalyst deactivation. Efficient technologies exist to remove sulfur components from the feed gas, but are economically not feasible, especially in an decentralized operation of PtG units. In addition, complete sulfur coverages of Ni can still be obtained at H_2S concentrations typically present after feed gas preprocessing [106]. Therefore, the development of poisoning resistant catalysts plays a key role in commercializing CO_2 methanation for renewable energy storage at an industrial scale. For the tailoring of such systems, an understanding of poisoning mechanisms has to be established. Thereby, deactivation studies can be combined with the development of a kinetic model for catalyst poisoning in order to predict catalyst life times.

A Appendix

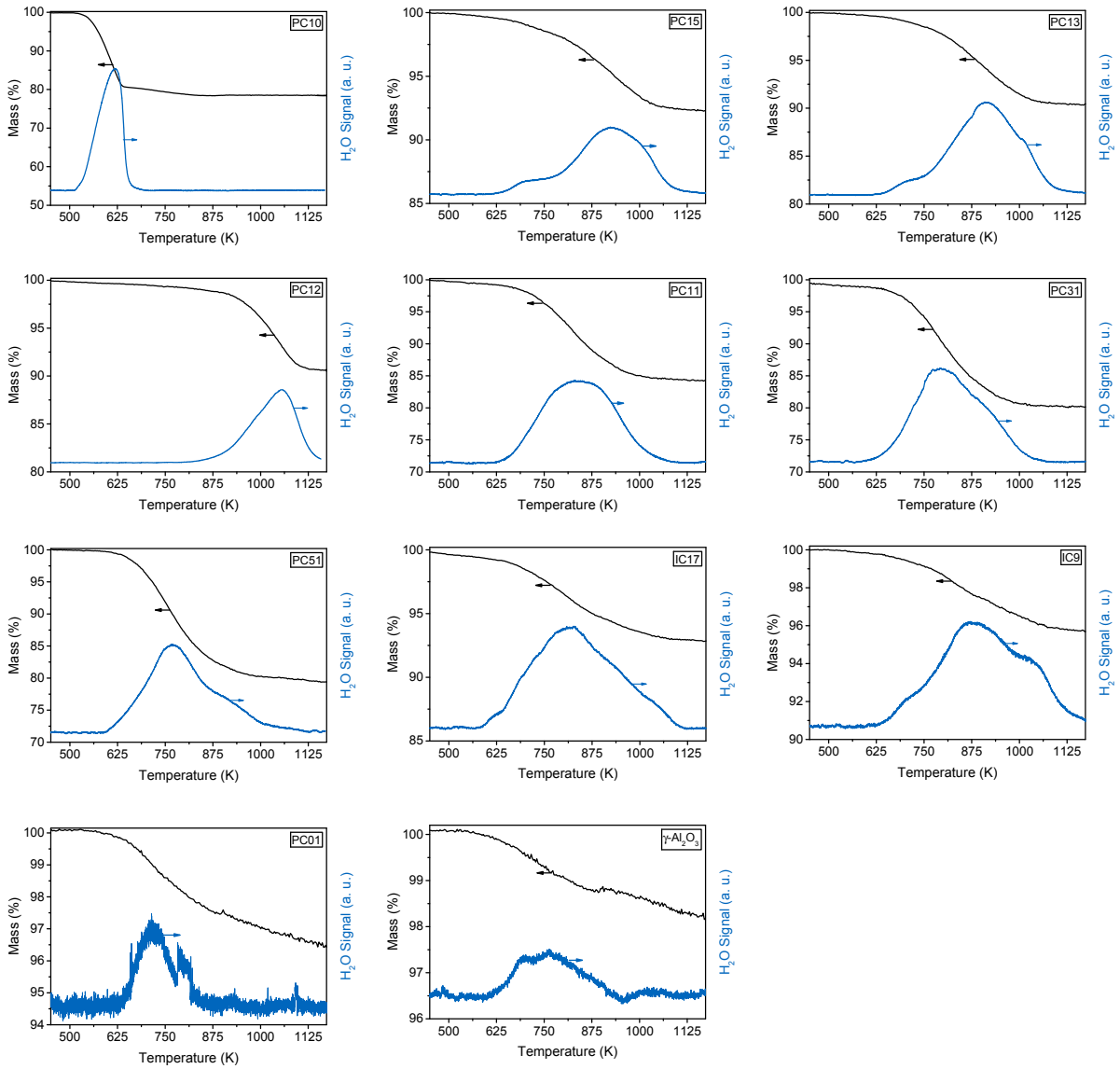

Figure A.1: Reduction profiles of synthesized catalyst samples.

B Bibliography

[1] M. R. Allen, O. P. Dube, W. Solecki, F. Aragón–Durand, W. Cramer, S. Humphreys, M. Kainuma, J. Kala, N. Mahowald, Y. Mulugetta, R. Perez, M. Wairiu, K. Zickfeld in *Global warming of 1.5°C. An IPCC Special Report on the impacts of global warming of 1.5°C above pre-industrial levels and related global greenhouse gas emission pathways, in the context of strengthening the global response to the threat of climate change, sustainable development, and efforts to eradicate poverty*, (Eds.: V. Masson-Delmotte, P. Zhai, H. O. Pörtner, D. Roberts, J. Skea, P. R. Shukla, A. Pirani, W. Moufouma-Okia, C. Péan, R. Pidcock, S. Connors, J. B. R. Matthews, Y. Chen, X. Zhou, M. I. Gomis, E. Lonnoy, T. Maycock, M. Tignor, W. T.), in press., **2018**.

[2] Framework Convention on Climate Change, *Adoption of the Paris Agreement*, (Ed.: United Nations), **2015**.

[3] J. Rogelj, D. Shindell, K. Jiang, S. Fifita, P. Forster, V. Ginzburg, C. Handa, H. Kheshgi, S. Kobayashi, E. Kriegler, L. Mundaca, R. Séférian, M. V. Vilariño in *Global warming of 1.5°C. An IPCC Special Report on the impacts of global warming of 1.5°C above pre-industrial levels and related global greenhouse gas emission pathways, in the context of strengthening the global response to the threat of climate change, sustainable development, and efforts to eradicate poverty*, (Eds.: V. Masson-Delmotte, P. Zhai, H. O. Pörtner, D. Roberts, J. Skea, P. R. Shukla, A. Pirani, W. Moufouma-Okia, C. Péan, R. Pidcock, S. Connors, J. B. R. Matthews, Y. Chen, X. Zhou, M. I. Gomis, E. Lonnoy, T. Maycock, M. Tignor, W. T.), in press., **2018**.

[4] H. de Coninck, A. Revi, M. Babiker, P. Bertoldi, M. Buckeridge, A. Cartwright, W. Dong, J. Ford, S. Fuss, J. Hourcade, D. Ley, R. Mechler, P. Newman, A. Revokatova, S. S., L. Steg, S. T. in *Global warming of 1.5°C. An IPCC Special Report on the impacts of global warming of 1.5°C above pre-industrial levels and related global greenhouse gas emission pathways, in the context of strengthening the global response to the threat of climate change, sustainable development, and efforts to eradicate poverty*, (Eds.: V. Masson-Delmotte, P. Zhai, H. O. Pörtner, D. Roberts, J. Skea, P. R. Shukla, A. Pirani, W. Moufouma-Okia, C. Péan, R. Pidcock, S. Connors, J. B. R. Matthews, Y. Chen, X. Zhou, M. I. Gomis, E. Lonnoy, T. Maycock, M. Tignor, W. T.), in press., **2018**.

[5] J. Roy, P. Tschakert, H. Waisman, S. Abdul Halim, P. Antwi-Agyei, P. Dasgupta, B. Hayward, M. Kanninen, D. Liverman, C. Okereke, P. F. Pinho, K. Riahi, A. G. Suarez Rodriguez in *Global warming of 1.5°C. An IPCC Special Report on the impacts of global warming of 1.5°C above pre-industrial levels and related global greenhouse gas emission pathways, in the context of strengthening the global response to the threat of climate change, sustainable development, and efforts to eradicate poverty*, (Eds.: V. Masson-Delmotte, P. Zhai, H. O. Pörtner, D. Roberts, J. Skea, P. R. Shukla, A. Pirani, W. Moufouma-Okia, C. Péan, R. Pidcock, S. Connors, J. B. R. Matthews, Y. Chen, X. Zhou, M. I. Gomis, E. Lonnoy, T. Maycock, M. Tignor, W. T.), in press., **2018**.

[6] BMWi, *Erneuerbare Energien Gesetz: EEG*, **2017**.

[7] Arbeitsgruppe Erneuerbare Energien-Statiskik (AGEE-Stat), *Entwicklung der erneuerbaren Energien in Deutschland im Jahr 2017*, (Ed.: BMWi), **2018**.

[8] Agora Energiewende, *Agarometer - Dokumentation*, **Oktober 2018**.

[9] S. Ewald, F. Koschany, D. Schlereth, M. Wolf, O. Hinrichsen, *Chemie in unserer Zeit* **2015**, *49*, 270–278.

[10] M. Sterner, *PhD Thesis*, Kassel University, **2009**.

[11] M. Specht, M. Sterner, J. Brellochs, V. Frick, B. Stuermer, U. Zuberbühler, G. Waldstein, *Erdöl Erdgas Kohle* **2010**, 342–346.

[12] M. A. A. Aziz, A. A. Jalil, S. Triwahyono, A. Ahmad, *Green Chemistry* **2015**, *17*, 2647–2663.

[13] S. Schiebahn, T. Grube, M. Robinius, L. Zhao, A. Otta, B. Kumar, M. Weber, D. Stolten in *Transition to Renewable Energy Systems*, (Eds.: D. Stolten, V. Scherer), Wiley-VCH, Weinheim, **2013**, pp. 813–848.

[14] F. Koschany, *PhD Thesis*, Technical University of Munich, **2016**.

[15] S. Rönsch, J. Schneider, S. Matthischke, M. Schluter, M. Gotz, J. Lefebvre, P. Prabhakaran, S. Bajohr, *Fuel* **2016**, *166*, 276–296.

[16] DVGW, Richtlinie G262, *Nutzung von Gasen aus regenerativen Quellen in der öffentlichen Gasversorgung*, **2011**.

[17] EN 16726 16726:2015, *Gasinfrastruktur – Beschaffenheit von Gas – Gruppe H*.

[18] T. Burger, F. Koschany, O. Thomys, K. Köhler, O. Hinrichsen, *Applied Catalysis A: General* **2018**, *558*, 44–54.

[19] A. E. Aksoylu, A. N. Akin, Z. İ. Önsan, D. L. Trimm, *Applied Catalysis A: General* **1996**, *145*, 185–193.

[20] Q. Pan, J. Peng, T. Sun, S. Wang, S. Wang, *Catalysis Communications* **2014**, *45*, 74–78.

[21] P. A. U. Aldana, F. Ocampo, K. Kobl, B. Louis, F. Thibault-Starzyk, M. Daturi, P. Bazin, S. Thomas, A. C. Roger, *Catalysis Today* **2013**, *215*, 201–207.

[22] P. Sabatier, J. Senderens, *Comptes Rendus de l'Acad'emie des Sciences* **1902**, *134*, 689–691.

[23] J. J. Gao, Y. L. Wang, Y. Ping, D. C. Hu, G. W. Xu, F. N. Gu, F. B. Su, *RSC Advances* **2012**, *2*, 2358–2368.

[24] J. J. Gao, Q. Liu, F. N. Gu, B. Liu, Z. Y. Zhong, F. B. Su, *RSC Advances* **2015**, *5*, 22759–22776.

[25] J. Xu, G. F. Froment, *AIChE Journal* **1989**, *35*, 88–96.

[26] D. Schlereth, O. Hinrichsen, *Chemical Engineering Research and Design* **2013**, *92*, 702–712.

[27] W. Wang, S. Wang, X. Ma, J. Gong, *Chemical Society Reviews* **2011**, *40*, 3703–3727.

[28] G. D. Weatherbee, C. H. Bartholomew, *Journal of Catalysis* **1984**, *87*, 352–362.

[29] F. Solymosi, A. Erdöhelyi, *Journal of Molecular Catalysis* **1980**, *8*, 471–474.

[30] F. Solymosi, A. Erdöhelyi, M. Kocsis, *Journal of Catalysis* **1980**, *65*, 428–436.

[31] F. Solymosi, A. Erdöhelyi, T. Bansagi, *Journal of Catalysis* **1981**, *68*, 371–382.

[32] A. Karelovic, P. Ruiz, *Applied Catalysis B: Environmental* **2012**, *113-114*, 237–249.

[33] A. Karelovic, P. Ruiz, *Journal of Catalysis* **2013**, *301*, 141–153.

[34] A. T. Bell, *Journal of Molecular Catalysis A: Chemical* **1995**, *100*, 1–11.

[35] K. P. Yu, W. Y. Yu, M. C. Kuo, Y. C. Liou, S. H. Chien, *Applied Catalysis B: Environmental* **2008**, *84*, 112–118.

[36] Z. L. Zhang, A. Kladi, X. E. Verykios, *Journal of Catalysis* **1994**, *148*, 737–747.

[37] F. Solymosi, I. Tombácz, J. Koszta, *Journal of Catalysis* **1985**, *95*, 578–586.

[38] K. J. Williams, A. B. Boffa, M. Salmeron, A. T. Bell, G. A. Somorjai, *Catalysis Letters* **1991**, *9*, 415–426.

[39] A. Beuls, C. Swalus, M. Jacquemin, G. Heyen, A. Karelovic, P. Ruiz, *Applied Catalysis B: Environmental* **2012**, *113-114*, 2–10.

[40] J. N. Park, E. W. McFarland, *Journal of Catalysis* **2009**, *266*, 92–97.

[41] J. H. Kim, D. J. Suh, T. J. Park, K. L. Kim, *Applied Catalysis A: General* **2000**, *197*, 191–200.

[42] J. Martins, N. Batail, S. Silva, S. Rafik-Clement, A. Karelovic, D. P. Debecker, A. Chaumonnot, D. Uzio, *Catalysis Communications* **2015**, *58*, 11–15.

[43] T. Abe, M. Tanizawa, K. Watanabe, A. Taguchi, *Energy & Environmental Science* **2009**, *2*, 315–321.

[44] Z. Kowalczyk, K. Stołecki, W. Raróg-Pilecka, E. Miśkiewicz, E. Wilczkowska, Z. Karpiński, *Applied Catalysis A: General* **2008**, *342*, 35–39.

[45] S. Tada, O. J. Ochieng, R. Kikuchi, T. Haneda, H. Kameyama, *International Journal of Hydrogen Energy* **2014**, *39*, 10090–10100.

[46] T. Li, S. Wang, D. N. Gao, S. D. Wang, *Journal of Fuel Chemistry and Technology* **2014**, *42*, 1440–1446.

[47] J. Xu, Q. Lin, X. Su, H. Duan, H. Geng, Y. Huang, *Chinese Journal of Chemical Engineering* **2016**, *24*, 140–145.

[48] G. Garbarino, P. Riani, L. Magistri, G. Busca, *International Journal of Hydrogen Energy* **2014**, *39*, 11557–11565.

[49] G. Garbarino, D. Bellotti, P. Riani, L. Magistri, G. Busca, *International Journal of Hydrogen Energy* **2015**, *40*, 9171–9182.

[50] K. Zhao, Z. Li, L. Bian, *Frontiers of Chemical Science and Engineering* **2016**, *10*, 273–280.

[51] K. B. Kester, E. Zagli, J. L. Falconer, *Applied Catalysis* **1986**, *22*, 311–319.

[52] A. E. Aksoylu, Z. İ. Önsan, *Applied Catalysis A: General* **1997**, *164*, 1–11.

[53] J. L. Falconer, A. E. Zagli, *Journal of Catalysis* **1980**, *62*, 280–285.

[54] C. K. Vance, C. H. Bartholomew, *Applied Catalysis* **1983**, *7*, 169–177.

[55] C. Schüler, *PhD Thesis*, Technical University of Munich, **2018**.

[56] J. Liu, C. Li, F. Wang, S. He, H. Chen, Y. Zhao, M. Wei, D. G. Evans, X. Duan, *Catalysis Science & Technology* **2013**, *3*, 2627–2633.

[57] R. Zhou, N. Rui, Z. Fan, C. J. Liu, *International Journal of Hydrogen Energy* **2016**, *41*, 22017–22025.

[58] S. Tada, T. Shimizu, H. Kameyama, T. Haneda, R. Kikuchi, *International Journal of Hydrogen Energy* **2012**, *37*, 5527–5531.

[59] S. Abate, C. Mebrahtu, E. Giglio, F. Deorsola, S. Bensaid, S. Perathoner, R. Pirone, G. Centi, *Industrial & Engineering Chemistry Research* **2016**, *55*, 4451–4460.

[60] D. C. D. da Silva, S. Letichevsky, L. E. P. Borges, L. G. Appel, *International Journal of Hydrogen Energy* **2012**, *37*, 8923–8928.

[61] K. Zhao, W. Wang, Z. Li, *Journal of CO_2 Utilization* **2016**, *16*, 236–244.

[62] C. Mebrahtu, S. Abate, S. Perathoner, S. Chen, G. Centi, *Catalysis Today* **2018**, *304*, 181–189.

[63] D. Pandey, G. Deo, *Journal of Industrial and Engineering Chemistry* **2016**, *33*, 99–107.

[64] H. Takano, K. Izumiya, N. Kumagai, K. Hashimoto, *Applied Surface Science* **2011**, *257*, 8171–8176.

[65] F. Ocampo, B. Louis, A. C. Roger, *Applied Catalysis A: General* **2009**, *369*, 90–96.

[66] F. Ocampo, B. Louis, L. Kiwi-Minsker, A.-C. Roger, *Applied Catalysis A: General* **2011**, *392*, 36–44.

[67] H. Muroyama, Y. Tsuda, T. Asakoshi, H. Masitah, T. Okanishi, T. Matsui, K. Eguchi, *Journal of Catalysis* **2016**, *343*, 178–184.

[68] S. Rahmani, M. Rezaei, F. Meshkani, *Journal of Industrial and Engineering Chemistry* **2014**, *20*, 1346–1352.

[69] H. C. Wu, Y. C. Chang, J. H. Wu, J. H. Lin, I. K. Lin, C. S. Chen, *Catalysis Science & Technology* **2015**, *5*, 4154–4163.

[70] C. Schüler, F. Betzenbichler, C. Drescher, O. Hinrichsen, *Chemical Engineering Research and Design* **2018**, *132*, 303–312.

[71] M. A. A. Aziz, A. A. Jalil, S. Triwahyono, S. M. Sidik, *Applied Catalysis A: General* **2014**, *486*, 115–122.

[72] M. A. A. Aziz, A. A. Jalil, S. Triwahyono, R. R. Mukti, Y. H. Taufiq-Yap, M. R. Sazegar, *Applied Catalysis B: Environmental* **2014**, *147*, 359–368.

[73] M. A. A. Aziz, A. A. Jalil, S. Triwahyono, M. W. A. Saad, *Chemical Engineering Journal* **2015**, *260*, 757–764.

[74] G. Du, S. Lim, Y. Yang, C. Wang, L. Pfefferle, G. L. Haller, *Journal of Catalysis* **2007**, *249*, 370–379.

[75] A. Quindimil, U. De-La-Torre, B. Pereda-Ayo, J. A. González-Marcos, J. R. González-Velasco, *Applied Catalysis B: Environmental* **2018**, *238*, 393–403.

[76] M. C. Bacariza, I. Graça, J. M. Lopes, C. Henriques, *Microporous and Mesoporous Materials* **2018**, *267*, 9–19.

[77] V. Hulea, D. Brunel, A. Galarneau, K. Philippot, B. Chaudret, P. J. Kooyman, F. Fajula, *Microporous and Mesoporous Materials* **2005**, *79*, 185–194.

[78] G. D. Weatherbee, C. H. Bartholomew, *Journal of Catalysis* **1982**, *77*, 460–472.

[79] F. Koschany, D. Schlereth, O. Hinrichsen, *Applied Catalysis B: Environmental* **2016**, *181*, 504–516.

[80] S. Abello, C. Berrueco, D. Montane, *Fuel* **2013**, *113*, 598–609.

[81] S. Abello, C. Berrueco, F. Gispert-Guirado, D. Montane, *Catalysis Science & Technology* **2016**, *6*, 2305–2317.

[82] S. Abate, K. Barbera, E. Giglio, F. Deorsola, S. Bensaid, S. Perathoner, R. Pirone, G. Centi, *Industrial & Engineering Chemistry Research* **2016**, *55*, 8299–8308.

[83] P. Marocco, E. A. Morosanu, E. Giglio, D. Ferrero, C. Mebrahtu, A. Lanzini, S. Abate, S. Bensaid, S. Perathoner, M. Santarelli, R. Pirone, G. Centi, *Fuel* **2018**, *225*, 230–242.

[84] L. He, Q. Lin, Y. Liu, Y. Huang, *Journal of Energy Chemistry* **2014**, *23*, 587–592.

[85] M. Gabrovska, R. Edreva-Kardjieva, D. Crişan, P. Tzvetkov, M. Shopska, I. Shtereva, *Reaction Kinetics Mechanisms and Catalysis* **2012**, *105*, 79–99.

[86] D. Wierzbicki, R. Baran, R. Dębek, M. Motak, T. Grzybek, M. E. Gálvez, P. Da Costa, *International Journal of Hydrogen Energy* **2017**, *42*, 23548–23555.

[87] D. C. Puxley, I. J. Kitchener, C. Komodromos, N. D. Parkyns in *Studies in Surface Science and Catalysis*, *Vol. 16*, (Eds.: G. Poncelet, P. Grange, P. A. Jacobs), Elsevier, **1983**, pp. 237–271.

[88] L. E. Alzamora, J. R. H. Ross, E. C. Kruissink, L. L. van Reijen, *Journal of the Chemical Society Faraday Transactions 1: Physical Chemistry in Condensed Phases* **1981**, *77*, 665–681.

[89] E. C. Kruissink, E. B. M. Doesburg, L. L. van Reijen, L. E. Alzamora, S. Orr, J. R. H. Ross, G. van Veen in *Studies in Surface Science and Catalysis*, *Vol. 3*, (Eds.: B. Delmon, P. Grange, P. Jacobs, G. Poncelet), Elsevier, **1979**, pp. 143–157.

[90] J. Zieliński, *Journal of Molecular Catalysis* **1993**, *83*, 197–206.

[91] P. Frontera, A. Macario, M. Ferraro, P. Antonucci, *Catalysts* **2017**, *7*, 59.

[92] Y. Mori, T. Mori, A. Miyamoto, N. Takahashi, T. Hattori, Y. Murakami, *Journal of Physical Chemistry* **1989**, *93*, 2039–2043.

[93] Y. Mori, T. Mori, T. Hattori, Y. Murakami, *Journal of Physical Chemistry* **1990**, *94*, 4575–4579.

[94] M. A. Henderson, S. D. Worley, *Surface Science* **1985**, *149*, L1–L6.

[95] M. Marwood, R. Doepper, A. Renken, *Applied Catalysis A: General* **1997**, *151*, 223–246.

[96] P. Panagiotopoulou, D. I. Kondarides, X. E. Verykios, *Journal of Physical Chemistry C* **2011**, *115*, 1220–1230.

[97] Y. X. Pan, C. J. Liu, Q. Ge, *Journal of Catalysis* **2010**, *272*, 227–234.

[98] S. Akamaru, T. Shimazaki, M. Kubo, T. Abe, *Applied Catalysis A: General* **2014**, *470*, 405–411.

[99] M. Jacquemin, A. Beuls, P. Ruiz, *Catalysis Today* **2010**, *157*, 462–466.

[100] Q. Pan, J. Peng, S. Wang, S. Wang, *Catalysis Science & Technology* **2014**, *4*, 502–509.

[101] E. Vesselli, M. Rizzi, L. De Rogatis, X. Ding, A. Baraldi, G. Comelli, L. Savio, L. Vattuone, M. Rocca, P. Fornasiero, A. Baldereschi, M. Peressi, *The Journal of Physical Chemistry Letters* **2010**, *1*, 402–406.

[102] E. Vesselli, J. Schweicher, A. Bundhoo, A. Frennet, N. Kruse, *Journal of Physical Chemistry C* **2011**, *115*, 1255–1260.

[103] S. Eckle, H. G. Anfang, R. J. Behm, *Journal of Physical Chemistry C* **2011**, *115*, 1361–1367.

[104] J. A. Moulijn, A. E. van Diepen, F. Kapteijn, *Applied Catalysis A: General* **2001**, *212*, 3–16.

[105] J. Sehested, *Catalysis Today* **2006**, *111*, 103–110.

[106] C. H. Bartholomew, *Applied Catalysis A: General* **2001**, *212*, 17–60.

[107] P. Forzatti, L. Lietti, *Catalysis Today* **1999**, *52*, 165–181.

[108] J. R. Rostrup-Nielsen, K. Pedersen, J. Sehested, *Applied Catalysis A: General* **2007**, *330*, 134–138.

[109] J. Zieliński, *Journal of Catalysis* **1982**, *76*, 157–163.

[110] J. Zieliński, *Applied Catalysis A: General* **1993**, *94*, 107–115.

[111] R. Lamber, G. Schulz-Ekloff, *Surface Science* **1991**, *258*, 107–118.

[112] S. Ewald, M. Kolbeck, T. Kratky, M. Wolf, O. Hinrichsen, *Applied Catalysis A: General* **2019**, *570*, 376–386.

[113] J. Sehested, J. A. P. Gelten, I. N. Remediakis, H. Bengaard, J. K. Nørskov, *Journal of Catalysis* **2004**, *223*, 432–443.

[114] J. Sehested, J. A. P. Gelten, S. Helveg, *Applied Catalysis A: General* **2006**, *309*, 237–246.

[115] J. Barrientos, M. Lualdi, R. Suárez París, V. Montes, M. Boutonnet, S. Järås, *Applied Catalysis A: General* **2015**, *502*, 276–286.

[116] W. M. Shen, J. A. Dumesic, C. G. Hill, *Journal of Catalysis* **1981**, *68*, 152–165.

[117] R. B. Pannell, K. S. Chung, C. H. Bartholomew, *Journal of Catalysis* **1977**, *46*, 340–347.

[118] M. Agnelli, M. Kolb, C. Mirodatos, *Journal of Catalysis* **1994**, *148*, 9–21.

[119] P. Munnik, M. E. Z. Velthoen, P. E. de Jongh, K. P. de Jong, C. J. Gommes, *Angewandte Chemie International Edition* **2014**, *53*, 9493–9497.

[120] J. Barrientos, N. González, M. Lualdi, M. Boutonnet, S. Järås, *Applied Catalysis A: General* **2016**, *514*, 91–102.

[121] C. H. Bartholomew, *Catalysis Reviews* **1982**, *24*, 67–112.

[122] S. Helveg, C. López-Cartes, J. Sehested, P. L. Hansen, B. S. Clausen, J. R. Rostrup-Nielsen, F. Abild-Pedersen, J. K. Nørskov, *Nature* **2004**, *427*, 426.

[123] F. Abild-Pedersen, J. K. Nørskov, J. R. Rostrup-Nielsen, J. Sehested, S. Helveg, *Physical Review B* **2006**, *73*, 115419.

[124] D. Duprez, M. C. DeMicheli, P. Marecot, J. Barbier, O. A. Ferretti, E. N. Ponzi, *Journal of Catalysis* **1990**, *124*, 324–335.

[125] B. Mutz, H. W. P. Carvalho, S. Mangold, W. Kleist, J.-D. Grunwaldt, *Journal of Catalysis* **2015**, *327*, 48–53.

[126] B. Nielsen, J. Villadsen, *Applied Catalysis* **1984**, *11*, 123–138.

[127] J. R. Rostrup-Nielsen, *Concepts in Syngas Manufacture*, Imperial College Press, London, **2011**.

[128] J. R. Rostrup-Nielsen, *Journal of Catalysis* **1973**, *31*, 173–199.

[129] J. R. Rostrup-Nielsen, K. Pedersen, *Journal of Catalysis* **1979**, *59*, 395–404.

[130] W. D. Fitzharris, J. R. Katzer, W. H. Manogue, *Journal of Catalysis* **1982**, *76*, 369–384.

[131] C. H. Bartholomew, P. K. Agrawal, J. R. Katzer in *Advances in Catalysis*, *Vol. 31*, (Eds.: D. D. Eley, H. Pines, P. B. Weisz), Academic Press, **1982**, pp. 135–242.

[132] B. Legras, V. V. Ordomsky, C. Dujardin, M. Virginie, A. Y. Khodakov, *ACS Catalysis* **2014**, *4*, 2785–2791.

[133] E. J. Erekson, C. H. Bartholomew, *Applied Catalysis* **1983**, *5*, 323–336.

[134] J. R. Rostrup-Nielsen, *Journal of Catalysis* **1971**, *21*, 171–178.

[135] J. Zieliński, *Polish Journal of Chemistry* **1995**, *69*, 1187–1195.

[136] J. R. Rostrup-Nielsen in *Catalysis Science and Technology*, *Vol. 5*, (Eds.: J. R. Anderson, M. Boudart), Springer, Berlin, **1984**, pp. 1–117.

[137] J. Zieliński, *Catalysis Letters* **1992**, *12*, 389–393.

[138] O. Levenspiel, *Journal of Catalysis* **1972**, *25*, 265–272.

[139] G. A. Fuentes, *Applied Catalysis* **1985**, *15*, 33–40.

[140] F. Schüth, M. Hesse, K. K. Unger in *Handbook of Heterogeneous Catalysis*, (Eds.: G. Ertl, H. Knözinger, F. Schüth, J. Weitkamp), Wiley-VCH, Weinheim, **2008**, pp. 100–119.

[141] C. H. Bartholomew, R. J. Farrauto, *Fundamentals of industrial catalytic processes*, Second ed., Wiley, Hoboken, New Jersey, **2006**.

[142] F. Schüth, M. D. Ward, J. M. Buriak, *Chemistry of Materials* **2018**, *30*, 3599–3600.

[143] K. S. Sing, D. H. Everett, R. A. W. Haul, L. Moscou, R. A. Pierotti, J. Rouquerol, T. Siemieniewska, *Pure and Applied Chemistry* **1985**, *57*, 603–619.

[144] S. Brunauer, P. H. Emmett, E. Teller, *Journal of the American Chemical Society* **1938**, *60*, 309–319.

[145] S. Lowell, J. E. Shields, M. A. Thomas, M. Thommes, *Characterization of Porous Solids and Powders: Surface Area, Pore Size and Density*, Kluwer Academic Publishers, Dordrecht, **2004**.

[146] D. Ongari, P. G. Boyd, S. Barthel, M. Witman, M. Haranczyk, B. Smit, *Langmuir* **2017**, *33*, 14529–14538.

[147] G. Bergeret, P. Gallezot in *Handbook of Heterogeneous Catalysis*, (Eds.: G. Ertl, H. Knözinger, F. Schüth, J. Weitkamp), Wiley-VCH, Weinheim, **2008**, pp. 738–765.

[148] M. Fadoni, L. Lucarelli, *Studies in Surface Science and Catalysis* **1999**, *120*, 177–225.

[149] S. Tada, M. Yokoyama, R. Kikuchi, T. Haneda, H. Kameyama, *Journal of Physical Chemistry C* **2013**, *117*, 14652–14658.

[150] C. H. Bartholomew, R. B. Pannell, *Journal of Catalysis* **1980**, *65*, 390–401.

[151] L. Spieß, G. Teichert, R. Schwarzer, H. Behnken, C. Genzel, *Moderne Röntgenbeugung*, Second ed., Vieweg+Teubner, Wiesbaden, **2009**.

[152] E. Lifshin, R. L. Snyder, *X-ray Characterization of Materials*, Wiley-VCH, Weinheim, **1999**.

[153] H. Krischner, B. Koppelhuber-Bitschnau, *Röntgenstrukturanalyse und Rietveldmethode: Eine Einführung*, Fifth ed., Springer Fachmedien, Wiesbaden, **1994**.

[154] V. Y. Young, G. B. Hoflund in *Handbook of Surface and Interface Analysis: Methods of Problem-Solving*, (Eds.: J. C. Rivière, S. Myhra), CRC-Press, Boca Raton, **2009**, pp. 19–64.

[155] J. F. Moulder, W. F. Stickle, P. E. Sobol, K. D. Bomben, *Handbook of X-Ray Photoelectron Spectroscopy*, Perkin-Elmer, Eden Prairie, **1992**.

[156] S. Bienz, L. Bigler, T. Fox, H. Meier, *Spektroskopische Methoden in der organischen Chemie*, Ninth ed., Georg Thieme Verlag, Stuttgart, **2016**.

[157] H. Günzler, H. U. Gremlich, *IR-Spektroskopie: Eine Einführung*, Fourth ed., Wiley-VCH, Weinheim, **2003**.

[158] W. D. Perkins, *Journal of Chemical Education* **1987**, *64*, A269.

[159] M. Wagner, *Thermal Analysis in Practice: Fundamental Aspects*, Carl Hanser Verlag, Munich, **2018**.

[160] S. Ewald, O. Hinrichsen, *Applied Catalysis A: General*, *submitted*.

[161] S. Ewald, S. Standl, O. Hinrichsen, *Applied Catalysis A: General* **2018**, *549*, 93–101.

[162] Y. Amenomiya, R. J. Cvetanovic, *Journal of Physical Chemistry* **1963**, *67*, 144–147.

[163] T. Genger, *PhD Thesis*, Ruhr-Universität Bochum, **2000**.

[164] M. Muhler, L. P. Nielsen, E. Törnqvist, B. S. Clausen, H. Topsøe, *Catalysis Letters* **1992**, *14*, 241–249.

[165] M. B. Fichtl, O. Hinrichsen, *Catalysis Letters* **2014**, *144*, 2114–2120.

[166] J. M. Kanervo, K. M. Reinikainen, A. O. I. Krause, *Applied Catalysis A: General* **2004**, *258*, 135–144.

[167] M. Peter, *PhD Thesis*, Technical University of Munich, **2012**.

[168] R. A. Demmin, R. J. Gorte, *Journal of Catalysis* **1984**, *90*, 32–39.

[169] R. J. Gorte, *Journal of Catalysis* **1982**, *75*, 164–174.

[170] J. M. Kanervo, T. J. Keskitalo, R. I. Slioor, A. O. I. Krause, *Journal of Catalysis* **2006**, *238*, 382–393.

[171] E. E. Ibok, D. F. Ollis, *Journal of Catalysis* **1980**, *66*, 391–400.

[172] J. S. Rieck, A. T. Bell, *Journal of Catalysis* **1984**, *85*, 143–153.

[173] M. B. Fichtl, J. Schumann, I. Kasatkin, N. Jacobsen, M. Behrens, R. Schlögl, M. Muhler, O. Hinrichsen, *Angewandte Chemie International Edition* **2014**, *53*, 7043–7047.

[174] O. Hinrichsen, T. Genger, M. Muhler, *Chemical Engineering & Technology* **2000**, *23*, 956–959.

[175] J. Dawody, L. Eurenius, H. Abdulhamid, M. Skoglundh, E. Olsson, E. Fridell, *Applied Catalysis A: General* **2005**, *296*, 157–168.

[176] S. R. Seyedmonir, D. E. Strohmayer, G. L. Geoffroy, M. A. Vannice, H. W. Young, J. W. Linowski, *Journal of Catalysis* **1984**, *87*, 424–436.

[177] P. H. M. De Korte, E. B. M. Doesburg, C. P. J. De Winter, L. L. Van Reijen, *Solid State Ionics* **1985**, *16*, 73–80.

[178] E. C. Kruissink, L. L. van Reijen, J. R. H. Ross, *Journal of the Chemical Society Faraday Transactions 1: Physical Chemistry in Condensed Phases* **1981**, *77*, 649–663.

[179] B. Bems, M. Schur, A. Dassenoy, H. Junkes, D. Herein, R. Schlögl, *Chemistry – A European Journal* **2003**, *9*, 2039–2052.

[180] R. Dębek, M. Motak, T. Grzybek, M. Galvez, P. Da Costa, *Catalysts* **2017**, *7*, 32.

[181] S. Kannan, A. Narayanan, C. S. Swamy, *Journal of Materials Science* **1996**, *31*, 2353–2360.

[182] K. V. R. Chary, P. V. R. Rao, V. Vishwanathan, *Catalysis Communications* **2006**, *7*, 974–978.

[183] M. Li, X. Wang, S. Li, S. Wang, X. Ma, *International Journal of Hydrogen Energy* **2010**, *35*, 6699–6708.

[184] G. Li, L. Hu, J. M. Hill, *Applied Catalysis A: General* **2006**, *301*, 16–24.

[185] C. Li, Y. W. Chen, *Thermochimica Acta* **1995**, *256*, 457–465.

[186] C. H. Bartholomew, R. B. Pannell, R. W. Fowler, *Journal of Catalysis* **1983**, *79*, 34–46.

[187] J. Hu, J. A. Schwarz, Y. J. Huang, *Applied Catalysis* **1989**, *51*, 223–233.

[188] J. L. Ewbank, L. Kovarik, F. Z. Diallo, C. Sievers, *Applied Catalysis A: General* **2015**, *494*, 57–67.

[189] J. A. Dalmon, G. A. Martin, *Journal of the Chemical Society Faraday Transactions 1: Physical Chemistry in Condensed Phases* **1979**, *75*, 1011–1015.

[190] J. Barrientos, M. Lualdi, M. Boutonnet, S. Järås, *Applied Catalysis A: General* **2014**, *486*, 143–149.

[191] X. Bai, S. Wang, T. Sun, S. Wang, *Reaction Kinetics Mechanisms and Catalysis* **2014**, *112*, 437–451.

[192] J. N. Dew, R. R. White, C. M. Sliepcevich, *Industrial & Engineering Chemistry* **1955**, *47*, 140–146.

[193] C. Schild, A. Wokaun, R. A. Koeppel, A. Baiker, *Journal of Physical Chemistry* **1991**, *95*, 6341–6346.

[194] M. Schoder, U. Armbruster, A. Martin, *Chemie Ingenieur Technik* **2013**, *85*, 344–352.

[195] B. W. Hoffer, A. Dick van Langeveld, J. P. Janssens, R. L. C. Bonné, C. M. Lok, J. A. Moulijn, *Journal of Catalysis* **2000**, *192*, 432–440.

[196] R. Geyer, J. Hunold, M. Keck, P. Kraak, A. Pachulski, R. Schödel, *Chemie Ingenieur Technik* **2012**, *84*, 160–164.

[197] M. A. Vannice, *Journal of Catalysis* **1975**, *37*, 449–461.

[198] M. B. Fichtl, D. Schlereth, N. Jacobsen, I. Kasatkin, J. Schumann, M. Behrens, R. Schlögl, O. Hinrichsen, *Applied Catalysis A: General* **2015**, *502*, 262–270.

[199] P. A. Redhead, *Vacuum* **1962**, *12*, 203–211.

[200] D. A. King, *Surface Science* **1975**, *47*, 384–402.

[201] J. Tabatabaei, B. Sakakini, M. Watson, K. Waugh, *Catalysis Letters* **1999**, *59*, 143–149.

[202] J. L. Falconer, J. A. Schwarz, *Catalysis Reviews* **1983**, *25*, 141–227.

[203] S. Smeds, T. Salmi, L. P. Lindfors, O. Krause, *Applied Catalysis A: General* **1996**, *144*, 177–194.

[204] L. Znak, J. Zieliński, *Langmuir* **2006**, *22*, 8758–8763.

[205] L. Znak, J. Zieliński, *Applied Catalysis A: General* **2008**, *334*, 268–276.

[206] T. J. Osinga, B. G. Linsen, W. P. van Beek, *Journal of Catalysis* **1967**, *7*, 277–279.

[207] J. J. F. Scholten, J. A. Konvalinka, *Transactions of the Faraday Society* **1969**, *65*, 2465–2473.

[208] A. Rudajevova, V. Pour, *Collection of Czechoslovak Chemical Communications* **1975**, *40*, 1126–1134.

[209] E. G. M. Kuijpers, M. W. C. M. A. Nieuwesteeg, G. J. Wermer, J. W. Geus, *Journal of Catalysis* **1988**, *112*, 107–115.

[210] Y. S. Ho, C. T. Yeh, *Journal of Molecular Catalysis* **1990**, *59*, 53–59.

[211] C. J. Wright, C. G. Windsor, D. C. Puxley, *Journal of Catalysis* **1982**, *78*, 257–261.

[212] S. Velu, S. K. Gangwal, *Solid State Ionics* **2006**, *177*, 803–811.

[213] P. I. Lee, J. A. Schwarz, *Journal of Catalysis* **1982**, *73*, 272–287.

[214] T. A. Jachimowski, B. Meng, D. F. Johnson, W. H. Weinberg, *Journal of Vacuum Science & Technology A: Vacuum Surfaces and Films* **1995**, *13*, 1564–1568.

[215] D. M. Stockwell, A. Bertucco, G. W. Coulston, C. O. Bennett, *Journal of Catalysis* **1988**, *113*, 317–324.

[216] B. S. Clausen, J. Schiøtz, L. Gråbæk, C. V. Ovesen, K. W. Jacobsen, J. K. Nørskov, H. Topsøe, *Topics in Catalysis* **1994**, *1*, 367–376.

[217] J. D. Grunwaldt, A. M. Molenbroek, N. Y. Topsøe, H. Topsøe, B. S. Clausen, *Journal of Catalysis* **2000**, *194*, 452–460.

[218] P. Väterlein, T. Krause, M. Bäßler, R. Fink, E. Umbach, J. Taborski, V. Wüstenhagen, W. Wurth, *Physical Review Letters* **1996**, *76*, 4749–4752.

[219] R. Sau, J. B. Hudson, *Journal of Vacuum Science and Technology* **1981**, *18*, 607–610.

[220] D. A. Hoffman, J. B. Hudson, *Surface Science* **1987**, *180*, 77–88.

[221] R. van Hardeveld, A. van Montfoort, *Surface Science* **1966**, *4*, 396–430.

[222] J. Zieliński, *Applied Catalysis* **1987**, *35*, 1–12.

[223] M. Streibel, N. Nakaten, T. Kempka, M. Kühn, *Energy Procedia* **2013**, *40*, 202–211.

[224] K. Ghaib, F. Z. Ben-Fares, *Renewable and Sustainable Energy Reviews* **2018**, *81*, 433–446.

[225] J. M. Rynkowski, T. Paryjczak, A. Lewicki, M. I. Szynkowska, T. P. Maniecki, W. K. Jóźwiak, *Reaction Kinetics and Catalysis Letters* **2000**, *71*, 55–64.

[226] M. Kuśmierz, *Catalysis Today* **2008**, *137*, 429–432.

[227] A. Kim, D. P. Debecker, F. Devred, V. Dubois, C. Sanchez, C. Sassoye, *Applied Catalysis B: Environmental* **2018**, *220*, 615–625.

[228] H. Y. Kim, H. M. Lee, J. N. Park, *Journal of Physical Chemistry C* **2010**, *114*, 7128–7131.

[229] R. A. Hubble, J. Y. Lim, J. S. Dennis, *Faraday Discussions* **2016**, *192*, 529–544.

[230] J. Ren, X. Qin, J. Z. Yang, Z. F. Qin, H. L. Guo, J. Y. Lin, Z. Li, *Fuel Processing Technology* **2015**, *137*, 204–211.

[231] L. Pastor-Pérez, E. L. Saché, C. Jones, S. Gu, H. Arellano-Garcia, T. R. Reina, *Catalysis Today* **2018**, *317*, 108–113.

[232] B. Mutz, A. Gänzler, M. Nachtegaal, O. Müller, R. Frahm, W. Kleist, J. D. Grunwaldt, *Catalysts* **2017**, *7*, 279.

[233] C. H. Bartholomew, *Applied Catalysis A: General* **1993**, *107*, 1–57.

[234] A. P. Grosvenor, M. C. Biesinger, R. S. C. Smart, N. S. McIntyre, *Surface Science* **2006**, *600*, 1771–1779.

[235] A. N. Mansour, *Surface Science Spectra* **1994**, *3*, 231.

[236] S. Tanuma, C. J. Powell, D. R. Penn, *Surface and Interface Analysis* **2003**, *35*, 268–275.

[237] R. Maatman, S. Hiemstra, *Journal of Catalysis* **1980**, *62*, 349–356.

[238] T. van Herwijnen, H. van Doesburg, W. A. Jong, *Journal of Catalysis* **1973**, *28*, 391–402.

[239] M. D. Argyle, C. H. Bartholomew, *Catalysts* **2015**, *5*, 145–269.

[240] J. Sehested, *Journal of Catalysis* **2003**, *217*, 417–426.

[241] J. I. Di Cosimo, C. R. Apesteguía, M. J. L. Ginés, E. Iglesia, *Journal of Catalysis* **2000**, *190*, 261–275.

[242] X. Wang, M. Shen, L. Song, Y. Su, J. Wang, *Physical Chemistry Chemical Physics* **2011**, *13*, 15589–15596.

[243] W. Xie, H. Peng, L. Chen, *Journal of Molecular Catalysis A: Chemical* **2006**, *246*, 24–32.

[244] C. Mebrahtu, F. Krebs, S. Perathoner, S. Abate, G. Centi, R. Palkovits, *Catalysis Science & Technology* **2018**, *8*, 1016–1027.

[245] F. Touahra, M. Sehailia, W. Ketir, K. Bachari, R. Chebout, M. Trari, O. Cherifi, D. Halliche, *Applied Petrochemical Research* **2016**, *6*, 1–13.

[246] M. F. L. Johnson, *Journal of Catalysis* **1990**, *123*, 245–259.

[247] H. Li, Y. Xu, C. Gao, Y. Zhao, *Catalysis Today* **2010**, *158*, 475–480.

[248] R. Dittmeyer, G. Emig in *Handbook of Heterogeneous Catalysis*, *Vol. 1*, (Eds.: G. Ertl, H. Knözinger, F. Schüth, J. Weitkamp), Wiley-VCH, Weinheim, **2008**, pp. 1727–1787.

[249] M. P. Andersson, F. Abild-Pedersen, I. N. Remediakis, T. Bligaard, G. Jones, J. Engbæk, O. Lytken, S. Horch, J. H. Nielsen, J. Sehested, *Journal of Catalysis* **2008**, *255*, 6–19.

[250] S. He, C. Li, H. Chen, D. Su, B. Zhang, X. Cao, B. Wang, M. Wei, D. G. Evans, X. Duan, *Chemistry of Materials* **2013**, *25*, 1040–1046.

[251] S. Tada, R. Kikuchi, *Catalysis Science & Technology* **2015**, *5*, 3061–3070.

[252] C. W. Hu, J. Yao, H. Q. Yang, Y. Chen, A. M. Tian, *Journal of Catalysis* **1997**, *166*, 1–7.

[253] C. Vogt, E. Groeneveld, G. Kamsma, M. Nachtegaal, L. Lu, C. J. Kiely, P. H. Berben, F. Meirer, B. M. Weckhuysen, *Nature Catalysis* **2018**, *1*, 127–134.

[254] R. B. Shalvoy, B. H. Davis, P. J. Reucroft, *Surface and Interface Analysis* **1980**, *2*, 11–16.

[255] G. Busca, V. Lorenzelli, *Materials Chemistry* **1982**, *7*, 89–126.

[256] J. I. Di Cosimo, V. K. Díez, M. Xu, E. Iglesia, C. R. Apesteguía, *Journal of Catalysis* **1998**, *178*, 499–510.

[257] C. Morterra, G. Magnacca, *Catalysis Today* **1996**, *27*, 497–532.

[258] W. Wei, G. Jinlong, *Frontiers of Chemical Science and Engineering* **2011**, *5*, 2–10.

[259] H. Du, C. T. Williams, A. D. Ebner, J. A. Ritter, *Chemistry of Materials* **2010**, *22*, 3519–3526.

[260] H. A. Prescott, Z. J. Li, E. Kemnitz, A. Trunschke, J. Deutsch, H. Lieske, A. Auroux, *Journal of Catalysis* **2005**, *234*, 119–130.

[261] Y. D. Ding, G. Song, X. Zhu, R. Chen, Q. Liao, *RSC Advances* **2015**, *5*, 30929–30935.

[262] T. Miyao, W. Shen, A. Chen, K. Higashiyama, M. Watanabe, *Applied Catalysis A: General* **2014**, *486*, 187–192.

[263] S. T. Korhonen, M. Calatayud, A. O. I. Krause, *Journal of Physical Chemistry C* **2008**, *112*, 16096–16102.

[264] A. Ueno, J. K. Hochmuth, C. O. Bennett, *Journal of Catalysis* **1977**, *49*, 225–235.

[265] S. Derrouiche, D. Bianchi, *Applied Catalysis A: General* **2006**, *313*, 208–217.

[266] S. Fujita, M. Nakamura, T. Doi, N. Takezawa, *Applied Catalysis A: General* **1993**, *104*, 87–100.

[267] L. Surnev, Z. Xu, J. T. Yates, *Surface Science* **1988**, *201*, 1–13.

[268] X. Zhu, Y. P. Zhang, C. J. Liu, *Catalysis Letters* **2007**, *118*, 306–312.

[269] S. G. Wang, D. B. Cao, Y. W. Li, J. Wang, H. Jiao, *Journal of Physical Chemistry C* **2005**, *109*, 18956–63.

[270] U. Burghaus, *Progress in Surface Science* **2014**, *89*, 161–217.

[271] L. Qian, Z.-F. Yang, *Journal of Natural Gas Chemistry* **2002**, *11*, 151–158.

Publication list

Publications

- S. Ewald, F. Koschany, M. Wolf, D. Schlereth, O. Hinrichsen, *Katalyse und Reaktionstechnik: Power-to-Gas*, Chemie in unserer Zeit, **2015**, *49*, 270-278.

- S. Ewald, S. Standl, O. Hinrichsen, *Characterization of nickel catalysts with transient methods*, Applied Catalysis A: General, **2018**, *549*, 93-101.

- S. Ewald, M. Kolbeck, T. Kratky, M. Wolf, O. Hinrichsen, *On the deactivation of Ni-Al catalysts in CO_2 methanation*, Applied Catalysis A: General, **2019**, *570*, 376-386.

- S. Ewald, O. Hinrichsen, *On the interaction of CO_2 with Ni-Al catalysts*, Applied Catalysis A: General, **2019**, *580*, 71-80.

Selected conference contributions

Oral presentations

- S. Ewald, O. Hinrichsen, *Catalyst deactivation during CO_2 methanation*, 50. Jahrestreffen Deutscher Katalytiker (Weimar, Germany, **2017**).

- S. Ewald, M. Kolbeck, O. Hinrichsen, *CO_2 methanation - Insights into catalyst deactivation*, 13th European Congress on Catalysis, (Florence, Italy, **2017**).

Poster presentations

- S. Ewald, O. Hinrichsen, *Kinetic Investigation of CO_2 Conversion with Transient Testing Methods*, European Symposium on Chemical Reaction Engineering, (Fürstenfeldbruck, Germany, **2015**).

- S. Ewald, O. Hinrichsen, *On the surface determination of a coprecipitated Ni/Al_2O_3 catalyst by chemisorption of N_2O and H_2*, 49. Jahrestreffen Deutscher Katalytiker, (Weimar, Germany, **2016**).

- S. Ewald, O. Hinrichsen, *On the surface determination of a coprecipitated Ni/Al_2O_3 catalyst by chemisorption of N_2O and H_2*, 16th International Congress on Catalysis, (Beijing, China, **2016**).

- S. Ewald, M. Kolbeck, O. Hinrichsen, *Interaction of CO_2 with Ni-Al catalysts*, 51. Jahrestreffen Deutscher Katalytiker, (Weimar, Germany, **2018**).

Declaration

The submitted thesis was supervised by Prof. Dr.-Ing. Kai-Olaf Hinrichsen.

Affirmation
Hereby, I affirm that I am the sole author of this thesis. To the best of my knowledge, I affirm that this thesis does not infringe upon anyone's copyright nor violate any proprietary rights. I affirm that any ideas, techniques, quotations, or any other material, are in accordance with standard referencing practices.

Moreover, I affirm that, so far, the thesis has not been forwarded to a third party nor is it published. I obeyed all study regulations of the Technische Universität München.

Remarks about the internet
Throughout the work, the internet was used for research and verification. Many of the keywords provided herein, references and other information can be verified on the internet. However, no sources are given, because all statements made in this work are fully covered by the cited literature sources.

Garching, February 13, 2019

Stefan Ewald